Advancing the Understanding of Sandwich Structures through Mechanical Behaviour Modelling and Failure Analysis of FSSW-Joined Honeycomb Core

A Thesis Submitted
In Partial Fulfillment of the Requirements
for the degree of

DOCTOR OF PHILOSOPHY

by

Avneesh Kumar

(196103010)

Department of Mechanical Engineering

Indian Institute of Technology Guwahati

Guwahati-781039, India

October, 2024

Certificate

It is certified that the work contained in the Thesis titled "**Advancing the Understanding of Sandwich Structures through Mechanical Behaviour Modelling and Failure Analysis of FSSW-Joined Honeycomb Core**" submitted by **Avneesh Kumar** to the Indian Institute of Technology Guwahati for the award of the degree of Doctor of Philosophy has been carried out under my supervision in the Department of Mechanical Engineering, Indian Institute of Technology Guwahati. This work has not been submitted elsewhere for the award of any other degree.

24th October, 2024

Prof. R. Ganesh Narayanan
Professor
Department of Mechanical Engineering
Indian Institute of Technology Guwahati
Guwahati — 781039

Prof. Nelson Muthu
Associate Professor
Department of Mechanical Engineering
Indian Institute of Technology Palakkad
Palakkad — 678623

Acknowledgements

This thesis is the result of five years of dedicated research at IIT Guwahati. The journey was challenging, and I am grateful to many people who offered guidance and support along the way. I would like to express my deep appreciation to all those who helped me during this time.

First, I want to sincerely thank my supervisors, Dr. Nelson Muthu and Prof. R. Ganesh Narayanan. Their support was essential for completing this research. I am also thankful to my doctoral committee members, Prof. D. Chakraborty, Prof. Prasenjit Khanikar, and Prof. Amit Shelke, for their valuable advice and suggestions.

I am grateful to the Head of the Department of Mechanical Engineering at IIT Guwahati for providing a supportive environment and giving me access to the Shimadzu UTM, which was crucial for my research. I also thank Mr. N. K. Das, Assistant Workshop Superintendent, for his timely help with experimental challenges. I appreciate the assistance of the technical staff at the Central Workshop, IIT Guwahati, who helped fabricate experimental specimens and customized fixtures. Thanks to Mr. Sanjib Sarma for his helpful suggestions during the testings. The companionship of my friends made my five years at IIT Guwahati enjoyable. I would like to thank Mr. Ashok Kumar, Dr. Atul Singh, and Mr. Rahul Kumar for their continuous support during my studies and in critical situations. I am also grateful to my labmates and seniors Dr. Pran, Dr. Sasanka, Dr. Atchuta, Dr. Sai, Mr. Lalit, Mr. Pabbu, and Mr. Rakesh, Mr. Sukant, Mr. Priyabrata for their support and discussions on research-related issues. I appreciate the Central Workshop and the Fracture Mechanics and Composite Structures Laboratory at IIT Guwahati for giving me access to the facilities I needed. I also want to thank the Central Instrument Facility, the Strength of Materials Laboratory, and the SHIMADZU UTM at IIT Guwahati for providing the necessary equipment for my experiments.

Finally, I want to thank my parents, my brother and my wife for their encouragement and emotional support, which helped me stay calm and focused throughout this journey. I'm also thankful to the Ministry of Human Resource Development, Government of India, for their financial support during my doctoral program.

24th October

Avneesh Kumar
IIT Guwahati


भारतीय प्रौद्योगिकी संस्थान गुवाहाटी
Indian Institute of Technology Guwahati

Abstract

The modern automotive industry is focused on addressing the global energy crisis and environmental issues by promoting energy conservation and pollution reduction, particularly through the development of lightweight vehicles, including electric cars, whose range is heavily dependent on their weight. Sandwich components have become widely used in the automotive industry due to their lightweight properties, high bending stiffness, energy absorption, and strength. Among these, honeycomb core structures are particularly advantageous as they offer superior control over mechanical and crash-worthiness features due to their customizable anisotropic properties and periodic structure. Recently, several investigations have attempted to reinforce sandwich structures using various joining techniques to enhance their mechanical properties, such as stiffness and strength. Traditionally, adhesives and mechanical fasteners have been commonly employed to join the sandwich cores and skins. For instance, adhesive bonding (AB) is extensively used in applications such as car interior parts, aircraft components, racing equipment, and marine applications. However, controlling the quality of AB joints can be challenging due to sensitivity to factors such as humidity, temperature, and surface treatments. While additive manufacturing (AM) techniques offer potential solutions, they face significant challenges related to material properties and high costs for industrial production, as AM parts often differ substantially from those produced by traditional methods. Mechanical fastening, such as using rivets, can cause deformation during joining, resulting in a hole in the rivet tail, reducing the residual compressive force, and making the joints prone to loosening. Stress concentrations around the fastener holes add extra weight to the structure. This ongoing quest for efficient, reliable, and cost-effective joining methods remains a critical area of research in manufacturing sandwich structures.

Amid these challenges, Friction Stir Spot Welding (FSSW) presents a promising energy-efficient, eco-friendly, and sustainable alternative that produces parts with minimal distortion. Although FSSW is effective for joining aluminum and polymer sandwich sheets, it primarily results in interfacial bonding between aluminum face sheets, with the polymer layer being extruded from the welded region. Consequently, FSSW alone may not achieve the desired mechanical properties for sandwich sheets. Hybrid bonding (HB), combining adhesive bonding and welding, has shown potential in increasing joint area and improving joint strength by

reducing stress concentration, making it particularly relevant for enhancing the mechanical properties of sandwich structures with honeycomb cores.

Despite progress in understanding various joint types, research on spot welding sandwich sheets, especially those with honeycomb cores, remains scarce. Most studies have focused on weld-only, adhesive-only, and hybrid bond joints, often overlooking the potential benefits of combining FSSW with AB in honeycomb core sandwich structures. This research gap has motivated the design and development of novel hybrid joints (FSSW+AB) for these sandwich structures. This work investigates the mechanical behavior of sandwich structures with honeycomb cores, with the aim of advancing the application and performance of lightweight materials in the automotive industry, thus contributing to the development of more efficient, reliable and environmentally friendly vehicles. This exploration into hybrid joining techniques not only has the potential to enhance the mechanical properties of sandwich structures, but also aligns with the broader goals of energy conservation and pollution reduction in the automotive industry.

The main objective of this thesis is to manufacture honeycomb core sandwich structures using FSSW joining strategies as a potential alternative or enhancement to existing AB methods. Research seeks to improve the mechanical properties, durability, and overall performance of honeycomb core sandwich structures, including the development of numerical simulations to predict joining performance. Key subobjectives include understanding the FSSW of sandwich sheets with different welding parameters, analyzing honeycomb core sandwich sheets produced by various fabrication processes, developing equivalent models for honeycomb cores and cohesive layers, and investigating failure behavior using cohesive zone modeling (CZM).). Mechanical performance evaluations, including lap shear tests, peel tests, three-point bending tests (3PBT), and mixed-mode bending tests (MMB), are performed to assess the strength and failure of these structures, with results compared to numerical simulations conducted using Abaqus® 2017 software.

Abbreviations

3PBT	Three-point bending
AB	Adhesive-bonded
CZM	Cohesive zone modelling
EDX	Energy-dispersive X-ray
FBD	Free body diagram
FE	Finite element
FEA	Finite element analysis
FEM	Finite element method
FSW	Friction stir welding
FSSW	Friction stir spot welding
FSSW_AB	FSSW with adhesive bonding
FSSW_D	FSSW with disc insert
FSSW_D_1.8	FSSW with disc insert at 1.8 mm plunge depth
FSSW_D_2	FSSW with disc insert at 2 mm plunge depth
FSSW_D_750	FSSW with disc insert at 750 rpm
FSSW_D_1200	FSSW with disc insert at 1200 rpm
FSSW_D_AB	FSSW with disc insert and adhesive bonding or hybrid bonding
FSSW_D_AB_1.8	FSSW with disc insert and adhesive bonding at 1.8 mm plunge depth
FSSW_D_AB_2	FSSW with disc insert and adhesive bonding at 2 mm plunge depth
FSSW_D_AB_750	FSSW with disc insert and adhesive bonding at 750 rpm
FSSW_D_AB_1200	FSSW with disc insert and adhesive bonding at 1200 rpm
MMB	Mixed mode bending
PBC	Periodic boundary conditions
RCE	Representative cell element
RVE	Representative volume element
RSW	Resistance spot welding
SEM	Scanning electron microscopy
UTM	Universal testing machine

Nomenclature

A_c	Projected cell area
A_s	Density of solid material
D	Scalar damage variable
E_s	Young's modulus of the material of the RCE
E_1	In-plane longitudinal Young's modulus
E_2	In-plane transverse Young's modulus
E_3	Out-of-plane Young's modulus
v	Poisson's ratio
v_{12}	In-plane Poisson's ratio
G_{12}	In-plane shear modulus
G_{13}, G_{23}	Out-of-plane shear modulus
G_s	Shear modulus of the material
G_n, G_{s_1}, and G_{s_2}	Fracture energies in the normal, primary and secondary shear directions
G_n^c, $G_{s_1}^c$, and $G_{s_2}^c$	Critical fracture energies in the normal, primary and secondary shear directions
h	Vertical cell wall length
l	Inclined cell wall length
t	Cell wall thickness
θ	cell angle
$\delta_n^0, \delta_s^0, \delta_m^0$	Normal, shear, and mixed mode separation corresponding to damage initiation along the cohesive zone
$\delta_n^f, \delta_s^f, \delta_m^f$	Normal, shear, and mixed mode final separation along the cohesive zone, respectively
δ^f	Ultimate separation corresponding mode
ρ_s	Density of solid material

σ_n	Normal cohesive stress
σ^0	Maximum cohesive strength corresponding mode
σ_n^c	Critical normal cohesive stress
σ_s	Shear cohesive stress
σ_s^c	Critical shear cohesive stress
$\sigma_{\max}^c, K^{\mathrm{n}}, G_c^{\mathrm{n}}$	Critical stress, stiffness, and critical fracture toughness in normal directions
$\tau_{\max}^c, K^{\mathrm{s}}, G_c^{\mathrm{s}}$	Critical stress, stiffness, and critical fracture toughness in shear directions
$\left(\sigma_{\mathrm{h}}^c\right)_{\mathrm{m}}, \left(\tau_{\mathrm{h}}^c\right)_{\mathrm{m}}, A_{\mathrm{h}}$	Maximum normal strength, shear strength and cross-sectional area of the RCE of the cohesive layer
$\left(\sigma_{\mathrm{ho}}^c\right)_{\mathrm{m}}, \left(\tau_{\mathrm{ho}}^c\right)_{\mathrm{m}}, A_{\mathrm{ho}}$	Maximum normal, shear strength, and cross-sectional area of the equivalent cohesive layer
$K_{\mathrm{h}}^n, K_{\mathrm{h}}^s$, and $K_{\mathrm{ho}}^n, K_{\mathrm{ho}}^s$	Normal and shear stiffness of the cohesive layer and its equivalent form, respectively
ψ	Mode mixity phase angle

Contents

CHAPTER 2 EQUIVALENT ORTHOTROPIC PROPERTIES OF PERIODIC HONEYCOMB STRUCTURE: STRAIN ENERGY APPROACH AND HOMOGENIZATION **29**

CHAPTER 7 PEEL TEST PERFORMANCE ANALYSIS OF HONEYCOMB CORE SANDWICH PANELS FABRICATED USING FSSW STRATEGIES 133

List of Figures

List of Tables

Chapter 1 Introduction, Literature review, Significance, and Objective of the work

1.1 Introduction

With the global energy shortage and the worsening environmental conditions, reducing energy consumption and emissions has become crucial in the modern automotive industry. One effective approach to these challenges is the development of lightweight vehicles, particularly electric cars, whose range depends significantly on their weight. Lightweight structures, such as sandwich components with two outer panels and light core material, are highly valued in the automotive industry for their specific bending stiffness, strength, and energy absorption. These structures are often used in front end bumpers and battery cases. However, the exact mechanisms of their failure are still topics of further research and optimization. Among the lightweight materials for sandwich cores, foam and honeycomb are popular choices. Honeycomb structures, because of their periodic nature and customizable anisotropic properties, offer better control over mechanical performance and crashworthiness than randomly structured foam cores.

Stiffness and strength are two mechanical properties that can be potentially improved in sandwich structures by reinforcement using different joining methods. Friction stir spot welding (FSSW) has emerged as a promising method for this purpose. FSSW has been widely accepted for joining various materials and is effective even for materials with different properties. Given its effectiveness with aluminium, FSSW has been used to join aluminium honeycomb core sandwich sheets. However, spot welding research for these sandwich sheets is limited. Most studies have concentrated on sandwich sheets with polymer cores, and there is no reported literature on spot welding of honeycomb core sandwich sheets. The inclusion of a honeycomb core makes the FSSW process particularly interesting compared to traditional adhesive-bonded (AB) joints.

The current research explores the potential use of a hybrid joining method (FSSW+AB) for the joining of sandwich structures as an alternative to traditional spot welding and adhesive joining methods. Therefore, the present work aims to investigate the mechanical behaviour of sandwich structures with honeycomb cores fabricated using the FSSW and the AB.

Additionally, this work seeks to predict the performance of these sandwich structures to facilitate efficient process design. The research aims to optimize the fabrication process to improve durability, strength, and overall structural integrity by understanding mechanical properties and performance characteristics.

1.2 Literature survey

This section analyzes the honeycomb core sandwich sheets, including their properties, advantages, disadvantages, and applications. In addition, an extensive review of the literature investigates the effects of process parameters on joint performance in friction stir welding (FSW) and FSSW. Subsequently, a detailed literature review investigates the joining of sandwich sheets and numerical analysis of the joining of sandwich sheets.

1.2.1 Introduction to honeycomb core sandwich sheets

Honeycomb cores are specialized materials known for their discrete and orthotropic properties, making them highly suitable for applications where weight is a critical factor. These cores are widely employed in aerospace, marine, and automotive sectors due to the exceptional stiffness-to-weight ratios when measured through their thickness. Honeycomb cores are a vital component in sandwich panels consisting of two thin face sheets. These face sheets are adhesively attached to less dense core filler materials, as shown in Figure 1.1.

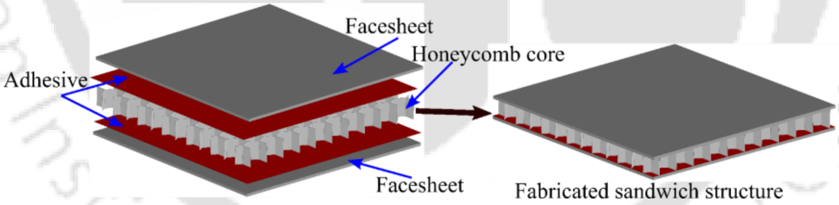

Figure 1.1 Honeycomb core sandwich structure

In these sandwich panels, the core is primarily responsible for carrying transverse shear loads and maintaining the separation between the face sheets. Meanwhile, the face sheets themselves bear the plane loads and bending moments. This configuration not only enhances the structural integrity of the panel but also contributes to its high flexural stiffness. This increased stiffness significantly improves the stability of the panel, making it an ideal choice for demanding structural applications.

Furthermore, honeycomb sandwich panels offer excellent fatigue resistance, which ensures their longevity even under cyclic loading conditions. Another notable advantage is their capability for noise abatement, making them useful in applications where sound reduction is desired. These combined features— noise abatement, increased stability, high flexural stiffness and good fatigue resistance—underscore the versatility and effectiveness of honeycomb sandwich panels in various high-performance engineering fields.

Honeycomb cores are available in a variety of cell wall materials and geometries, each with its own set of advantages for the strength, rigidity, weight, and manufacturability of sandwich panels. These cores are manufactured from a wide variety of materials, some of which are metallic and others of which are non-metallic [1,2]. The diversity in materials allows for custom solutions to meet specific engineering requirements.

As illustrated in Figure 1.2, honeycomb cores often include cell forms that consist of hexagons and their variations, flex, and square-core configurations [1]. Among these, hexagonal cells are the most prevalent due to the manufacturing efficiencies they provide. The hexagonal geometry is particularly advantageous because it balances material usage with structural performance, making it a cost-effective option for many applications.

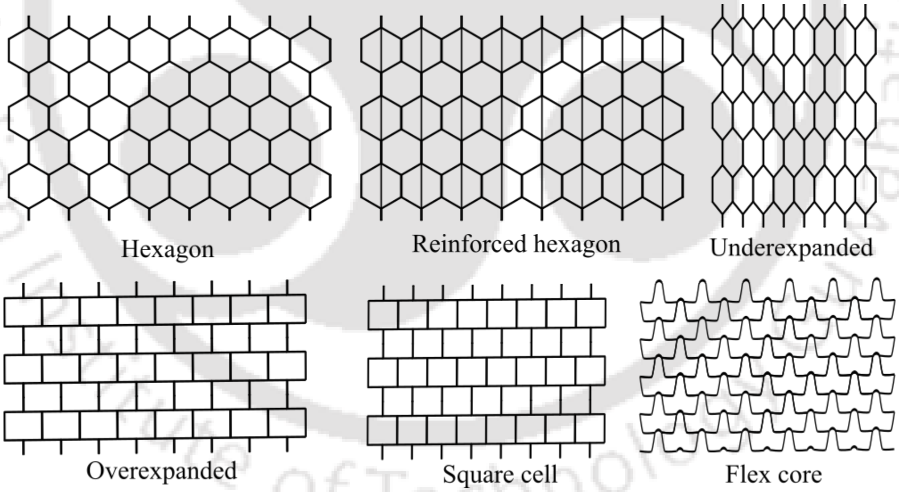

Figure 1.2 Various honeycomb configurations [1]

Other cell geometries, such as squares and flex-core shapes, are essentially variants of the hexagonal configuration. These variations are designed to attain different mechanical characteristics for the core. For instance, specific shapes may be optimized for enhanced flexibility, greater strength, or better energy absorption, depending on the intended application of the honeycomb core.

Honeycomb cores are often manufactured using a variety of processes, including diffusion bonding, brazing, adhesive bonding, resistance welding, and thermal fusing. The most popular approach is adhesive bonding. This procedure requires putting adhesive lines on the sheet material, which is subsequently turned into the honeycomb core using one of two methods: expansion or corrugation, as shown in Figure 1.3. The sheet material is expanded during the expansion process to generate the honeycomb structure. On the contrary, the corrugation method includes corrugating the sheet material before bonding it to make the honeycomb. Notably, the adhesive lines may account for up to 10% of the honeycomb weight in corrugated cores, but in expanded cores, it is only 1% or less [1].

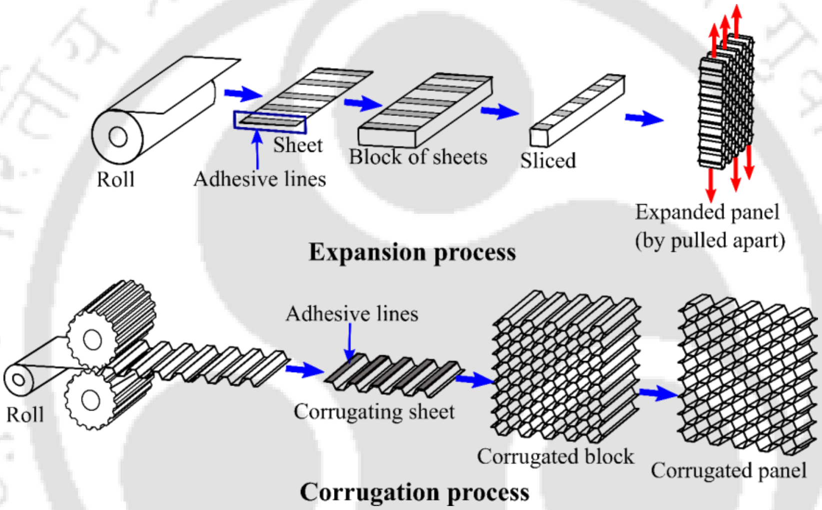

Figure 1.3 Manufacturing of an adhesively bonded honeycomb structure [1]

Adhesively bonded honeycomb core geometry consists of double, single, and inclined cell walls. Figure 1.4 shows the core cell geometry, which is often employed in theoretical and numerical analyses presented in the literature. This cell simplifies the complicated structure, making it easier to model and analyze and providing a standardized reference for comparing research and optimizing core designs.

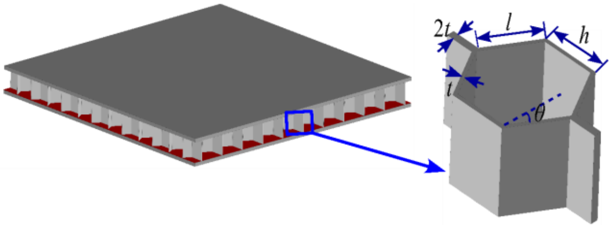

Figure 1.4 A core cell of the honeycomb sandwich structure

Depending on the material properties of the core, a sandwich structure responds differently to different types of loading. Therefore, many analytical and computational models have been developed to investigate the equivalent elastic characteristics of honeycomb structures to understand the response of the material. The equivalent material properties can be calculated by choosing a unit cell of the core called representative cell element (RCE) or representative volume element (RVE). As the regular honeycomb core is periodic, it is possible to isolate a basic RCE that can be replicated to generate the whole honeycomb core and examine only the RCE rather than the entire honeycomb core. Various RCEs that have been used before are shown in Figure 1.5.

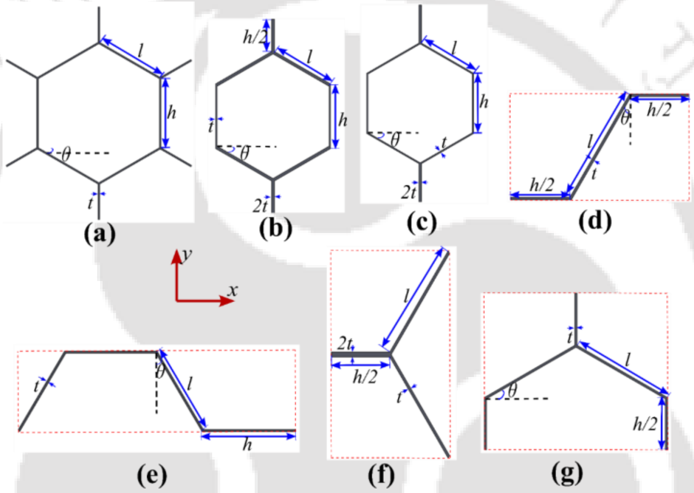

Figure 1.5 The RCE used by (a) Gibson and Ashby [2], (b) Hedayati *et al.*[3], Malek and Gibson [4], Sorohan *et al.* [5], Qiu *et al.* [6], and Zhao *et al.* [7], (c) Penado [8], (d) Catapano and Montemurro [9], (e) Kelsey *et al.* [10], (f) Pan *et al.* [11], and (g) Goswami [12]

Numerous efforts have been made by researchers to estimate the in-plane and out-of-plane properties of honeycomb cores. Gibson and Ashby [2] developed some of the earliest and most influential models for honeycomb cores, modelled the cell walls as beams and assumed in-plane properties were isotropic. They determined the out-of-plane properties based on the basis of relative density of the cell wall material, with the in-plane Poisson's ratio set to unity. Using theorems of minimum potential and complementary energy, they derived upper and lower constraints for the transverse shear moduli, concluding that the accurate values for transverse shear properties could only be obtained through numerical solutions.

Masters and Evans [13] approached the problem by dividing the deformation of the hexagonal unit cell into three parts: flexure, stretching, and hinging. They derived stiffness constants for each deformation mode based on simple force-displacement relationships and rewrote the formulae of Gibson and Ashby [2] in terms of these constants. Masters and Evans [13] concluded that the behaviour of the hexagonal core is isotropic in the in-plane directions, providing a more nuanced understanding of the mechanical response of the honeycomb cores.

Several studies have been conducted by several researchers to find out the properties of honeycomb cores that have double cell wall thickness, which are often produced by manufacturing methods such as expansion or corrugation.Burton and Noor [14] developed analytical equations comparable to the Gibson and Ashby [2] models, but included the influence of double thickness in their analyses. This resulted in more accurate estimates for the nine elastic constants of the honeycomb core. However, their model predictions are restricted to idealized honeycomb core unit cells and low-strain regimes. Balawi and Abot [15] improved this method by developing a theoretical model for commercial honeycombs that account for cell wall curvatures at the junction points of hexagon. Their proposed RVE consisted of one-fourth of the unit cell, separated into straight and curved sections. Their study considered three types of deformations: bending, shear, and axial. They found that the effective properties in both directions for curved cell walls were sensitive to the curvature radius. They further attributed the anisotropic behaviour of the core to the curvature of the cell wall and the effect of cell wall thickness, which is noticeable in honeycombs with a greater relative density. Their predictions were consistent with the results of Masters and Evans [13] for regular honeycomb cores having straight cell walls. The experimental validation of their model showed excellent agreement with the predicted values.

Malek and Gibson [4] created an analytical model to determine the effective elastic characteristics of honeycombs with uniform, double-thick vertical cell walls. They added nodes at the junction of the vertical and inclined components to the analysis that Gibson and Ashby [2] had originally proposed. According to the research, these nodes have minimal influence on effective elastic properties in honeycomb cores with low relative densities, but their impact increases the densities. Malek and Gibson [4] derived closed-form equations for these predictions, unlike the Gibson and Ashby [2] model. Their model predictions closely matched those of Gibson and Ashby [2] honeycombs with low relative density, but discrepancies were slightly higher at higher relative densities. However, the derived results agreed well with numerical and experimental results at higher relative densities.

Mukhopadhyay and Adhikari [16] created a theoretical model to calculate the elastic modulus of irregular honeycombs that exhibit variations in cell angles due to structural defects or manufacturing errors. Their unit cell-based approach showed that these variations significantly impact the in-plane effective elastic constants. The study highlighted the importance of accounting for such uncertainties in the elastic moduli of honeycombs during analysis and design processes.

The majority of the mathematical models mentioned so far are primarily relevant to perfect honeycomb cores, often ignoring aspects such as the adhesive layer and fillet area in the analysis. Furthermore, these models are often restricted to honeycomb cores consisting of isotropic materials, making modelling composite honeycomb cores more difficult. Furthermore, these predictions from the models are often accurate only in situations where the in-plane deformations of the core are limited to within a restricted strain range. Numerical analysis has emerged as a compelling and powerful approach to address these limitations. Several researchers have used numerical models to obtain the in-plane behaviour of honeycomb cores, offering a more comprehensive understanding of their mechanical properties.

Kayran and Aydincak [17] studied the elastic properties of the honeycomb core using various analytical models. Employing a 3D Finite Element Method (FEM), they modelled the honeycomb core based on existing continuum models. According to their results, the most accurate results for core modelling were obtained by integrating the transverse out-of-plane shear characteristics determined by Grediac [18] with the in-plane parameters determined by Masters and Evans [13].

Grediac [18] used FEM to analyze the transverse shear behaviour in honeycomb cores, specifically focusing on how core thickness affects the shear modulus. The study involved a comprehensive comparison between the FEM results, analytical results and experimental test data for the transverse shear modulus.

Meraghni *et al.* [19] investigated the shear modulus of honeycomb cores, assuming zero in-plane characteristics and predicting out-of-plane values using an improved FEM approach based on Grediac's work. FEM results were compared with test data and analytic formulations, demonstrating a consistent underestimation of transverse shear stiffness.

Penado [8] employed a 3D FEM of the one-eighth part of the unit cell to simulate core behaviour using shell elements. Validation was achieved through experimental and published data of cores made of aluminium and further estimated 3D elastic properties for core cell walls made of various composite materials.

Catapano and Montemurro [9] performed a 3D numerical analysis on honeycombs with double-thickness cell walls, utilizing RVE with solid elements and comparing their results with analytical models. While out-of-plane modulus estimates were consistent, in-plane elastic properties varied significantly, particularly for thick-walled cores. This was attributed to shell-based inability of models to capture unit cell geometry accurately, neglecting the prevalent 3D stress state in the honeycomb cores.

Qiu *et al.* [6] developed a numerical approach based on strain energy equality of RVE cells and corresponding homogeneous solids to determine effective stiffness matrix components for honeycomb cores. Their numerical results closely matched the experimental results for the in-plane modulus.

Malek and Gibson [4] used 4-node shell elements and 8-node solid brick elements with incompatible modes to determine the equivalent elastic characteristics of honeycomb cells and the analytical formulation. The results were found to be consistent for those with thinner cell walls but not for those with thicker ones. Furthermore, they observed that their analytical results matched only the results that were generated by the solid elements.

Several researchers have thoroughly studied sandwich panels with honeycomb cores to understand their behaviour and impact on panel performance as an entire unit. Comprehensive panel-level research has given insights into structural integrity, load distribution, and core mechanics.

Examining the mechanical properties of the sandwich structure with honeycomb core is the key to enhancing its applications due to its aforementioned advantages [20,21]. One study by Kee *et al.* [22] involved three-point bending (3PBT), axial compression, and lateral crushing of honeycomb core sandwich structures, all aimed at assessing the structural performance of lightweight designs. Tube structures with fillers (inserts) also play a significant role in applications that require axial load-carrying capabilities, often as reinforcement elements. Zhang *et al.* [23] investigated the enhancement of mechanical properties in aluminium honeycomb sandwich structures by incorporating metallic tubes. Both experimental and numerical methods were used to study the compressive and 3PBT performances of these modified structures. The inclusion of tubes resulted in significant improvements: the elastic modulus increased by 26%, the specific compressive strength by 16%, and the energy absorption by 73%. Additionally, the specific bending load and stiffness improved by 42% and 62%, respectively. Similarly, Yan *et al.* [24] proposed enhancement in the sandwich structure by integrating an absorbent agent by filling CFRP tubes into Nomex honeycomb. Compared to empty honeycomb configurations, their study demonstrated remarkable improvements in mechanical properties: peak stress increased by 621.69%, elastic modulus by 55.74% and energy absorption by 327.86%. Furthermore, the tube-reinforced absorbent honeycomb showed a 30.34% increase in energy absorption. Wang *et al.* [25] showed an improvement in the energy absorption ability of honeycomb cells filled with circular tubes when subjected to quasi-static axial compression and three-point bending tests.

Honeycombs have also been reinforced with fibres and foams in an effort to increase their strength and capacity for energy absorption. Liu *et al*. [26] strengthened aluminium honeycomb structures by filling them with foam. This modification led to higher peak strength, higher total energy absorption, higher mean crushing strength, under axial compression, and higher specific energy absorption (SEA). Similarly, Antali *et al*. [27] inserted carbon fiber plastic tubes into the holes of aluminium honeycombs, significantly increasing the SEA capacity during compression tests. The incorporation of foam proved to dramatically improve the mechanical behaviour of the honeycombs, highlighting the effectiveness of these reinforcement strategies in enhancing the structural performance of the honeycomb materials.

1.2.1.1 Advantages

Honeycomb sandwich sheets offer a range of benefits that make them highly desirable in various applications. They are known for their exceptional strength-to-weight ratio, which provides structural strength without significantly increasing weight. This makes them ideal for industries where weight savings are crucial, such as aerospace, automotive, and construction. The core material, often a honeycomb, provides excellent thermal and acoustic insulation, improving the comfort and energy efficiency of buildings and vehicles. Sandwich sheets are also highly resistant to corrosion and environmental degradation, ensuring durability and longevity. Additionally, its layered structure can be tailored to specific performance requirements, offering flexibility in design and functionality.

1.2.1.2 Disadvantages

Despite their many advantages, honeycomb sandwich sheets have certain limitations. One major drawback is their manufacturing complexity, which can result in higher production costs compared to traditional materials. The bonding between the core and the face sheets must be carefully managed to prevent delamination [28,29], which can compromise structural integrity. Repairing damaged sandwich sheets can be challenging and often requires specialized techniques, which can increase maintenance costs. Moreover, while they offer excellent performance under specific conditions, sandwich sheets may not be suitable for applications involving high impact or point loads, as the core material can be relatively weak compared to the face sheets.

1.2.1.3 Applications

Honeycomb sandwich sheets are used extensively in various industries due to their unique properties. In aerospace, they are used in aircraft fuselage panels, flooring, and control surfaces, where their lightweight and high strength contribute to fuel efficiency and performance. The automotive industry uses sandwich sheets in body panels, roofs, and interior components to reduce vehicle weight and improve fuel economy. In construction, sandwich panels are used for walls, roofs, and floors, providing excellent thermal insulation and structural stability. The marine industry uses them in boat hulls and decks for their corrosion resistance and buoyancy. In addition, sandwich sheets are found in wind turbine blades, sporting equipment, and even furniture, showcasing their versatility and adaptability to various applications.

1.2.2 FSW

Before the invention of FSW, friction welding was a widely used method for joining solid-state materials. Two metal parts are pressed together and moved in relation to each other during this procedure. The heat developed by the friction between the two surfaces causes the material in the joint region to become plasticized. The softened material is subsequently subjected to pressure to establish a robust metallurgical joint.

While friction welding is a relatively straightforward process, it consists of some limitations, particularly in terms of the dimensions of the specimens that can be welded and its range of applications. These constraints have led to the development and adoption of FSW, which overcomes some of the limitations of traditional friction welding.

Researchers at The Welding Institute (TWI) have worked for many years on research and development and industrial applications of FSW. During this time, W. Thomas proposed a novel method for joining two materials using a rotating tool equipped with a material that is harder than the workpiece. This rotating tool was found to plasticize the workpiece material, and as the tool moved along the joint, it facilitated an effective material transportation mechanism. This process allowed the plasticized material to join the workpieces together, leading to the invention of FSW [30].

1.2.2.1 Terminologies

FSW involves several specific terminologies that are essential for accurately understanding and describing the process. According to Threadgill [31], these terms are crucial for professionals working with FSW to communicate effectively and ensure precise control over welding operations.

The material that needs to be welded in the FSW process is known as the workpiece. It can also be called part, sample, welded plate, or specimen. The term 'workpiece' highlights the role of the material as the subject of the welding process, ensuring clarity when discussing the preparation, welding, and evaluation of the joint. The tool, also known as the FSW tool, is the rotating part of the system that produces heat by generating friction with the workpiece. This tool comprises two main parts: the probe (or pin) and the shoulder. The probe, also known as the pin, is the part of the tool that penetrates the surface of the workpiece. It is mainly referred to as a pin when it has a cylindrical shape. The shoulder refers to the section of the tool that comes into direct contact with or is partially embedded in the surface of the workpiece during the welding process. The primary function of the shoulder is to generate heat through friction and help consolidate the material on the surface. The part of the shoulder that penetrates the workpiece the most when the tool is tilted during the welding operation is referred to as the heel. The maximum penetration of the shoulder into the workpiece is the depth of the heel plunge. These terms are essential to understand the interaction of the tool with the material and ensure the correct setup for effective welding. The tilt or travel angle is the angle formed by the rotating axis of the tool with respect to the workpiece plane. This angle influences heat generation and material flow, affecting the quality of the weld. The travel rate of the tool along the workpiece interface is referred to as the welding speed, the traversing speed, or the travel speed. This speed is crucial to determine the amount of heat generated and the efficiency of the welding process. The rotation rate or rotational speed is the angular velocity of the tool. This parameter is critical for generating the necessary frictional heat to soften the material. The forces applied during the welding process are also essential to understand. Downforce is the force parallel to the tool's rotation axis. This force helps to maintain the contact of the tool with the workpiece and ensures proper penetration. The traversing force is defined as the force applied parallel to the welding direction, while the side force is the component of the sideways force created at right angles to the direction of motion. Finally, the advancing and retreating sides describe the local directions of the tool rotation relative to the welding direction. The advancing side has the same tool rotation direction as the traversing direction, whereas the retreating side has the opposite pattern. These sides are important for understanding the material flow and the characteristics of the weld.

These specific terminologies provide a comprehensive framework for understanding the FSW process.

1.2.2.2 Working principle

FSW is a solid-state joining process that fuses materials without melting them, using a specially designed tool with a shoulder and a probe, as shown in Figure 1.6. The process begins with the tool placed at the joint line of two workpieces. Rotating at high speeds, the tool is plunged into the material, generating frictional heat that softens the material around the pin without melting it. This localized heat generation avoids common welding defects such as porosity and cracking from solidification. After a short dwell period, the tool begins to traverse along the joint line. The combination of the tool rotation and the downward pressure from the shoulder maintains the material in a softened state, allowing it to flow plastically around the pin. This action effectively stirs and mixes materials from both sides of the joint. The shoulder plays a crucial role by generating additional heat and helping to forge the material behind the pin, consolidating the softened material into a solid joint as the tool advances. This results in a fine-grained microstructure in the weld zone, which improves the mechanical properties of the joint. As the tool progresses along the joint, the material behind the pin cools and solidifies, forming a strong and continuous bond. At the end of the weld, the tool is gradually withdrawn, leaving a keyhole in the workpiece.

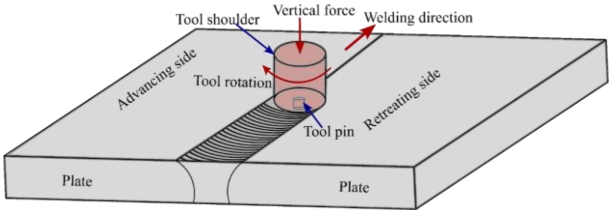

Figure 1.6 FSW process

1.2.3 FSSW

FSSW is a novel adaptation of the FSW process, designed to meet the growing demand for efficient, high-quality and environmentally friendly joining techniques in the automotive and aerospace industries. Like FSW, FSSW is a solid-state welding process. This characteristic helps mitigate common welding problems such as porosity, cracking, and distortion, resulting in robust and reliable joints [32].

1.2.3.1 Background

FSSW emerged as a solution to traditional resistance spot welding (RSW) limitations, mainly when working with lightweight materials like aluminium alloys [33]. These materials pose challenges because of their high thermal conductivity and susceptibility to defects when welded with conventional methods. FSSW addresses these challenges by leveraging frictional heat to soften the materials, making it possible to join them without melting. This process has been especially beneficial in the automotive industry, where the demand for lightweight and high-strength components continues to increase.

1.2.3.2 Terminologies

As the FSSW process is a variant of the FSW process, the terminologies are similar to those used in the previous section.

1.2.3.3 Working principle

The FSSW process consists of three main stages: plunging, stirring, and retracting. These processes are shown in Figure 1.7. In the plunging stage, the rotating pin gradually penetrates the overlapping sheets to a predetermined depth. Next, the rotating pin generates heat during the stirring stage and plasticizes the material. The tool continues to rotate for a set period, which allows the materials from both sheets to mix thoroughly and form a strong metallurgical bond.

Finally, the rotating tool is withdrawn from the sheets in the retracting stage, leaving behind a keyhole [32,33].

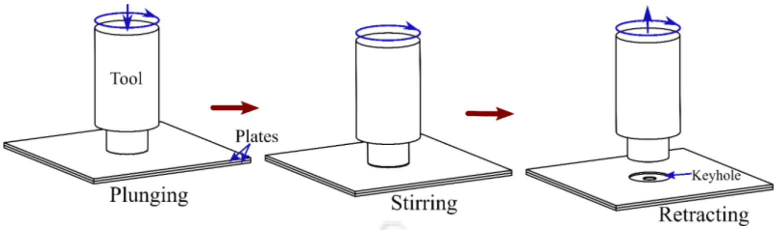

Figure 1.7 Stages of the FSSW process

1.2.3.4 *Process parameters and their influence*

The geometry of the tool and the process parameters affect both the quality and performance of the FSSW sheets. The depth of the plunge, the duration of dwell, the rotation rate, and the speed of the plunge are important process variables. The important features of the tool geometry that impact the joint characteristics are the pin and shoulder profiles. FSSW, unaffected by tool wear or surface conditions, can achieve equivalent or higher weld strength with improved uniformity compared to RSW [34]. Similarly to linear FSW, FSSW maintains temperatures below the melting point, preventing defect formation. FSSW can be used to join various materials, including polymers, aluminium alloys, magnesium alloys, copper, steels, dissimilar metals/composites, metal matrix composites (MMC), and non-ferrous/ferrous metals. The spot welded area in FSSW is influenced by tool design and various joining frameworks [33,34].

Zhang *et al.* [35] explored the impact of different dwell times and tool rotational speeds on the mechanical behaviour of 1 mm thick AA5052-H112 sheets. Their research revealed that the strength of the welded joint decreased with increasing tool rotation speed, while the dwell time did not significantly affect it. Ugurlu and Cakan [36] examined spot joints created through the FSSW of AA7075-T6, keeping the dwell time constant at 20 s and varying the tool rotation speeds up to 1500 rpm. They found that higher tool rotation rates improved joint quality, with the highest rotation speed producing the best tensile strength.

Prasomthong *et al.* [37] examined the impact of various tool rotation speeds and dwell periods on the lap shear strength and hardness of dissimilar lap joints made of aluminium and copper. They found that the weld zone hardness profiles were lower than the base material, and the welding conditions of 3500 rpm and a 4 mm/min plunge rate at a 4-s dwell time resulted in joints with the maximum lap shear strength. Su *et al.* [32] stated that FSSW involves discrete material flow zones. In the first flow zone, located around the perimeter of the rotating pin, the top welded sheet moves downwards in an anticlockwise direction. Simultaneously, in the second flow zone, the bottom sheet of the welded materials moves in a spiral motion, flowing both upward and outward. These flow patterns contribute to the effective joining of materials during the welding operation.

Rana *et al.* [38] studied how the plunge rate affects FSSW in sandwich sheets made of aluminum-polymer-aluminum. They observed significant alterations in the geometry of the hook as the plunge rate increased. The highest joint performance, with respect to both cross-tension and lap shear, was successfully obtained using plunge rates of 6 mm/min and 8 mm/min, respectively. Furthermore, during peel tests, higher plunge rates were found to result in the maximum failure load.

The effect of plunge depth on the lap-shear failure stress of FSSW joints between aluminium and magnesium alloy sheets was investigated by Rao *et al.* [39]. They discovered that when different materials were weld at high temperatures, increasing the depth of the plunge caused a rapid rise in temperature due to increased load. This may lead to the generation of hard and brittle intermetallic compounds. However, SEM micrographs demonstrated interlocking of magnesium and aluminium sheets between intermetallic compounds in their investigation. Furthermore, they noticed that the weld width improved with increasing plunge depth, indicating that during lap shear tensile testing, a greater tool shoulder plunge depth resulted in a larger failure load.

Bozzi *et al.* [40] conducted an experiment to join two sheets of AA 5182-O using FSSW at a constant rotational speed while independently changing the plunge depth. The experimental results indicated that variations in pin plunge depth had no significant effect on tensile shear strength. However, changes in shoulder plunge depth had a substantial impact. Increasing the shoulder plunge depth initially improved joint strength by flattening the interface tip, thereby reducing the likelihood of crack initiation during shear testing. Moreover, when the shoulder plunge depth was too high, it caused excessive localized top sheet thinning, which in turn concentrated severe stress and decreased joint strength.

Mitlin *et al.* [41] investigated the influence of the plunge depth of the tool on the lap shear strength of FSSW 6111 aluminium sheets. They discovered that increasing tool penetration boosted lap shear strength by enlarging the partly metallurgical bond region beneath the tool shoulder. However, excessive penetration of the tool caused the creation of a hole, reducing the strength of the joint. Arul *et al.* [42] investigated the failure mechanisms of the FSSW 6111-T4 aluminium alloy sheets at various rotational speeds. They found two basic modes, shear fracture and mixed-mode fracture, and discovered that fracture mode is governed by hook shape, which is affected by rotation speed. Their lap shear tensile testing found that the failure load initially increased with rotating speed before decreasing. Higher rotating speeds produced more frictional heat, resulting in a larger bonded zone and increased strength up to a point [43].

Bilici and Yükler [43] used FSSW to join polyethene sheets and investigated how tool geometry and process factors affected weld mechanical qualities. Their lap shear tensile tests revealed that the failure load initially increased with rotating speed, owing to the greater bonded area formed by high friction heat. However, higher rotation rates lowered the strength owing to more stress on the top sheet. Many studies show that the effective width of the weld considerably affects the weld strength, which increases with the tool rotation speed. Greater effective weld width improves joint strength. Shen *et al*. [44] used FSSW to join 6061-T4 aluminium alloy sheets in a range of rotation speeds and durations. They discovered that the lap shear strength of the welded samples increased with higher rotation speeds for any given time period.

Choi *et al.* [45] investigated the development of intermetallic compounds and their influence on the mechanical characteristics of FSSW joints between 6K21 Al alloy and AZ31 Mg alloy sheets. It was discovered that the lap shear strength of the joint decreased as the dwell periods increased due to the creation of thicker intermetallics caused by the increase in heat input.

According to Lin *et al.* [46], the main factor influencing the failure behaviour in FSSW is the width of the bond. The researchers studied the impact of different parameters on the tensile strength of FSSW AZ61 magnesium alloy. They observed an enhanced strength when the dwell times were increased as a result of the larger bonding area. However, an excessive increase in dwell times resulted in a reduction in the strength of the FSSW as a result of coarsening of the grain.

The geometric properties of the tool, such as the pin and shoulder profiles, as well as other process variables, significantly impact the performance of sheet metal joined by the FSSW.

The impact of various pin profiles on the lap shear strength of dissimilar magnesium alloy sheets bonded by FSSW was investigated by Yin *et al.* [47]. They employed two types of threaded and one type of non-threaded tool, each having unique pin characteristics. For every kind of tool, they made a huge number of samples at various rotational speeds. According to their lap shear tensile test findings, all threaded tools increased joint strength compared to non-threaded tools.

Lin *et al.* [48] used two different kinds of tools—one with a flat shoulder and the other with a concave shoulder—to study the failure mechanisms of FSSW in lap-shear specimens of aluminium 6111-T4 sheets. According to their testing results, the joint created by the tool with the concave shoulder had a greater lap shear strength than the joint generated by the tool with the flat shoulder.

In the study by Badarinarayan *et al.* [49], the FSSW of 5754-O aluminium alloy sheets, 1.32 mm thick, revealed that the axial load for the tool with a triangular pin was lower compared a cylindrical pin. This difference highlighted the significant influence of the pin geometry and tool shoulder profile on power consumption during FSSW. However, the use of the tool with an unthreaded triangular pin did not result in prominent stir zone (SZ) formation and there was no noticeable downward material flow. Instead, the triangular pin caused a drilling effect during tool plunge, leading to the removing of small fragments from the upper sheet.

In another study by Garg and Bhattacharya [50], during the FSSW of AA 6061 sheets, 0.9 mm thick, a high temperature of approximately 878 K was generated. They observed that a circular pin induced minimal stress at the stirring spot. Maximum shear fracture strength of the joint was achieved using a square pin. However, both square and triangular pins experienced considerable wear and severely damaged the sheets during welding.

1.2.3.5 Advantages

FSSW offers several advantages, including eliminating the need for filler material, which reduces costs and simplifies the process. The low heat input characteristic of the FSSW minimizes thermal distortion and residual stresses, leading to high joint strength with excellent mechanical properties. Environmentally, FSSW is beneficial as it does not produce harmful fumes or require shielding gases. It is effective in joining different materials, such as aluminium and steel, and requires minimal surface preparation. Furthermore, FSSW is suitable for automation, increasing efficiency and consistency, and is particularly advantageous for welding thin materials.

1.2.3.6 Disadvantages

FSSW has disadvantages. The welding tool can wear out, especially when working with harder materials, leading to increased maintenance costs. The process is generally limited to relatively thin materials, which may not be suitable for all applications. The initial investment in FSSW equipment can be high, and the process can leave tool marks on the surface of welded materials, necessitating additional finishing. Additionally, it may not be as effective for complex joint geometries compared to other welding methods.

1.2.3.7 Applications

FSSW finds applications in various industries. In the automotive industry, it is used to join lightweight materials in body structures, such as aluminium and magnesium alloys. The aerospace industry utilizes FSSW to manufacture aircraft components, including fuselage panels and wings. It is used in the railway industry to assemble lightweight train components and enhance fuel efficiency and performance. In electronics, FSSW is used to produce housings and enclosures, where thermal management is crucial. The shipbuilding industry applies FSSW to construct lightweight and corrosion resistant ship structures. In building and construction, FSSW fabricates aluminium and steel panels for building façades and structures. Consumer goods, such as bicycles and sporting equipment, also benefit from the strong, lightweight joints produced by FSSW. In addition, the renewable energy sector uses FSSW to manufacture lightweight components for wind turbines and solar panels.

1.2.4 Joining of sandwich sheet

The methods of joining sandwich sheets can be broadly categorized into adhesive, mechanical, and hybrid methods. Each method has its advantages and limitations, depending on the materials used and the intended application.

Adhesive bonding (AB) is a widely used method to join sandwich structures such as car interior parts, aircraft components, racing equipment, and marine applications. This method uses adhesives such as epoxies, polyurethanes, and acrylics to bond the face sheets to the core and join sandwich panels together. The advantages of AB include uniform stress distribution and preservation of the integrity of the core material. Epoxy adhesives are known for their excellent bonding strength and durability, and they are suitable for metallic and composite face sheets. Polyurethane adhesives offer good flexibility and impact resistance, making them ideal for thermal expansion and contraction applications. Acrylic adhesives are valued for their fast curing times and good bonding strength, especially for thermoplastic face sheets and cores.

However, controlling the quality of AB joints can be challenging due to their sensitivity to humidity, temperature, and surface treatments. Achieving the required strength often requires rigorous surface treatment procedures, adding complexity to the manufacturing process. For instance, Feng *et al*. [51] found that pre-grinding surfaces raised failure load by 29.87% compared to untreated joints. Additionally, additive manufacturing (AM) techniques [52–55] offer potential solutions but face challenges in material properties and high costs for industrial production. Oliveira *et al.* [56] proposed innovative sandwich structures with bottle cap cores, enhancing mechanical properties using epoxy connections, and explored ultrasonic spot welding for joining upcycled bottle caps to skin sheets, achieving weight-specific flexural properties up to 45% better than adhesive-bonded structures.

Although AB offers advantages such as uniform stress distribution and the creation of continuous joints, which are beneficial for structural integrity. However, this method is often time-consuming and costly because of the extensive surface preparation required to ensure proper adhesion and the lengthy curing times involved. Additionally, adhesives can contain toxic chemicals that pose risks to human health and the environment, emphasizing the importance of handling and disposal protocols.

Mechanical joining methods include bolting, riveting, clinching, and self-piercing rivets (SPRs). These methods are preferred for their simplicity and potential for disassembly if necessary. Bolting and riveting provide strong and reliable joints, but require drilling holes through the face sheets and core, which can compromise structural integrity and introduce stress concentrations. Clinching mechanically interlocks sheets without additional fasteners are suitable for joining thin face sheets but may not provide sufficient strength for thicker cores or high-load applications. SPRs are useful for joining dissimilar materials without pre-drilled holes and are commonly used in the automotive industry for aluminium and steel sheets.

Mechanical fastening using rivets can develop holes in the rivet tail, reducing residual compressive force and making the joints prone to loosening. Stress concentrations are also created around the holes, and the fasteners add weight to the structure [57]. Pickin *et al.* [58] explored self-pierce riveting for joining polymer core sandwich sheets, which showed promise but exhibited drawbacks like uneven deformation and weak joints. Balle *et al.* [57] also explored ultrasonic spot welding for joining aluminium to carbon fiber-reinforced plastic, limited to joining small parts.

Attaching a thick core to skin sheets to manufacture sandwich panels using mechanical fasteners presents certain challenges that require solutions [58]. Although mechanical fasteners such as bolts or rivets offer practical advantages such as ease of assembly and disassembly, they also introduce potential drawbacks. Predrilled holes required for mechanical fastenings can create stress concentrations around the hole regions, which may compromise the structural integrity of the sandwich structure. Additionally, the use of consumable fasteners adds weight to the overall structure, which is a critical consideration, especially in weight-sensitive applications such as aerospace and automotive industries. Therefore, an alternative way to join the core sandwich sheets is required.

The solid-state processes are energy efficient, eco-friendly, sustainable, and produce parts with less distortion [59,60]. Rana *et al.* [61] achieved the FSSW of sandwich sheets composed of AA5052/HDPE/AA5052, having potential applications in weight reduction in vehicles. However, they noted that interfacial bonding occurred only between the top and bottom aluminium face sheets, as the HDPE layer was extruded from the welded region. Ravi *et al.* [62] conducted experiments on sandwich sheets to assemble two sandwich sheets using different pin tool geometries. Lap shear tests revealed that the pin with a square profile produced the strongest joints with moderate hook height, hook distance, and hook width, with a larger bond area. Naik *et al.* [63] used spot welding to create a new joining technique for metal-polymer sandwich panels, including a wire mesh. They used uniaxial tensile, peel and double lap shear tests to assess the mechanical behaviour and interface strength of sandwich sheets. The results demonstrated that the peel and shear strengths of the interface in these panels were significantly higher than those achieved by adhesive bonding in previous studies. The enhanced interface strength was attributed to the metallurgical bond formed between the wire mesh and the steel sheet.

Spot welding may not be sufficient alone to fabricate sandwich sheets with the required mechanical properties; therefore, researchers have also explored hybrid joining techniques.

Hybrid joining methods combine spot welding or mechanical fasteners with adhesive bonding to take advantage of both techniques. This approach improves joint strength, fatigue resistance, and tolerance to damage. Bolted/bonded joints, which combine the mechanical strength of bolts with the uniform stress distribution of adhesives, are used in aerospace applications for critical structural joints. Riveted/bonded joints use rivets instead of bolts and are suitable for joining thin face sheets, providing good load transfer and fatigue resistance. Spot welding/bonded joints provide both mechanical and metallurgical bonding of sandwich structures, making them much stronger joints.

The hybrid bond (HB) procedure, which combines adhesive bonding and welding, increases the joint area and improves joint strength. Pouranvarih and Safikhani [64] demonstrated that resistance spot hybrid bonding (RSHB) of stainless steel exhibited 100% increase in failure load and a 110% increase in energy absorption compared to resistance spot welding (RSW). The addition of the adhesive layer enhanced fatigue strength by reducing the stress concentration factor in the HB joint. Comparing the fatigue performance of the RSW and RSHB joints showed that within the specified fatigue life period, the S-N curve of the RSHB joints was higher than that of the RSW joints, showing improved fatigue performance in the HB joints [65]. Additionally, using an adhesive layer reduced the formation of intermetallic compounds while joining dissimilar sheets and enhanced the joint mechanical performance [65]. Campilho *et al.* [66] discovered that hybrid bonding increased the strength (about 6%), whereas the total deformation increased significantly (by approximately 100%). On the other hand, Almeida *et al.* [67] found that the T-peel test strength of hybrid joints was significantly higher than that of AB joints. Marques *et al.* [68] investigated the effectiveness of adhesives with varying degrees of ductility in spot-welded hybrid joints compared to purely bonded joints, aiming to identify the most suitable adhesive for these applications. They found that ductile adhesives are beneficial for hybrid joints because they can accommodate large joint deformations induced by the weld nugget. The study reported maximum load improvements for hybrid joints over bonded joints as follows: 39.1% with Araldite® AV138, 58.4% with Sikaforce® 7752, and 22.8% with Araldite® 2015, based on experimental values.

Previous studies have focused primarily on evaluating the static and fatigue performance of weld-only joints, adhesive-only joints, and HB joints. However, there has been limited research on spot welding of sandwich sheets with polymer cores. Furthermore, there is a notable absence of literature addressing the FSSW of honeycomb core sandwich structures. The integration of a honeycomb core between two metallic sheets adds complexity and interest to FSSW processes. Despite the growing interest in FSSW of sandwich structures, the mechanical behaviour of honeycomb core sandwich structures during FSSW remains critically under-investigated in the existing literature.

1.2.5 Numerical modelling of joining of sandwich sheet

The modelling of sandwich sheets with AB, FSSW, and hybrid joints of different material properties poses a significant challenge. However, to simulate interfacial fracture, the cohesive zone model (CZM) provides a strong foundation within the damage mechanics. Cohesive layer is a numerical representation used in FEM to simulate the behaviour of interfaces or bonding regions between materials. Unlike physical layers, such as adhesives, a cohesive layer does not have a direct experimental equivalent but is a mathematical construct that captures the mechanical response of interfaces, including their strength, stiffness, and failure behaviour. The necessity of introducing a cohesive layer arises from the need to model the complex interactions at interfaces, such as debonding, crack propagation, or load transfer, which cannot be adequately represented using traditional continuum elements. In numerical simulations, the cohesive layer is defined by specific properties, such as traction-separation laws, which describe how the interface resists separation under loading. These properties are critical for accurately predicting the behavior of bonded joints, such as AB or welded joints.

Researchers have used CZM effectively to simulate fractures in various materials, including concrete, metals, polymers, ceramics, and composites [67,69–77]. Jang *et al.* [78] used CZM in FE simulation of a composite sheet made of steel and polymer that was prone to delamination. The interaction between the steel and polymer layers was accurately defined in their work using CZM, and the numerical results were supported by peel tests. Similarly to this, Liu *et al.* [79] used CZM to examine the formability of a sandwich sheet made of a polyethene core and an AA5052 skin. CZM was used in that instance to describe the adhesion between the various layers of the composite. The study also explored two additional interface conditions, namely separation and sticking. Among the three scenarios, CZM-based adhesion yielded a notably favorable agreement with the experimental results. Stigh *et al.* [80] underscored CZM's effectiveness in simulation, as it comprehensively represented interface conditions with minimal variables. Unlike traditional crack propagation studies that require separate geometric models, the CZM enables interfacial failure to simulate crack propagation, effectively separating adjacent surfaces to act as a crack. Gilchrist and Smith [81] conducted the first investigation into the damage propagation of hybrid peel joints. They utilized CZM in their fatigue strength research to describe how damage initiates, propagates, and grows in these joints. Their research results indicated that within the adhesive layer, the growth of cohesive cracks begins at the adhesive fillet located near the edge of the bond. These cracks then propagate inward towards the inner sections of the bond. Campilho *et al.* [82] studied the behaviour of hybrid bonded lap joints through experiments and finite element (FE) stress analysis using CZM. Given the accuracy, efficiency, and cost-effectiveness of numerical techniques combined with CZM to predict fractures in bonded joints, extending the approach for FSSW and hybrid joints is crucial.

Rana *et al.* [71] conducted numerical simulations of FSSW on sandwich sheets using CZM to monitor interface delaminations. Their study demonstrated that the final joint shape and hook geometry obtained from CZM FE simulations closely matched experimental observations. The numerical predictions of the load-displacement response behaviour in lap shear and peel tests showed good agreement with the experimental results, validating the effectiveness of CZM in simulating and understanding the FSSW process for sandwich structures.

Park *et al.* [83] integrated the CZM with finite element analysis (FEA) to investigate the delamination behaviour of sandwich sheets under bending. According to their results, delamination is significantly influenced by the essential energy release rate and initial stiffness of the cohesive layer. The initial stiffness of the cohesive layer affects how the load is initially distributed across the material, while the critical energy release rate determines the energy required for a crack to propagate through the layer. Together, these factors influence the overall integrity and durability of the sandwich structure under mechanical stress.

In a related study, Akour and Maaitah [84] also used finite element analysis to examine the mechanical properties of sandwich sheets, focusing on the relationship between core stiffness and load-carrying capacity. They found that the total load carrying capacity of the sandwich sheets was positively correlated with the stiffness of the core. This correlation suggests that a stiffer core enhances the structural performance of sandwich sheets, allowing them to support greater loads without experiencing significant deformation or failure.

Marques et *al.* [68] investigated the application of adhesives with varying ductility in spot-welded hybrid joints. They used the CZM technique alongside experimental methods to map stress distributions, assess the damage variable, and predict the joint strength of lap shear specimens. The results confirmed accuracy and demonstrated how strength increases differently between hybrid joints and bonded joints depending on the adhesive used.

1.3 Significance of work

The modern automotive industry is intensely focused on addressing the global energy crisis and environmental issues by promoting energy conservation and pollution reduction. This is particularly crucial for the development of lightweight vehicles, especially electric cars, whose range is highly dependent on their weight. Sandwich components are widely used in the automotive industry due to their lightweight properties and high bending stiffness, energy absorption, and strength. Among these, honeycomb core structures are particularly advantageous because they offer superior control over mechanical and crash-worthiness features because of their customizable anisotropic properties and periodic structure. Recently, several investigations have attempted to reinforce sandwich structures using various joining techniques to enhance their mechanical properties, such as stiffness and strength. Traditionally, adhesives and mechanical fasteners have been used to join the sandwich cores and skins. For example, AB is extensively used to join sandwich structures in various applications, including automotive interior parts, aircraft components, racing equipment, and marine applications. However, controlling the quality of AB joints can be challenging due to their sensitivity to factors such as humidity, temperature, and surface treatments. Although AM techniques offer potential solutions, they face significant challenges related to material properties and high costs for industrial production, as the characteristics of AM parts often differ substantially from those of base materials produced using traditional methods. In mechanical fastening, using rivets leads to deformation at the time of joining, resulting in the development of a hole in the rivet tail, which reduces the residual compressive force and makes the joints prone to loosening. Additionally, stress concentrations are created around the holes of the mechanical fasteners, which add extra weight to the structure. This ongoing search for efficient, reliable, and cost-effective joining methods remains a critical area of research in the manufacturing of sandwich structures.

Amid these challenges, FSSW presents a promising energy-efficient, eco-friendly, and sustainable alternative that produces parts with minimal distortion. While FSSW is effective for joining aluminium and polymer sandwich sheets, it primarily results in interfacial bonding between aluminium face sheets, with the polymer layer being extruded from the welded region. Consequently, FSSW alone may not achieve the desired mechanical properties of sandwich sheets. HB, combining adhesive bonding and welding, has demonstrated potential in increasing joint area and improving joint strength by reducing stress concentration. This technique is particularly relevant for enhancing the mechanical properties of sandwich structures with honeycomb cores.

Despite the progress in understanding the performance of various joint types, there has been little research focused on spot welding sandwich sheets, particularly those with honeycomb cores. Existing studies have concentrated on weld-only joints, adhesive-only joints, and hybrid bond joints, often overlooking the potential benefits of combining FSSW with AB in sandwich structures featuring honeycomb cores. This gap in research has provided the impetus for the design and development of novel hybrid joints (FSSW+AB) for these sandwich structures. This work addresses this gap by investigating the mechanical behaviour of sandwich structures with honeycomb cores. This research endeavours to advance the application and performance of lightweight materials in the automotive industry, contributing to the development of more efficient, reliable, and environmentally friendly vehicles. This exploration into hybrid joining techniques not only has the potential to enhance the mechanical properties of sandwich structures, but also aligns with the broader goals of energy conservation and pollution reduction in the modern automotive industry.

1.4 Objective of the work

The primary objective of this thesis is to manufacture honeycomb core sandwich structures using FSSW joining strategies. This approach aims to serve as a potential alternative or enhancement to existing AB methods currently used in the production of such structures. Using FSSW, the thesis aims to improve the mechanical properties, durability, and overall performance of honeycomb core sandwich structures. In addition, the research includes the development of numerical simulations to predict the joining performance of these structures.

The important sub-objectives are given below:

- Understanding the FSSW of sandwich sheets by different welding parameters.
- Analysis of honeycomb core sandwich sheets manufactured by different fabrication processes.
- Analysis of the honeycomb core and development of the equivalent model for the honeycomb core is termed homogenization of the core.
- To develop the equivalent cohesive layer properties for the adhesive layer, a homogenization of the cohesive layer.

Mechanical performance evaluations, including lap shear tests, peel tests, 3PBT, and MMB tests, are performed to assess the strength and failure of honeycomb core sandwich structures. The behaviours observed in these tests are then compared with numerical simulations performed using Abaqus® 2017 software.

1.5 Organization of Thesis

The thesis is organized as follows:

Chapter 1 provides the introduction and literature review of honeycomb core sandwich structures, the FSSW process, joining of sandwich sheets, numerical modelling of joining of sandwich sheets, and the significance and objectives of the current work.

Chapter 2 shows the detailed theoretical formulations and numerical analysis to obtain equivalent orthotropic properties of periodic honeycomb structures using the strain energy approach.

Chapter 3 presents a preliminary investigation on FSSW of honeycomb core sandwich sheets without disc inserts.

Chapter 4 presents a preliminary investigation on FSSW of honeycomb core sandwich sheets with disc inserts.

Chapter 5 outlines the manufacture of honeycomb core sandwich structures by hybrid approaches, including analysis using lab-scale experiments and numerical simulations.

Chapter 6 discusses enhancing the performance of honeycomb core sandwich structures through FSSW strategies and the fracture of lap shear specimens.

Chapter 7 describes the prediction of peel strength of sandwich sheets made of aluminium alloys fabricated by FSSW-based hybrid processes using cohesive zone modelling and finite element simulations.

Chapter 8 presents a detailed experimental and numerical analysis of mixed-mode bending of adhesive and hybrid bonded honeycomb core sandwich structures.

Chapter 9 concludes the thesis work and outlines future work based on this research.

Chapter 2 Equivalent orthotropic properties of periodic honeycomb structure: Strain energy approach and homogenization

---

In this work, we propose a novel representative cell element (RCE) towards computing all the elastic properties of the honeycomb core, as shown in Figure 2.1.

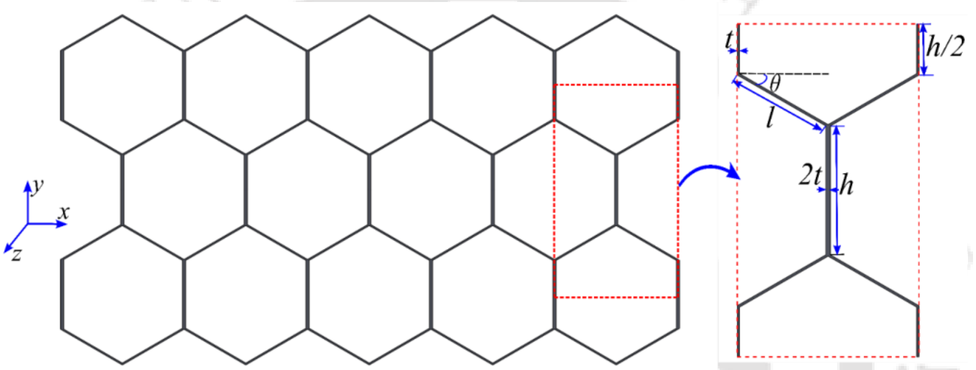

Figure 2.1 Honeycomb core with a hexagonal form that is placed in a periodic pattern, RCE is highlighted with the red dotted line.

In this Figure 2.1, *h* and *l* represent lengths of vertical and inclined cell walls, respectively. θ represents the cell angle, and *t* represents the wall thickness.

2.1 Theoretical analysis of the in-plane and out-of-plane elastic properties of the honeycomb

The chosen RCE (Figure 2.1) was symmetrical vertically and horizontally. The relative density for an RCE of the material can be obtained as

$$\frac{\rho}{\rho_s} = \frac{A_s}{A_c} \tag{2.1}$$

where ρ_s, A_s is the density and cross-section area of the solid material, and A_c is the projected cell area of the RCE given by

$$
\begin{aligned}
A_s &= 4t(h+l) \\
A_c &= 4l\cos\theta(h+l\sin\theta)
\end{aligned}
\tag{2.2}
$$

$$
\frac{\rho}{\rho_s} = \left(\frac{t}{l}\right)\frac{\left(1+\dfrac{h}{l}\right)}{\cos\theta\left(\dfrac{h}{l}+\sin\theta\right)}
\tag{2.3}
$$

In the following subsections, all the in-plane and out-of-plane elastic properties of the honeycomb core were determined using Castigliano's second theorem on the chosen RCE.

2.1.1 In-Plane longitudinal Young's modulus (E_1)

In order to obtain Young's modulus (E_1) in the x-direction, unidirectional compressive stress σ_x was applied in the x-direction to produce a longitudinal deflection in the RCE (Figure 2.2(a)). The contribution by the vertical walls to the longitudinal deflection σ_x would be negligible; therefore, the strain energy associated with the vertical walls for determining E_1 was neglected. The free-body diagram (FBD) of an inclined cell wall is shown in Figure 2.2(b). The generated force in the inclined cell wall is P_x due to the applied unidirectional compressive stress.

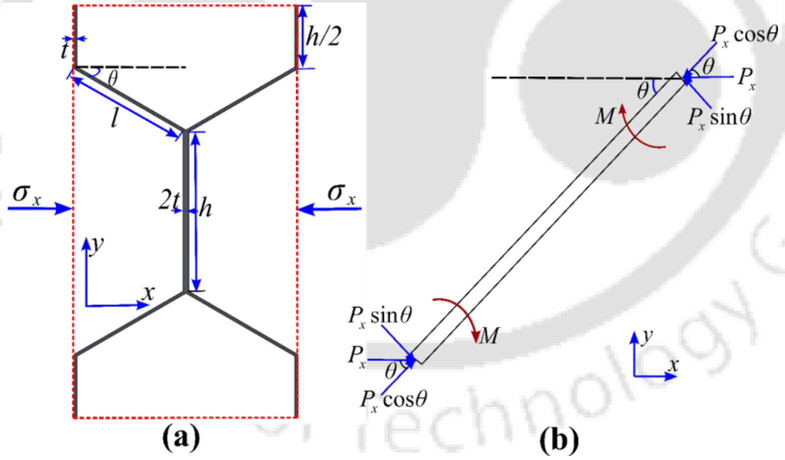

Figure 2.2 RCE with FBD of an inclined cell wall to determine E_1

Therefore, the total strain energy in the inclined cell wall will be the combination of axial strain energy (U_{ax}) and bending strain energy (U_{bx})

$$
U = 4U_{ax} + 4U_{bx}
\tag{2.4}
$$

The axial strain energy can be obtained as (U_{ax}):

$$U_{ax} = \int_0^l \left(\frac{(P_x \cos\theta)^2}{2A_c E_s} \right) \mathrm{d}x \tag{2.5}$$

$$U_{ax} = \frac{P_x{}^2 l \cos^2\theta}{2A_c E_s} \tag{2.6}$$

where $A_c = bt$.

The bending strain energy can be obtained as (U_{bx}):

$$U_{bx} = 2\int_0^{l/2} \left(\frac{\{(P_x \sin\theta)x\}^2}{2E_s I} \right) \mathrm{d}x \tag{2.7}$$

$$U_{bx} = \frac{P_x{}^2 \sin^2\theta}{3E_s I} \frac{l^3}{8} \tag{2.8}$$

where $I = \frac{1}{12} bt^3$ is the second moment of inertia of the inclined cell wall. So, the total strain energy will be

$$U = 2\left[\frac{P_x{}^2 l \cos^2\theta}{btE_s} + \frac{P_x{}^2 l^3 \sin^2\theta}{bt^3 E_s} \right] \tag{2.9}$$

where b is the width, and E_s is Young's modulus of the material of the RCE.

Now, using the second theorem of Castigliano, the deflection in the x-direction can be calculated by

$$\frac{\partial U}{\partial P_x} = \delta_x = \frac{4P_x l \cos^2\theta}{btE_s} + \frac{4P_x l^3 \sin^2\theta}{bt^3 E_s} \tag{2.10}$$

The developed strain is

$$\varepsilon_x = \frac{\delta_x}{2l\cos\theta} = \frac{2P_x \left(\cos^2\theta + \frac{l^2}{t^2} \sin^2\theta \right)}{btE_s \cos\theta} \tag{2.11}$$

Accordingly, the elastic modulus in the x-direction will be,

$$E_1 = \frac{\sigma_x}{\varepsilon_x} \tag{2.12}$$

where compressive stress σ_x is

$$\sigma_x = \frac{P_x}{2(h + l\sin\theta)\,\mathrm{b}} \tag{2.13}$$

$$E_1 = \frac{\left(\frac{t}{l}\right) E_s \cos\theta}{\left(\frac{h}{l} + \sin\theta\right)\left[\cos^2\theta + \left(\frac{l}{t}\right)^2 \sin^2\theta\right]} \tag{2.14}$$

For a regular honeycomb structure, $h = l$ and $\theta = 30^\circ$

$$E_1 = \frac{4}{\sqrt{3}} E_s \frac{\left(\frac{t}{l}\right)}{\left[3 + \left(\frac{l}{t}\right)^2\right]} \tag{2.15}$$

It is to be noted that the shear deformation of the inclined wall in Figure 2.2(b) was neglected towards deriving E_1. It was neglected in theoretical derivations as its contribution would not be significant [2]. However, the procedure to determine the E_1 would remain the same if the shear effects were considered.

2.1.2 In-plane transverse Young's modulus (E_2)

To determine the in-plane transverse Young's modulus, unidirectional compressive stress σ_y was applied in the *y*-direction, as shown in Figure 2.3. Due to the applied compressive stress, the walls will be subjected to both axial force and bending moment. The strain will be developed in both the vertical and inclined walls, but the amount of strain on vertical walls would be negligible compared to the inclined walls [2]. The load (P_y) developed will be equally distributed in both the inclined walls. So, this load has two components: one in the perpendicular direction and another in the axial direction of the inclined wall.

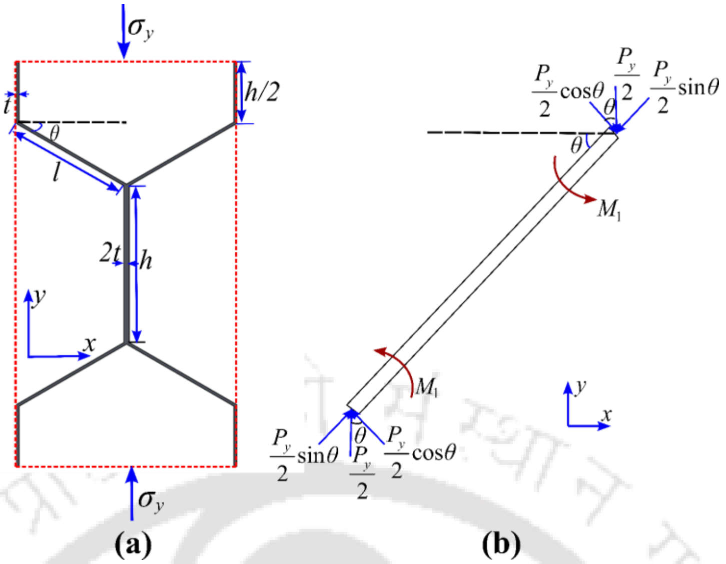

Figure 2.3 RCE with free body diagram of an inclined cell wall to determine E_2

The strain energy produced in the half portion of the RCE will comprise the axial strain energy (U_{ay}) and the bending strain energy (U_{by}).

$$U = 4U_{ay} + 4U_{by} \tag{2.16}$$

$$U_{ay} = \frac{P_y^{\,2} l \sin^2\theta}{8A_c E_s} \tag{2.17}$$

$$U_{by} = \frac{P_y^{\,2}\cos^2\theta}{4E_s I}\frac{l^3}{24} \tag{2.18}$$

So from the Eq. (2.16)

$$U = 4\left[\frac{P_y^{\,2} l \sin^2\theta}{8A_c E_s} + \frac{P_y^{\,2}\cos^2\theta}{4E_s I}\frac{l^3}{24}\right] \tag{2.19}$$

Now, using the second theorem of Castigliano, the deflection in the *y*-direction is

$$\frac{\partial U}{\partial P_y} = \delta_y = \left[\frac{P_y l \sin^2\theta}{A_c E_s} + \frac{P_y\cos^2\theta}{E_s I}\frac{l^3}{12}\right] \tag{2.20}$$

The strain developed along the *y*-direction will be

$$\varepsilon_y = \frac{\delta_y}{2(h + l\sin\theta)} \tag{2.21}$$

Therefore, the transverse Young's modulus will be

$$E_2 = \frac{\sigma_y}{\varepsilon_y} \tag{2.22}$$

where compressive stress σ_y is given by

$$\sigma_y = \frac{P_y}{2lb\cos\theta} \tag{2.23}$$

$$E_2 = \frac{E_s\left(\frac{t}{l}\right)\left(\frac{h}{l} + \sin\theta\right)}{\cos\theta\left[\sin^2\theta + \left(\frac{l}{t}\right)^2\cos^2\theta\right]} \tag{2.24}$$

and, for a regular honeycomb structure $h = l$ and $\theta = 30^\circ$, therefore

$$E_2 = 4\sqrt{3}E_s\frac{\left(\frac{t}{l}\right)}{\left[1 + 3\left(\frac{l}{t}\right)^2\right]} \tag{2.25}$$

2.1.3 In-plane Poisson's ratio ν_{12}

The Poisson's ratio (ν_{12}) was obtained by calculating the ratio of transverse strain to longitudinal strain when the load was applied along the longitudinal direction, as shown in Figure 2.4.

$$\boldsymbol{\nu}_{12} = -\frac{\varepsilon_2}{\varepsilon_1} \tag{2.26}$$

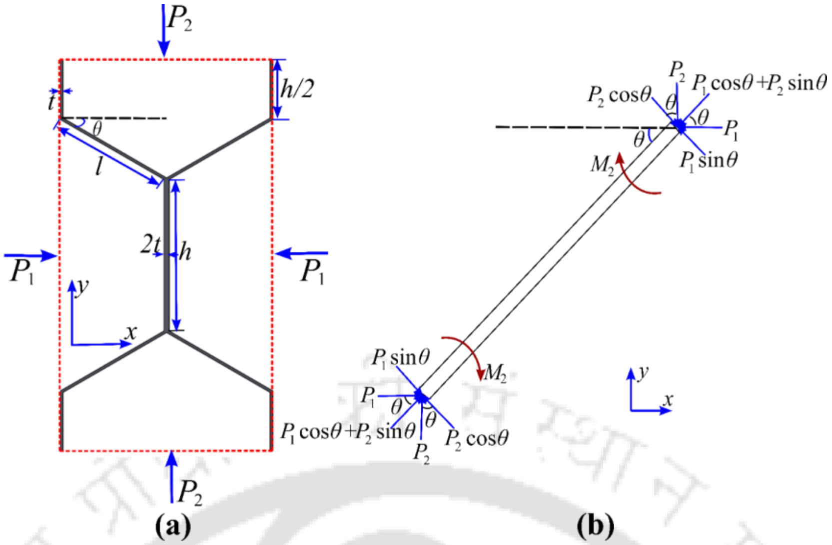

Figure 2.4 RCE with FBD of an inclined cell wall to determine ν_{12}

The bending strain energy developed in the cell wall due to the load applied along the x-direction will be

$$U_{bx} = \frac{(P_1 \sin\theta + P_2 \cos\theta)^2 l^3}{24 E_s I} \tag{2.27}$$

and the axial strain energy developed in the cell wall will be

$$U_{ax} = \frac{(P_1 \cos\theta + P_2 \sin\theta)^2 l}{2 A_c E_s} \tag{2.28}$$

So, total strain energy is the sum of bending and axial strain energy, which is given by

$$U = \frac{(P_1 \cos\theta + P_2 \sin\theta)^2 l}{2 A_c E_s} + \frac{(P_1 \sin\theta + P_2 \cos\theta)^2 l^3}{24 E_s I} \tag{2.29}$$

Now, using the second theorem of Castigliano, the deflection in the x-direction, the point of application of load P_1 along its line of action is given by

$$\left.\frac{\partial U}{\partial P_1}\right|_{P_2=0} = \frac{(P_1 \cos\theta) l \cos\theta}{A_c E_s} + \frac{(P_1 \sin\theta) \sin\theta l^3}{12 E_s I} \tag{2.30}$$

Therefore

$$\delta_x = \frac{P_1 l\cos^2\theta}{A_c E_s} + \frac{P_1 l^3 \sin^2\theta}{12 E_s I} \tag{2.31}$$

Similarly, the deflection in the *y*-direction when the load is applied along the longitudinal direction

$$\delta_y = \frac{P_1 l\sin\theta\cos\theta}{A_c E_s} + \frac{P_1 l^3 \sin\theta\cos\theta}{12 E_s I} \tag{2.32}$$

The strain generated along the *x* and *y* direction will be

$$\varepsilon_1 = \frac{-\delta_x}{l\cos\theta} \tag{2.33}$$

$$\varepsilon_2 = \frac{\delta_y}{(h + l\sin\theta)} \tag{2.34}$$

The Poissons's ratio (ν_{12}) is given by

$$\nu_{12} = \frac{\sin\theta\left[1+\left(\frac{l}{t}\right)^2\right]}{\left(\frac{h}{l}+\sin\theta\right)\left[1+\left(\frac{l}{t}\right)^2\tan^2\theta\right]} \tag{2.35}$$

For a regular honeycomb structure $h = l$ and $\theta = 30^\circ$

$$\nu_{12} = 1 - \frac{2}{3+\left(\frac{l}{t}\right)^2} \tag{2.36}$$

If the inclined cell wall length is much greater than the cell wall thickness, then $\nu_{12} \approx 1$

2.1.4 Analysis of in-plane Poisson's ratio ν_{21}

The Poisson's ratio ν_{21} can be obtained in a similar procedure as outlined in Section 2.1.3 for determining ν_{12}. The only difference is that the load will be applied in the *y*-direction.

Therefore, the Poisson's ratio (ν_{21}) is given by

$$\boldsymbol{\nu}_{21}=-\frac{\varepsilon_1}{\varepsilon_2} \tag{2.37}$$

$$\nu_{21}=\frac{\left(\frac{h}{l}+\sin\theta\right)\left[1+\left(\frac{l}{t}\right)^2\right]}{\left[\sin\theta+\cos\theta\cot\theta\left(\frac{l}{t}\right)^2\right]} \tag{2.38}$$

For a regular honeycomb structure $h=l$ and $\theta=30^\circ$, therefore

$$\nu_{21}=1+\frac{2}{1+3\left(\frac{l}{t}\right)^2} \tag{2.39}$$

if $l>>t$ then, $\nu_{21}\approx 1$

Further, it is evident from Eq. (2.14), Eq. (2.24), Eq. (2.35), and Eq. (2.35), that the following reciprocal relation is satisfied, i.e.,

$$E_1\nu_{21}=E_2\nu_{12} \tag{2.40}$$

2.1.5 In-plane shear modulus (*G*12)

In-plane shear stress τ_{12} was applied to the RCE to determine the in-plane shear modulus - G_{12} as shown in Figure 2.5(a). The FBD due to the applied shear stress on a quarter of the RCE is shown in Figure 2.5(b). The vertical force *S* can be calculated by taking a moment about point B. It is given by

$$S=\frac{F}{2}\frac{\left(\frac{h}{l}+\sin\theta\right)}{\cos\theta} \tag{2.41}$$

The generated force *F* is due to the shear stress τ , $F=2\tau lb\cos\theta$. The strain energy due to axial and shear deformation is neglected as they contribute marginally compared to the bending. So, the total strain energy only involves bending strain energy, which is given by

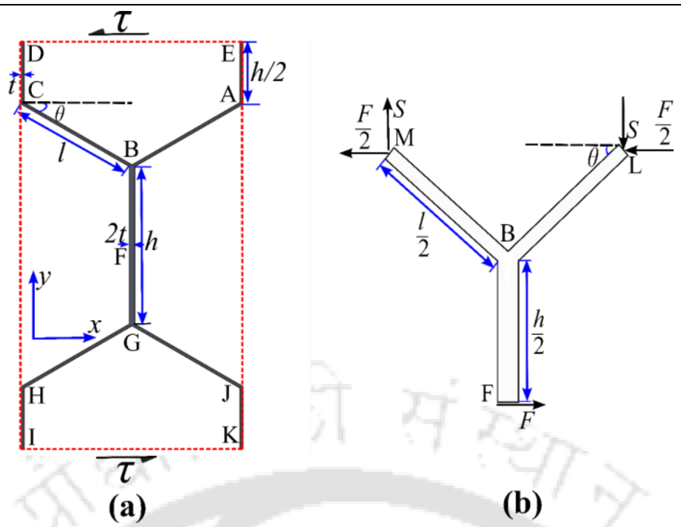

Figure 2.5 RCE with FBD of a quarter of the RCE to determine G_{12}

$$U = 8(U)_{\mathrm{BM}} + 4(U)_{\mathrm{BF}} \tag{2.42}$$

$$U = 8\int_0^{\frac{l}{2}} \frac{\left\{\left(S\cos\theta - \frac{F}{2}\sin\theta\right)x\right\}^2}{2E_s I}\mathrm{d}x + 4\int_0^{\frac{h}{2}} \frac{(Fy)^2}{2E_s I_{\mathrm{BF}}}\mathrm{d}y \tag{2.43}$$

where $I_{\mathrm{BF}} = \frac{1}{12}b(2t)^3$ is the second moment of inertia of the cell wall BF

$$U = \frac{F^2 h^2}{2E_s bt^3}\left(l + \frac{h}{4}\right) \tag{2.44}$$

Now, using the second theorem of Castigliano, the total lateral deformation will be

$$\frac{\partial U}{\partial F} = \delta_l = \frac{Fh^2}{E_s bt^3}\left(l + \frac{h}{4}\right) \tag{2.45}$$

And, the shear strain of the RCE will be

$$\gamma = \frac{\delta_l}{2(h + l\sin\theta)} \tag{2.46}$$

The shear modulus of the RCE can then be obtained as

$$G_{12} = \frac{\tau}{\gamma} \tag{2.47}$$

$$G_{12} = \left(\frac{t}{l}\right)^3 \left(\frac{l}{h}\right)^2 E_s \frac{\left(\frac{h}{l} + \sin\theta\right)}{\cos\theta\left(1 + \frac{h}{4l}\right)} \tag{2.48}$$

For a regular honeycomb structure $h = l$ and $\theta = 30^\circ$, therefore,

$$G_{12} = \frac{4\sqrt{3}}{5} E_s \left(\frac{t}{l}\right)^3 \tag{2.49}$$

2.1.6 Out-of-plane Young's modulus (E_3)

A tensile force P_z was applied perpendicular to the RCE, as shown in Figure 2.6, to derive the expression for out-of-plane Young's modulus E_3. The axial strain energy due to the deformation in the RCE along the *z*-direction is given by

$$U = \int_0^b \frac{P_z^2}{2A_s E_s} \mathrm{dz} = \frac{P_z^2 b}{2A_s E_s} \tag{2.50}$$

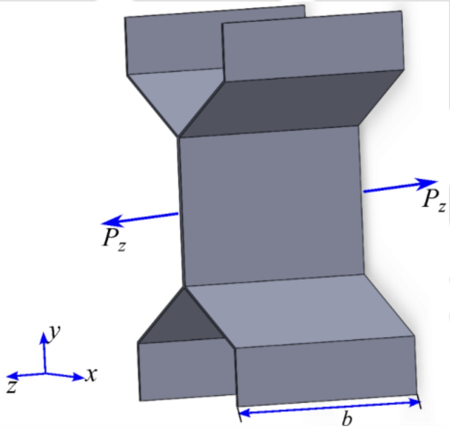

Figure 2.6 RCE to find the out-of-plane Young's modulus E_3

Using the second theorem of Castigliano, the displacement in the *z*-direction is

$$\frac{\partial U}{\partial P_z} = \delta_z = \frac{P_z b}{A_s E_s} \tag{2.51}$$

where A_s is the cross-section area of the RCE. The out-of-plane Young's modulus of the RCE can be obtained as per the expression given below.

$$E_3 = \frac{\sigma_z}{\varepsilon_z} \tag{2.52}$$

The normal stress along the *z*-direction is given by

$$\sigma_z = \frac{P_z}{A_c} \tag{2.53}$$

where A_c is the projected area of the RCE, and the normal strain in the *z*-direction is given by

$$\varepsilon_z = \frac{\delta_z}{b} \tag{2.54}$$

$$E_3 = \frac{A_s}{A_c} E_s \tag{2.55}$$

From Eq. (2.2) & Eq. (2.55), we get

$$E_3 = \left(\frac{t}{l}\right) E_s \frac{\left(1 + \frac{h}{l}\right)}{\cos\theta\left(\frac{h}{l} + \sin\theta\right)} \tag{2.56}$$

For a regular honeycomb structure with a double-thick vertical cell wall $h = l$ and $\theta = 30^\circ$

$$E_3 = \frac{8}{3\sqrt{3}}\left(\frac{t}{l}\right) E_s \tag{2.57}$$

2.1.7 Out-of-plane shear modulus (G_{13})

A shear force F_x is applied in the *x*-direction, as shown in Figure 2.7. The shear stress τ_{xz} is transferred as shear flow only to the inclined cell walls (Figure 2.8); no shearing occurs in the vertical cell walls [85].

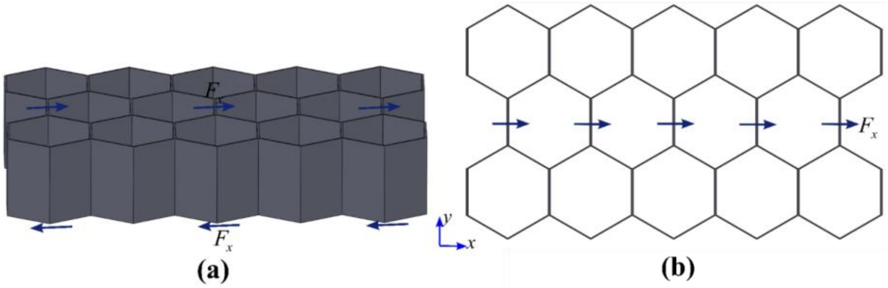

Figure 2.7 Shear flow-through cell walls, (a) 3-D view of shear force F_x acting in the x-direction, (b) 2-D view of shear force F_x acting in the x-direction

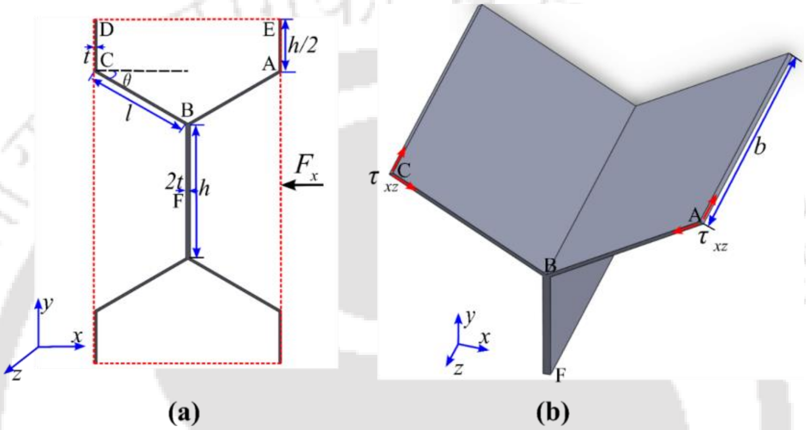

Figure 2.8 (a) Shear force F_x acting on the RCE, (b) representation of shear flow due to the shear force F_x

So, the force F_x acting on the RCE is equally distributed across the four inclined cell walls.

$$F_{\mathrm{AB}} = \frac{F_x}{4\cos\theta} \tag{2.58}$$

The total strain energy developed by the applied shear load (F_x) equals the shear strain energy developed in the inclined cell walls.

$$U = 4\int_0^b \frac{{F_{\mathrm{AB}}}^2}{2A_s G_s}\mathrm{dz} \tag{2.59}$$

where $A_s = lt$ is the cross-section area of wall AB, and G_s = Shear modulus of the material

$$U = \frac{{F_x}^2 b}{8ltG_s\cos^2\theta} \tag{2.60}$$

Now by the second theorem of Castigliano, the shear deformation will be

$$\frac{\partial U}{\partial F_x} = \delta_{xz} = \frac{F_x b}{4ltG_s \cos^2\theta} \tag{2.61}$$

and the shear strain is

$$\gamma_{xz} = \frac{\delta_{xz}}{b} = \frac{F_x}{4ltG_s \cos^2\theta} \tag{2.62}$$

$$F_x = \tau_{xz} A_c \tag{2.63}$$

where $A_c = 2l\cos\theta(2h + 2l\sin\theta)$ is the projected area of the RCE. Now, the equivalent out-of-plane shear modulus in the *x*-direction is

$$\mathrm{G}_{13} = \frac{\tau_{xz}}{\gamma_{xz}} \tag{2.64}$$

$$\mathrm{G}_{13} = \left(\frac{t}{l}\right) G_s \frac{\cos\theta}{\left(\frac{h}{l} + \sin\theta\right)} \tag{2.65}$$

For a regular honeycomb structure with a double-thick vertical cell wall $h = l$, and $\theta = 30^\circ$

$$\mathrm{G}_{13} = \frac{1}{\sqrt{3}}\left(\frac{t}{l}\right) G_s \tag{2.66}$$

2.1.8 Analysis of out-of-Plane Shear modulus (G_{23})

As shown in Figure 2.9, when the honeycomb core is subjected to an out-of-plane shear force (F_y), the shear stress (τ_{yz}) is transferred in the form of shear flow along the straight and inclined cell walls (Figure 2.10).

$$\text{As } \tau_{\mathrm{EA}} = \tau_{\mathrm{AB}} = \tau_{\mathrm{BG}} = \tau_{yz} \tag{2.67}$$

If the member EA is subjected to shear force F_{EA}, then load on member AB and BG will be

$$\begin{aligned} F_{\mathrm{AB}} &= 2F_{\mathrm{EA}}\left(\frac{l}{h}\right) \\ F_{\mathrm{BG}} &= 4F_{\mathrm{EA}} \end{aligned} \tag{2.68}$$

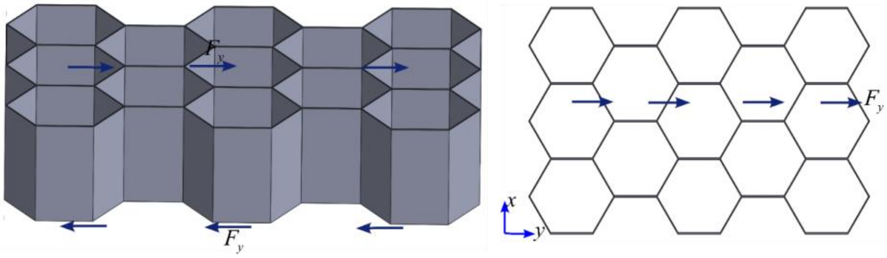

(a) (b)

Figure 2.9 Shear flow-through cell walls (a) 3-D view of shear force F_y acting in the y-direction, (b) 2-D view of shear force F_y acting in the y-direction

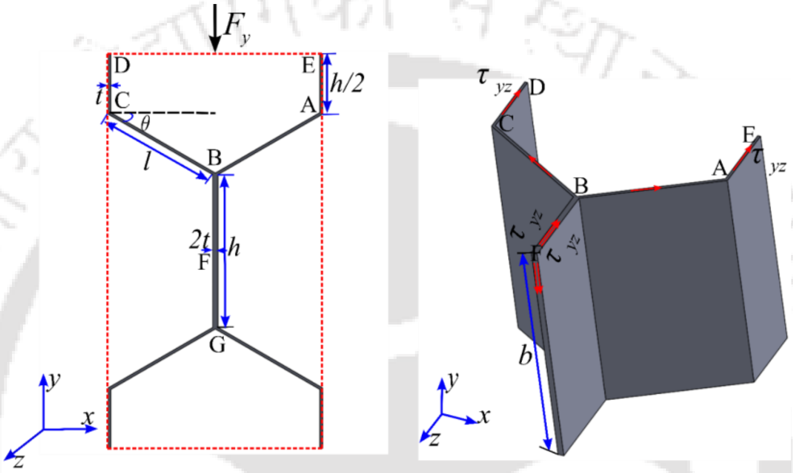

(a) (b)

Figure 2.10 (a) Shear force F_y acting on the RCE, (b) representation of shear flow due to the shear force F_y

The total force(F_y) in the y-direction is equal to the sum of the forces acting on each cell wall of RCE.

$$F_y = 4F_{\mathrm{EA}} + 4F_{\mathrm{AB}}\sin\theta + F_{\mathrm{BG}} \tag{2.69}$$

So, the shear forces acting on the cell walls EA, AB, and BG can be obtained as

$$F_{\mathrm{EA}} = \frac{F_y}{8\left(1+\frac{l}{h}\sin\theta\right)},\quad F_{\mathrm{AB}} = \frac{F_y\left(\frac{l}{h}\right)}{4\left(1+\frac{l}{h}\sin\theta\right)},\quad F_{\mathrm{BG}} = \frac{F_y}{2\left(1+\frac{l}{h}\sin\theta\right)} \tag{2.70}$$

The total strain energy developed due to the applied shear load (F_y) equals the shear strain energy developed in the straight and inclined cell walls. Therefore, the total strain-energy will be

$$U = 4\int_0^b \frac{F_{\mathrm{EA}}{}^2}{2(A_s)_{\mathrm{EA}} G_s}\mathrm{dz} + 4\int_0^b \frac{F_{\mathrm{AB}}{}^2}{2(A_s)_{\mathrm{AB}} G_s}\mathrm{dz} + \int_0^b \frac{F_{\mathrm{BG}}{}^2}{2(A_s)_{\mathrm{BG}} G_s}\mathrm{dz} \tag{2.71}$$

where $(A_s)_{\mathrm{EA}} = \frac{ht}{2}$, $(A_s)_{\mathrm{AB}} = lt$, $(A_s)_{\mathrm{BG}} = 2ht$ are the shear area of cell wall EA, AB, and BG, respectively

$$U = \frac{F_y{}^2 b(h+l)}{8tG_s(h+l\sin\theta)^2} \tag{2.72}$$

Now, by the second theorem of Castigliano, the shear deformation is

$$\frac{\partial U}{\partial F_y} = \delta_{yz} = \frac{F_y b(h+l)}{4tG_s(h+l\sin\theta)^2} \tag{2.73}$$

And the shear strain is

$$\gamma_{xz} = \frac{\delta_{yz}}{b} = \frac{F_y(h+l)}{4tG_s(h+l\sin\theta)^2} \tag{2.74}$$

where $F_y = \tau_{yz} A_c$, and $A_c = 2l\cos\theta(2h+2l\sin\theta)$, is the projected area of the RCE. Now, the equivalent out-of-plane shear modulus in the *y*-direction is

$$\mathrm{G}_{23} = \frac{\tau_{yz}}{\gamma_{yz}} \tag{2.75}$$

$$\mathrm{G}_{23} = \left(\frac{t}{l}\right) G_s \frac{\left(\frac{h}{l} + \sin\theta\right)}{\cos\theta\left(1+\frac{h}{l}\right)} \tag{2.76}$$

For a regular honeycomb structure with a double-thick vertical cell wall, *h*=*l*, and $\theta = 30^\circ$

$$\mathrm{G}_{23} = \frac{\sqrt{3}}{2}\left(\frac{t}{l}\right) G_s \tag{2.77}$$

2.1.9 Analysis of out-of-plane Poisson's ratios

The out-of-plane Poisson's ratios are equal to the Poisson ratio of solid material itself [2], i.e.

$$\nu_{31} = \nu_{32} = \nu \tag{2.78}$$

The remaining of Poisson's ratios are determined by the reciprocal theorem.

$$\begin{aligned} \nu_{13} &= \nu \frac{E_1}{E_3} \\ \nu_{23} &= \nu \frac{E_2}{E_3} \end{aligned} \tag{2.79}$$

2.2 Finite element analysis and results

This section contains the FE analysis of the RCE using the periodic boundary conditions (PBCs). Two kinds of FE analyses were performed — in the first case, the FE analysis of RCE was done through the homogenization approach to compute the equivalent properties of the honeycomb core using PBCs. Later, problems of practical relevance involving the 3PBT, edge compression test, buckling, and modal analysis of honeycomb and homogenized core were simulated, and the results were compared with each other to demonstrate the efficiency of the proposed approach.

2.2.1 Determination of Equivalent Properties

In this work, the homogenized continuum material properties of the honeycomb core were obtained using the PBCs [86,87]. A RCE, as shown in Figure 2.11(a), was considered for this purpose.

If σ_{ij} and ε_{ij} are the stress and strain fields, respectively, at any point of RCE, then the average stress-strain [88,89] can be calculated by

$$\bar{\sigma}_{ij} = \frac{1}{V_{RCE}} \int_V \sigma_{ij}(y_1, y_2, y_3)\mathrm{d}V \tag{2.80}$$

$$\bar{\varepsilon}_{ij} = \frac{1}{V_{RCE}} \int_V \varepsilon_{ij}(y_1, y_2, y_3)\mathrm{d}V \tag{2.81}$$

where V_{RCE} is the volume of the RCE. The honeycomb core is considered to be made of aluminium material whose Young's modulus (E_s) is 70 GPa, and Poissons's ratio (ν) is 0.3.

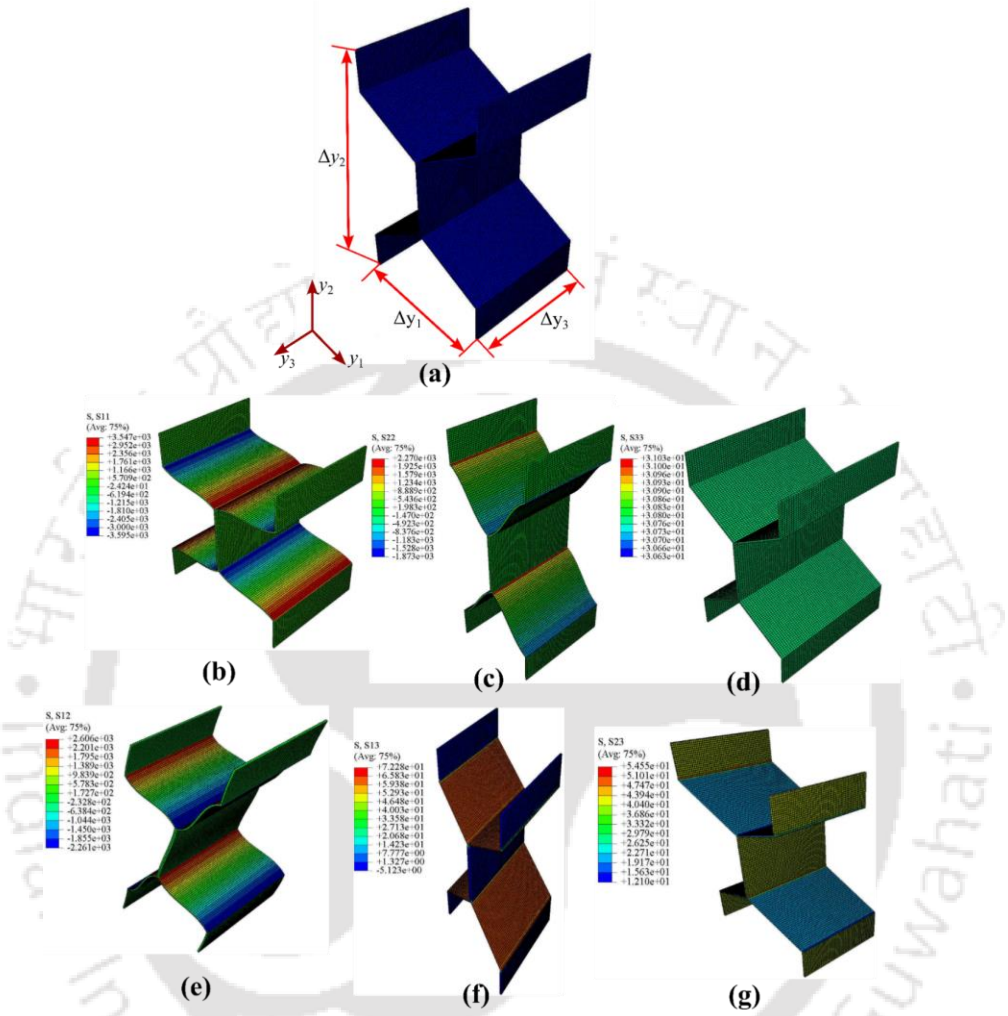

Figure 2.11 Computational models of (a) undeformed shape of RCE, deformed shape of RCE to obtain the (b) E_1, (c) E_2, (d) E_3, (e) G_{12}, (f) G_{13}, and (g) G_{23}

The constitutive relation of the homogenized RCE may be expressed (in Voigt notation) as

$$\begin{Bmatrix} \bar{\sigma}_1 \\ \bar{\sigma}_2 \\ \bar{\sigma}_3 \\ \bar{\sigma}_4 \\ \bar{\sigma}_5 \\ \bar{\sigma}_6 \end{Bmatrix} = \begin{bmatrix} C_{11} & C_{12} & C_{13} & 0 & 0 & 0 \\ C_{12} & C_{22} & C_{23} & 0 & 0 & 0 \\ C_{13} & C_{23} & C_{33} & 0 & 0 & 0 \\ 0 & 0 & 0 & C_{44} & 0 & 0 \\ 0 & 0 & 0 & 0 & C_{55} & 0 \\ 0 & 0 & 0 & 0 & 0 & C_{66} \end{bmatrix} \begin{Bmatrix} \bar{\varepsilon}_1 \\ \bar{\varepsilon}_2 \\ \bar{\varepsilon}_3 \\ 2\bar{\varepsilon}_4 \\ 2\bar{\varepsilon}_5 \\ 2\bar{\varepsilon}_6 \end{Bmatrix} \tag{2.82}$$

Hill-Mandel theorem [90], RCE energy is equal to the average of its components' energies:

$$\varepsilon_i C_{ij} \varepsilon_j = \frac{1}{V_{RCE}} \int_V \mathrm{Tr}\left[\sigma\varepsilon\right] \mathrm{d}V \tag{2.83}$$

Using linear combinations of applied loads on RCE, all the components of the orthotropic stiffness matrix C_{ij} can be found, and the equations to obtain the orthotropic elasticity tensor can be found in Gornet *et al.* [91] and Ijaz *et al.* [92].

The RCE forms a continuous body, so it is essential to meet two requirements at the boundaries of neighbouring RCEs. The first requirement is that the displacement should be continuous. In other words, neighbouring RCEs must not be separated or intruded upon. Secondly, the traction distribution must be equal and opposite at the opposite parallel sides of RCE. The displacement field of two parallel faces [93–95].

$$u_i^{\,j+} = \bar{\varepsilon}_{ik} y_k^{\,j+} + u_i^{*} \tag{2.84}$$

$$u_i^{\,j-} = \bar{\varepsilon}_{ik} y_k^{\,j-} + u_i^{*} \tag{2.85}$$

PBCs encompass two boundary conditions: exact values of displacement at nodal degrees of freedom to restrict the rigid body motion and relative values of displacement at some degrees of freedom which originates from the periodic function u_i^{*}. This is the same for both opposite sides of the RCE; *j*+ and *j*- are the two opposite parallel boundary surfaces of the RCE. So, the difference between the Eqs. (2.84) and (2.85)is

$$u_i^{\,j+} - u_i^{\,j-} = \bar{\varepsilon}_{ik} \left(y_k^{\,j+} - y_k^{\,j-}\right) = \bar{\varepsilon}_{ik} \Delta y_k^{\,j} \tag{2.86}$$

Since Δy_k is constant, the right portion of the Eq. (2.86) is constant for each pair of boundary surfaces for a specific $\bar{\varepsilon}_{ik}$. As a result, it may be implemented as a nodal displacement constraint to a FE model while ensuring traction and displacement continuity conditions [96,97].

The RCE shown in Figure 2.11(a) is modelled using three-dimensional quadratic brick elements with 20 nodes, C3D20. Micromechanics plugin was used for the Homogenization in Abaqus® 2017 software. The different strains were applied to an RCE, and therefore unique load conditions were generated to identify unknown elements in stiffness matrix ***C***. FE simulations were then carried out to obtain the orthotropic constitutive stiffness matrix [97]. The deformed model of the RCE, toward the determination of all the elastic properties, are shown in Figure 2.11 (b-g). For a regular honeycomb structure of $h=l=3.7$ mm, $t=0.08$ mm and $\theta=30^{\circ}$, the obtained properties are $E_1=1.65$ MPa, $E_2=1.58$ MPa, $E_3=2273.33$ MPa, $G_{12}=1.024$ MPa, $G_{13}=441.54$ MPa, $G_{12}=635.4$ MPa, $v_{12}=0.998$, $v_{13}=0.000241$, $v_{23}=0.0002298$.

Table 2.1 Different analytical expressions are used as reference solutions

Property	Expression
E_1 [2]	$\dfrac{\left(\frac{t}{l}\right)^3 E_s\cos\theta}{\left(\frac{h}{l}+\sin\theta\right)\sin^2\theta}$
E_2 [2]	$\dfrac{\left(\frac{t}{l}\right)^3\left(\frac{h}{l}+\sin\theta\right)E_s}{\cos^3\theta}$
ν_{12} [2]	$\dfrac{\cos^2\theta}{\left(\frac{h}{l}+\sin\theta\right)\sin\theta}$
G_{12} [5]	$\left(\frac{t}{l}\right)^3 E_s\dfrac{\left(\frac{h}{l}+\sin\theta\right)}{\left(\frac{h}{l}\right)^2\cos\theta\left(1+\frac{h}{4l}\right)}$
E_3 [98]	$\left(\frac{t}{l}\right)E_s\dfrac{\left(1+\frac{h}{l}\right)}{\cos\theta\left(\frac{h}{l}+\sin\theta\right)}$
G_{13} [98]	$\left(\frac{t}{l}\right)G_s\dfrac{\cos\theta}{\left(\frac{h}{l}+\sin\theta\right)}$
G_{23} [98]	$\left(\frac{t}{l}\right)G_s\dfrac{\left(\frac{h}{l}+\sin\theta\right)}{\cos\theta\left(1+\frac{h}{l}\right)}$

The theoretical results obtained from the strain energy approach and the FE homogenized results were compared with the reference results (Table 2.1) of comparable honeycomb material properties in the following subsections. For all subsequent computational analyses, the inclined cell wall is assumed to have a length of 3.70 mm, cell thickness is taken as 0.08 mm for the case of constant cell wall thickness, and Young's modulus of the RCE is taken as E_s=70 GPa.

2.2.1.1 The in-plane Young's modulus

Figure 2.12(a) shows the variation of the longitudinal Young's modulus E_1 at various cell angles (θ) for different h/l ratios at constant t/l ratio. The obtained theoretical and FEM results were compared with the analytical solutions of Gibson and Ashby [2]. Both the theoretical and FEM results were in good agreement with the analytical solution of Gibson and Ashby [2]. The E_1 values decrease with an increase in cell angle (θ) and the h/l ratio. Also, the E_1 values converge as the cell angle increases, irrespective of the h/l ratio.

Figure 2.12(b) shows the absolute % error between the obtained theoretical results and the computed FE results of E_1 for various cell angles and h/l ratios at the constant t/l ratio of 0.0216. The same trend in % error is observed up to the h/l=2 at all cell angles (θ). For $\theta \geq 30^{\circ}$, the % error is approximately equal at all h/l ratios. The % error observed between the theoretical and FE results and their relation to cell angles (θ) are evaluated by adopting the results obtained using the strain energy approach on the proposed representative cell element (RCE).

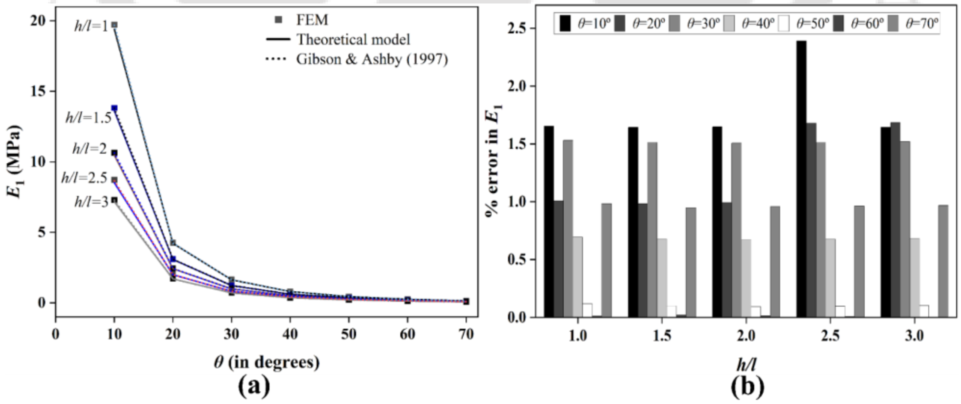

Figure 2.12 (a) E_1 at various cell angles (θ) for different h/l ratios, at the constant t/l ratio, (b) absolute % error in E_1 between the FE and theoretical results (current approach) at different h/l ratios and cell angles (θ), at the constant t/l ratio

For all h/l ratios, the average % error at the 60° cell angle is 0.01%, significantly less than at other cell angles. The maximum % error is observed for 10° cell angles on all h/l ratios.

Figure 2.13 depicts the variation in E_1 at various t/l ratios for different cell angles (θ) and h/l ratios. The obtained theoretical and FEM results were compared with analytical solutions of the Gibson and Ashby [2] and found to be in good agreement with each other. The E_1 values increase with the t/l ratio and reach 1000 % from the t/l ratio of 0.01 to 0.1. So, varying the t/l ratios can be a helpful way to obtain the desired longitudinal Young's modulus (E_1). There is a marginal increase in % error with an increase in the t/l ratio.

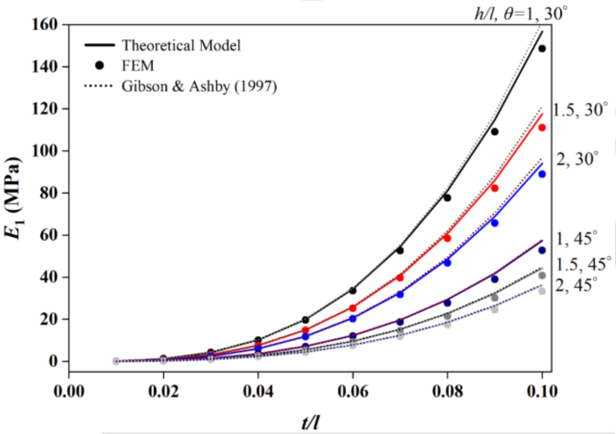

Figure 2.13 E_1 at various t/l ratios for different cell angles (θ) and h/l ratios

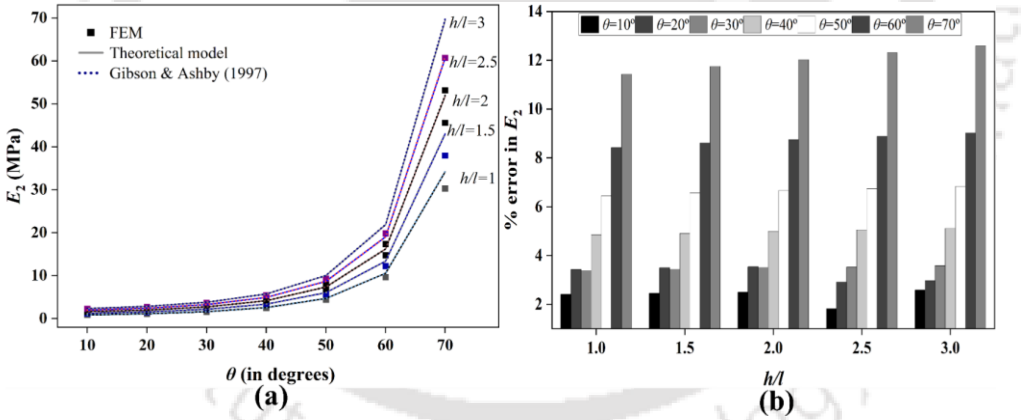

Figure 2.14 (a) E_2 at various cell angles (θ) for different h/l ratios, at the constant t/l ratio, (b) absolute % error in E_2 between the FE and theoretical results (current approach) at different h/l ratios and cell angles (θ), at the constant t/l ratio

An opposite trend in the transverse Young's modulus (E_2) estimation was observed when compared to the E_1 study for variation in cell angles (θ) at different h/l ratios, at a constant t/l ratio of 0.0216 as shown in Figure 2.14(a).

The E_2 values were found to increase with the increase in both the cell angles (θ) and the h/l ratio. The E_2 values converge with the decrease in the cell angles irrespective of the h/l ratio.

The theoretical results overestimate the E_2 by 5.92% compared to the FE results. This may be attributed to neglecting the shear effects in the analysis. The absolute % error is approximately the same for $30^\circ \leq \theta \leq 60^\circ$, whereas for 70°, there is a slight increase with the increase in the *h/l* ratios (Figure 2.14(b)).

The E_2 values increase rapidly with the *t/l* ratio, as shown in Figure 2.15, which was plotted for different cell angles and the *h/l* ratio. Accordingly, the *t/l* ratio can be chosen for designing the core to achieve the desired transverse Young's modulus. It was observed that the absolute % error in E_2 increases with the increase in the *t/l* ratio. As the *t/l* ratio increases, more shear deformation occurs, whose effects were neglected, and therefore, the % error between the theoretical results and FE results increases with the *t/l* ratio. A minimum error of 0.2% was observed at $\theta = 30^\circ$, $t/l = 0.01$, and $h/l = 1$, whereas a maximum error of 32% was observed at $\theta = 45^\circ$, $t/l = 0.1$, and $h/l = 2$.

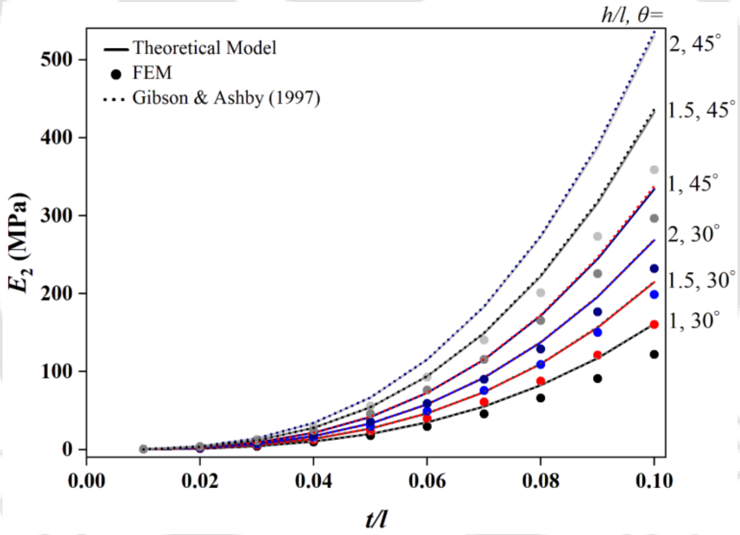

Figure 2.15 E_2 at various *t/l* ratios for different cell angles (θ) and *h/l* ratios

2.2.1.2 The in-plane Poisson's ratio

Figure 2.16 and Figure 2.17 show the variation of in-plane Poisson's ratio (ν_{12}) with different cell angles (θ) and the *t/l* ratio, respectively. The obtained theoretical and FE results were remarkably similar to the analytical results obtained by Gibson and Ashby [2]. As shown in Figure 2.16(a), the ν_{12} values at constant *t/l* ratio converge with the increase in cell angle (θ) and the *h/l* ratio, attaining a zero value at 90° cell angles. The absolute % error lies between 1.88 % and 6.16 %, as seen in Figure 2.16(b), which is calculated for various cell angles and different *h/l* ratios; for a given *h/l* ratio, this % error increases with the cell angle but is almost constant at a particular cell angle for all *h/l* ratios. It can be observed from Figure 2.17 that the in-plane Poisson's ratio (ν_{12}) values were almost constant with variation in *t/l* ratios. Both the results from the theoretical analysis and Gibson and Ashby [2] underpredict ν_{12} for higher values of *t/l* ratios.

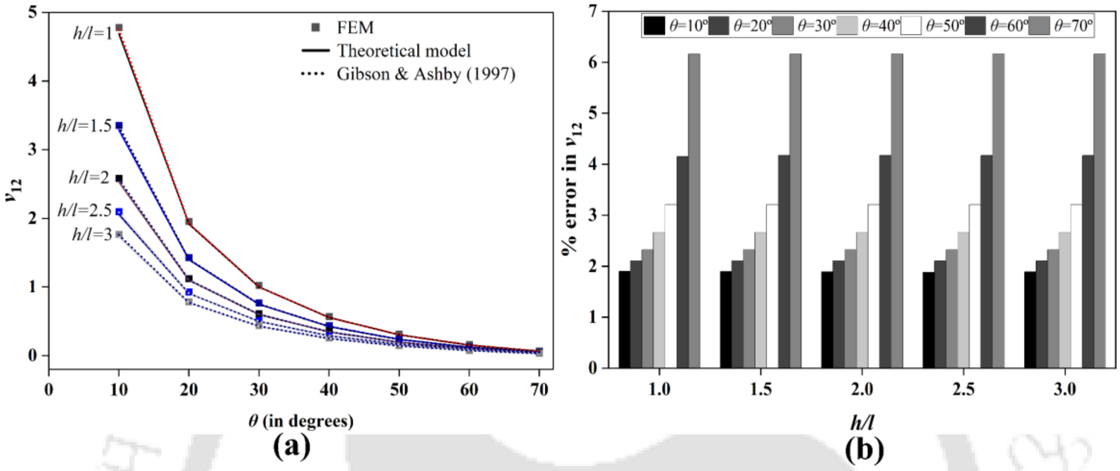

(a) (b)

Figure 2.16 (a) ν_{12} at various cell angles (θ) for different *h/l* ratios, at the constant *t/l* ratio, (b) absolute % error in ν_{12} between the FE and theoretical results (current approach) at different *h/l* ratios and cell angles (θ), at the constant *t/l* ratio

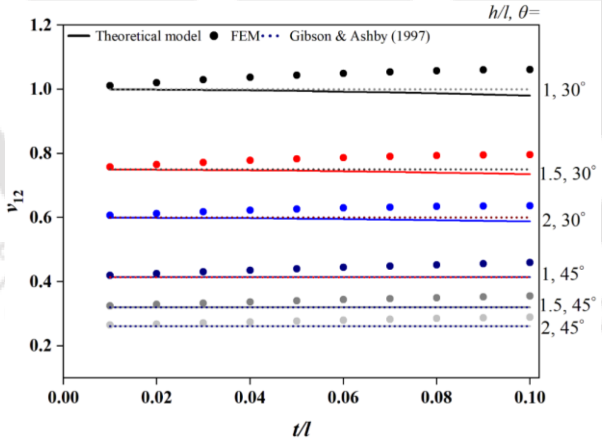

Figure 2.17 ν_{12} at various *t/l* ratios for different cell angles (θ) and *h/l* ratios

2.2.1.3 The in-plane shear modulus

Figure 2.18 and Figure 2.19 show the variations of the in-plane shear modulus G_{12} with cell angles (θ) and *t/l* ratio, respectively. In this case, the obtained theoretical and FE results were compared with the analytical solutions of Sorohan *et al.* [5] instead of Gibson and Ashby's [2] work, as the latter focused on studying the honeycomb structure for a single constant cell wall thickness.

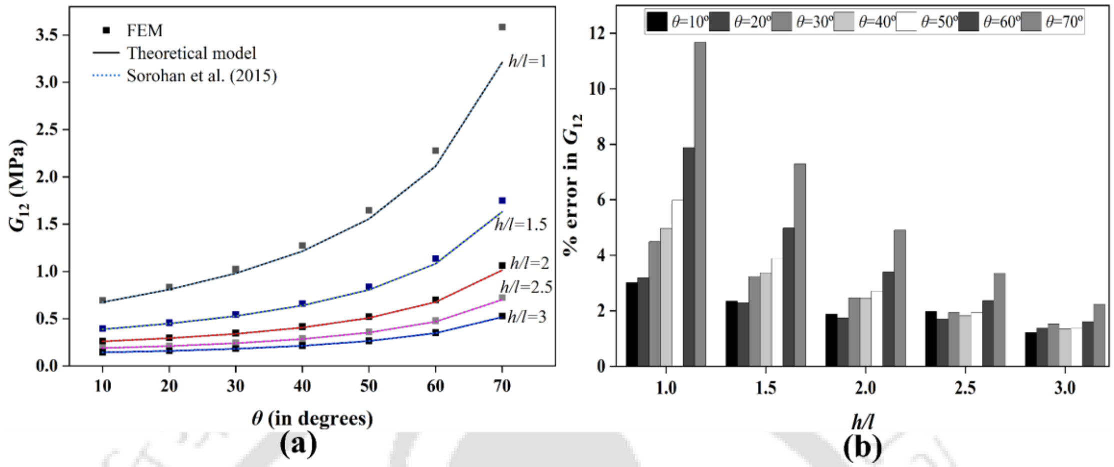

Figure 2.18 (a) G_{12} at various cell angles (θ) for different *h/l* ratios, at the constant *t/l* ratio, (b) absolute % error in G_{12} between the FE and theoretical results (current approach) at different *h/l* ratios and cell angles (θ), at the constant *t/l* ratio

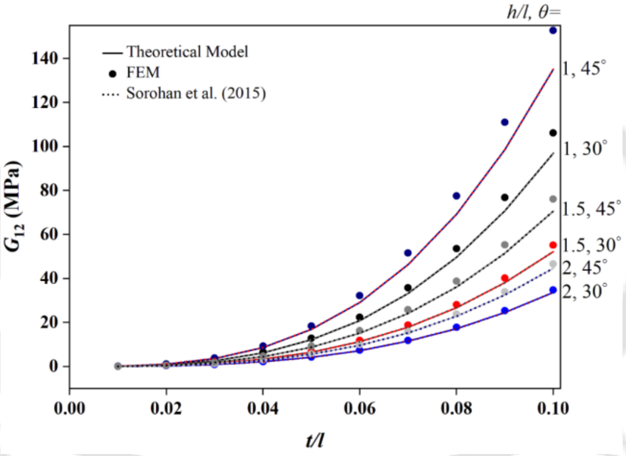

Figure 2.19 G_{12} at various *t/l* ratios for different cell angles (θ) and *h/l* ratios

The G_{12} values at a constant *t/l* ratio of 0.0216 increase with increased cell angle and decrease with *h/l* ratios, as shown in Figure 2.18(a). Likewise, the G_{12} value increases rapidly with the *t/l* ratio (Figure 2.19). Therefore, increasing the core thickness would enhance the in-plane shear modulus. At a constant *t/l* ratio, the absolute % error in theoretical and FE results of G_{12} decreases with the *h/l* ratio and increases with the cell angle (θ) (Figure 2.18(b)). The maximum (11.67%) and minimum (1.22%) % error was observed at $\theta = 70^{\circ}$, *h/l* =1, and $\theta = 10^{\circ}$, *h/l* =3 respectively. From Figure 2.19, the % error in G_{12} was found to increase with the *t/l* ratio and was approximately 2% more than that of the % error observed at the constant *t/l* ratio.

2.2.1.4 *The out-of-plane Young's modulus*

The E_3 values at a constant t/l ratio of 0.0216 were found to increase with cell angle (θ), but it decreases with the increase in h/l ratios, as seen in Figure 2.20(a). It is to be noted that for low values of h/l ratio, there is a drop in E_3 value before the increase with θ. The obtained theoretical and FE results were very close to the analytical results obtained by Zhang and Ashby [98]. For a constant t/l ratio, Figure 2.20(b) shows the absolute % error in E_3 between the FE and theoretical results at different h/l ratios. The % error shows an almost constant trend varying from 2.15% to 5.94% for different h/l ratios but increases with the cell angle (θ).

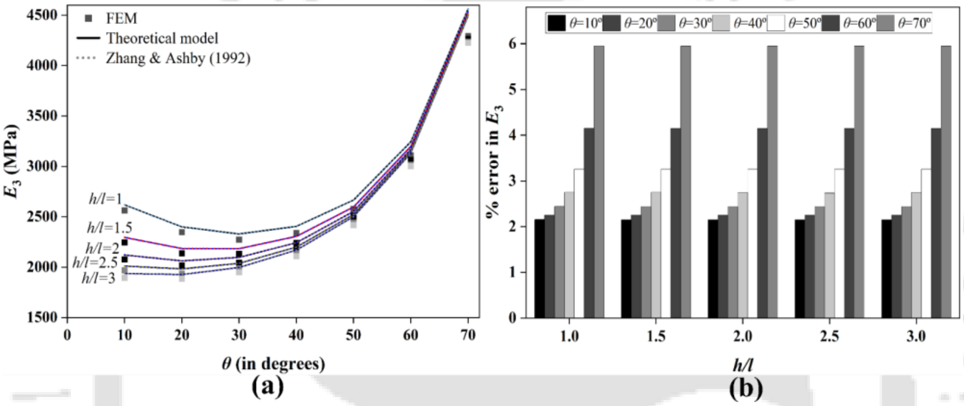

Figure 2.20 E_3 at various cell angles (θ) for different h/l ratios, at the constant t/l ratio, (b) absolute % error in E_3 between the FE and theoretical results (current approach) at different h/l ratios and cell angles (θ), at the constant t/l ratio

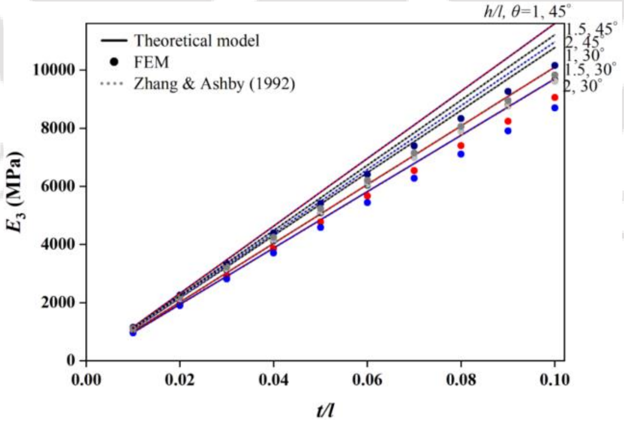

Figure 2.21 E_3 at various t/l ratios for different cell angles (θ) and h/l ratios

Figure 2.21 shows that the E_3 values steadily increase with an increase in t/l ratio, and the highest value of 11598 MPa was obtained at $\theta = 45^{\circ}$, $t/l = 0.1$, and $h/l = 1$.

2.2.1.5 Out-of-plane Shear moduli - G_{13} and G_{23}

For a constant t/l ratio of 0.0216, the out-of-plane shear modulus (G_{13}) value decrease with an increase in cell angle (θ) and h/l ratio, as shown in Figure 2.22(a). The theoretical and the FE results agreed well with the analytical results obtained by Zhang and Ashby [98].

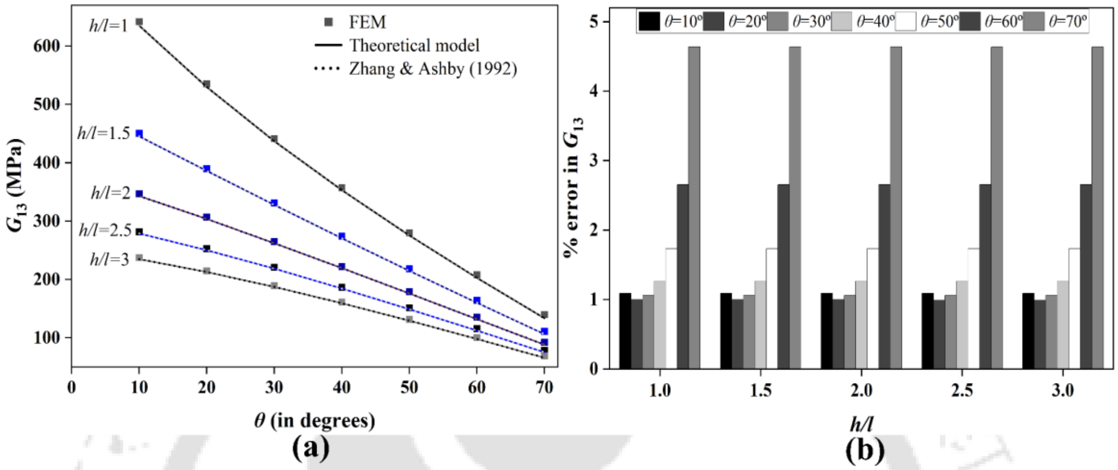

Figure 2.22 (a) G_{13} at various cell angles (θ) for different h/l ratios, at the constant t/l ratio, (b) absolute % error in G_{13} between the FE and theoretical results (current approach) at different h/l ratios and cell angles (θ), at the constant t/l ratio

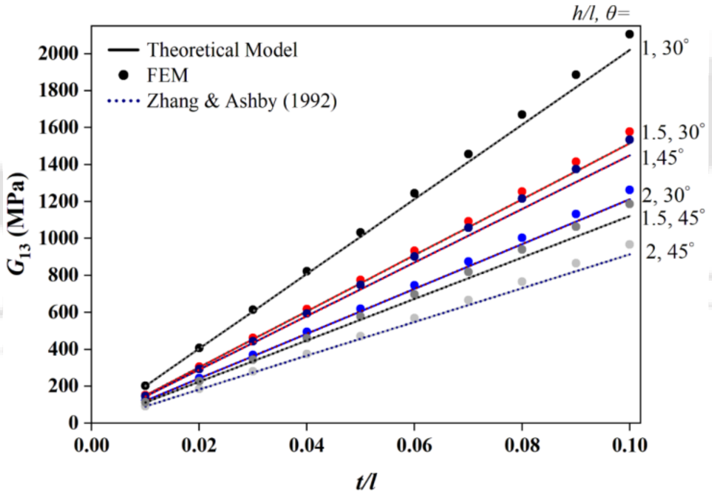

Figure 2.23 G_{13} at various t/l ratios for different cell angles (θ) and h/l ratios

Again for a constant t/l ratio of 0.0216, Figure 2.22(b) shows that the % error in G_{13} has similar trends for different h/l ratios across the cell angles. For $10^{\circ}<\theta\leq70^{\circ}$, the % error increases with θ at any h/l ratio. Figure 2.23 shows a linear trend similar to that of variation of the E_3 at various t/l ratios for different cell angles (θ) and h/l ratios — as the t/l ratio increases, the G_{13} values increases.

The out-of-plane shear modulus (G_{23}) increases with an increase in the cell angle, as shown in Figure 2.24(a). The obtained theoretical and FEM results were in good agreement with the analytical results obtained by Zhang and Ashby [98].

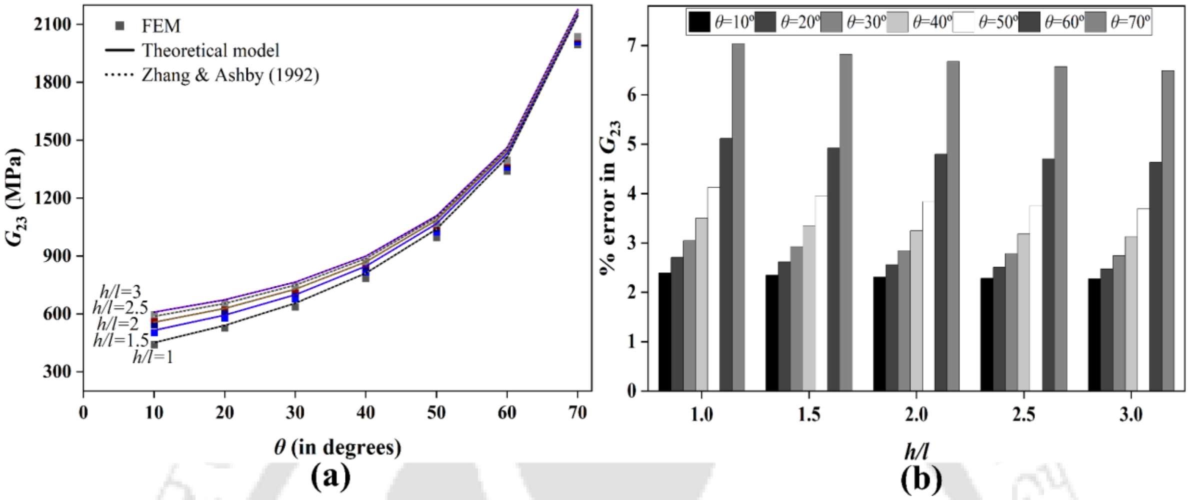

Figure 2.24 (a) G_{23} at various cell angles (θ) for different *h/l* ratios, at the constant *t/l* ratio, (b) absolute % error in G_{23} between the FE and theoretical results (current approach) at different *h/l* ratios and cell angles (θ), at the constant *t/l* ratio

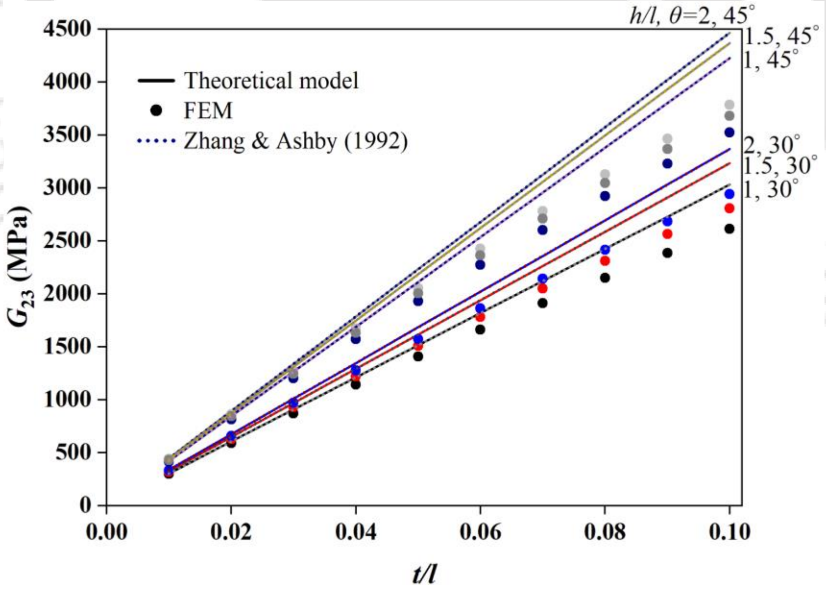

Figure 2.25 G_{23} at various *t/l* ratios for different cell angles (θ) and *h/l* ratios

The % error in G_{23} between the FE and theoretical results is shown in Figure 2.24(b). The % error in G_{23} was observed to marginally decrease with an increase in the *h/l* ratio at a particular cell angle, but it increases with the cell angle. G_{23} has an average % error of 3.78 % at a constant *t/l* ratio. Figure 2.25 shows that the G_{23} values steadily increase with an increase in t/l ratio. The G_{23} shows a similar trend as that of the G_{13}. In comparison to G_{13}, the G_{23} values were higher.

Although there is a close agreement between the theoretical results and the reference results, the % error between the numerical and the theoretical results increases with the cell angle θ, for $\theta \geq 30°$, except for E_1. The theoretical and the reference results are based on a statically admissible stress field. Another approach to obtaining effective properties is imposing a kinematically admissible displacement field. It was shown in the literature that these approaches give rise to the lower and upper bound [99]. So, there will be some difference between the values obtained through both of these approaches with cell angle and therefore, this may contribute to the error between the results obtained using the PBC and the theoretical approach.

In summary, the honeycomb core's in-plane and out-of-plane elastic properties increase rapidly with an increase in the t/l ratios, except the Poisson's ratio. The other effects on the elastic properties with parameter variations are illustrated in Table 2.2. So that one can design and develop the honeycomb core structure according to the structural property requirements.

Table 2.2 Effects on the elastic properties with variations in parameters

Property	θ (↑)	h/l (↑)	t/l (↑)
E_1	(↓)	(↓)	(↑)
E_2	(↑)	(↑)	(↑)
v_{12}	(↓)	(↓)	≈ Constant
G_{12}	(↑)	(↓)	(↑)
E_3	(↓↑)	(↓)	(↑)
G_{13}	(↓)	(↓)	(↑)
G_{23}	(↑)	(↑)	(↑)

2.2.2 Finite Element Analysis of Different Tests and Analyses

This section used both obtained elastic properties (by FEM and theoretical model) to simulate the 3PBT and the edge compression test. Further, buckling and modal analysis of the core was performed. FE simulations were done on the honeycomb and homogenized core using the ABAQUS software, and the results were compared. A Poisson's ratio of 0.3 was assumed in all the subsequent case studies.

2.2.2.1 3PBT

Two 3PBTs were done on the sandwich structure, the first with the actual honeycomb core as the core material and the second with the homogenized core, as shown in Figure 2.26. The dimensions of the face sheets were 210 mm long, 89 mm wide, and 0.9 mm thick. The actual honeycomb and homogenized cores had the same length and width as the face sheet, but the core height was 10 mm. The rigid indenter and rigid support diameters and lengths were 30 mm and 89 mm, respectively. The dimension of the RCE of the honeycomb core was taken as $h=l=3.7$ mm and $t=0.08$ mm for all the analyses. A tie constraint was used to bind the core and face sheets. The movable rigid indenter was set to move in the negative *z*-direction by a constant displacement of 5 mm; other movements and rotations were restricted. Rigid supports were constrained in all directions. The face sheet and core materials were discretized with 3-D linear eight-node brick elements — C3D8 and the indenter with 3-D bilinear rigid quadrilateral elements with four nodes — R3D4.

As expected, the computation time for the homogenized core was significantly less — which was about 4 % of the computational time required for honeycomb core FE analysis (Table 2.3). As a result, the homogenized core may be used to perform complex FE simulations involving honeycomb structures within a linear elastic framework. Figure 2.27 shows the load-displacement curve obtained in both cases. Because all the constitutive elastic properties of the honeycomb core were estimated solely using the fundamental material’s elastic properties, the load-displacement curve was similar to each other.

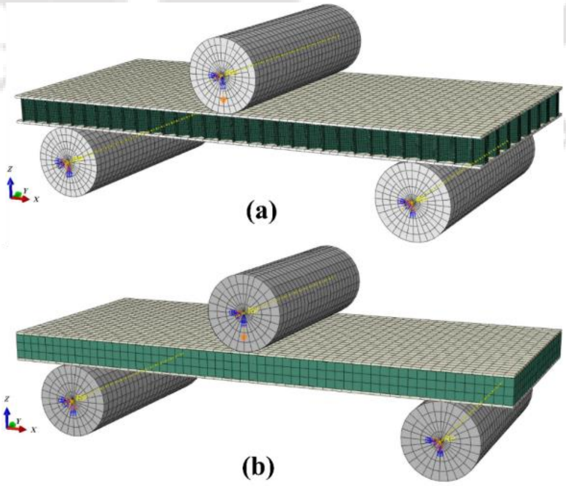

Figure 2.26 3PBT specimen (a) actual honeycomb core, (b) homogenized core

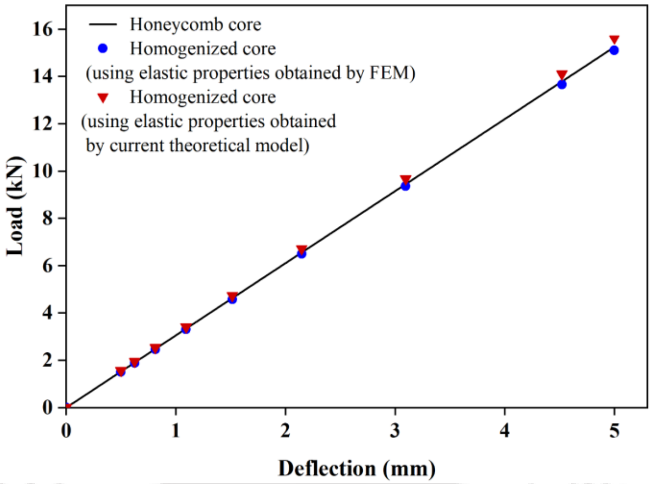

Figure 2.27 Load vs. deflection curve for 3-PBT

2.2.2.2 Edge-Compression Test

As shown in Figure 2.28, the edge-compression test was performed on both the honeycomb and homogenized core. The supporting plate length, width, and thickness were 89 mm, 10 mm, and 0.9 mm, respectively. The actual honeycomb and homogenized core have identical dimensions of 105 mm, 89 mm, and 10 mm. The core is placed between two rigid plates, one of which is fixed and the other moving at the top. The core and the rigid plates have no frictional contact. The rigid moving plate was set to move along the negative *x*-direction by a constant displacement of 5 mm, with the remaining movements restricted.

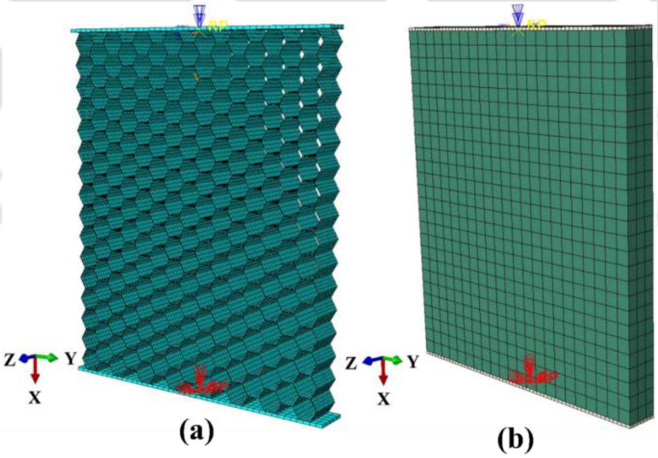

Figure 2.28 Edge-compression test specimen (a) with the honeycomb core and (b) with the homogenized core

For the FE simulations, the supporting rigid sheet materials were modelled using 3-D bilinear rigid quadrilateral elements with four nodes, R3D4, and the honeycomb and homogenized core were modelled with 3-D quadratic brick elements with 20 nodes — C3D20. The computation time and the number of elements used during the simulation can be seen in Table 2.3. The computation time for the homogenized core was only 1.55% of honeycomb core.

The load vs deflection curve for the honeycomb core and homogenized core's edge-compression test is shown in Figure 2.29. Both curves follow a similar trend within the elastic limits. Plastic properties can be incorporated into understanding the crushing behaviour of the core.

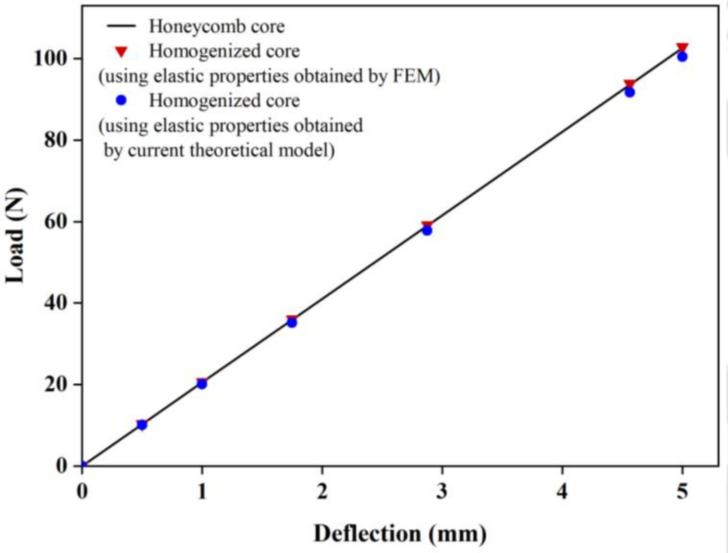

Figure 2.29 Load vs. deflection curve for edge-compression test

2.2.2.3 *Buckling Analysis*

The linear perturbation approach is often used in buckling analysis to determine the critical buckling load of structures. This analysis can be performed on an unloaded or preloaded structure. It may be used to represent measured initial overall and local geometric defects and examine imperfection sensitivity when measurements are unavailable. The eigenvalue buckling method is often used to calculate the critical buckling loads of stiff structures.

The buckling analysis was performed on both the honeycomb and homogenized core structures. The honeycomb core and homogenized core have the same length, width, and thickness of 105 mm, 29.7 mm, and 5 mm and were modelled with 3-D quadratic brick elements with 20 nodes — C3D20 for FE simulations. The geometry and boundary conditions for the buckling analysis are shown in Figure 2.30. The computational time is an essential parameter during the FE simulation. The computation time taken during the buckling analysis of the honeycomb core was about 30 times that of the homogenized material. The obtained critical buckling load in the honeycomb and homogenized core (using elastic properties obtained by the FEM and theoretical model) was 5.35 N and 5.37 N, 5.28 N, respectively.

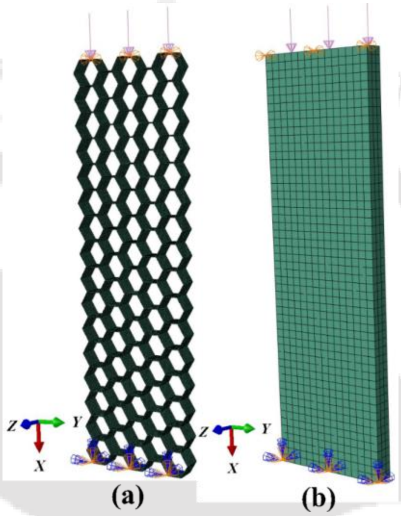

Figure 2.30 Buckling analysis for the specimen (a) with the honeycomb core. (b) with the homogenized core

2.2.2.4 *Modal Analysis*

Natural frequencies and mode shapes must be considered while designing a structure that can sustain dynamic loading conditions. The modal analysis shows the movement of different parts of the actual honeycomb and homogenized honeycomb structures under dynamic loading by analyzing the structure's natural frequencies and mode shapes. Modes are an intrinsic feature of a structure. Both mode shapes and natural frequencies will change with the different boundary conditions, but they are independent of the external loads.

A total of six modes were observed in the modal analysis of both the honeycomb and homogenized core structures. Both the dimensions of structure and modelling were identical to those used in the buckling analysis. The boundary conditions are shown in Figure 2.31. The density of the honeycomb core was taken 2730 kg/m^3, and for the homogenized core, it was obtained from Eq. (2.3) as 90.88 kg/m^3. For both honeycomb and homogenized structures, the frequencies of different modes — primary out-of-plane bending (Mode 1), in-place bending modes (Mode 2 and Mode 5), secondary out-of-plane bending (Mode 3), torsional (Mode 4), and axial (Mode 6) modes were almost comparable. There is not much variation in frequency between the remainder of the modes. The frequencies and mode shapes obtained are presented in Table 2.4 and Figure 2.32, respectively. The computational time for the homogenized core was only 2.23% of the honeycomb core.

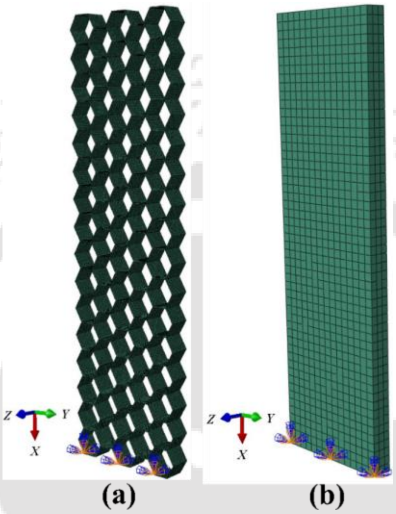

Figure 2.31 Modal analysis for specimen (a) with the honeycomb core. (b) with the homogenized core

The natural frequency values between the honeycomb core and homogenized material simulations using effective properties obtained from the homogenization technique show some differences. This can be alleviated by including the shear effects in the theoretical formulations.

Table 2.3 Comparison of computation time for different analyses/tests

Analysis/Test	No. of elements		Computation time %
	Honeycomb core	Homogenized core	$\left(\frac{\text{Homogenized core}}{\text{Honeycomb core}}\times 100\right)$
3PBT	162720	10795	3.382
Edge-compression Test	32573	3632	1.547
Buckling analysis	24900	1677	3.371
Modal analysis	222325	1512	2.230

Table 2.4 Different modes and their frequencies of both core structures

Mode S. No	Mode shape	Frequency obtained for Honeycomb core (Hz)	Frequency obtained for Homogenized core (FEM)(Hz)	Frequency obtained for Homogenized core (Theoretical) (Hz)
1	Primary out-of-plane bending	22.822	24.526	24.617
2	Primary in-plane bending	66.909	61.169	58.707
3	Secondary out-of-plane bending	149.43	152.96	152.56
4	Torsional	161.04	160.39	160.92
5	Secondary in-plane bending	328.67	314.2	301.46
6	Axial	357.07	347.76	333.79

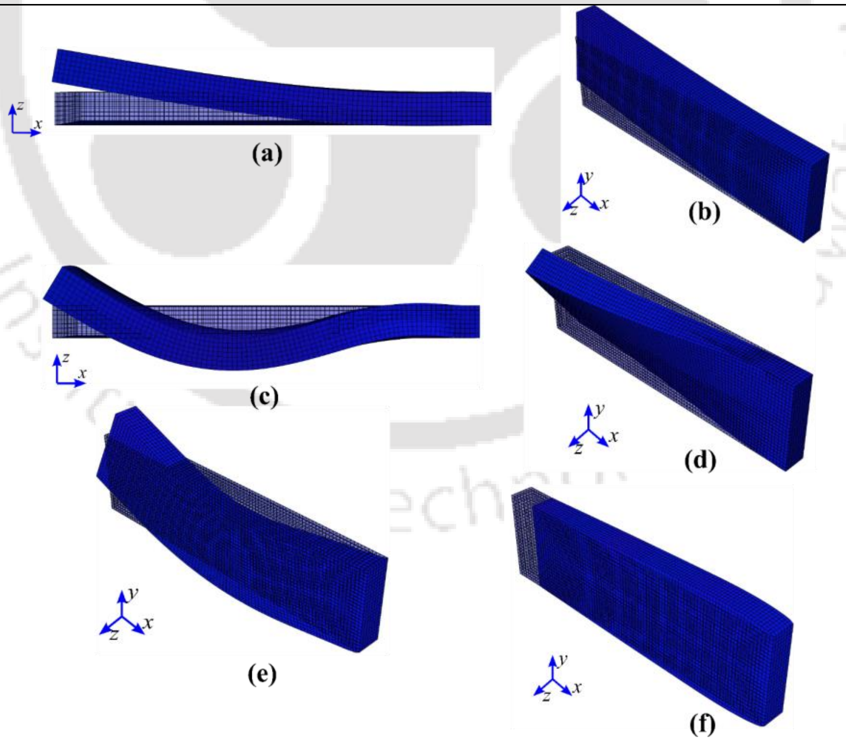

Figure 2.32 Different mode shapes (a) primary out-of-plane bending, (b) primary in-plane bending, (c) secondary out-of-plane bending, (d) torsional, (e) secondary in-plane bending, and (f) axial

Table 2.3 shows the reduction in computational time for the homogenized core FE analysis compared to the honeycomb core analysis. In the case of modal analysis, a large number of elements were needed to obtain the converged results compared to the analysis using the homogenized material. Thus, the computational time and effort to carry out a complex analysis involving the honeycomb structure will be significantly reduced using the proposed homogenization procedure.

2.3 Summary

In this work, all nine elastic constants that define the equivalent material orthotropic elasticity tensor of the honeycomb core structure were determined analytically using the strain-energy method. The same constitutive tensor was estimated using the principle of homogenization in the FE analysis by incorporating the PBCs. A novel RCE was chosen for homogenization within the FE framework. The elastic properties results obtained by the strain energy method and FE analysis were found to be in good agreement with the reference results. Four case studies were presented to demonstrate the effectiveness of both the analytical and the numerical methodology: 3PBT, edge compression test, buckling, and modal analysis. It is noteworthy that the computational time of the homogenized core is significantly less — a reduction of 96% was observed compared to the honeycomb core computations without loss of accuracy in the 3PBT, edge compression test, and buckling analysis. In the modal analysis, the natural frequencies of the out-of-plane bending, which is relevant in practical scenarios, and torsional modes were in good agreement with each other. However, there were differences between the honeycomb core and the homogenized material simulations using effective properties obtained from the theoretical procedure using the strain-energy approach. This can be reduced by taking into account the shear stress effects in the theoretical formulations.

Chapter 3 A preliminary investigation on friction stir spot welding of honeycomb core sandwich sheet without disc insert

3.1 Experimental process

This section discusses the methods used for the welding process, specimen preparation, load and torque measurement during welding, mechanical testing of the welded joint, and their failure pattern.

3.1.1 Materials and FSSW

Raw materials used were (i) rolled sheets of AA5052-H32 grade with 0.95 mm thickness as face sheets and (ii) a honeycomb core made of AA3003 with a height of 6 mm. The unit cell dimensions of the core, the cell height, single wall thickness, and vertical and inclined cell wall length were 6 mm, 0.08 mm, and 3.7 mm, respectively. Skin and core were commercially available. The stress-strain data of skin and core in their original forms from tensile tests and compression tests are provided in Figure 3.1.

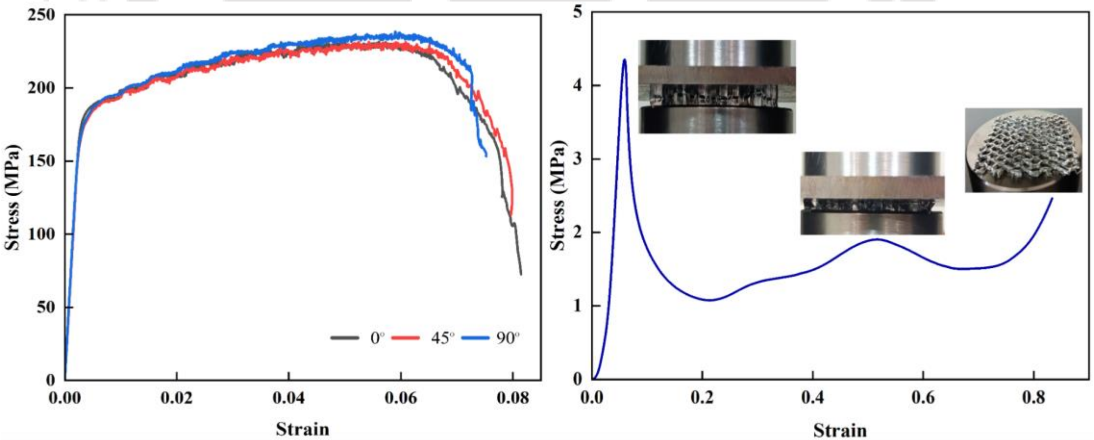

(a) (b)

Figure 3.1 Mechanical properties of raw materials (a) tensile behaviour of skin and compressive behaviour of (b) honeycomb core

The ASTM standard E8 was used for skin sheet, and for the honeycomb core, ASTM C365M-11 was used [100–102]. The tensile and compressive tests were performed at room temperature on a universal testing machine (Shimadzu UTM, Model: AGX-V) at a 1 mm/min cross-head speed (0.03125 per min for tensile test and 0.1667 per min for compressive test). Each set of tests included three specimens to assure consistency and accuracy; the average result was used for analysis. Energy-dispersive X-ray (EDX) analysis was used to identify the chemical composition of the materials, which is shown in Table 3.1 and in Figure 3.2.

Table 3.1 Chemical composition of materials used for sandwich construction

Alloy	Zn	Cu	O	Si	Ni	Mn	Fe	Mg	Al
AA5052-H32 (skin)	-	0.2	-	-	0.9	-	0.4	2.5	Bal.
AA3003 (core)	0.1	-	-	0.4	-	0.9	0.4	-	Bal.

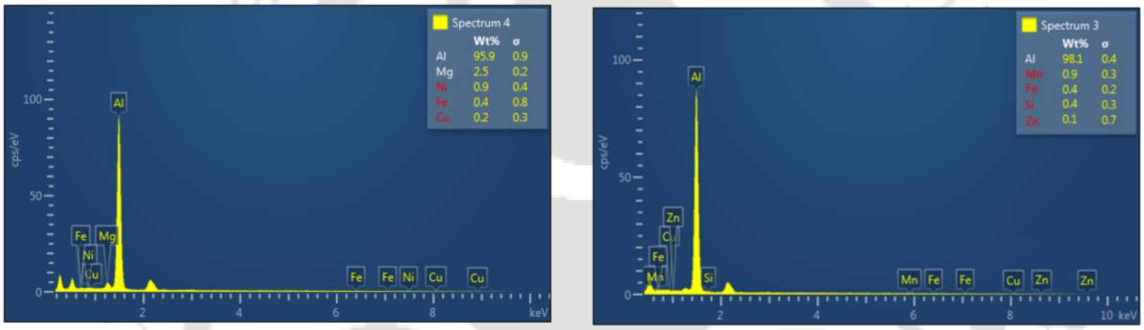

(a) (b)

Figure 3.2 EDX analysis of (a) AA5052-H32 and (b) AA3003

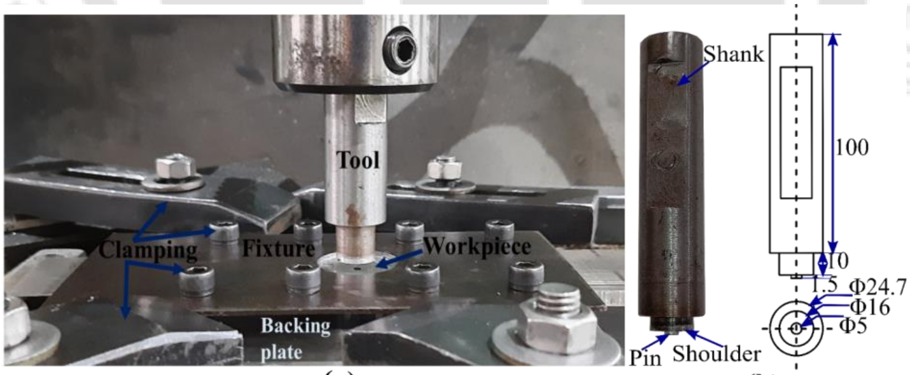

(a) (b)

Figure 3.3 FSSW details (a) FSSW setup (b) FSSW tool (all dimensions are in mm)

The FSSW joints were produced using a vertical-type three-axis FSW machine, as shown in Figure 3.3(a). Acetone was used to thoroughly clean all surfaces of metallic sheets to eliminate dirt and oil. All of the relevant specimen pieces were overlapping and arranged on the bed of the machine. There was no movement in any direction since the specimen was completely clamped. The procedure involved plunging, stirring, and retracting. During the initial phase of the plunging process, the rotation of the tool was confined, and the tool was permitted to plunge up to a specific depth. The tool rotation was initiated in the second stage of plunging, and further plunging was performed to reach a specific depth. The tool was made of H13 steel and had two parts: a straight cylindrical pin that measured 1.5 mm in length and diameter and a flat shoulder that measured 16 mm (Figure 3.3(b)).

As shown in Table 3.2, six separate parameter sets were used for the joining. Only the rotational speed varies between 233 rpm-1200 rpm. Other parameters, such as plunge speed, dwell time, and plunge depth, were maintained constant. A standardized process for the fabrication of the honeycomb sandwich structure through the FSSW is shown in Figure 3.4. The second stage is unique for the FSSW of the honeycomb sandwich structure.

Table 3.2 Parameters used during welding

Serial no.	Rotational speed (rpm)	Plunge depth (without rotation) (mm)	Plunge depth (when rotation starts) (mm)	Plunge speed (mm/min)	Dwell time (s)
1	233	6.2	1.5	2	5
2	342				
3	462				
4	612				
5	900				
6	1200				

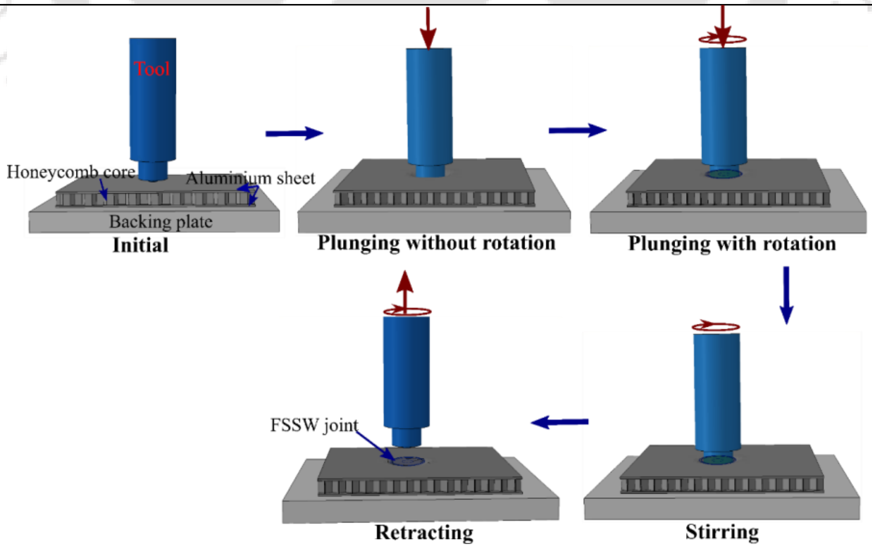

Figure 3.4 FSSW stages used for fabrication of the sandwich structure

3.1.2 Specimen preparation

Two distinct sandwich sheet specimens were made for testing during the FSSW. The dimensions of the lap shear and peel test specimens were chosen following the AWS D8.9-97 standards (Figure 3.5) [103]. Both tests were conducted on the Shimadzu (AGX-V) UTM (Figure 3.6), which can handle loads up to 100 kN. The assessments were conducted at room temperature with a 1 mm/min test speed.

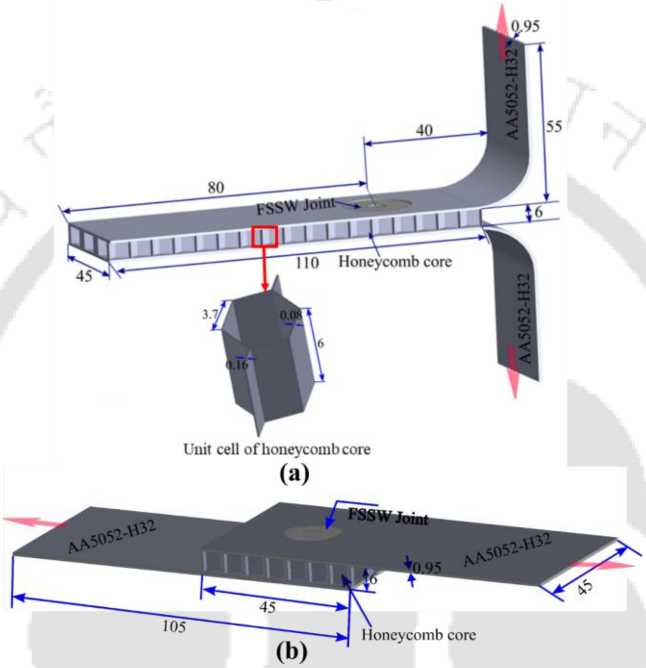

Figure 3.5 Schematic of (a) peel test specimen with honeycomb configuration (b) lap-shear test specimen (all dimensions are in mm)

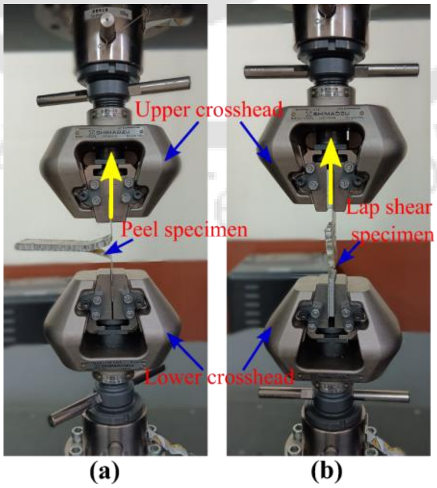

Figure 3.6 Samples undergoing (a) peel test (b) lap-shear test in UTM

3.2 Results and discussion

This section investigates the variation in the load and the torque during the FSSW of the sandwich. The joint performance of the welded sandwich structure was compared and correlated at six different rotational speeds by the lap shear and peel test. Lastly, the fracture behaviour was studied on the fractured surfaces of the lap shear and peel-tested sandwich sheets.

3.2.1 Load and torque response

The MP31C09 strain data logger was used to record torque and axial load while welding. The data logger was equipped with integrated sensors to accurately capture and record the torque and axial load during welding. The load and torque responses with time during welding are shown in Figure 3.7. These graphs are plotted during plunging with the tool rotation.

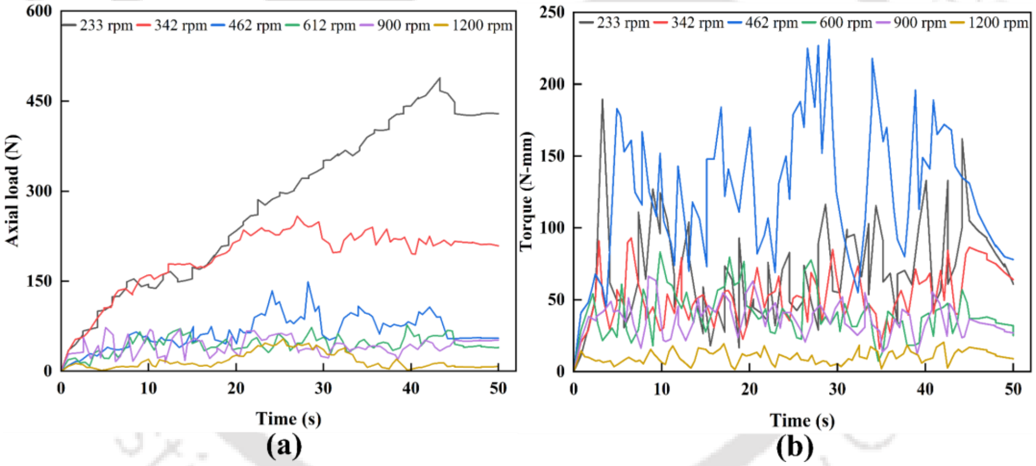

Figure 3.7 Variation of the (a) axial load and (b) torque during the FSSW

The plunging or axial load decreases with the increase in the rotational speed as the flow stress decreases at increased temperatures. The welding torque follows the same pattern with the rotational speed except at 462 rpm. The maximum load of 489 N is reached at 233 rpm, while the maximum torque of 233 N-mm is obtained at 462 rpm. We can observe from the figure that the axial load is almost constant at dwell time, i.e., at 45 s to 50 s; because the tool movement is stopped, only the stirring process takes place. There is a fluctuation in both plunging load and torque during welding; it occurs because of the breaking of the honeycomb core into tiny particles, as the honeycomb core has a much lower wall thickness of 0.08 mm.

3.2.2 Mechanical performance

The strength of the joint in the FSW process was evaluated based on its failure load due to the uncertainty surrounding the exact load-bearing area. In the lap-shear test of the honeycomb core sandwich structure, which was conducted at six rotational speeds, the relationship between maximum load and displacement leading to fracture was analyzed and depicted in Figure 3.8(a). Notably, the highest fracture load of 1572 N was recorded at a rotational speed of 1200 rpm, while the lowest fracture load of 350 N occurred at 233 rpm. Generally, the fracture load and failure displacement demonstrated an increasing trend with increasing rotational speed, except for the instance at 900 rpm. Across all rotational speeds, the displacement during failure was roughly proportional to the peak load, which correlated with the elongation of the welded portion. It was observed that FSSW joints with stronger shear strength exhibited enhanced ductility, while poorly welded joints displayed reduced ductility [41].

In the peel test of the honeycomb core sandwich structure conducted at six different rotational speeds, the maximum load and displacement resulting in fracture were analyzed and shown in Figure 3.8(b). The fracture load and failure displacement both are increasing with the rotational except at 900 rpm, as the same behaviour was observed during shearing.

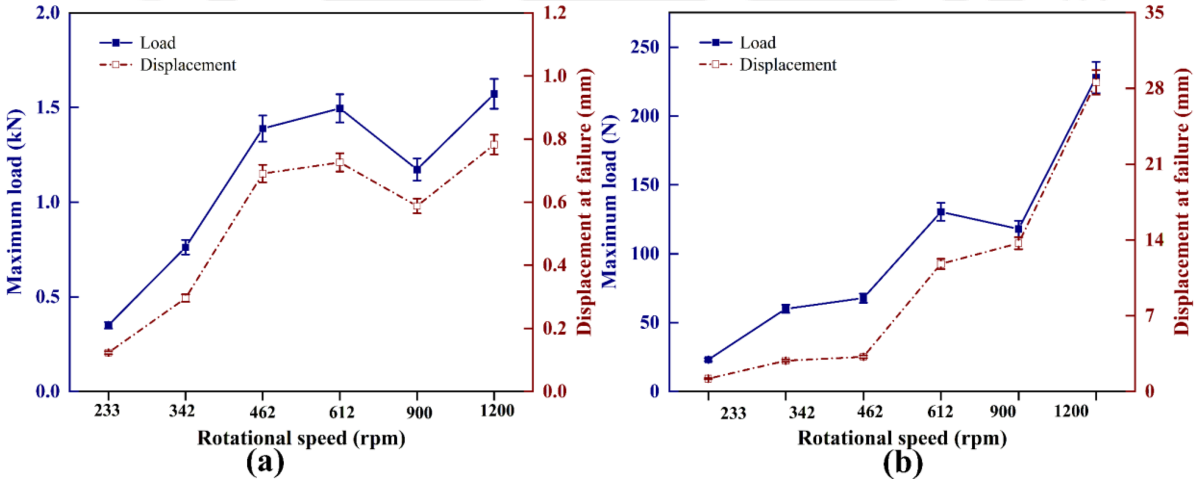

Figure 3.8 Maximum fracture load and displacement at failure in (a) lap-shear test (b) peel test of the sandwich sheets

3.2.3 Failure modes

The outcomes of the failure modes of the lap-shear and peel tests are shown in Figure 3.9 (a) and (b). Various failure modes were observed during the lap shear test, including nugget pull-out, partial nugget fracture, and shear failures. A shear fracture mode was observed at a rotational speed of 462 rpm, while nugget pull-out failures were encountered at rotational speeds of 233, 342, 900, and 1200 rpm. Additionally, a partial nugget fracture occurred at 612 rpm. At the lower rotational speeds of 233 and 342 rpm, the plates and core completely separated, whereas at higher rotational speeds (462, 612, 900, and 1200 rpm), the core remained attached to the top sheet even though separation occurred. In the peel test, the predominant mode of failure was nugget pull-out, except at 900 rpm and 1200 rpm where partial nugget fracture and nugget fracture were observed, respectively.

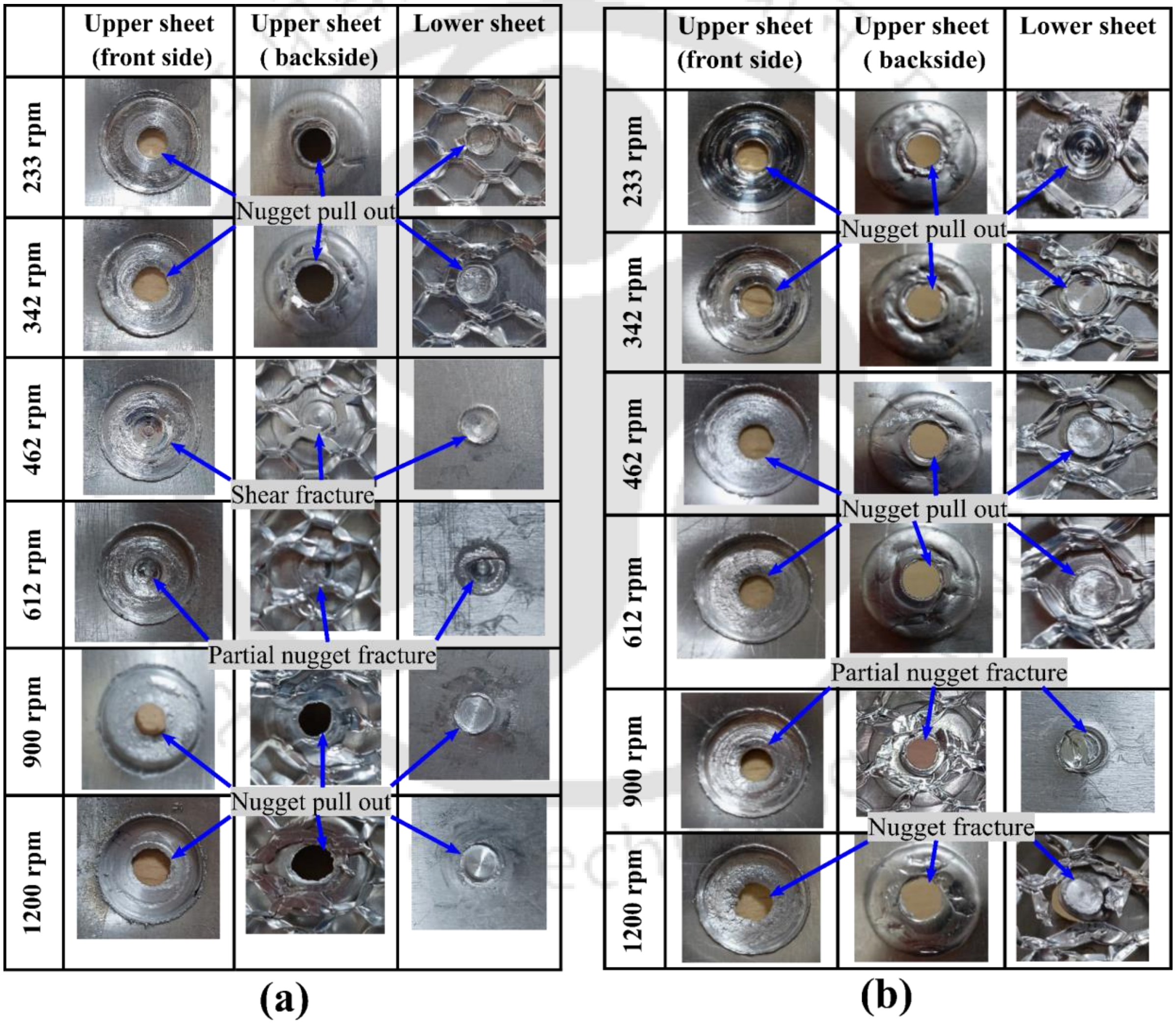

Figure 3.9 Failure modes during (a) lap-shear test (b) peel test

3.3 Summary

The FSSW process was employed to join the honeycomb core sandwich structure, considering six rotational speeds: 233 rpm, 342 rpm, 462 rpm, 612 rpm, 900 rpm, and 1200 rpm. A comprehensive comparison was conducted involving load and torque requirements during FSSW, and mechanical performances and fracture patterns from the lap shear and peel test were observed. Based on these findings, the following conclusions can be drawn:

- With increase in rotational speed, the axial load experienced during plunging decreases due to a reduction in flow stress, except at 900 rpm. Meanwhile, the welding torque increased, except at 462 rpm.
- Both the fracture load and failure displacement exhibited an increasing trend with rotational speed, except at 900 rpm. The failure displacement remained proportional to the peak load for all rotational speeds.
- Analysis of lap-shear results revealed various failure modes, including nugget pull-outs, partial nugget fractures, and shear failures. Shear fracture mode was evident at 462 rpm, while nugget pull-out failures occurred at 233, 342, 900, and 1200 rpm. A partial nugget fracture was observed at 612 rpm.
- During the peel test, the dominant failure mode was nugget pull-out, with exceptions at 900 rpm and 1200 rpm, where partial nugget fracture and nugget fracture were observed, respectively.

Chapter 4 A preliminary investigation on friction stir spot welding of honeycomb core sandwich sheet with disc insert

4.1 Experimental process

The procedure for the welding process, specimen preparation, load, torque measurement during the welding process, mechanical testing of the welded joint, and failure pattern are discussed in this section.

4.1.1 Specimen preparation and FSSW

The components were joined together using three distinct materials: in which skin and core materials having same material and dimensions as used in the Section 3.1.1 of Chapter 3, a disc insert having 6 mm and 20 mm height and diameter, respectively, made of AA2024. The disc was fabricated from AA2024 rod of larger diameter purposefully to show that such hybrid joints are possible, though the materials grades are different. The stress-strain data and chemical composition of skin and core were already presented in Section 3.1.1 of Chapter 3. The compressive behaviour of the disc was obtained using ASTM E9-09, shown in Figure 4.1 [102]. EDX analysis was used to identify the chemical composition of the disc insert, which is shown in Table 4.1 and Figure 4.2.

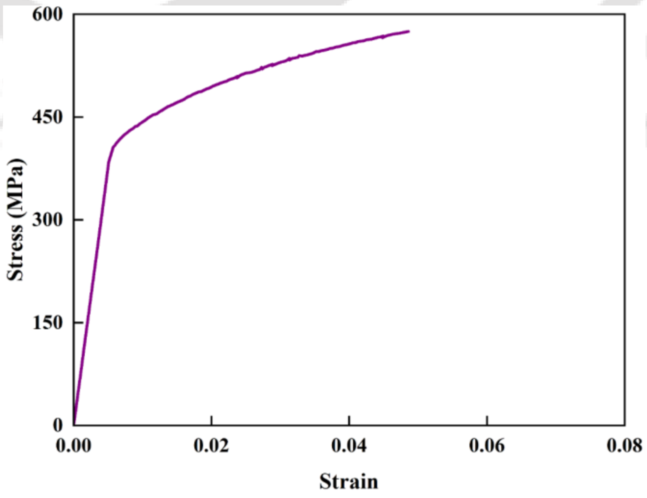

Figure 4.1 Compressive behaviour of disc insert

Table 4.1 Chemical composition of disc insert

Alloy	Zn	Cu	O	Si	Ni	Mn	Fe	Mg	Al
AA2024(disc insert)	-	4.2	2.3	0.5	-	0.6	0.4	1.2	Bal.

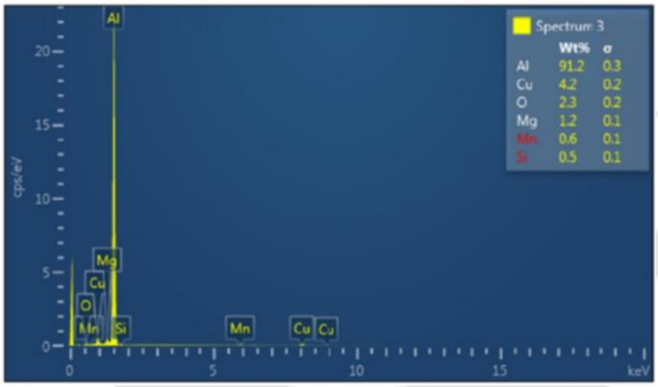

Figure 4.2 EDX analysis of AA2024

Three plunge depths were used to conduct the FSSW experiment: 1.9, 2.1, and 2.3 mm. The tool rotational speed, dwell time, and plunge speed remained constant throughout the tests at 900 rpm, 10 s, and 2 mm/min, respectively. The choice of these specific plunge depths was determined through a series of trials ranging from 1.7 to 2.5 mm, with increments of 0.1 mm. However, the joint could not be formed when attempting a plunge depth of 1.6 mm on the sandwich sheet due to insufficient plunging. Conversely, at a plunge depth of 2.5 mm, the top sheet in the joint area experienced excessive thinning. The tool rotational speed, plunge speed, and dwell time values were chosen in accordance with the existing literature on the FSSW of metallic materials.

The sandwich structure consists of two sheets separated by a honeycomb core with a disc insert. The honeycomb core was cut in the centre to create a space where the disc insert would be placed. Subsequently, the core, disc and the face sheet were positioned in an overlapping manner. Typically, the adhesive was used to join the sandwich sheets but to minimize interfering with the FSSW process, no adhesive was used in this instance. The FSSW was done at the location of the disc as per the conventional procedure meant for two overlapped sheets. However, it was conducted on both sides of the joint, namely the front side welding and the back side welding, as shown in Figure 4.3. The front-side welding was performed first, followed by the back-side welding.

Two different types of sandwich specimens with disc insert were prepared: lap shear and peel test specimens. The dimensions and testing procedure for lap shear and peel tests were already explained in Section 3.1.2 of Chapter 3.

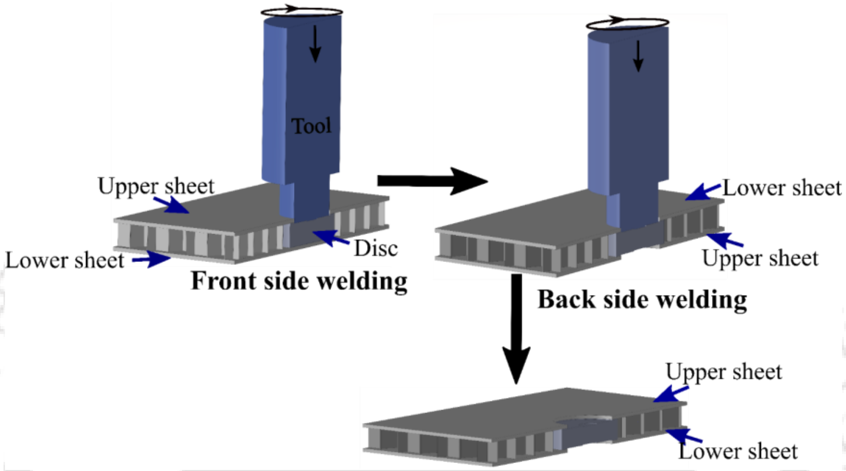

Figure 4.3 Cross-sectional view of the FSSW process of honeycomb core sandwich

4.2 Results and discussion

This section investigates load/torque variation during FSSW, joint performance at different plunge depths, and fracture behavior from lap shear and peel tests.

4.2.1 Load and torque response

In Figure 4.4, noticeable changes in the axial load and torque that occur during the FSSW process of a sandwich sheet, both at its front and back sides, are observed. Regardless of the plunge depth, the axial load applied during the FSSW process was consistently higher at the sandwich sheet's front side than at the backside. The difference was due to the heat absorption by the disc and skins during the welding of the front side. A similar pattern is also observed for the torque applied at the time of the FSSW of the sandwich sheets. The response of the load and torque to welding time is approximately the same at different plunge depths by keeping all other parameters constant and only varying the plunge depth. During the dwell period of the FSSW process, where the tool remains stationary and only the stirring action occurs, there is a continuous decrease in both the axial load and torque. The decline in load is attributed to a reduction in flow stress at elevated temperatures.

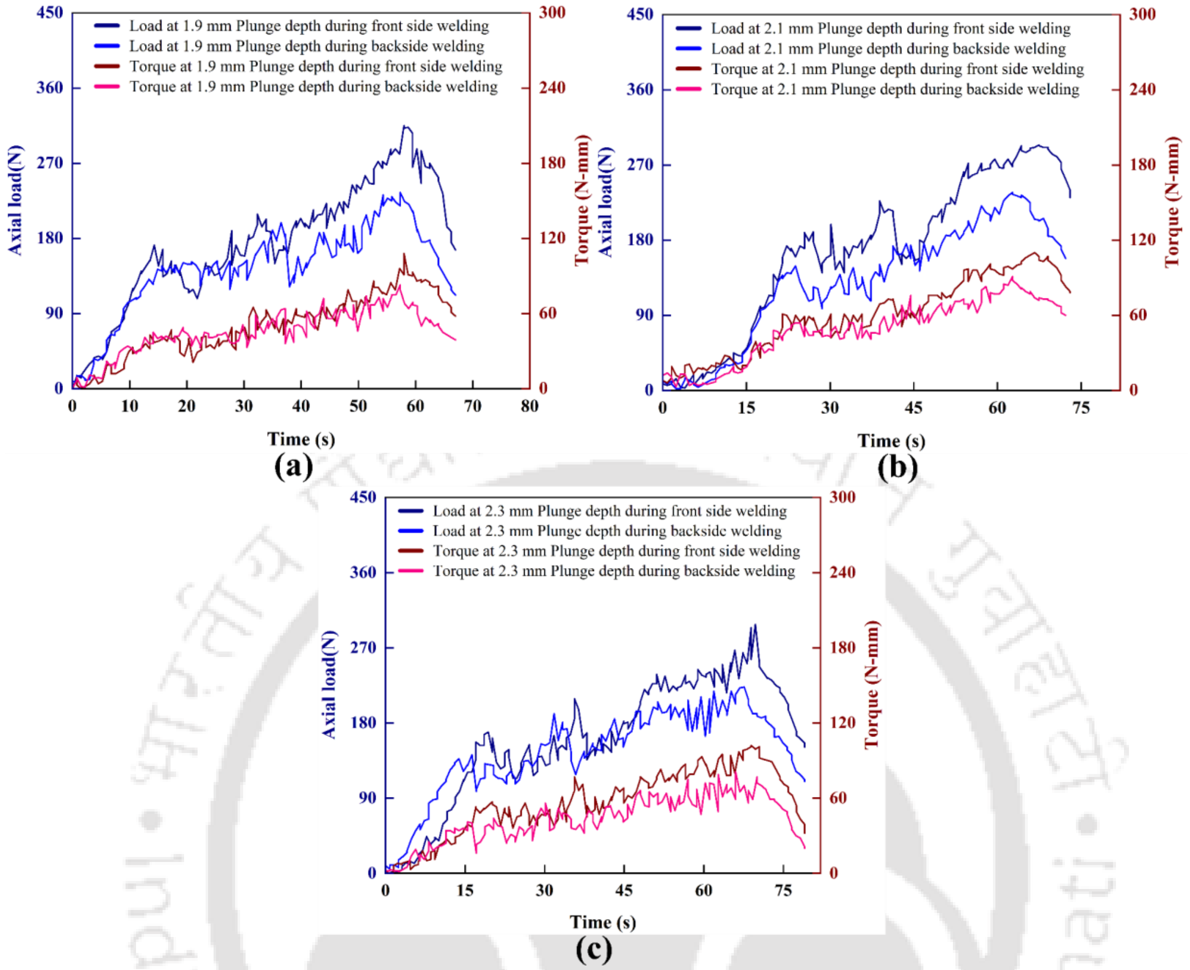

Figure 4.4 Load and torque variation with welding time at plunge depths of (a) 1.9 mm, (b) 2.1 mm, (c) 2.3 mm

4.2.2 Mechanical performance and failure pattern

Figure 4.5 illustrates the influence of the tool plunge depth on the strength and displacement of the honeycomb sandwich sheet joint under different loading conditions. Increasing the tool plunge depth causes betterment in both ductility and joint strength of the sandwich sheets. The lap shear test, as illustrated in Figure 4.5(a), revealed a consistent trend where the joint strength of the sandwich sheet showed a progressive increase with the increase in plunge depths. Moreover, the uniform displacement also exhibits an increase, particularly up to a plunge depth of 2.3 mm. Similarly, peel tests (shown in Figure 4.5(b)) consistently demonstrate enhanced joint strength and ductility when tool plunge depth increases. It is essential to note that the displacement measured in the peel test represents sheet bending as well as displacement within the joint.

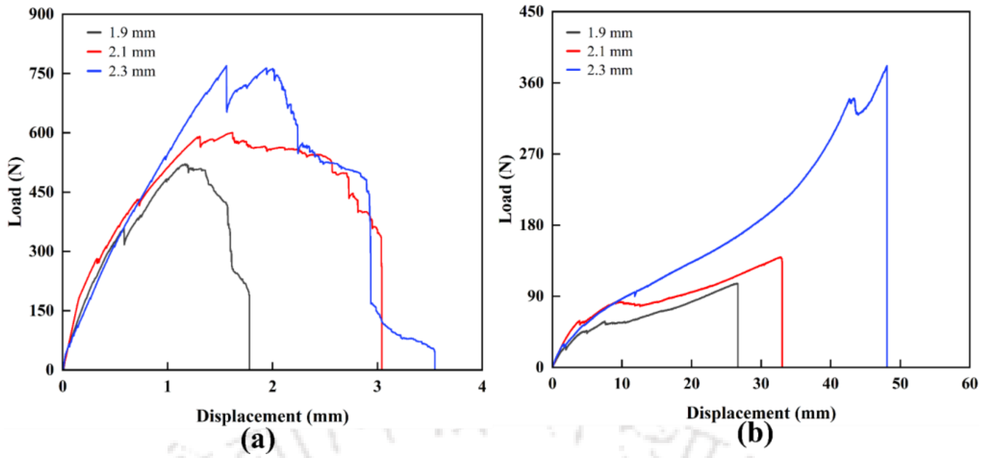

(a) (b)

Figure 4.5 Variation of load with displacement during (a) lap-shear test and (b) peel test at different tool plunge depth

Figure 4.6 and Figure 4.7 show the fracture surfaces of the tested sandwich sheets. All the joints fractured between the upper sheet and the disc (front side welding); no joints were observed to fail between the lower sheet and the disc (back side welding). The back side welding exhibited a strong joint as the disc and lower sheet were preheated during the front side welding. It is found that the predominant fracture mode observed in both lap shear and peel tests is "nugget pullout," regardless of the plunge depth used. However, in the case of the peel test of the sandwich sheet welded at a 2.3 mm plunge depth, a nugget fracture occurred, which shows a strong joint formed between the disc and the upper sheet.

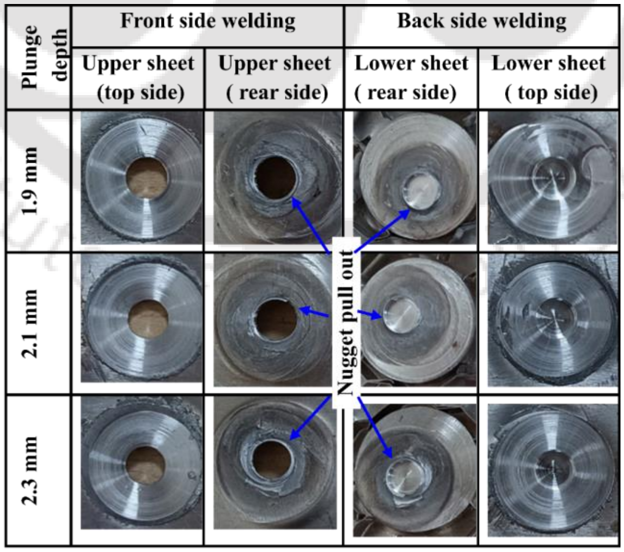

Figure 4.6 Failure modes of the sandwich in the lap-shear test

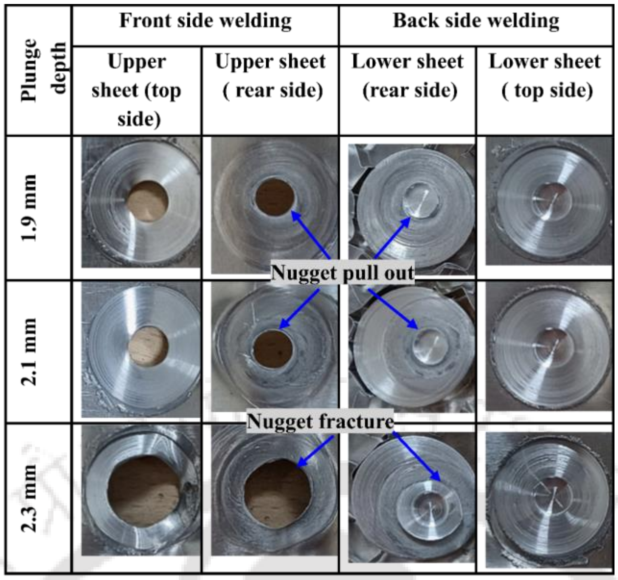

Figure 4.7 Failure modes of the sandwich in the peel test

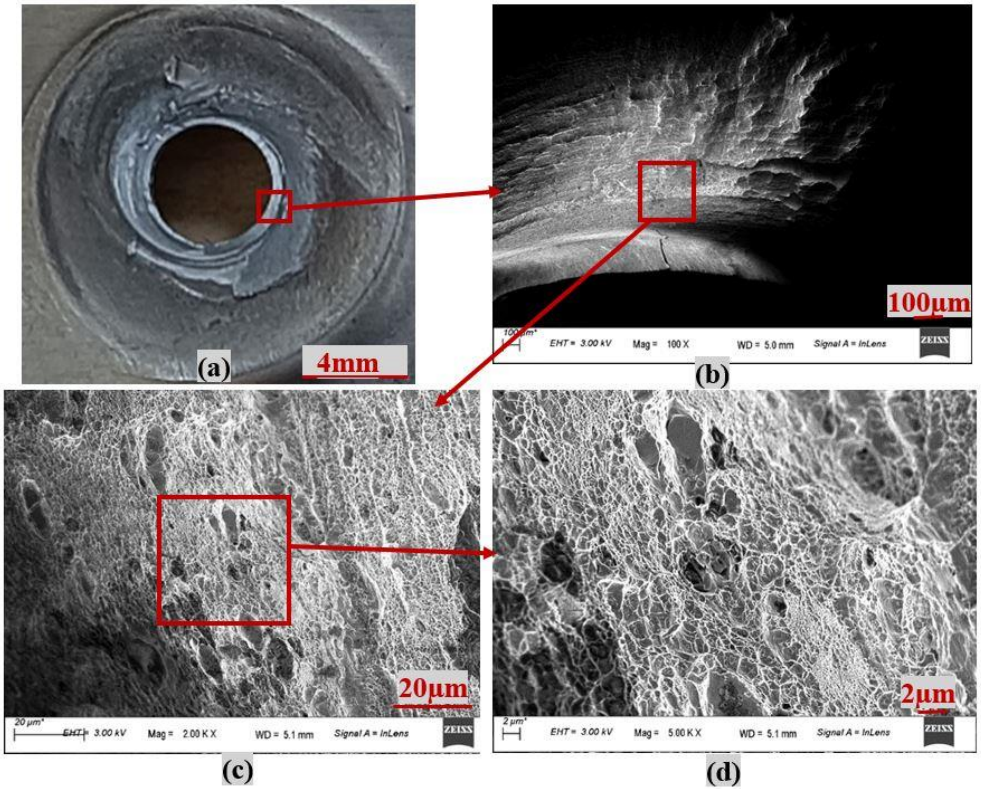

Figure 4.8 SEM image of the fracture surface of the lap-shear specimen at 2.3 mm plunge depth (a) image of the upper sheet backside, (b) magnified view of the marked region in Fig. (a), (c) magnified view of the marked region in Fig. (b), (d) magnified view of the marked region in Fig. (c)

SEM analysis was performed to examine the fracture surfaces on the rear side of the fractured upper sheet of lap shear specimen. The analysis was conducted at a 2.3 mm plunge depth. The results are shown in Figure 4.8. It is apparent from the results that the joint experienced a fracture that originated through the right side of the joint. To highlight the usual features of the fracture surface, a specific area indicated with a red rectangle is further magnified in Figure 4.8(c). Noteworthy ridges are observed towards the outer periphery of the nugget, suggesting that the fracture may have initiated and propagated in that direction. Furthermore, we can see elongated dimples that are more amplified in Fig. Figure 4.8(d). It indicates that the top sheet and disc have a stronger bonding performance.

4.3 Summary

The honeycomb core sandwich structure with disc insert was successfully fabricated by the FSSW at three different plunge depths: 1.9 mm, 2.1 mm, and 2.3 mm. By comparing the load and torque demands throughout the FSSW process, as well as examining lap shear test, peel test results, and fracture patterns, we can draw the following conclusions from the analysis:

- The plunge load and torque were similar for both the front side and back side welding at all plunge depths, but the front side FSSW required a slightly higher load and torque than the backside.
- The lap shear and peel tests revealed a uniform enhancement in the joint strength and displacement of the sandwich sheet as the plunge depth increased. Moreover, the fracture load and failure displacement also exhibited an upward trend with plunge depth. Notably, the failure displacement demonstrated a proportional relationship with the peak load across all plunge depths.
- Nugget pullouts were observed as the dominant failure mode in lap-shear and peel tests, except for the peel test at 2.3 mm plunge depth, where nugget fracture occurred.
- Fracture morphology at the rear side of the upper sheet in the lap-shear specimen at a 2.3 mm plunge depth revealed prominent ridges towards the outer circumference of the nugget, along with elongated dimples, indicating a better joining performance between the upper sheet and the disc.
- The fabrication of honeycomb core sandwich sheets can be done with hybrid bonding. i.e., FSSW with AB, which can increase more strength of the joint.

Chapter 5 Manufacture of honeycomb core sandwich structures by hybrid approaches: experiments and numerical simulations

5.1 Experimental process

This section describes the methods for conducting FSSW trials, preparing sandwich samples using different strategies, and performing mechanical testing.

5.1.1 Material

The mechanical properties of skin sheets and honeycomb core are already discussed in Section 3.1.1 of Chapter 3, and the mechanical properties of the disc insert in Section 4.1.1 of Chapter 4. The material properties of the constituents of the sandwich sheet are shown in Table 5.1.

Table 5.1 Material properties of the face sheet (skin), disc, and honeycomb core

Layers	Density (kg/m^3)	Poisson's ratio	Young's modulus (GPa)	Yield strength (MPa)
AA5052-H32 (skin)	2680	0.30	70	189±2
AA3003 (core) [23]	2730	0.30	69	185±1
AA2024 (disc)	2780	0.33	74	405±3

5.1.2 Joining strategies

The five different joining strategies for fabricating sandwich structures with honeycomb core are described here.

5.1.2.1 AB

Figure 5.1(a) shows the AB of individual components of the honeycomb core sandwich. An epoxy adhesive (hardener FINEHARD-3486 and resin Epofine-1564) was utilized with 100:34 hardener-to-resin weight ratio to create a strong bond between the honeycomb core and skin. A bond thickness of 0.12±0.015 mm was maintained during the AB. Acetone was used to clean the skin and core before applying adhesive onto the skin surfaces.

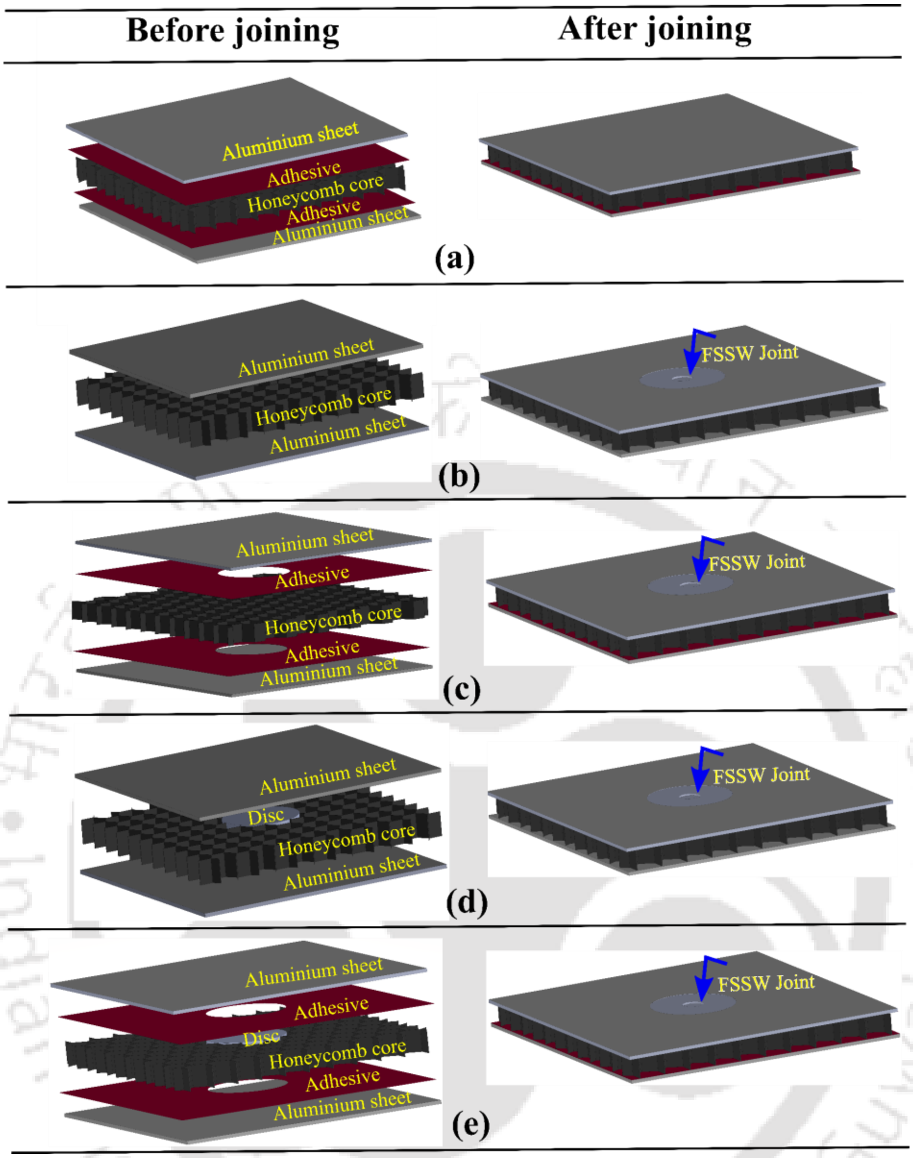

Figure 5.1 Fabrication of honeycomb core sandwich structures by different strategies (a) AB (b) FSSW (c) FSSW_AB (d) FSSW_D (e) FSSW_D_AB

The honeycomb core was then carefully positioned onto the adhesive-coated region, ensuring precise alignment. Pressure was evenly applied to establish a solid contact between the adhesive and the substrates with proper clamping during curing. The joining process involved joining separately both sheets to the core: the lower sheet was joined to the core and then cured for 24 h at room temperature. The same procedure was adopted to join the upper sheet and the core. This procedure was primarily adopted to prevent the flowability of adhesive through the sheet and core.

5.1.2.2 FSSW

The fabrication of honeycomb core sandwich by the FSSW method is already discussed in Section 3.1.1 of Chapter 3. Figure 5.1(b) shows the layup of the skin and core along with the FSSW joint.

Other constant parameters were tool rotational speed: 900 rpm, tool plunge speed: 2 mm/min, tool plunge depth without rotation: 6.2 mm, tool plunge depth with rotation: 1.5 mm, and dwell time: 5 s.

5.1.2.3 FSSW with Adhesive bonding (FSSW_AB)

The samples underwent a simple preparation process involving treatment with sandpaper and cleaning with acetone. The core and skin with adhesive were joined serially, i.e., first the welded area was marked, and then adhesive was applied to the remaining area. Afterwards, the core was properly placed on the skin, and slight pressure was applied by placing weight on the core. Then, the skin was allowed to cure. After curing, the same procedure was considered for the second skin. After curing, the FSSW was performed directly at the designated location, where no adhesive had been applied (Figure 5.1(c)). The stages and parameters remain the same as those of the FSSW process.

5.1.2.4 FSSW with disc insert (FSSW_D)

The initial steps of the process, including the face sheet, core cutting, and cleaning, remained unchanged from the previous procedures. The fabrication process using this method is explained in Section 4.1.1 of Chapter 4.

The tool rotational speed, tool plunge speed, and dwell time were 900 rpm, 2 mm/min, and 5 s, respectively, whereas 2 mm plunge depth was used on both sides of the joint.

5.1.2.5 FSSW with disc insert and adhesive bonding (FSSW_D_AB)

This method was identical to the previous one FSSW_D process, with one key difference: an adhesive was introduced between the skin and honeycomb after FSSW on the front side (Figure 5.1(e)). During the front side welding, the FSSW specifically targeted the joining between the face sheet and the disc, with the core serving as a supportive medium; no joining involving the core occurred until this stage. Following the completion of the front side welding, the core was extracted. Subsequently, adhesive was applied to the inner section of the face sheet of the front side welded specimen and the second face sheet, excluding the disc insert area. The core was then delicately positioned between them, and the entire assembly was cured at room temperature for 24 h. Finally, the back side FSSW was carried out at the disc location.

5.1.3 Testing of sandwich sheets and joint characterization

Three distinct kinds of sandwich sheet specimens, with three sets of each type, were made for testing during the FSSW. The lap shear and peel tests used two kinds, whereas the macrostructural examination used a third. The dimensions of the lap shear and peel test specimens were chosen following the AWS D8.9-97 standards, already shown in Figure 3.5 of Chapter 3.

In order to analyze the macro cross-sectional characteristics of the sandwich samples, the specimens were bisected along the diametric axis of the joint. Subsequently, the cross-sectional segments were placed within a mold to facilitate polishing involving various grades of emery sheets, up to 2000-grade sheets, followed by velvet cloth polishing utilizing Silvo liquid metal polish. The desired surface quality was obtained at the end. A subsequent macro cross-sectional analysis was conducted using a stereo microscope with optical microscopy capabilities.

5.1.4 Comparison of bending of sandwich panels: Experiments and numerical simulations

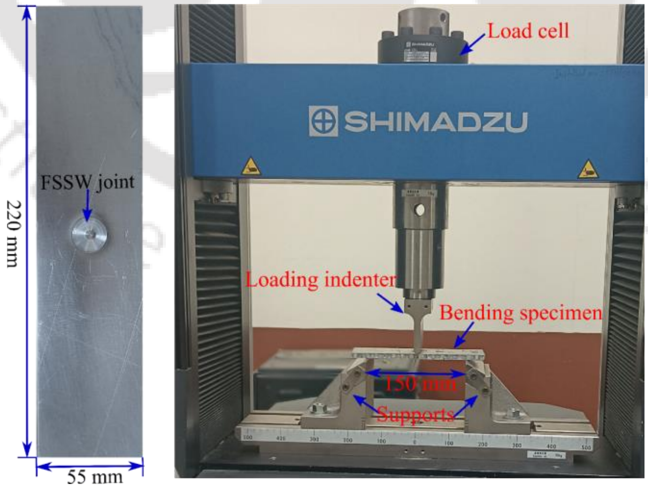

Figure 5.2 Sample dimensions and experimental setup in 3PBT specimens

The 3PBT were conducted on samples prepared following the ASTM C393 standard [104] using Shimadzu UTM with a consistent 1 mm/min loading rate at room temperature

(Figure 5.2). The support length was fixed at 150 mm, and the diameters of the support and loading indenters were 4 mm and 10 mm, respectively. The load evolution curves of sandwich structures fabricated by AB, FSSW_AB, and FSSW_D_AB were compared to study the prominence of the hybrid method.

Numerical simulations were conducted to gain a deeper understanding of the changes and factors contributing to the changes in the bending behaviour of the sandwich structures. The ABAQUS/Explicit was used for the numerical simulation of the 3PBT. Table 5.1 shows the material properties incorporated during simulations.

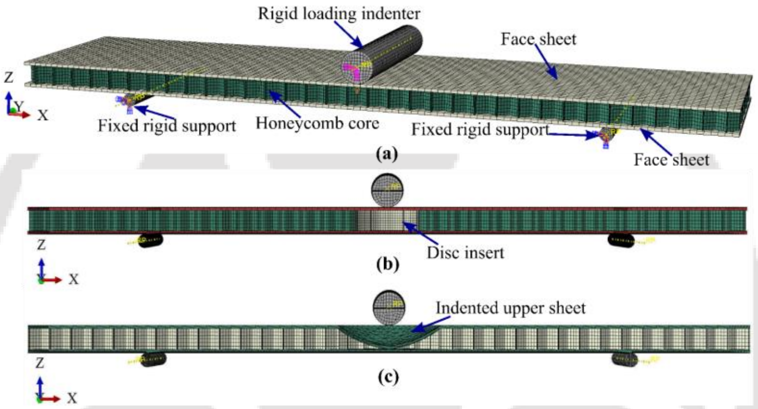

Figure 5.3 Description of FE models (a) initial model for 3PBT, and cross-sectional view of 3PBT of (b) FSSW_D_AB (c) FSSW_AB sandwich panels

The arrangement shown in Figure 5.3 illustrates the initial FE model of 3PBT and cross-sectional views of the FSSW_D_AB and the FSSW_AB sandwich panels. In the FSSW_AB process, the welding was done after plunging the tool until the top face sheet touched the lower sheet. During this stage, the core was crushed beneath the indented sheet. Therefore, the FSSW_AB sandwich panel was modelled equivalently by making an indentation on the upper sheet and removing the core beneath the indentation area, which is shown in Figure 5.3(c). The upper sheet and core were made using Solidworks software and later exported to Abaqus for FE simulations. The 3PBT setup involves the support of a sandwich panel by two fixed and rigid supports, with the upper indenter exerting downward displacement on the structure along the *z*-axis. To represent the thin nature of the aluminum honeycomb appropriately, S4R shell elements were employed. The aluminum face and disc were simulated using C3D8R solid elements, while the upper sheet of the FSSW_AB sandwich panel, due to its indented surface, was modelled using C3D10M solid elements. The rigid component was modelled using R3D4 rigid elements. A tie constraint was implemented to simulate the adhesive and welding joint between the honeycomb, face sheets, and the disc. The FE simulation was conducted under quasi-static loading conditions with a speed of 100 mm/s, and a Coulomb's coefficient of friction of 0.2 was set to govern interactions between various surface pairs. As shown in Figure 5.4, the quasi-static nature of the FE simulation was confirmed by the total internal energy surpassing the overall kinetic energy significantly throughout the bending process [105]. Additionally, mesh size sensitivity analyses were performed for all FE models. For instance, Table 5.2 shows the mesh sensitivity analysis of 3PBT of the AB sandwich panel. A similar study was done for 3PBT of the FSSW_AB and FSSW_D_AB sandwich panels. The data presented in Row 3 and Row 4 of Table 5.2 indicates that as the number of mesh elements increased, the peak load and stiffness values remained relatively stable. Hence, a total of 77,935 elements were used in the numerical simulation as this quantity of elements was found sufficient to maintain accuracy while significantly reducing the time required for the simulation process.

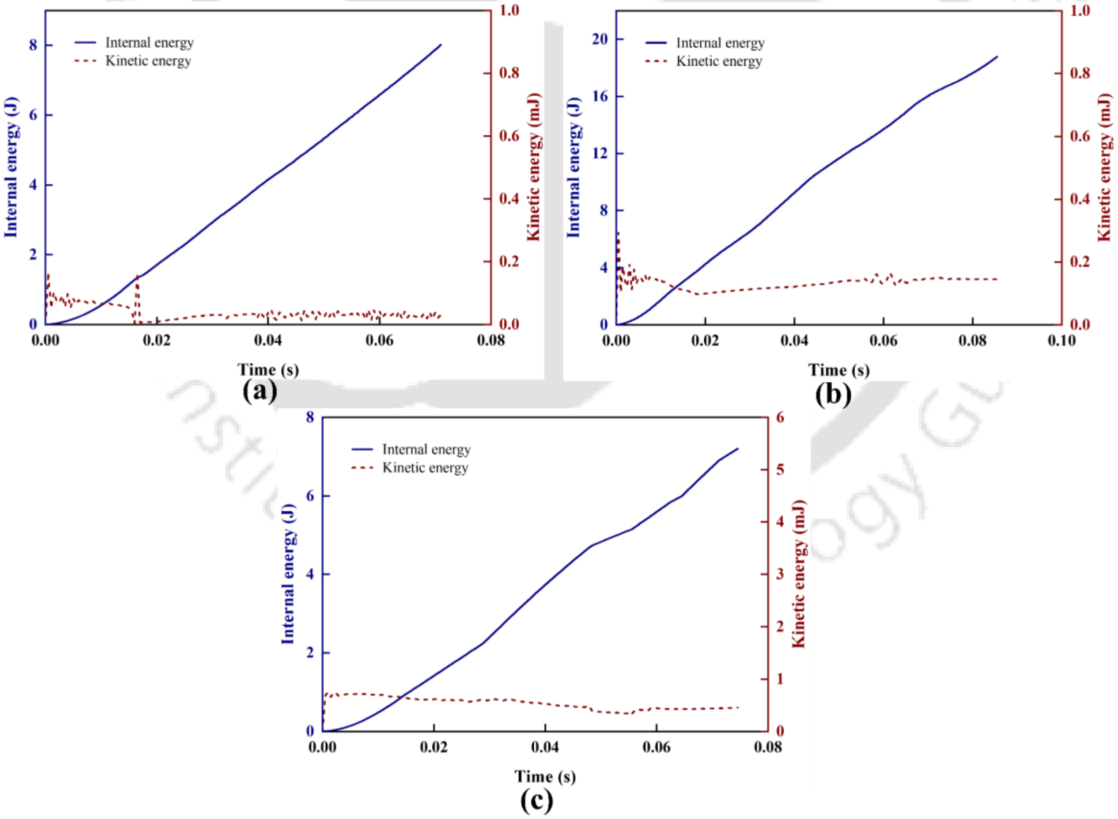

(a)

(b)

(c)

Figure 5.4 Variations in internal energy and kinetic energy during 3PBT of (a) AB sandwich, (b) FSSW_D_AB sandwich, (c) FSSW_AB sandwich panels

Table 5.2 Mesh sensitivity analysis of 3PBT of AB sandwich panel

Row no.	Total elements	Peak load (kN)	Stiffness (kN/mm)
1	36730	1.71	1.21
2	56958	1.68	1.19
3	77935	1.6	1.25
4	123918	1.62	1.25

5.1.5 Scaled-up forming panel fabrication and forming

Two sandwich panels were manufactured through the AB and the FSSW_D_AB (the best among FSSW strategies) to compare the forming characteristics. The fabrication of the scaled-up sandwich panel is shown in Figure 5.5(a). The dimensions of the panels and spot weld locations are depicted in Figure 5.5(b).

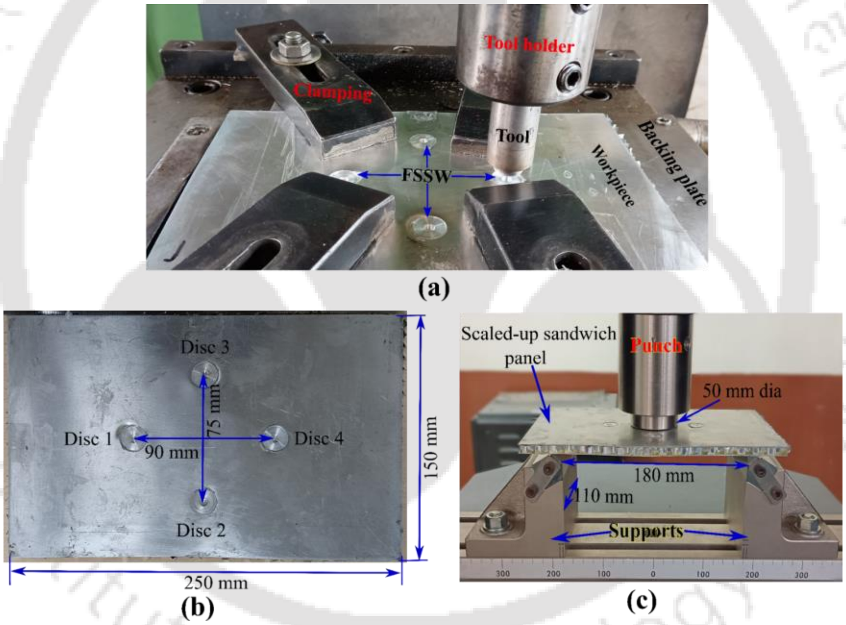

Figure 5.5 Scaled-up sandwich sheet forming (a) fabrication setup on FSSW (b) sandwich panel fabricated by FSSW_D_AB (c) forming setup

In the FSSW_D_AB, four-disc inserts were incorporated. The spacing between these discs was determined based on the dimensions of the panels and the span length of the setup. The arrangement ensured that there would be no contact between the loading punch and the inserted discs during forming. Forming was carried out on Shimadzu UTM with supports having a diameter and length of 4 mm and 110 mm, respectively, at ambient temperature with a constant loading rate of 2 mm/min (Figure 5.5(c)). The load-displacement curves of the two panels were compared.

5.2 Results and discussion

This section examines macro-cross-sections, load/torque variation during welding, joint performance, and fracture behaviour from lap shear and peel tests. It also includes 3PBT and scaled-up sandwich panel forming analysis, along with numerical analysis of 3PBT for AB, FSSW_AB and FSSW_D_AB specimens.

5.2.1 Macro cross-sections

Figure 5.6(a-j) illustrates the schematic and actual cross-sectional views of sandwich sheets fabricated by five strategies. Figure 5.6(a, b) shows intact bonding between skin and core during AB. In FSSW and FSSW-AB, the core was crushed during the plunging stage without tool rotation before the skins established contact (Figure 5.6d, f). As the tool advances in the FSSW, it exerts downward pressure on the materials undergoing stirring. This action causes a thorough mixing of the material below and surrounding the tool. In this phase, a metallurgical bond is formed between the sheets in FSSW and FSSW_AB (Figure 5.6d, f).

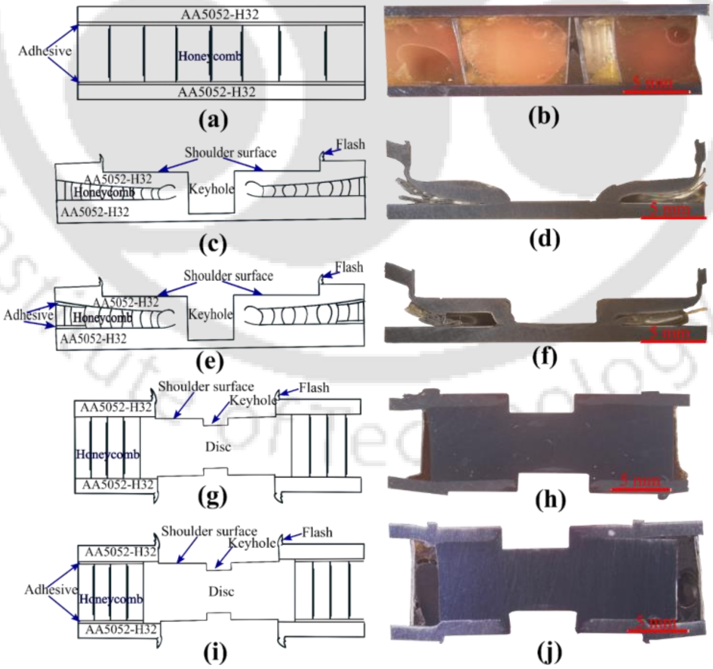

Figure 5.6 Schematic and fabricated views of the joint cross-section of the AB in (a) and (b), FSSW in (c) and (d), FSSW_AB in (e) and (f), FSSW_D in (g) and (h), and FSSW_D_AB in (i) and (j)

Similarly, a metallurgical bond is developed between the sheet and the disc in the case of the FSSW_D and FSSW_D_AB (Figure 5.6h, j). The macrographs of the FSSW and the FSSW_AB show that the gap between the sheets, excluding the pin (shoulder) area, is higher in the FSSW_AB. The variance arises from the fact that during the plunging stage without tool rotation, the adhesive-bonded honeycomb core and the sheet around the welding zone, which is to be joined, hinder the downward movement of the sheet. It is important to note that no adhesive is employed within the welding area. In contrast, in cases where discs are inserted, there is no observable gap around the shoulder region following the joining process.

5.2.2 Load and torque responses

The maximum axial load and spindle torque for each case are illustrated in Figure 5.7. In all the cases, both the axial load and torque increased in the manner FSSW < FSSW_AB < FSSW_D < FSSW_D_AB. The hybrid joints, i.e., FSSW_AB and FSSW_D_AB, demonstrated the highest axial load and torque compared to the FSSW joint without the AB, while the cases with disc-insert, the FSSW_D, and the FSSW_D_AB, exhibited a higher axial load and torque trend compared to the conventional FSSW cases, FSSW and FSSW_AB. The error (scatter) bars shown in Figure 5.7 indicate that there is minimal variation in axial load and torque. Therefore, all the FSSW variants are stable and repeatable on lab scale. Moreover, the statistical variations indicate that AB has changed the axial load significantly as compared to the torque.

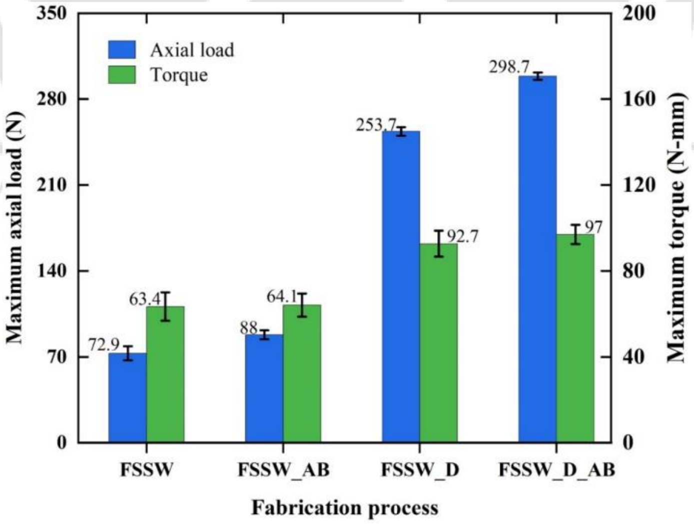

Figure 5.7 Maximum axial load and torque during fabrication of sandwich by FSSW strategies

The axial load and torque evolution show a similar trend in all these cases (Figure 5.8a, b). FSSW_D and FSSW_D_AB were completed in 65 s, including 5 s dwell time, while FSSW and FSSW_AB were completed in 50 s with 5 s dwelling. During FSSW and FSSW_AB, there were more fluctuations observed in the axial load and torque. The honeycomb core fracturing into tiny particles and being stuck below the tool shoulder caused these fluctuations (Figure 5.8a, b). As a result, there was insufficient heat generation to soften and plasticize the core, leading to axial load and torque variations. The peak axial load and torque were observed at the end of the plunging stage, followed by a gradual decrease during the dwell stage and a sudden drop at the end. The drop in the dwell stage was evident across all observed cases, primarily due to the constrained tool linear movement during this phase, wherein only the stirring process took place. Consequently, this stirring process facilitated a rapid softening of the materials involved. So, this highlights the importance of controlled tool movement in affecting the kinetics of material softening during the dwell stage, offering useful insights into optimizing manufacturing processes for increased efficiency and product quality.

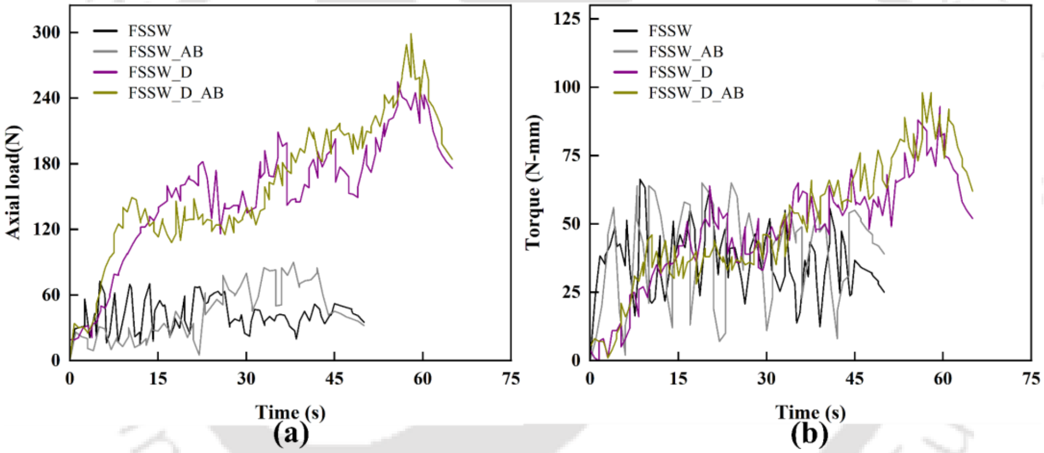

Figure 5.8 Axial load and torque variation during fabrication of sandwich sheets by FSSW methods

5.2.3 Mechanical performance and fracture pattern

Figure 5.9(a, b) and Table 5.3 show the load evolution and changes in fracture load and displacement at fracture during peel tests. Both the figures suggest improvement in load-bearing ability and displacement at fracture of sandwich structures made by FSSW strategies as compared to those made by AB only. Specifically, the fracture load for FSSW, FSSW_AB, FSSW_D, and FSSW_D_AB joints improved by 232%, 463%, 374%, and 705%, respectively, compared to the AB joints. Moreover, the AB enhanced the performance compared to those without it. There is about 70% improvement in fracture load while comparing FSSW_AB to FSSW and FSSW_D_AB to FSSW_D, indicating hybrid joint as a better candidate for fabricating sandwich structure with honeycomb core. The displacement at fracture was directly proportional to the fracture load. FSSW_D_AB specimen achieved the highest displacement of 59.5 mm among the different fabrication processes. Pathak *et al.* [106] suggested that higher displacements allow the joints to absorb more energy before failure, which is considered a safer outcome. This implies that the energy required to delaminate the joint completely was highest for FSSW_D_AB. Overall, these results demonstrate the ability of FSSW strategies to improve the mechanical properties and energy absorption capabilities of sandwich structures, particularly when combined with AB, thereby increasing their suitability for a variety of engineering applications.

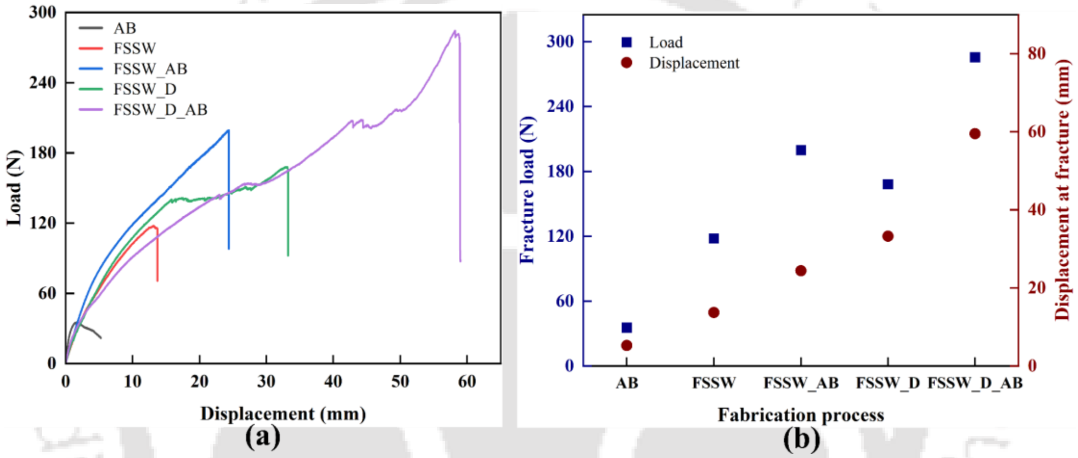

Figure 5.9 Peel test results (a) load evolution (b) fracture load and displacement at fracture

Table 5.3 Fracture load and displacement during the peel and lap shear test

		AB	FSSW	FSSW_AB	FSSW_D	FSSW_D_AB
Peel test	Fracture load (N)	35.5	117.9	199.7	168.2	285.6
	Displacement at fracture (mm)	5.24	13.7	24.37	33.23	59.5
Lap shear test	Fracture load (N)	124	1173	1383.2	827.7	1181.9
	Displacement at fracture (mm)	1.23	0.6	0.64	4.32	5.4

In the case of hybrid joints, the load evolution curves exhibited a stiffening effect before reaching the fracture load. Initially, there was significant bending of the sandwich structure between the loading points and the joint. However, at a certain point, the weld nugget aligned almost perfectly with the applied load, resulting in a higher overall stiffness of the joint.

Consequently, the hybrid joints showed improved deformation resistance and structural integrity, contributing to their better load performance than non-hybrid joints.

Figure 5.10(a, b) and Table 5.3 show results from lap shear tests. The FSSW_AB joint exhibited the highest fracture load among the various fabrication processes, even better than the FSSW_D_AB, which exhibited a larger peel load. In Figure 5.10(a), the stiffness of the disc inserted FSSW_D and FSSW_D_AB lap shear specimen is less than that of the FSSW and FSSW_AB specimens. A bending moment is generated in the disc-inserted specimens on both upper and lower sheets. This is attributed to the distance between nuggets, i.e., the distance between the front and backside welds, which was significantly higher compared to the FSSW/FSSW_AB specimens. Such a load transfer mechanism is not present in the peel test and therefore, the stiffness of the proposed hybrid joints remains almost the same.

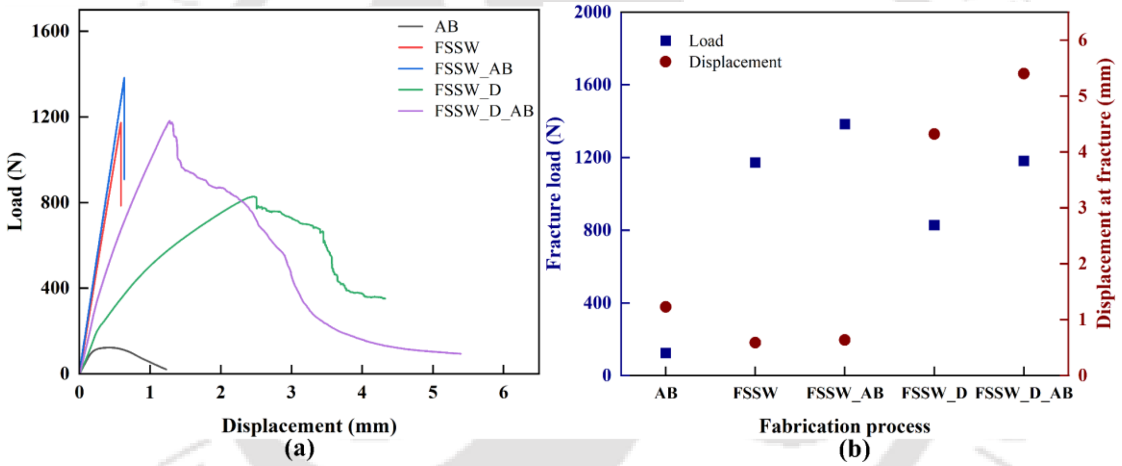

Figure 5.10 Lap shear test results (a) load evolution (b) fracture load and displacement at fracture

In the lap shear experiments, the disc-inserted samples bend more under the action of tensile load (Figure 5.11); consequently, there is nugget rotation owing to the bending of upper and lower sheets in opposite directions [107]. The FSSW_D_AB joint experienced the largest displacement at fracture, indicating its higher ductility under load, while the FSSW joint had the lowest, followed by the FSSW_AB joint. Fracture loads of FSSW strategies show significant improvement as compared to AB strategy: FSSW – improved by 846%, FSSW_AB – improved by 1015.5%, FSSW_D – improved by 568%, and FSSW_D_AB – improved by 853%. This significant increase in fracture loads demonstrates the benefits of FSSW procedures for achieving strong joints compared to conventional AB methods. Additionally, when comparing the hybrid strategies (FSSW_AB, FSSW_D_AB) to the corresponding conventional ones (FSSW, FSSW_D), an improvement of 18% and 43% in shear fracture load is seen, indicating their potential for widespread applications where superior joint strength and performance are critical factors.

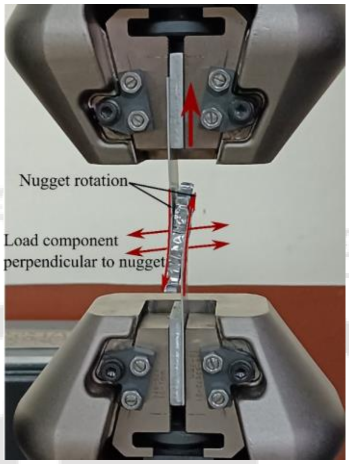

Figure 5.11 Nugget rotation in lap shear specimen of FSSW_D or FSSW_D_AB

Figure 5.12 shows the improvement in the quality of sandwich sheets fabricated through various FSSW strategies compared to the AB. The calculations were based on samples prepared for the peel and the lap shear tests. There was about 9-11% weight reduction in sandwich samples fabricated by the FSSW. While peak load (fracture strength) enhancement was already showed, there was also an improvement in the peak load-to-weight ratio. For instance, it was 639% for the FSSW_D_AB and 1016% for the FSSW_AB during peeling and shearing, respectively. Fracture energy, which is the area under the load curve, was highest for the FSSW_D_AB. Improvement was about 6105% in the case of the peel sample and 2516% in the case of the shear sample.

As mentioned in a previous section, the fabrication processes of sandwich sheets through FSSW and FSSW_AB involved plunging a tool until the upper sheet touches the lower sheet, which leads to core damage and high stresses on the face sheet. Consequently, early crack generation, propagation, and fracture at a very low displacement were believed to occur. In contrast, the FSSW_D and FSSW_D_AB processes replaced the joint area with a metal disc, effectively resolving the issue of core damage, offering a solution to the challenges associated with FSSW and FSSW_AB. The disc insert offers additional support and distributes stresses more uniformly, consequently minimizing the possibility of early formation of cracks and subsequent failure.

These observations and the superior performance of sandwich structures fabricated by the FSSW_D_AB in terms of peak load, peak load-to-weight ratio, and fracture energy suggest the effectiveness of the FSSW_D_AB approach as a prominent and feasible manufacturing method for honeycomb sandwich structures. In addition to improving structural reliability, FSSW_D_AB has the potential for larger applications where improved performance and reliability are critical factors by tackling the basic issues related to core damage and stress concentration.

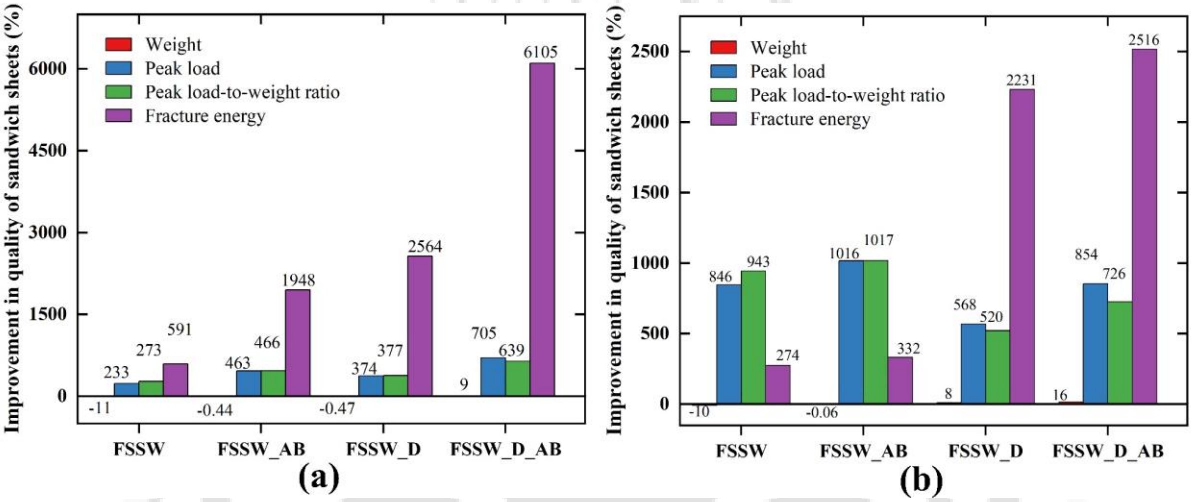

Figure 5.12 Improvement in the quality of sandwich sheets fabricated by different strategies compared to AB during (a) peeling, (b) shearing

The fracture surfaces of the tested sandwich sheets were analyzed as presented in Figure 5.13. FSSW cases fractured between the upper and lower sheets displaying nugget pull-out fracture mode. On the other hand, all the structures fabricated by disc inserts revealed fractures between the upper sheet and the disc, indicating strong joints at the front side welding. Interestingly, the interface between the lower sheet and the disc did not suffer fracture, which is likely due to preheating during front-side welding, yielding a stronger joint. The primary fracture mode observed in both lap shear and peel tests was "nugget pull out". The FSSW_D_AB joints showed a "nugget" fracture during peeling and shearing. Figure 5.14 presents a schematic illustrating the difference between "nugget pull-out" and "nugget" fracture modes. While "nugget pull-out" involves the extraction or separation of the nugget from the surrounding material, "nugget" fracture mode implies a different failure mechanism where the nugget itself fractures, potentially indicating variations in material properties or welding conditions.

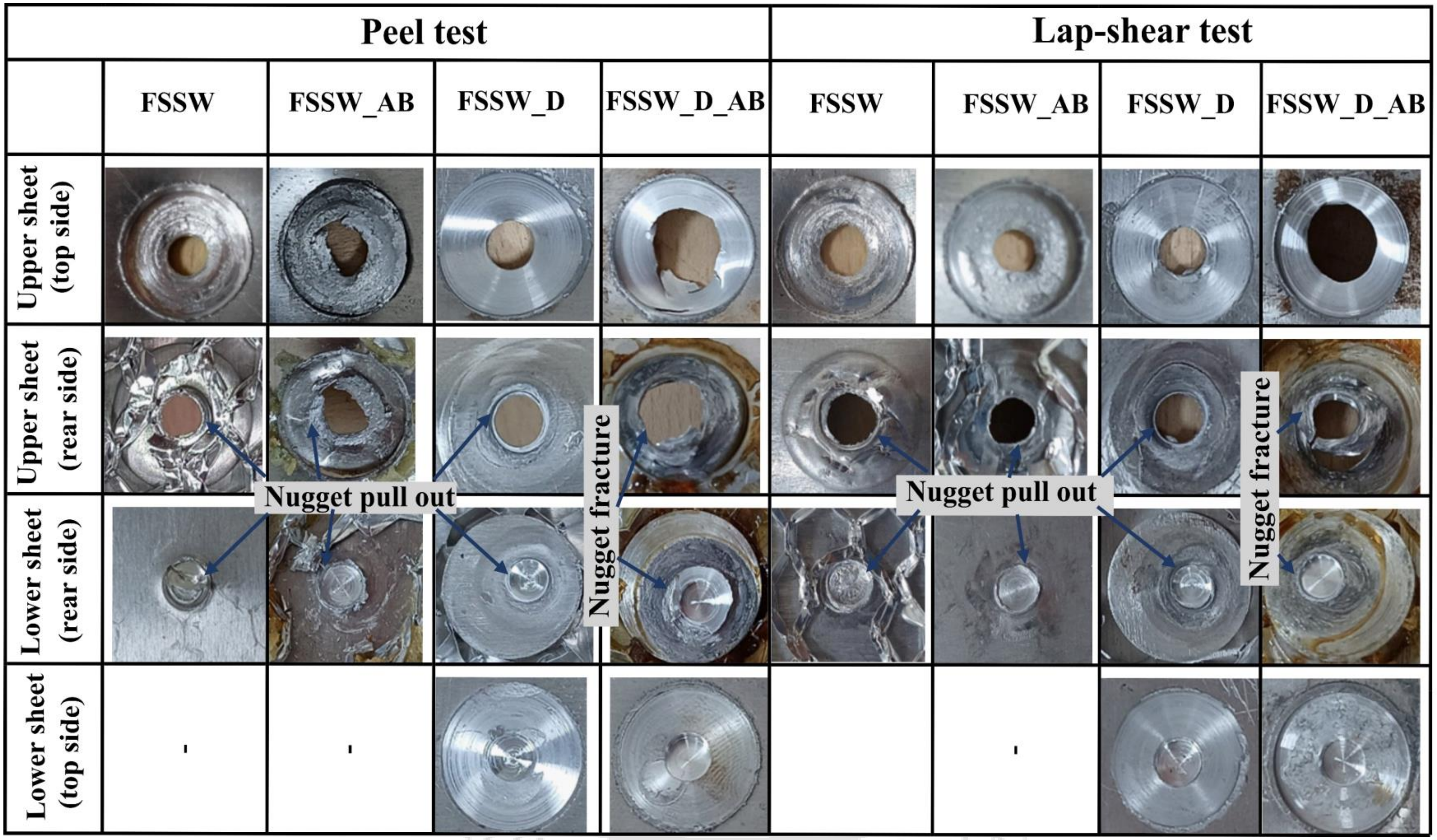

Figure 5.13 Failure modes of the sandwich sheets in the peel test and lap shear test

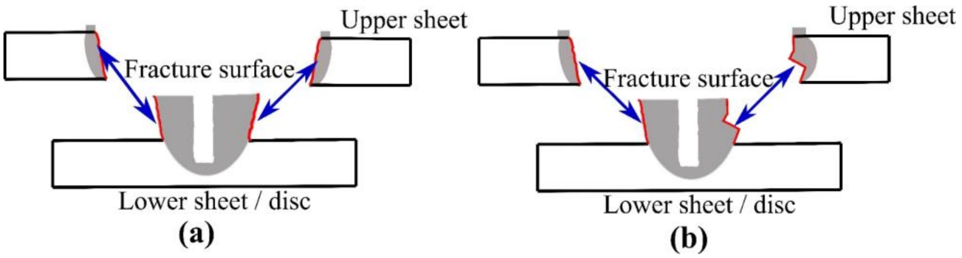

Figure 5.14 Schematic of (a) nugget pull out (b) nugget fracture

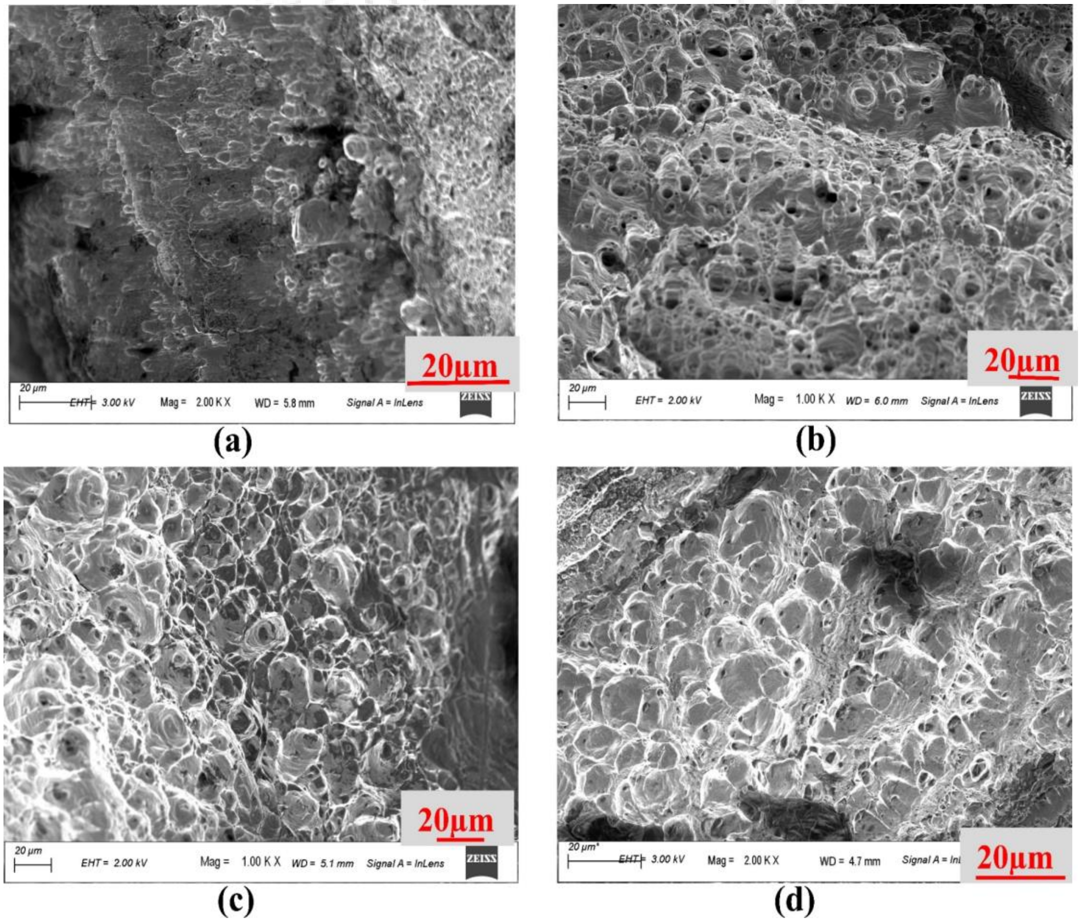

Figure 5.15 SEM images of the fracture surface of the peel test specimen (a) FSSW (b) FSSW_AB (c) FSSW_D (d) FSSW_D_AB

Fracture surfaces after peel tests (Figure 5.15) reveal the existence of dense and large dimples in sandwich sheets produced through FSSW, FSSW_AB, FSSW_D, and FSSW_D_AB methods. The observation suggests a progressive increase in the ductility of the joint. The enhanced ductility of the sandwich sheet joint is further supported by the results presented in

Figure 5.9. The appearance of dense and large dimples on the fracture surfaces is indicative of the ability of the material to deform plastically and absorb energy before fracture occurs. Such ductile behavior is particularly desirable in structural applications as it signifies the ability of the joint to withstand varying loads. Moreover, the presence of these dimples suggests that the joint undergoes significant deformation and energy dissipation mechanisms during the peeling process, contributing to its overall toughness and durability.

5.2.4 Bending of AB, FSSW_D_AB, and FSSW_AB sandwich panels

The comparison between the load evolution of sandwich panels fabricated by the AB, the FSSW_D_AB, and the FSSW_AB is illustrated in Figure 5.16(a), and Figure 5.16(b) shows the bar chart with an error bar of peak load and stiffness of 3PBT of AB, FSSW_D_AB, and FSSW_AB specimens. It was evident that incorporating the disc insert and employing the FSSW alters the load-deflection curve of the sandwich panel, notably enhancing its stiffness and load-bearing capacity. The FSSW_AB specimen exhibited low stiffness and load-bearing capability among the three. The effect is also statistically significant as the variations in peak load and stiffness appear to be minimal indicating that the FSSW variants are stable and statistically reliable. Figure 5.17 provides insights into fracture initiation and evolution in the panels at intermittent bending deflections, as marked in the load evolution curves (from A to L – See Figure 5.16(a)).

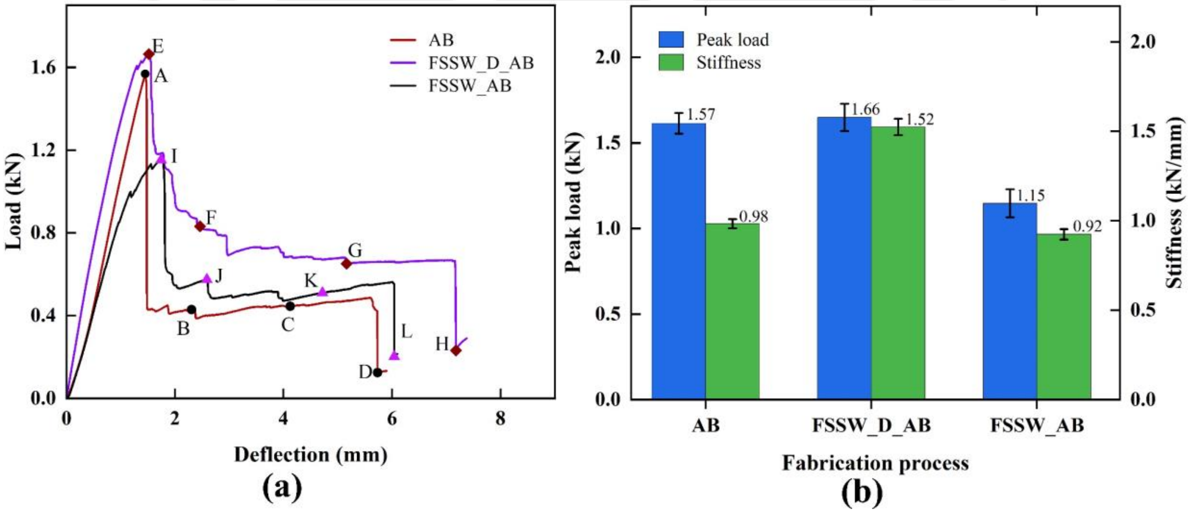

Figure 5.16 (a) Load evolution of AB, FSSW_D_AB, and FSSW AB specimens during 3PBT. (b) Peak load and stiffness variation in AB, FSSW_D_AB, and FSSW_AB specimens during 3PBT

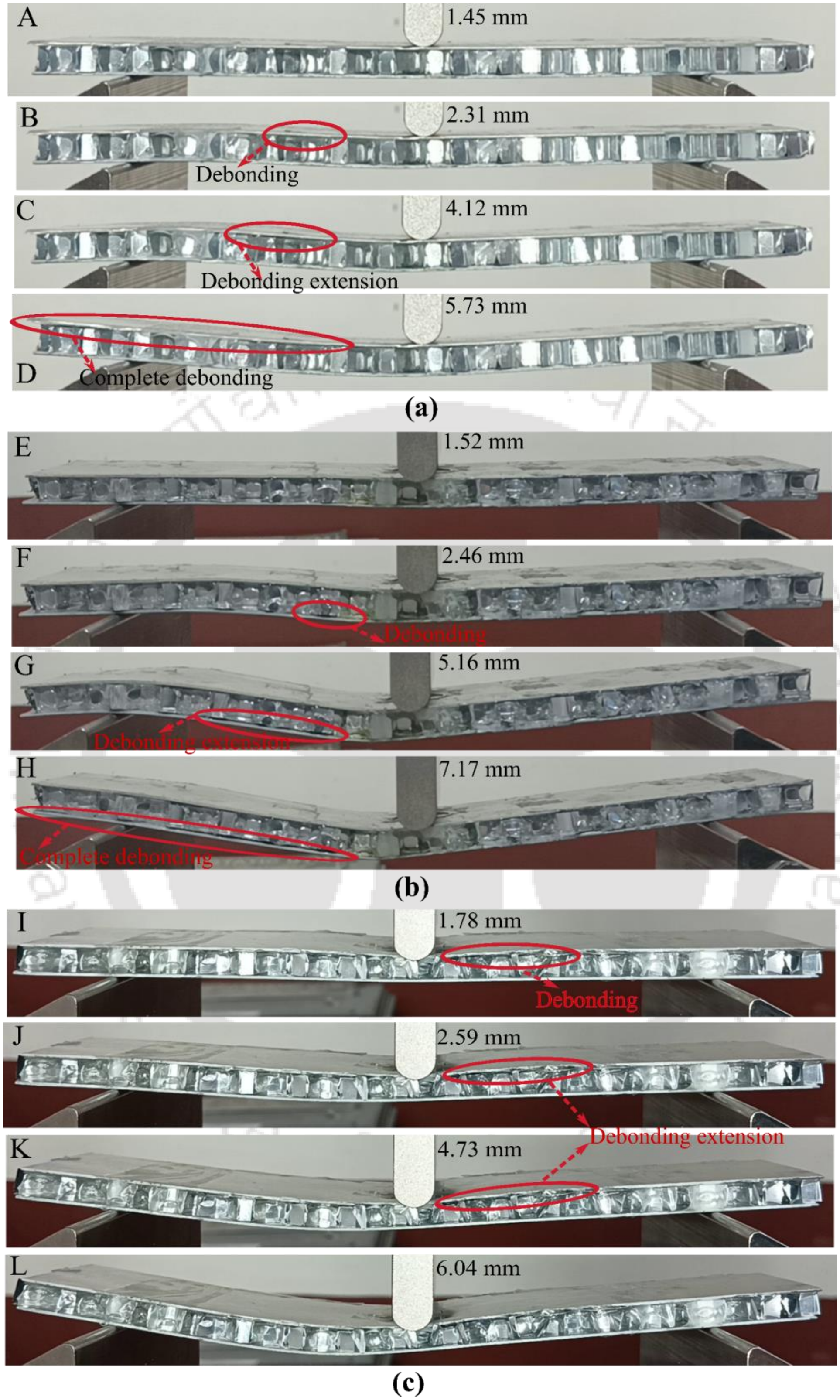

Figure 5.17 Images showing the status of fracture at different stages of load evolution of 3PBT (a) AB (b) FSSW_D_AB, and (c) FSSW_AB sandwich panel

As shown in Figure 5.16(a), the AB sandwich panel exhibited a pattern where the bending load first increased linearly and then nonlinearly until it reached its peak at 1.57 kN at point A. Following this peak, the bending load sharply decreased due to the debonding of the upper face sheet indicated by the red ellipse in Figure 5.17(a). In contrast, the load-deflection curve for the FSSW_D_AB sandwich panel displayed both linear and nonlinear stages before reaching a peak load of 1.66 kN. Subsequently, a rapid drop in the load occurred due to the debonding of the lower face sheet caused by local debonding, which is due to the adhesive failure. The status of the fracture of the panel can be seen at different deflection points (E to H) in Figure 5.16(a) (for FSSW_D_AB) and Figure 5.17(b). The FSSW_AB sandwich panel follows the same pattern in load evolution; however, before reaching the peak load, a slight drop occurred in the load, possibly due to the further core crushing at the joint location. After reaching the peak value, the debonding continued to extend with the downward movement of the indenter. The debonding pattern at different deflection points of the FSSW_AB sandwich panel is indicated in Figure 5.16(a) and Figure 5.17(c). The complete debonding of the FSSW_AB sandwich panel was not observed in the front view of Figure 5.17(c) at L point. It was observed in the back view.

Besides a noticeable increase in peak load, the FSSW_D_AB sandwich panel also demonstrated a significant enhancement in bending stiffness. It improved from 984.34 N/mm to 1524.36 N/mm. The stiffness and peak load of the FSSW_AB sandwich panel decreased by 6.5% and 26.7%, respectively, compared to the AB panel. The primary fracture mode for all the sandwich panels was debonding at the peak load (Figure 5.17).

Figure 5.18(a) illustrates that the load estimation for the AB honeycomb sandwich panel closely resembled the experimental results until reaching the peak load. However, after this point, the simulation failed to capture the softening pattern, as the FE model used a tie constraint to connect the core and face sheet. Moving on to the FSSW_D_AB panel in Figure 5.18(b), the simulated load-deflection curves showed good agreement with the experimental curve only up to the first peak load. Beyond this point, even the load-decrement pattern was not accurately predicted, and the simulated values were notably higher.

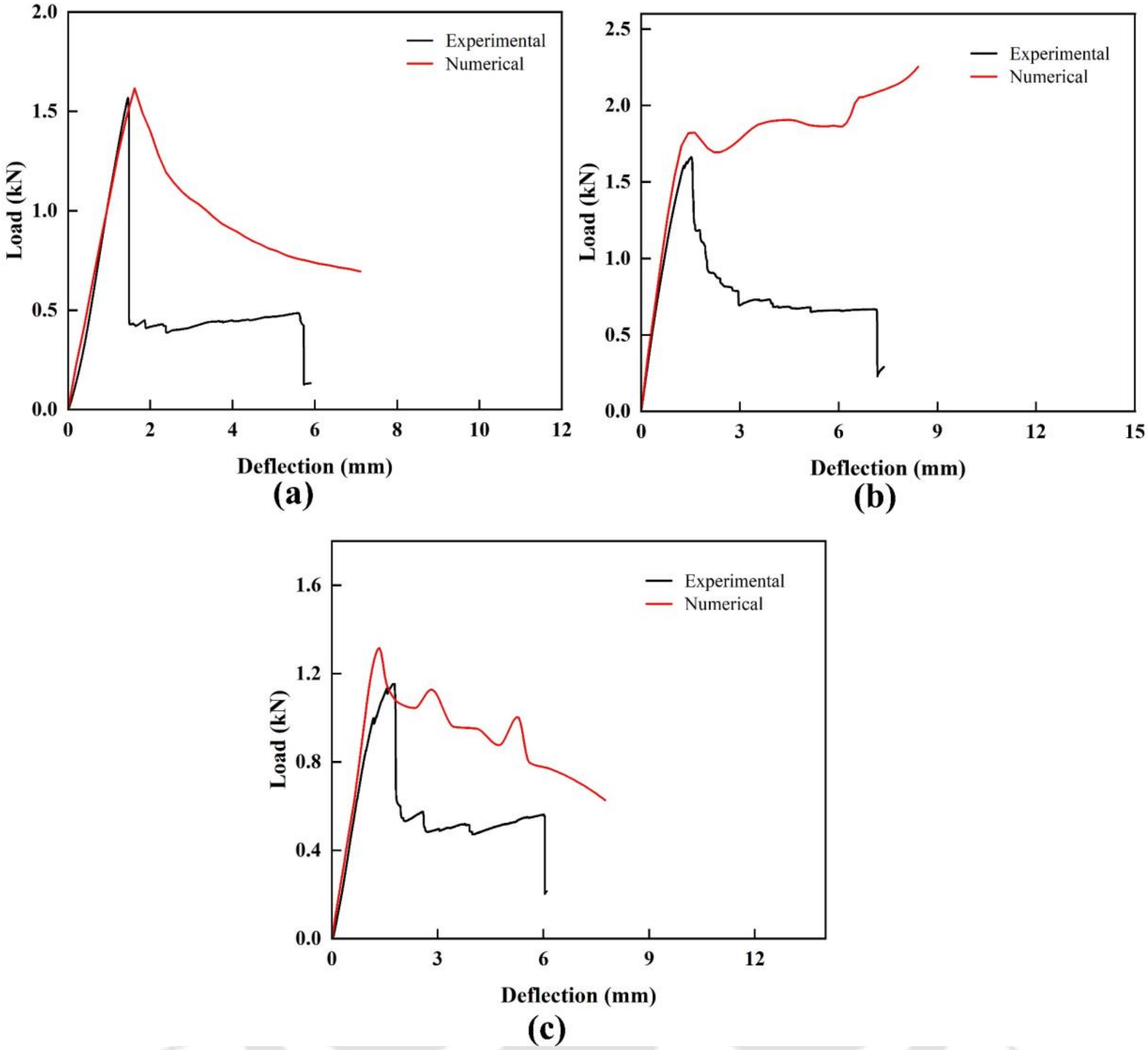

Figure 5.18 Comparison of 3PBT load-deflection curves from experiments and FE simulations of (a) AB (b) FSSW_D_AB (c) FSSW_AB sandwich panel

As for the FSSW_AB panel, as seen in Figure 5.18(c), the FE model performed well in predicting the load-deflection data but only up to the peak load. Afterwards, while the load-decreasing pattern matched, the load values were not accurately predicted, with the numerically estimated peak load being 7.2% higher than the experimental value. The discrepancy between the numerical and experimental results after the peak load point was attributed to the debonding between the honeycomb core and the face sheets in experiments, which the FE model could not predict due to ideal bonding conditions. One way of circumventing this discrepancy is by introducing the damage model in the FE simulations. These models, like cohesive zone or continuum damage mechanics models, can simulate the load vs. deflection response after the peak load.

Figure 5.19 illustrates different stages of the FE simulation of 3PBT and the distribution of Von Mises stress in the sandwich panels. While Von Mises stress is primarily concentrated on the indenter location within a small region (Figure 5.19(a)) with limited local collapse in the AB sandwich panel, the stress concentration area is just outside the indenter location, expanded to a larger region in the case of the FSSW_D_AB (Figure 5.19(b)). Due to the expansion in the stress distribution, the stress between the core and the face sheet increased rapidly, leading to the debonding of the core and face sheet. A rapid drop in load was observed at this stage in the experimental data of FSSW_D_AB (point E in Figure 5.16(a)). In contrast, the numerical data of the FSSW_D_AB increased even beyond this point because of the ‘tie’ constraint and low deformation in the disc. Von Mises stress was predominantly concentrated in the indented region of the top face sheet and the core beneath the loading indenter in the FSSW_AB sandwich panel, as shown in Figure 5.19(c). Notably, because there was no core material beneath the indented top face sheet area, the load-deflection curve exhibited a different behaviour after reaching its peak load, as shown in Figure 5.18(c). The deviation was due to the distribution of Von Mises stress between the indented top face sheet and the bottom face sheet in the absence of core material beneath the indented region (Figure 5.19(c)). As presented in Table 5.4, although the numerical model slightly overpredicted the averaged experimental data, such as peak load and specific stiffness, the superiority of FSSW_D_AB was well predicted.

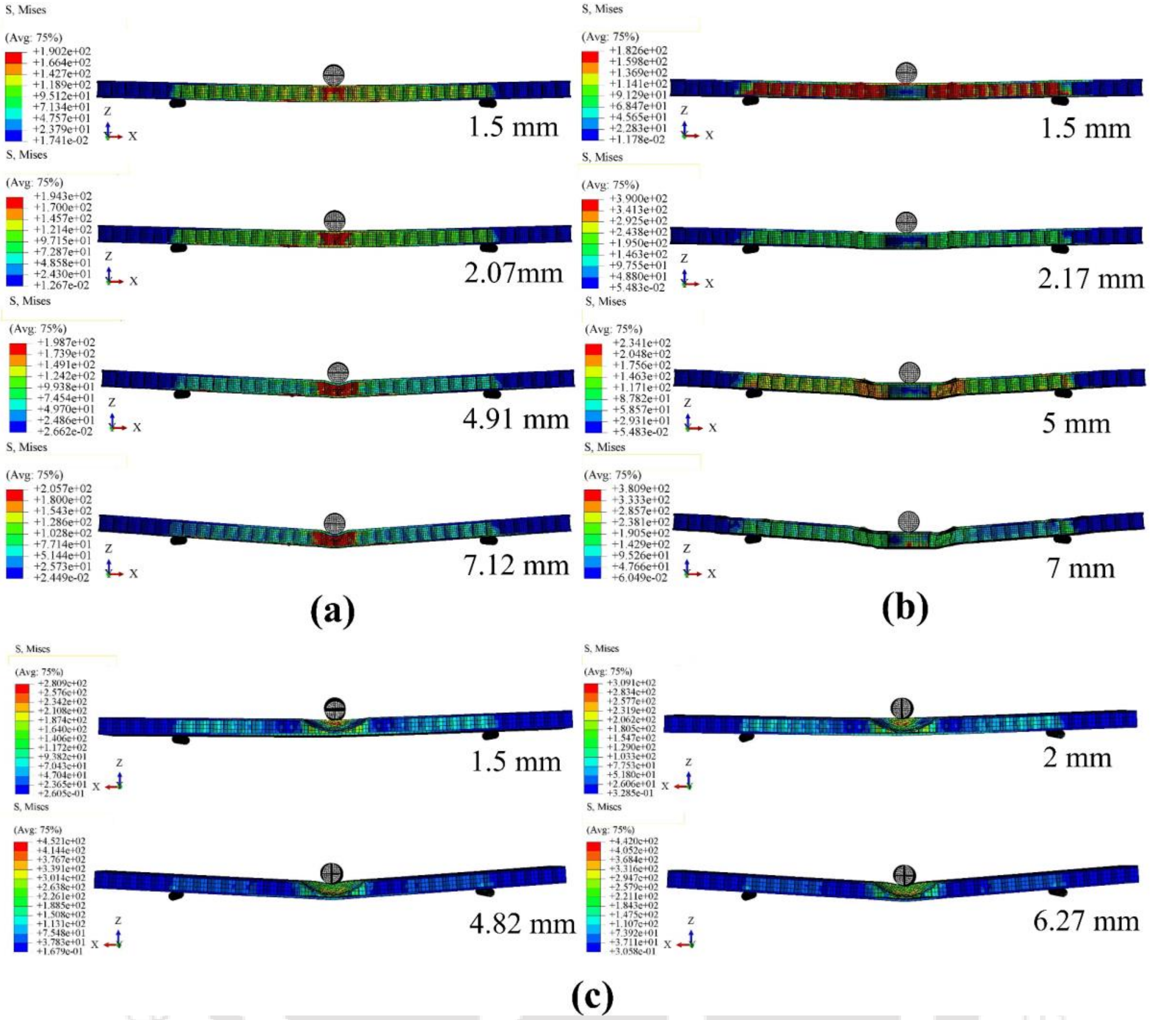

Figure 5.19 Cross-sectional views of numerically simulated 3PBT sandwich structures of (a) AB (b) FSSW_D_AB (c) FSSW_AB

Table 5.4 Comparison of experimental (averaged value) and numerical results of 3PBT

3PBT	Density of the panel (kg/m^3)	Peak load (kN)	Specific stiffness (J-m/kg)
AB (experimental)	777	1.57	1266
AB (numerical)	714	1.62	1753
FSSW_D_AB (experimental)	825	1.66	1848
FSSW_D_AB (numerical)	767	1.82 (first peak)	2114
FSSW_AB (experimental)	775	1.15	1193
FSSW_AB (numerical)	747	1.24	1401

5.2.5 Fabrication of scaled-up sandwich panel

The load evolution of scaled-up sandwich panels fabricated by the AB and FSSW_D_AB is illustrated in Figure 5.20(a), and Figure 5.20(b) shows the changes in peak load and stiffness during forming of AB and FSSW_D_AB scaled-up sandwich panels.

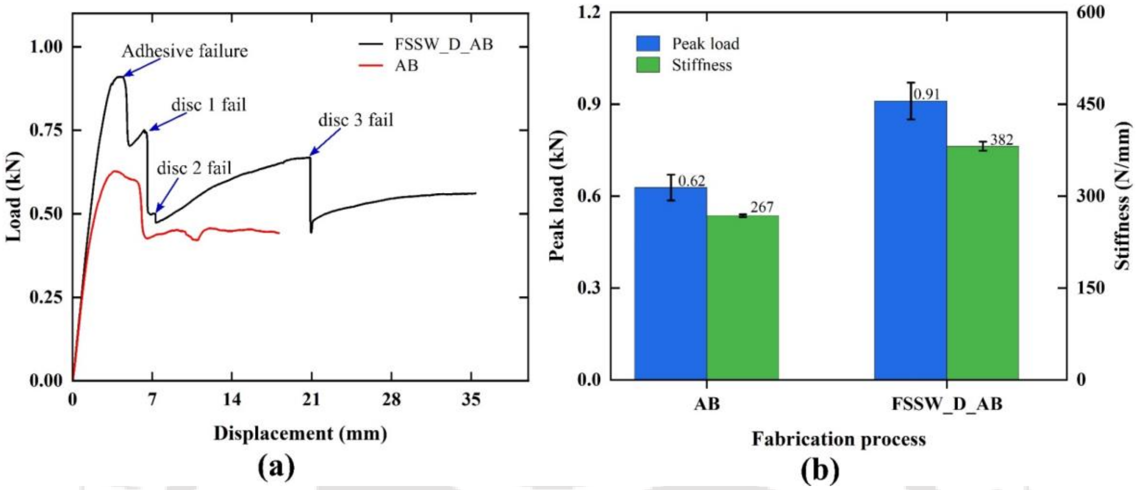

Figure 5.20 (a) Load evolution during the forming of AB and FSSW_D_AB sandwich panels, (b) Peak load and stiffness variation during the forming of the AB and FSSW_D_AB scaled-up sandwich panels

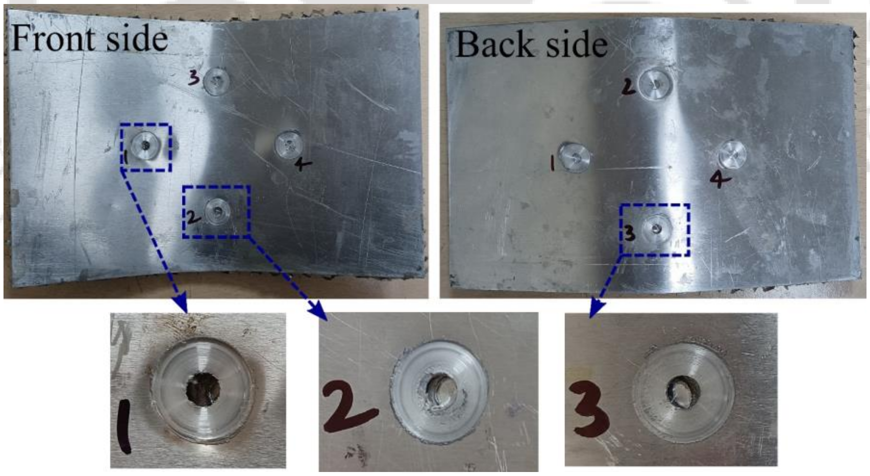

Figure 5.21 Failed disc during the forming process of FSSW_D_AB sandwich panel

Figure 5.20(a) shows that the forming load decreased after a linear and nonlinear increase in the case of the AB panel. The load then entered a plateau phase. This trend indicates the progressive deformation and eventual stabilization of the panel during forming. Conversely, the FSSW_D_AB sandwich panel exhibited a different trend. The forming load declined after reaching its peak load due to adhesive failure. Subsequently, there was a load increase before the disc 1 failure, followed by increments before the disc 2 and 3 failed, with significant increments before the disc 3 failure. The data showed a plateau region without experiencing the disc 4 failure. It appears from Figure 5.20(b) that the statistical variations in peak load and stiffness are minimal, indicating that the FSSW variants are stable and reliable, similar to that depicted in the bending test. Figure 5.21 shows that discs 1 and 2 failed on the front side, whereas disc 3 failed on the backside of the FSSW_D_AB sandwich panel. This failure distribution indicates a balanced load distribution between the adhesive and the disc insert bonding, contributing to the improvement in the load-bearing ability of the panel. The primary factor behind load reduction in the AB panel was the delamination of adhesive between the face sheet and the honeycomb core, which constituted the dominant failure mode. In contrast to the AB panel, where the load distribution primarily relied on the adhesive bonding between the face sheet and the honeycomb core, the FSSW_D_AB panel demonstrated a better distribution in the load-bearing mechanism. This betterment was attributed to the presence of metallurgical bonds at the four-disc insert locations, which provided additional reinforcement and structural integrity to the sandwich panel. The comparison of peak forming force indicated that the FSSW_D_AB panel improved by 46% compared to the AB sandwich panel. Additionally, the specific stiffness of the FSSW_D_AB panel witnessed a substantial increase of 35%. The scaled-up sandwich panel's density, peak load, and specific stiffness are shown in Table 5.5.

Table 5.5 Scaled-up panels comparison

Forming of	Density of the panel (kg/m^3)	Peak load (kN)	Specific stiffness (J-m/kg))
AB panel	854	0.62	314
FSSW_D_AB panel	902	0.91	423

In summary, the FSSW_D_AB sandwich panel demonstrates improved load capacity and specific stiffness compared to the AB panel due to the presence of solid-state metallurgical bonding created by FSSW. One can optimize the number of such spot welds and disc inserts required for fabricating FSSW_D_AB sandwich panels that can surpass the performance of AB panels. This way, honeycomb core sandwich panels can be manufactured in a shorter process duration through eco-friendly and sustainable hybrid manufacturing routes like FSSW+AB.

5.3 Summary

The main aim of the current work was to manufacture the novel honeycomb core sandwich structures by the FSSW joining strategies to augment the existing adhesive bonded structures. Four different strategies, namely FSSW, FSSW_D, FSSW_AB, and FSSW_D_AB, were implemented and compared with the lap shear, peel, and bending tests performance of the conventional adhesive bonded sandwiches. Finally, the scaled-up forming of sandwich structures was also compared to expose the prominence of the hybrid manufacturing method.

In the peel test, the peak load of the FSSW, the FSSW_AB, the FSSW_D, and the FSSW_D_AB joints increased by 232%, 463%, 374%, and 705%, respectively, compared to the AB joints. In the lap-shear test, an increase in the peak load was 846%, 1015%, 568%, and 853%, respectively was observed. The primary fracture mode observed in lap shear and peel tests were "nugget pull-out failure". In terms of the peak load-to-weight ratio and fracture energy during shearing and peeling, the FSSW_D_AB specimens outperformed other joining and fabrication methods.

The 3PBT results of AB, FSSW_AB, and FSSW_D_AB from the numerical simulations and the experiments showed good agreement up to peak load. After that, a significant difference was seen due to assumed ideal bonding conditions in the FE model. Additionally, when compared to the AB panel, the FSSW_D_AB sandwich panel demonstrated significant enhancements in the peak load and the specific stiffness, with improvements of 6.12% and 46%, respectively. Therefore, the FE model predicts the improvement in the performance of sandwich structures appropriately before the onset of damage in the specimens. FE simulations considering the damage models can predict the load evolution beyond the peak load. This can be done by using a cohesive zone model or a continuum damage mechanics model to simulate the load vs. deflection response after the peak load. The scaled-up sandwich panel fabricated by the FSSW_D_AB demonstrated improved peak load and specific stiffness by 46% and 35% compared to the AB panel. This is similar to the observation during shearing and pealing. The proposed fabrication strategies are novel attempts in the manufacture of honeycomb sandwich sheets. The treatment of spot joints during FE analyses is also unique in obtaining quick results and computationally less expensive solutions of hybrid sandwich sheets.

Chapter 6 Lap shear performance analysis of honeycomb core sandwich panels fabricated through FSSW strategies

6.1 Experimental process

This section describes the methods for conducting FSSW trials, preparing sandwich samples, and performing lap shear testing. The mechanical properties of skin sheet and honeycomb core are already discussed in Section 3.1.1 in Chapter 3, whereas the mechanical properties of disc insert are discussed in Section 4.1.1 in Chapter 4. All the material properties of sandwich sheets are presented in Table 5.1 of Chapter 5.

6.1.1 Sandwich fabrication methods

The three different joining strategies for fabricating sandwich structures with honeycomb core are described here.

6.1.1.1 AB

The joining strategies using AB is already explained in Section 5.1.2.1 of Chapter 5. The fabrication processes of lap-shear specimens are shown in Figure 6.1.

6.1.1.2 FSSW_D

The joining process is the same as discussed in Section 5.1.2.4 of Chapter 5. The following welding parameters were selected: a plunge depth of 2.2 mm, a tool plunge speed of 2 mm/min, and a dwell time of 5 s. Tool rotation speeds of 750 and 1200 rpm were used on both sides of the welding process. FSSW_D_750 specimens were welded using rotational speeds of 750 rpm on both the front and back sides of the welding. Similarly, the FSSW_D_1200 specimen was welded at rotational speeds of 1200 rpm on both the front and back sides of the welding. A fabricated lap-shear specimen is shown in Figure 6.2.

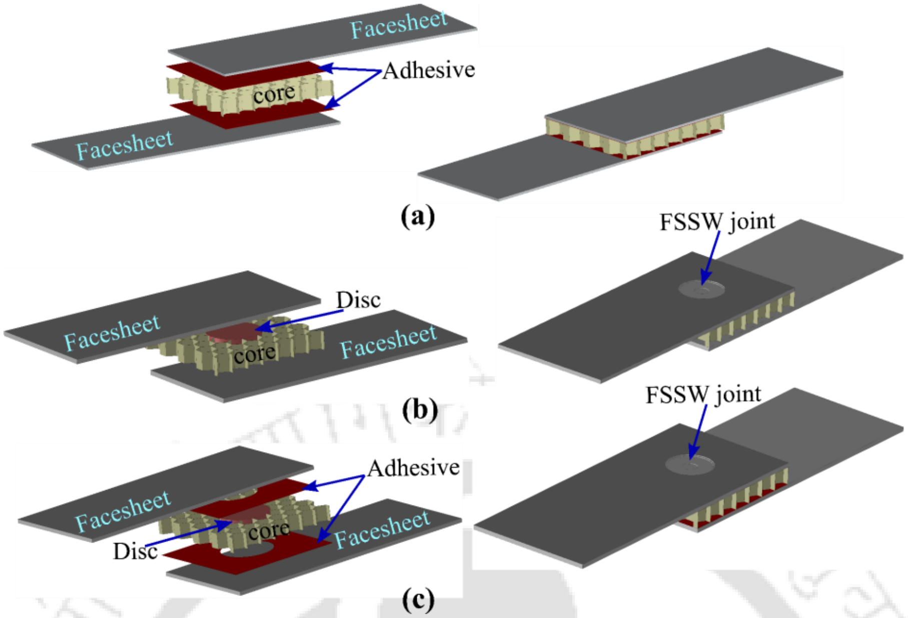

Figure 6.1 Fabrication of lap shear sandwich sheets by (a) AB (b) FSSW_D (c) FSSW_D_AB

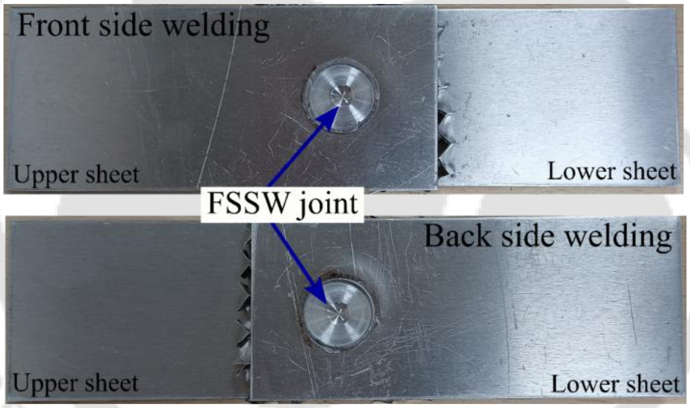

Figure 6.2 Fabricated lap shear specimen by FSSW_D process

6.1.1.3 FSSW_D_AB

The joining process is the same as discussed in Section 5.1.2.5 of Chapter 5.

6.1.2 Sample preparation and joint characterization

The dimensions of lap shear specimens are already shown in Figure 3.5(b) of Chapter 3.

At the joint cross-section, macrostructural examinations of the welded samples were carried out. After being properly polished, the samples were subjected to chemical etching at room temperature using a solution made up of 20 ml H_2O, 10 ml HNO_3, 6 ml HCl, and 4 ml HF. A stereo microscope was used for macro cross-sectional investigation. Additionally, a Carl

Zeiss optical microscope was used to do the microstructural analysis of the stir zone in FSSW_D_AB specimens. By etching for 15 to 20 s with the same chemical solution, microstructures were revealed.

6.2 Numerical analysis

Numerical analysis was carried out in Abaqus® software employing CZM with the honeycomb core featuring a cohesive layer, the homogenized core and equivalent cohesive layer. The homogenization procedure of the honeycomb core is already discussed theoretically and numerically in Sections 2.1 and 2.2.1 of Chapter 2. The method for determining the equivalent cohesive layer is described in this section.

6.2.1 Cohesive zone modelling

In this study, CZM was used to analyze the bonding between the core-skin and the skin-disc. As per CZM, the cohesive forces operating between these surfaces provide resistance to their separation at the interface. These cohesive forces effectively prevent the separation of the joined surfaces. A traction-separation curve describes the relationship between the cohesive resistance and the separation between the joined surfaces. CZM has been proven to be effective in simulating fractures in various materials. A triangular shape (bi-linear) with a mixed-mode formulation for the traction-separation curve, as depicted in Figure 6.3, can be assumed, although exponential and trapezoidal shapes are also commonly employed. At first, the curve displays elastic behaviour up to σ_n^0, which is the pure mode I or tension-based maximum cohesive strength; σ_s^0, which is the pure mode II or shear-based maximum cohesive strength; or σ_m^0, which is the mixed mode based maximum cohesive strength. As the material's characteristics deteriorate until they fail entirely, the curve shifts to show linear softening behaviour. In this case, displacement failure commencement are δ_n^0 in mode I, δ_s^0 in mode II, and δ_m^0 in mixed mode. The displacement at ultimate failure in mode I is represented by δ_n^f, mode II by δ_s^f, and mixed mode by δ_m^f.

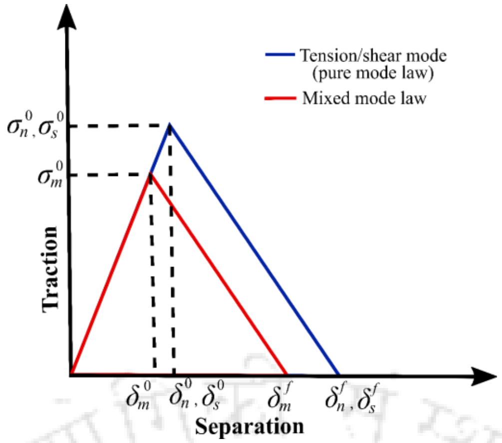

Figure 6.3 Traction-separation law linear softening for pure and mixed-mode laws

The traction-separation behaviour until the start of damage can be written as

$$\sigma = \begin{bmatrix} \sigma_n \\ \sigma_{s_1} \\ \sigma_{s_2} \end{bmatrix} = \begin{bmatrix} K_{nn} & K_{ns_1} & K_{ns_2} \\ K_{ns_1} & K_{s_1s_1} & K_{s_1s_2} \\ K_{ns_2} & K_{s_1s_2} & K_{s_2s_2} \end{bmatrix} \begin{bmatrix} \varepsilon_n \\ \varepsilon_{s_1} \\ \varepsilon_{s_2} \end{bmatrix} = K\varepsilon \tag{6.1}$$

Critical values for the normal, primary, and secondary shear directions are σ_n^c, $\sigma_{s_1}^c$, and $\sigma_{s_2}^c$, respectively, whereas the corresponding stresses are σ_n, σ_{s_1} and σ_{s_2}, respectively.

An appropriate model for adhesive layers and FSSW delamination may be specified using $K_{nn} = K_n, K_{s_1s_1} = K_{s_2s_2} = K_s, K_{ns_1} = K_{ns_2} = K_{s_1s_2} = 0$ particular parameters. Several factors may be used to identify when damage has been initiated. The quadratic nominal stress criteria [68] were used to characterize damage initiation, as shown by the equations below.

$$\left(\frac{\sigma_n}{\sigma_n^c}\right)^2 + \left(\frac{\sigma_{s_1}}{\sigma_{s_1}^c}\right)^2 + \left(\frac{\sigma_{s_2}}{\sigma_{s_2}^c}\right)^2 = 1 \tag{6.2}$$

When the condition mentioned above is satisfied, Eq. (6.2) indicates that a complete separation will occur. The energy required to fail in the pure modes follows a linear power-law relationship, which predicts the separation as per [68,82],

$$\left(\frac{G_n}{G_n^c}\right) + \left(\frac{G_{s_1}}{G_{s_1}^c}\right) + \left(\frac{G_{s_2}}{G_{s_2}^c}\right) = 1 \tag{6.3}$$

where the fracture energies in the normal, primary and secondary shear directions, G_n, G_{s_1}, and G_{s_2} are equal to G_n^c, $G_{s_1}^c$, and $G_{s_2}^c$.

The area under the curve corresponds to toughness and can be calculated for the triangular shape as follows:

$$G_c = \frac{1}{2}\sigma^0\delta^f \tag{6.4}$$

$$\sigma = (1-D)\sigma^{\text{und}} \tag{6.5}$$

where σ^0 and δ^f are the maximum cohesive strength and ultimate failure corresponding mode. D and σ^{und} are scalar damage variable and undamaged stress, respectively [71,108,109].

D can be explained as

$$D = 1 - \frac{\delta^0(\delta^f - \delta)}{\delta(\delta^f - \delta^0)} \tag{6.6}$$

While δ^0 is separation at maximum strength at corresponding mode, the variable δ is the current separation.

The parameters of the CZM, such as stiffness, maximum stress, and critical fracture energy, were derived from separate lap shear and peel tests of only adhesive-bonded and welded specimens (FSSW with disc insert without adhesive bonding). To commence the optimization procedure, initial values for these parameters were identified. Subsequently, the experimental load-displacement curve was compared with the simulation load-displacement curve. The optimization procedure, depicted in Figure 6.4, involved iteratively adjusting these parameters and rerunning the simulation until the results aligned with the desired results [68,69,71,108,110,111]. The parameters used in the finite element simulations are presented in Table 6.1.

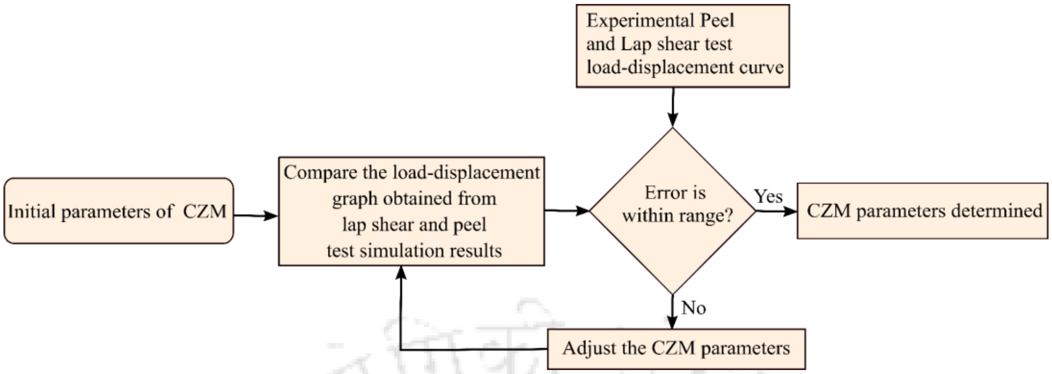

Figure 6.4 Flow chart for optimization of CZM parameters

Table 6.1 Optimized CZM parameters

Layer	$\sigma^{c}_{\max}$ (MPa)	$\tau^{c}_{\max}$ (MPa)	K^{n} (MPa/mm)	K^{s} (MPa/mm)	G^{n}_{c} (N/mm)	G^{s}_{c} (N/mm)
AB (cohesive layer)	2.26	2	22	42	1.41	0.22
(FSSW_D_750)	38	46	150	100	74	78
(FSSW_D_1200)	47	51	150	115	93	106

where $\sigma^{c}_{\max}$, K^{n}, G^{n}_{c}, and $\tau^{c}_{\max}$, K^{s}, G^{s}_{c} are critical stress, stiffness, and critical fracture toughness in normal and shear directions, respectively.

The cohesive layer was used to analyze the joining behavior in both adhesive-bonded and welded configurations, between the skin-core and skin-disc interfaces. For AB, the cohesive properties of the adhesive layer were used to represent the joining characteristics. In the case of FSSW_D, the welded cohesive layer properties were adapted to reflect the interface behavior. For FSSW_D_AB, the combination of both adhesive and welded cohesive layer properties was applied to accurately simulate the hybrid joining mechanism, capturing the combined effects of adhesive bonding and welding on joint performance.

6.2.2 Homogenization of the honeycomb core and equivalent cohesive layer

The simulation involving the honeycomb core is time-consuming, and this can be reduced by substituting it with its equivalent core. Replacing the honeycomb core with its equivalent form also changes the cohesive layer area. Therefore, the homogenization process for the honeycomb core and the equivalent model of the cohesive layer are required. These are described here.

6.2.2.1 Homogenization of honeycomb core

The homogenization procedure is already discussed theoretically and numerically in Sections 2.1 and 2.2.1 of Chapter 2. The obtained orthotropic properties of the honeycomb core for Homogenization are shown in Table 6.2.

Table 6.2 Orthotropic properties of honeycomb core for Homogenization

E_1 (MPa)	E_2 (MPa)	E_3 (MPa)	ν_{12}	ν_{13}	ν_{23}	G_{12} (MPa)	G_{13} (MPa)	G_{23} (MPa)
1.65	1.57	2273.35	0.998	0.000234	0.000234	1.02	442	635.20

6.2.2.2 Equivalent cohesive layer

Equivalent cohesive layer properties can be derived from lap–shear and cross-tension tests. The cohesive layer, the honeycomb core and the corresponding equivalent forms used in both tests are depicted in Figure 6.5. The primary objective of the testing methods is to evaluate the normal and tangential shear strength of the materials by applying a constant normal load and tangent load to the normal and shear areas.

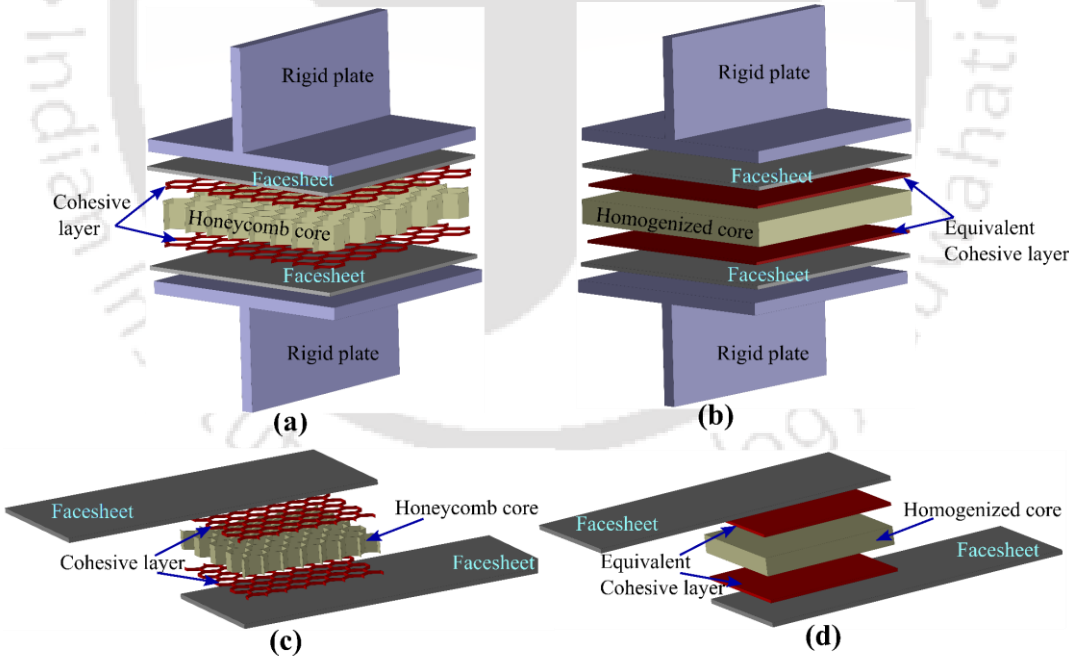

Figure 6.5 Sandwich sheet cross-tension test with (a) honeycomb and (b) homogenized cores. Sandwich sheet lap shear test with (c) honeycomb core and (d) homogenized core

The equivalent property of the cohesive layer was determined by selecting a RCE (the same as used for the honeycomb core) to represent the cohesive layer. Figure 6.6(a) and (b) show both the RCE of the cohesive layer and its corresponding equivalent cohesive layer. Figure 6.6(a-d) presents the application of normal and shear forces on the RCE of the cohesive layer and on the equivalent cohesive layer. F_{h} and F_{ho} are normal forces, while P_{h} and P_{ho} are shear forces.

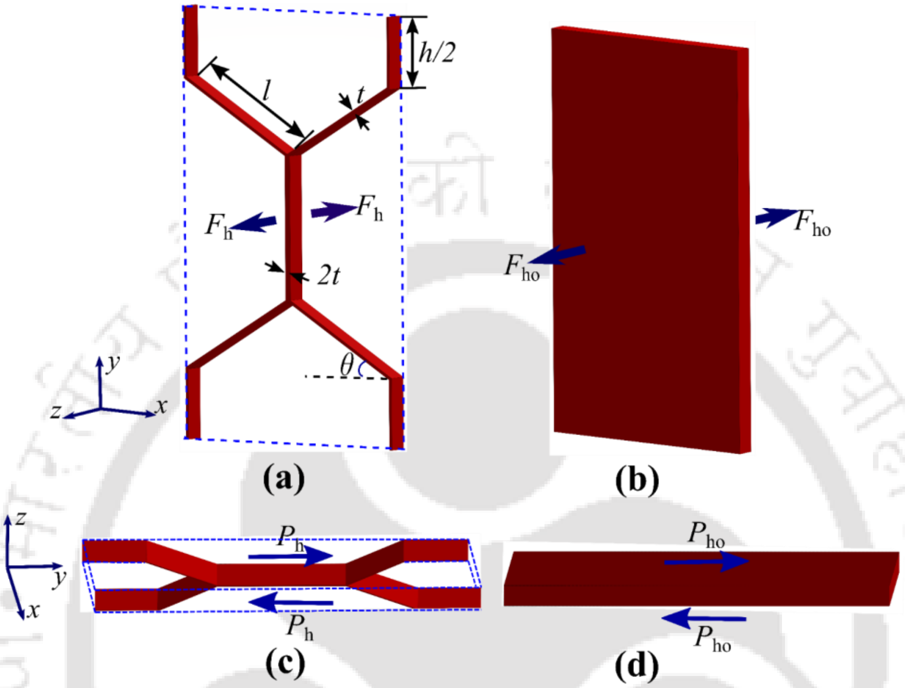

Figure 6.6 Representation of (a) normal load on RCE of cohesive layer, (b) normal load on the equivalent cohesive layer, (c) shear load on RCE of cohesive layer, and (d) shear load on the equivalent cohesive layer

If the maximum normal load and the maximum shear load applied to the RCE are equal to the maximum normal load and the maximum shear load applied to its equivalent form. In that case it is possible to determine the maximum normal $\left(\sigma_{\mathrm{ho}}^{c}\right)_{\mathrm{m}}$ and shear strength $\left(\tau_{\mathrm{ho}}^{c}\right)_{\mathrm{m}}$ of the equivalent cohesive layer by ensuring that the loads that are acting on the equivalent model are the same as those that were acting on the original RCE.

$$A_{\mathrm{ho}}\begin{bmatrix}\left(\sigma_{\mathrm{ho}}^{c}\right)_{\mathrm{m}}\\ \left(\tau_{\mathrm{ho}}^{c}\right)_{\mathrm{m}}\end{bmatrix}=A_{\mathrm{h}}\begin{bmatrix}\left(\sigma_{\mathrm{h}}^{c}\right)_{\mathrm{m}}\\ \left(\tau_{\mathrm{h}}^{c}\right)_{\mathrm{m}}\end{bmatrix} \tag{6.7}$$

where $\left(\sigma_{\mathrm{h}}^{c}\right)_{\mathrm{m}}$, $\left(\tau_{\mathrm{h}}^{c}\right)_{\mathrm{m}}$, and A_{h} are the maximum normal strength, shear strength and cross-sectional area of the RCE of the cohesive layer, respectively, and A_{ho} is the cross-sectional area of the equivalent cohesive layer. These are given below.

$$\begin{aligned} A_{\mathrm{h}} &= 4(h+l)t \\ A_{\mathrm{ho}} &= 4l\cos\theta(h+l\sin\theta) \end{aligned} \tag{6.8}$$

From Eqs. (6.7) and (6.8)

$$\begin{bmatrix} \left(\sigma_{\mathrm{ho}}^{c}\right)_{\mathrm{m}} \\ \left(\tau_{\mathrm{ho}}^{c}\right)_{\mathrm{m}} \end{bmatrix} = \left(\frac{t}{l}\right)\frac{(h+l)}{\cos\theta\left(h+l\sin\theta\right)}\begin{bmatrix} \left(\sigma_{\mathrm{h}}^{c}\right)_{\mathrm{m}} \\ \left(\tau_{\mathrm{h}}^{c}\right)_{\mathrm{m}} \end{bmatrix} \tag{6.9}$$

For a conventional (regular) honeycomb, $h = l$ and $\theta = 30^{\circ}$. Therefore,

$$\begin{bmatrix} \left(\sigma_{\mathrm{ho}}^{c}\right)_{\mathrm{m}} \\ \left(\tau_{\mathrm{ho}}^{c}\right)_{\mathrm{m}} \end{bmatrix} = \frac{8}{3\sqrt{3}}\left(\frac{t}{l}\right)\begin{bmatrix} \left(\sigma_{\mathrm{h}}^{c}\right)_{\mathrm{m}} \\ \left(\tau_{\mathrm{h}}^{c}\right)_{\mathrm{m}} \end{bmatrix} \tag{6.10}$$

The traction-separation behaviour until the start of damage can be written as

$$\begin{bmatrix} \sigma \\ \tau \end{bmatrix} = \begin{bmatrix} K^{n} & 0 \\ 0 & K^{s} \end{bmatrix}\begin{bmatrix} \delta_{n} \\ \delta_{s} \end{bmatrix} \tag{6.11}$$

The maximum load separation in the honeycomb and homogenized core is equal, according to Eqs. (6.9) and (6.11).

$$\begin{bmatrix} K_{\mathrm{ho}}^{n} & 0 \\ 0 & K_{\mathrm{ho}}^{s} \end{bmatrix}\begin{bmatrix} \delta_{n} \\ \delta_{s} \end{bmatrix} = \left(\frac{t}{l}\right)\frac{(h+l)}{\cos\theta\left(h+l\sin\theta\right)}\begin{bmatrix} K_{\mathrm{h}}^{n} & 0 \\ 0 & K_{\mathrm{h}}^{s} \end{bmatrix}\begin{bmatrix} \delta_{n} \\ \delta_{s} \end{bmatrix} \tag{6.12}$$

where $K_{\mathrm{h}}^{n}, K_{\mathrm{h}}^{s}$, and $K_{\mathrm{ho}}^{n}, K_{\mathrm{ho}}^{s}$ are the normal and shear stiffness of the cohesive layer and its equivalent form, respectively, and δ_{n}, δ_{s} are the separation in normal and shear directions, respectively.

For a conventional honeycomb, $h = l$ and $\theta = 30^{\circ}$. Therefore,

$$\begin{bmatrix} K_{\mathrm{ho}}^{n} & 0 \\ 0 & K_{\mathrm{ho}}^{s} \end{bmatrix}\begin{bmatrix} \delta_{n} \\ \delta_{s} \end{bmatrix} = \frac{8}{3\sqrt{3}}\left(\frac{t}{l}\right)\begin{bmatrix} K_{\mathrm{h}}^{n} & 0 \\ 0 & K_{\mathrm{h}}^{s} \end{bmatrix}\begin{bmatrix} \delta_{n} \\ \delta_{s} \end{bmatrix} \tag{6.13}$$

It is possible to determine the corresponding fracture toughness of the cohesive layer by equating the fracture energies of two sandwich sheets. The area under the load-displacement curve is the definition of fracture energy, therefore

$$\begin{bmatrix}\left(G_c^n\right)_{\text{ho}}\\ \left(G_c^s\right)_{\text{ho}}\end{bmatrix}=\frac{a_{\text{h}}}{a_{\text{ho}}}\begin{bmatrix}\left(G_c^n\right)_{\text{h}}\\ \left(G_c^s\right)_{\text{h}}\end{bmatrix} \tag{6.14}$$

Where "a_{h}" and "a_{ho}" represent the load-bearing regions within sandwich sheets formed by honeycomb and homogenized cores, respectively. Meanwhile, "$(G_c)_{\text{h}}$" and "$(G_c)_{\text{ho}}$" denote the fracture toughness values for the cohesive layer and its equivalent, respectively.

6.2.2.3 Performance comparison

To evaluate the performance of sandwich structures, lap shear test simulations were performed in Abaqus® 2017 software with sample dimensions presented in Fig. 4(a). The sandwich designs included two different kinds of core: the honeycomb core and the homogenized core, each with its corresponding cohesive layer. The orthotropic values of the homogenized core were given in Table 6.1, while the material properties for the honeycomb core and face sheets were provided in Table 5.1 of Chapter 5. Table 6.3 also shows the cohesive parameters of the adhesive that was utilized on the honeycomb core. The equivalent cohesive layer properties for the homogenized core were obtained from the cohesive layer properties of the adhesive layer used with the honeycomb core presented in Table 6.1 and with Eqs. (6.10),(6.13),and (6.14).

Table 6.3 Cohesive parameters for honeycomb and homogenized core

Layer	K^{n} (MPa/mm)	K^{s} (MPa/mm)	$\sigma^c_{\max}$ (MPa)	$\tau^c_{\max}$ (MPa)	G_c^{n} (N/mm)	G_c^{s} (N/mm)
Adhesive (cohesive layer)	22	42	2.26	2	1.41	0.22
Adhesive (equivalent cohesive layer)	0.732	1.4	0.075	0.066562	0.046	0.008

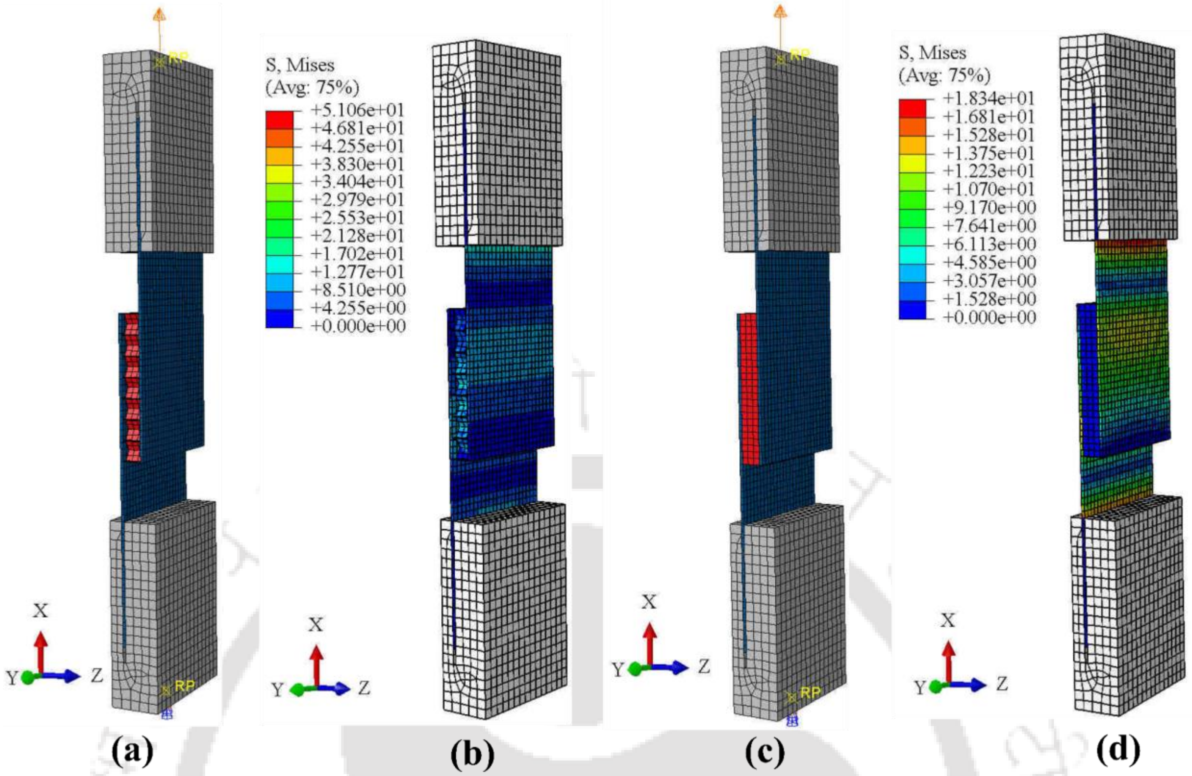

Figure 6.7 Numerical analyses of lap shear of sandwich made of honeycomb core, (a) undeformed, (b) deformed model. Sandwich made of homogenized core, (c) undeformed, and (d) deformed model

The boundary conditions and comparable forms of the simulated sandwich specimens are shown in Figure 6.7. Figure 6.8(a, b) presents mesh convergence studies for the lap shear test of sandwich structures. Convergence was specifically achieved using 17592 elements for the sandwich sheet, including the honeycomb core, and 5604 elements for the homogenized core. The progression of the load from the homogenized core and the honeycomb core is shown in Figure 6.8(c), demonstrating good agreement until and just after the maximum load. The lap shear simulation with homogenized core requires significantly fewer elements compared to the lap shear test with the honeycomb core. Consequently, the computation time (CPU time) of the lap shear test with the homogenized core was approximately less than 7% of the time required for the honeycomb core. This indicates that the benefits of quicker computations with equal mechanical performance characteristics may be obtained by employing the homogenized core with the corresponding cohesive layer in numerical simulations.

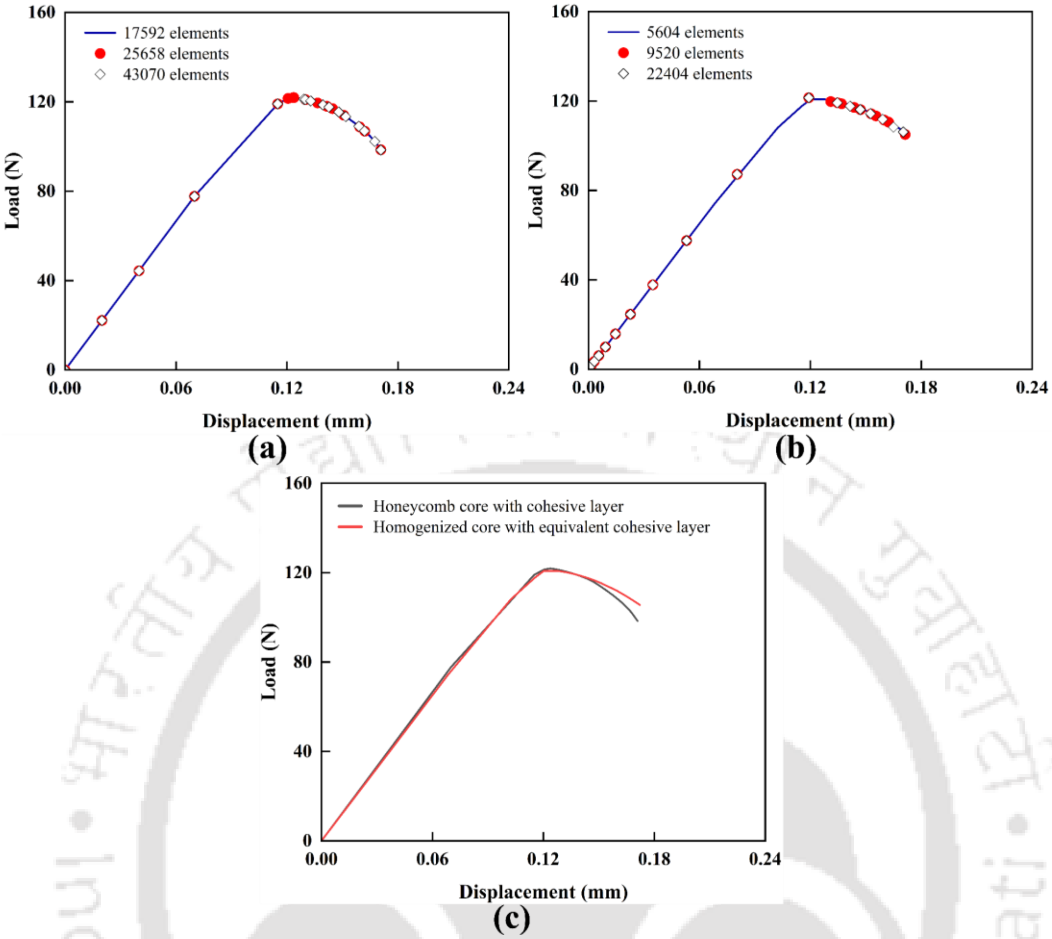

Figure 6.8 Lap shear test mesh convergence analysis for sandwiches with their corresponding cohesive layer (a) honeycomb core, (b) homogenized core, and (c) load evolution comparison

6.3 Results and Discussions

This section presents experimental results from lap shear tests of FSSW sandwich structures are presented. Later, numerical simulation results, joint strength analysis, and simulation validation are also discussed.

6.3.1 Macro cross-sectional view and microstructure observations

Figure 6.9(a-d) shows cross-sectional views of sandwiches manufactured at 750 and 1200 rpm rotational speeds. These images reveal that the sheet and the disc are joining together to create a metallurgical bond. The circumferential expansion of top sheet beyond the welding tool is greatly affected by the rotational speed. The axial force that is applied by the welding tool, on the other hand, inhibits the free flow of the upper sheet, which causes it to bend around the tool. As the rotational speed increases, the bending effect grows in prominence, as illustrated in Figure 6.9(a) and (c) and Figure 6.9(b) and (d). This indicates a clear correlation between tool rotational speed and the deformation behaviour of the top sheet during the FSSW.

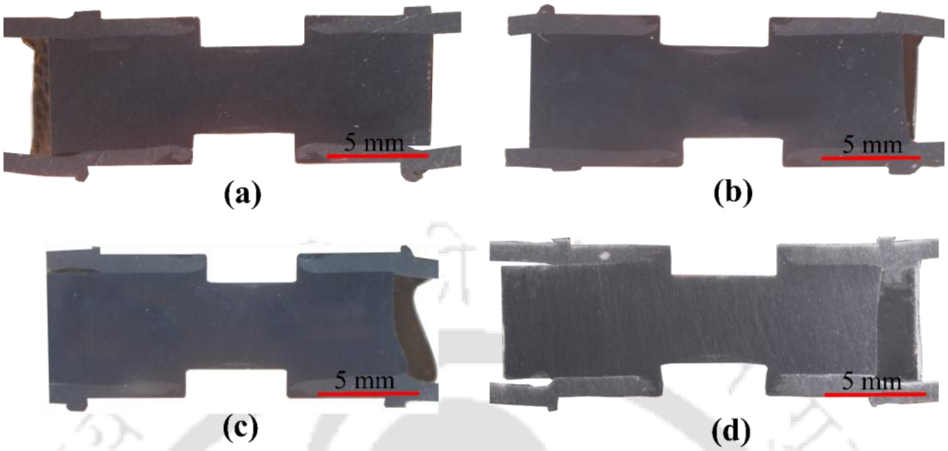

(a) (b) (c) (d)

Figure 6.9 Cross-sections of specimens fabricated by (a) FSSW_D_750, (b) FSSW_D_AB_750, (c) FSSW_D_1200, and (d) FSSW_D_AB_1200 methods

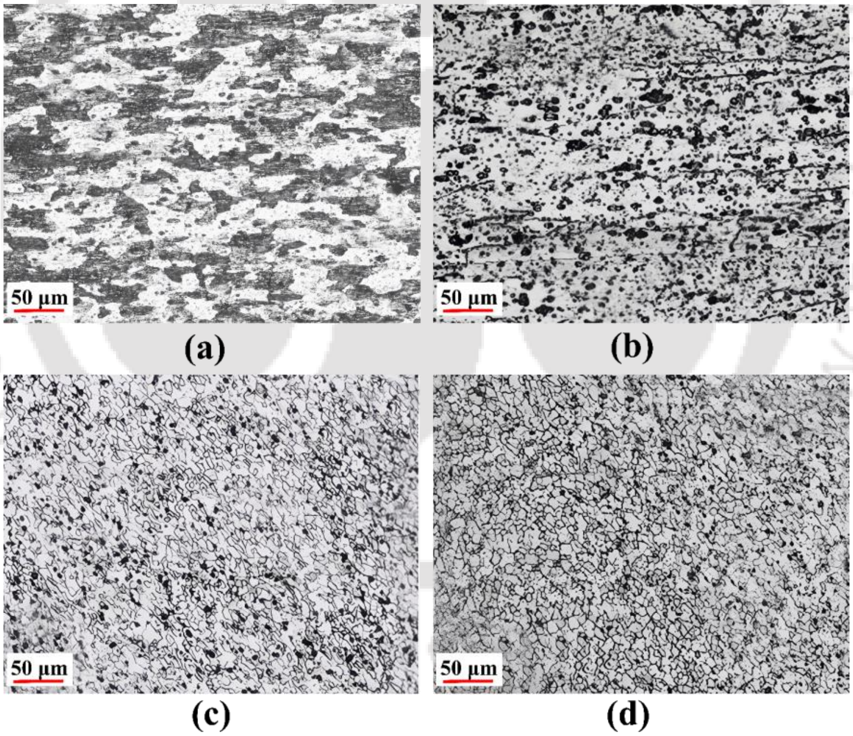

(a) (b) (c) (d)

Figure 6.10 Microstructure of base metal (a) face sheet and (b) disc insert. Microstructure at stir zone of FSSW_D_AB specimen at (c) 750 rpm and (d) 1200 rpm

Figure 6.10(a–d) shows the microstructures of the base metals and the stir zone of the sandwich sheets FSSW_D_AB at 750 and 1200 rpm. The microstructures in the stir zone of all FSSW_D_AB joints consist mainly of fine grains resulting from dynamic recrystallization while welding. Furthermore, It was observed that the increase in the rotational speed leads to 3.9 µm for 750 rpm and 4.8 µm for 1200 rpm grain sizes [33]. The development of coarse grains has been connected to increased frictional heat generated during welding, which promotes grain growth [112].

6.3.2 Experimental results

Figure 6.11(a) illustrates load evolution during lap shear tests of FSSW sandwich sheets produced at rotation speeds of 750 and 1200 rpm and AB sheets. Compared to joints with disc inserts (FSSW_D, FSSW_D_AB), AB samples are less efficient, showing the least joint strength. AB joints have lower displacement at fracture, followed by FSSW_D joints; however, FSSW_D_AB joints demonstrated greater ductility under lap shear load. The stiffness of the lap shear specimen presented in Figure 6.11(b) demonstrated that the stiffness of the FSSW_D and FSSW_D_AB lap shear samples with disc inserts is lower than that of the AB specimens. However, there is a slight improvement in the stiffness when rotational speed is increased in the cases of FSSW_D and FSSW_D_AB.

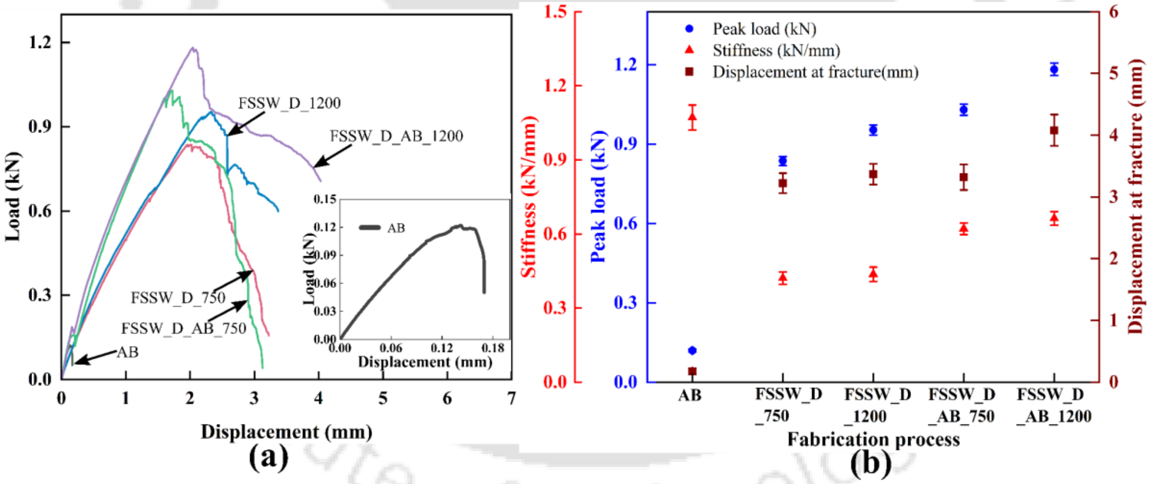

Figure 6.11 Sandwich samples tested in lap shear mode (a) load-displacement responses, (b) peak load and displacement at fracture

The FSSW_D_AB joints show a notable enhancement of about 14% and 15% in peak load with increase in rotational speed (Figure 6.11b). In particular, with respect to the AB joints, the peak loads for the FSSW_D_750, FSSW_D_AB_750, FSSW_D_1200, and FSSW_D_AB_1200 joints demonstrated substantial improvements of 592%, 752%, 689% and 878%, respectively.

Figure 6.12 demonstrates the enhancement in the quality of sandwich sheets produced at 750 and 1200 rpm compared to AB sheets. In addition to the improvements shown previously, the peak load-to-weight ratio also improved. Specifically, there is an improvement of about 542%, 638%, 632%, and 747% over the AB joints. These results show that the FSSW_D_AB technique is an efficient and suitable manufacturing process for honeycomb sandwiches. FSSW_D_AB has the potential to be used in general applications where reliability and performance are critical, solving basic problems with stress concentration and core damage.

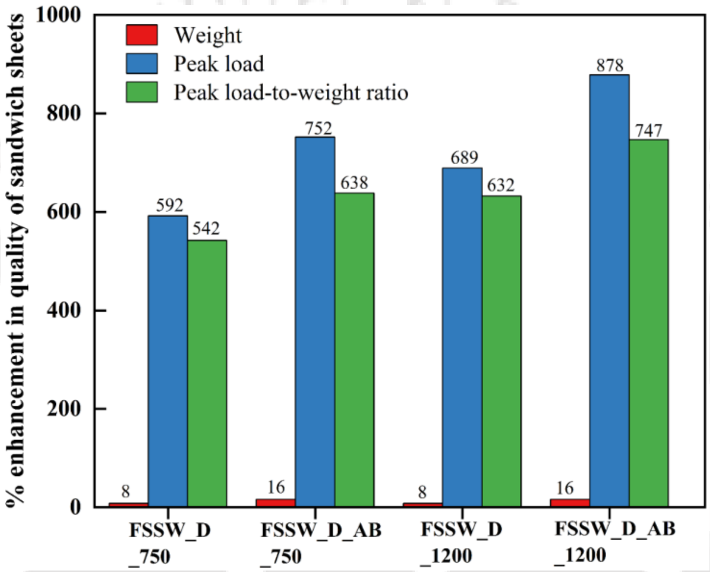

Figure 6.12 Enhancements in the quality of FSSW_D and hybrid-bonded FSSW_D_AB sandwich sheets compared to the AB sandwich sheets during lap shearing

The fractured surfaces that underwent shearing are illustrated in Figure 6.13. During these experiments, all joints were fractured on the front side of the weld between the upper sheet and the disc. This implies that back side welding may have contributed to further softening of the front side of the spot joint, resulting in a potentially stronger back side. The "nugget pull-out" was found in disc-inserted specimens (FSSW_D) at all rotational speeds used during joining. On the other hand, the FSSW_D_AB specimens made at different rotational speeds had a "nugget fracture", indicating robust joint formation in these cases, which aligns with peak load data in Figure 6.11. "Nugget fracture" denotes an alternative failure mechanism in which the nugget itself fractures, while "nugget pull-out" describes the procedure of extracting or removing the nugget from the surrounding material. These fracture patterns may indicate differences in the material's characteristics or the welding process.

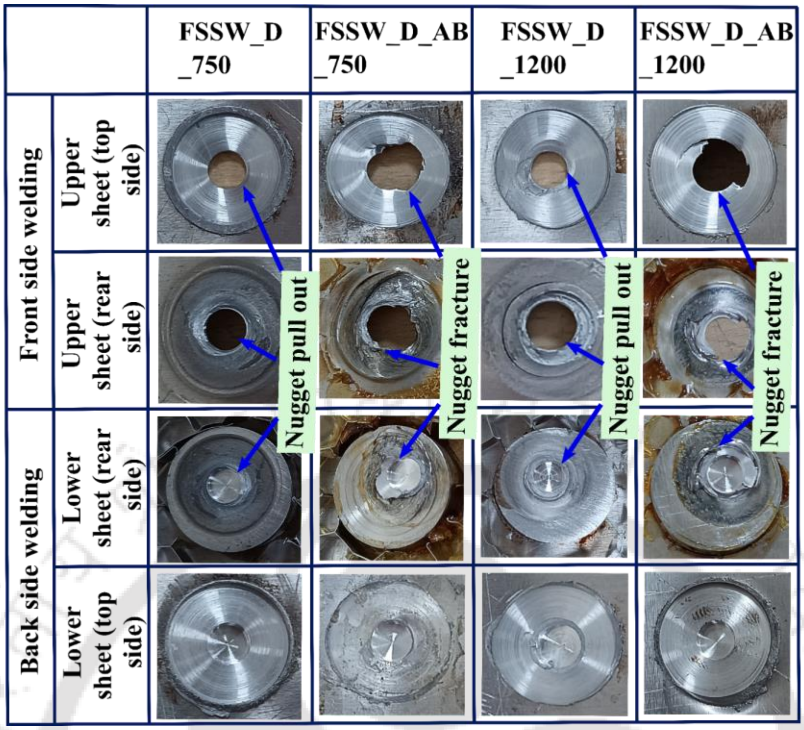

Figure 6.13 Fracture patterns in the lap shear test

The SEM pictures of the lap shear fracture specimens of FSSW_D_1200 and FSSW_D_AB_1200 are shown in Figure 6.14. Large and dense dimples in the sandwich sheets of the FSSW_D_AB_1200 specimen show an increase in joint ductility. The results shown in Figure 6.14(a) further confirm the ductility improvement. When the joint is subjected to the shearing process, these dimples provide evidence that the joint undergoes substantial deformation and absorbs a significant amount of energy. This kind of ductile behaviour is especially desired in structural applications.

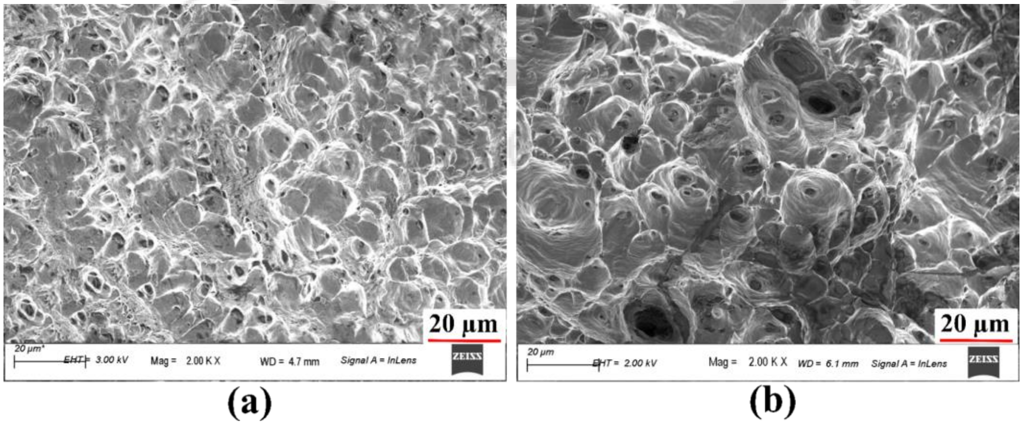

Figure 6.14 SEM images of fractured surface (a) FSSW_D_1200 and (b) FSSW_D_AB_1200

6.3.3 Numerical results

6.3.3.1 FE model of the lap shear test of FSSW sandwich structures

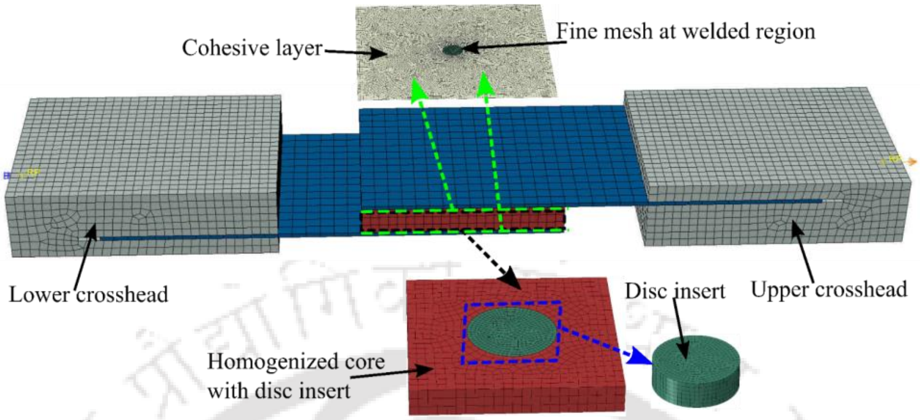

Figure 6.15 FE model of the FSSW joint used for lap shear test simulations

Using Abaqus® 2017 software, FE simulations were conducted on three different types of joints and compared with the experimental results. Since both disc inserts and spot welds were included in the models, a 3D analysis was needed. As a result, R3D4 elements were used to simulate rigid crossheads, while C3D8 elements were applied to mesh the disc insert, skin, and core. However, to simulate the progression of damage in the spot weld and adhesive layer, triangular CZM elements (COH3D8) were used. A viscosity value of 0.00001 was used to prevent convergence problems that may arise during simulation. Smaller elements were generated around the spot-welded region to obtain a precise solution. The cohesive layer was joined to the top, bottom, homogenized core, and disc by a "tie" constraint to ensure the connection between them. Figure 6.15 shows the FE simulation setup with boundary conditions that were used in the analysis.

6.3.3.2 Joint strength analysis

6.3.3.2.1 AB joints

Figure 6.16(a) shows the load developed during lap shear test simulations of AB sandwiches. The results show that numerical simulations agree well with experimental tests. Up to the peak load, the behaviour is linear. After that, it becomes non-linear as the fracture propagates across the adhesive layer, with the load gradually decreasing. Moreover, there is a strong correlation between the load-displacement curve of the homogenized core with the equivalent cohesive layer and the numerical and experimental data obtained from the real one. Accurate predictions with minimal variations in stiffness and peak load of the AB joints were also achieved when a homogenized core was used (Figure 6.16b). Additional benefits, such as a reduction in elements and computing time, were also achieved, as presented in the previous section. Therefore, the homogenized core with the equivalent cohesive layer can be adopted to model large-scale sandwich structures in real time applications.

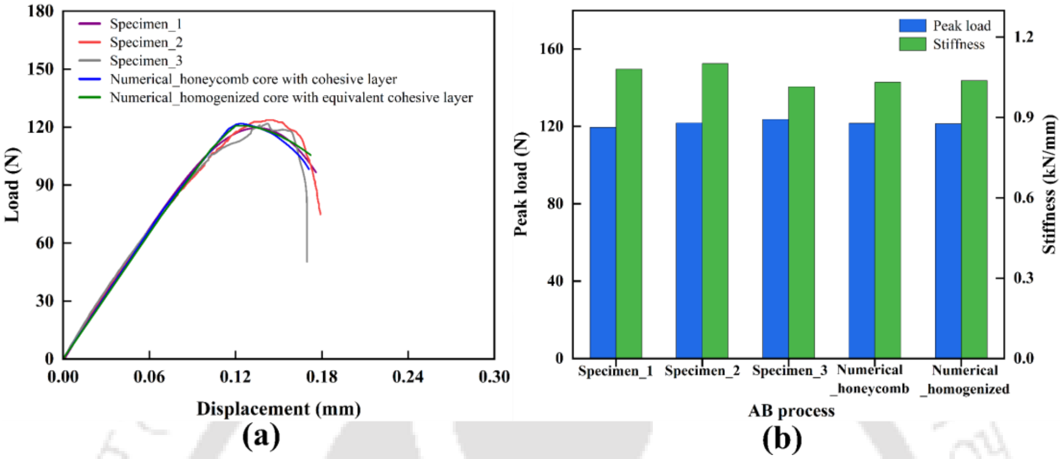

Figure 6.16 Validation of lap shear test responses of the AB sandwich (a) load developed, (b) peak load and stiffness

6.3.3.2.2 FSSW_D joints

Figure 6.17 presents the validation of lap shear test simulations of the FSSW_D joints for two rotational speeds. The cohesive zone data presented in Table 6.1 was used for the simulations. There is good agreement between the data from numerical simulations and experiments. Moreover, with the increase in the rotational speed, improvements in peak load is observed, which has been captured by simulations correctly.

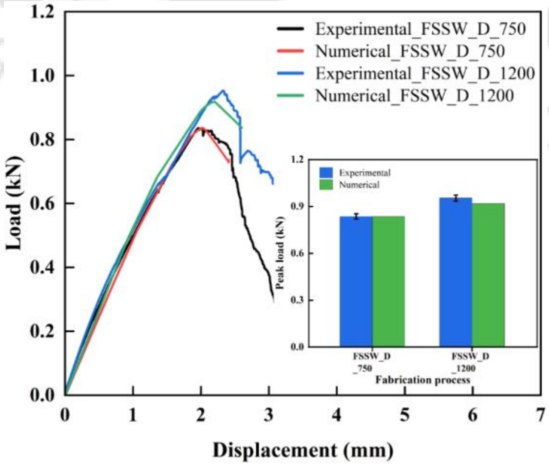

Figure 6.17 Lap shear test responses of sandwiches made by FSSW_D at 750 rpm and 1200 rpm

6.3.3.2.3 FSSW_D_AB joints

The FSSW_D_AB sandwich sheet lap shear test FE simulations were conducted using the cohesive zone parameters listed in Table 6.1 and Table 6.3. A reasonable agreement is observed in both rotational speeds (Figure 6.18a and b). In the FSSW_D_AB joints, the adhesive layer experienced the initial failure, resulting in a sudden downfall of load at points A and D. This behaviour suggests a decrease in joint stiffness, possibly compromising its structural integrity. Subsequently, the peak load was attained at points B and E. Subsequently, the weld nugget experienced gradual plasticization, allowing it to carry loads for a certain displacement before the final fracture, either at the interface between the weld nugget or in the surrounding bonded region (points C, F). Numerical models accurately predict the observed phenomena, such as peak load and discrete phases, with acceptable precision.

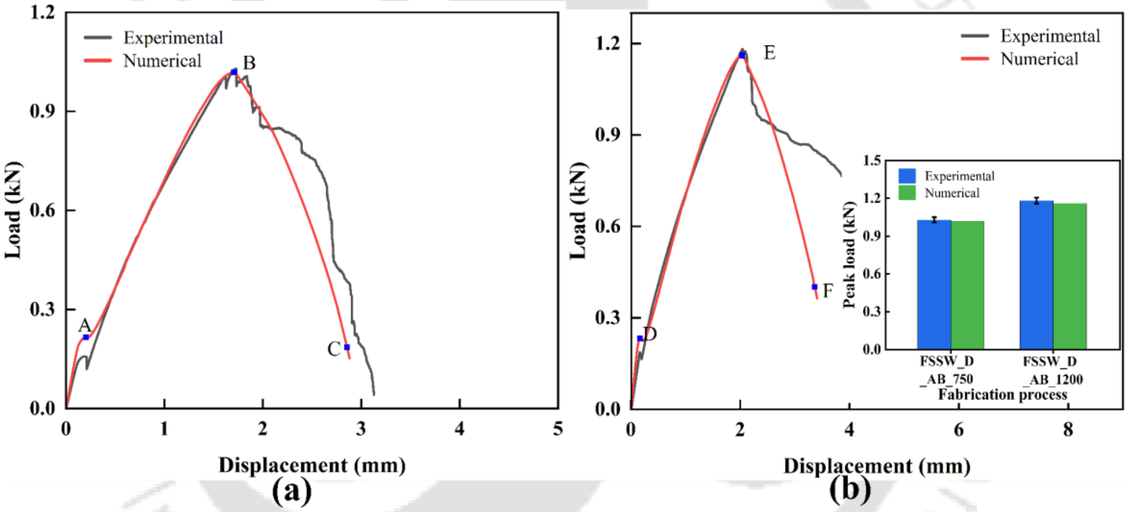

Figure 6.18 Validation of lap shear test responses of sandwich made by (a) FSSW_D_AB_750, (b) FSSW_D_AB_1200

The validation of peak load from lap shear test simulations of sandwich sheets fabricated by FSSW_D and FSSW_D_AB, as shown in Figure 6.17 and Figure 6.18 (insets), indicates a good correlation. The numerically predicted values are marginally lower by 0.1% for FSSW_D_750 and 3.6% for FSSW_D_1200 compared to the experimental data. Predictions in the case of FSSW_D_AB joints are also encouraging - 1.05% lower for FSSW_D_AB_750 specimens and 1.75% lower for the FSSW_D_AB_1200 specimens. Therefore, it can be said that CZM-based numerical predictions are suitable for modelling and predicting joint strengths of sandwich structures. It is important to note that while other authors have investigated FE and

CZM modelling of AB joints, the application of this work to the development of FSSW joints, particularly for the fabrication of sandwich sheets, provides a novel contribution.

6.3.3.3 Stress analysis

The normal and shear stress distribution are predicted in the overlap area of the joints at the middle of the cohesive layer at the peak load (Figure 6.19). Figure 6.20 shows the distribution of Von Mises stress within the AB joint at peak load, while Figure 6.21 shows the normal and shear stress distributions along the overlap length on the upper interface. These distributions are depicted at the interfaces of skin and core. The joint rotation makes the adherends on the overlap area separated and compressed, resulting in the observed profiles of normal stress [68,82]. Remarkably, normal stresses are hardly non-existent in the inner overlap zone and some have compressive normal stress. However, shear stress distributions demonstrate an approximately concave downward shape, peaking at about 15 mm overlap length.

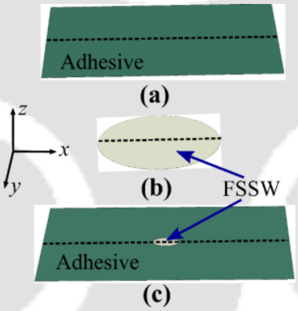

Figure 6.19 Stress distribution analysis along the middle of (a) the adhesive layer, (b) the FSSW_D joint, (c) the FSSW_D_AB joint

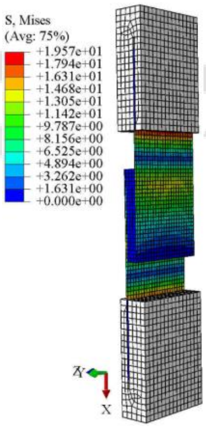

Figure 6.20 Von Mises stress in AB joint

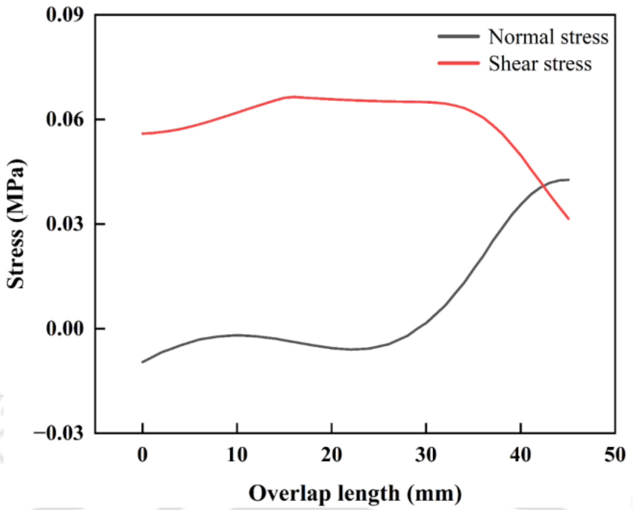

Figure 6.21 Normal and shear stress distributions of AB joint

Figure 6.22 shows the Von Mises stresses for the sandwich sheets made of FSSW_D joints. It shows the substantial joint rotation caused by the mode-mixity, and the maximum stresses were detected near the boundary of the weld nugget (Figure 6.23), which experiences plasticity as a result of the sudden change in geometry [113,114]. It can be seen in Figure 6.23 that shear is the dominant mode of load transmission between the joints, with peak shear stresses evenly distributed at the perimeter of the weld nugget as a result of the sharp geometric change between layers. Figure 6.23 illustrates that both the normal and shear stresses on the weld nugget increased with rotational speeds.

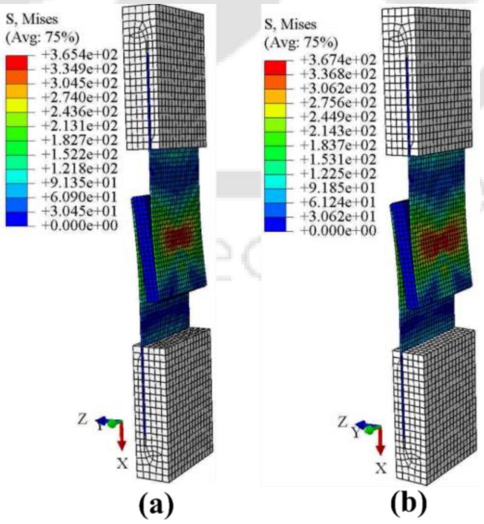

Figure 6.22 Von Mises stress in (a) FSSW_D_750, (b) FSSW_D_1200 joint

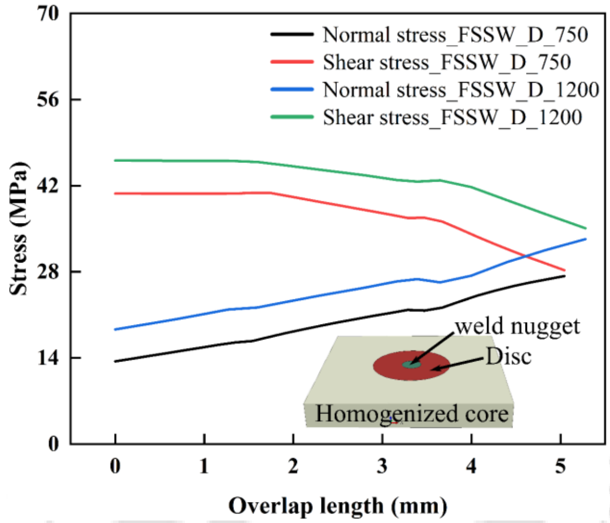

Figure 6.23 Normal and shear stress distributions in FSSW_D joints at the weld nugget

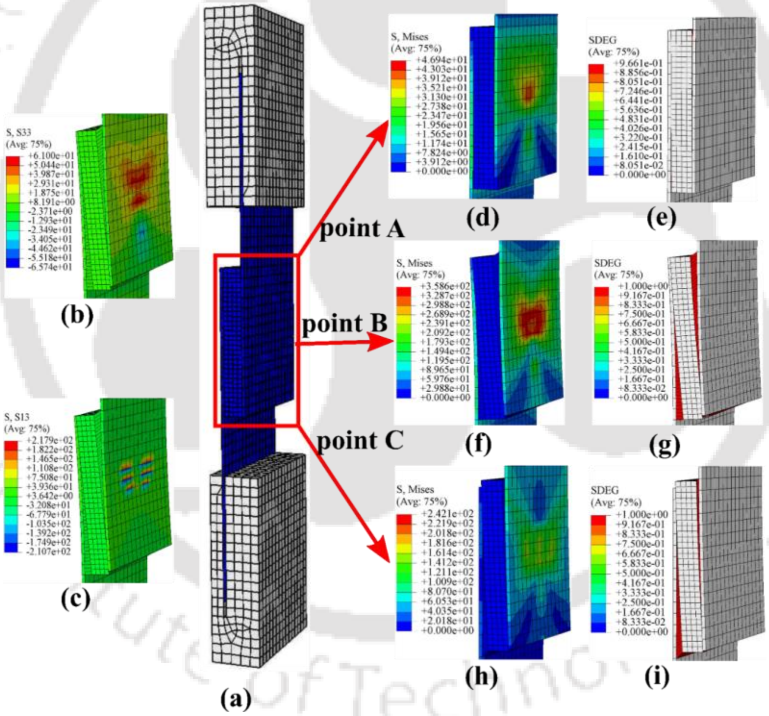

Figure 6.24 Simulation results of the FSSW_D_AB_750 lap shear test (a) lap shear model, (b) normal stress, and (c) shear stress at peak load. Joint interface stress (d) first curve drop (point A), (e) at the maximum load (point B), (f) final stage (point C) of the lap shear test. Joint interface damage (g) first curve drop (point A), (h) at the maximum load (point B), (i) final stage (point C) of the lap shear test (points A, B, C are referred with respect to Figure 6.18a)

The numerical results of the lap shear test of FSSW_D_AB specimens produced at 750 rpm and 1200 rpm are shown in Figure 6.24 to Figure 6.26. Since the fracture patterns in both cases are similar, the following discussion is focused only on the FSSW_AB_D_750 case. The model of the lap shear specimen within the sandwich sheet is shown in Figure 6.24(a). Furthermore, Figure 6.24(b, c) shows the distributions of normal and shear stresses throughout the interface to assess the relative importance of mode II (in-plane shear) loading compared to mode I (opening) loading.

The distribution of Von Mises stress on the joint surfaces at three different stages (points A, B, and C in Figure 6.18a) is shown in Figure 6.24(d, f, h). Additionally, damage within the joint region is shown in Figure 6.24(e, g, i) at the A, B, and C points. An entirely intact interface is represented by a Von Mises stress of zero, whereas total interface damage is represented by a value of one, shown in blue.

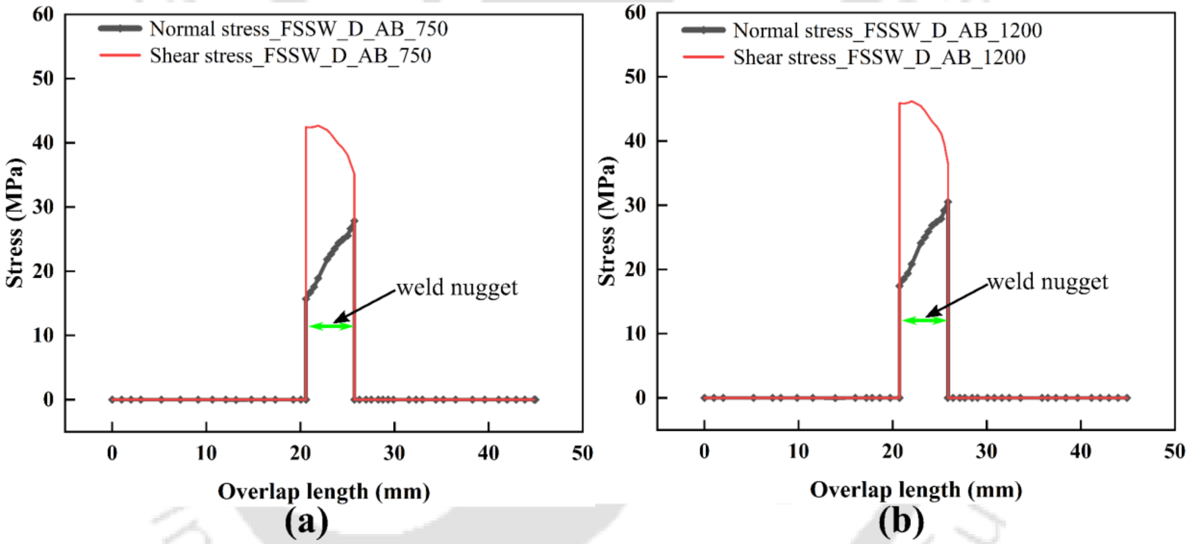

Figure 6.25 Normal and shear stress distributions in (a) FSSW_D_AB_750, (b) FSSW_D_AB_1200 joint

The weld nugget in the FSSW_D_AB joints supports all normal stresses, whereas compressive normal stresses in the surrounding bonded areas strengthen the resistance of the adhesive layer. Peeling often leads to early failures of the adhesive layer. As shown in Figure 6.25, failure around the weld location results in zero normal and shear stresses. The shear stresses in the FSSW_D_AB joint (Figure 6.25) differ significantly from the AB joint (Figure 6.21) and are mainly influenced by the weld nugget. The weld nugget enhances load transmission within the typically weak inner overlap area and withstands higher shear stresses than the adhesive due to stiffness differences [82,113]. Stress peaks occur near the nugget perimeter in hybrid joints (Figure 6.25), similar to welded joints (Figure 6.23). A similar pattern is also seen in the FSSW_D_AB_1200 joints. Additionally, Figure 6.25 shows that normal and shear stresses increased with rotational speeds.

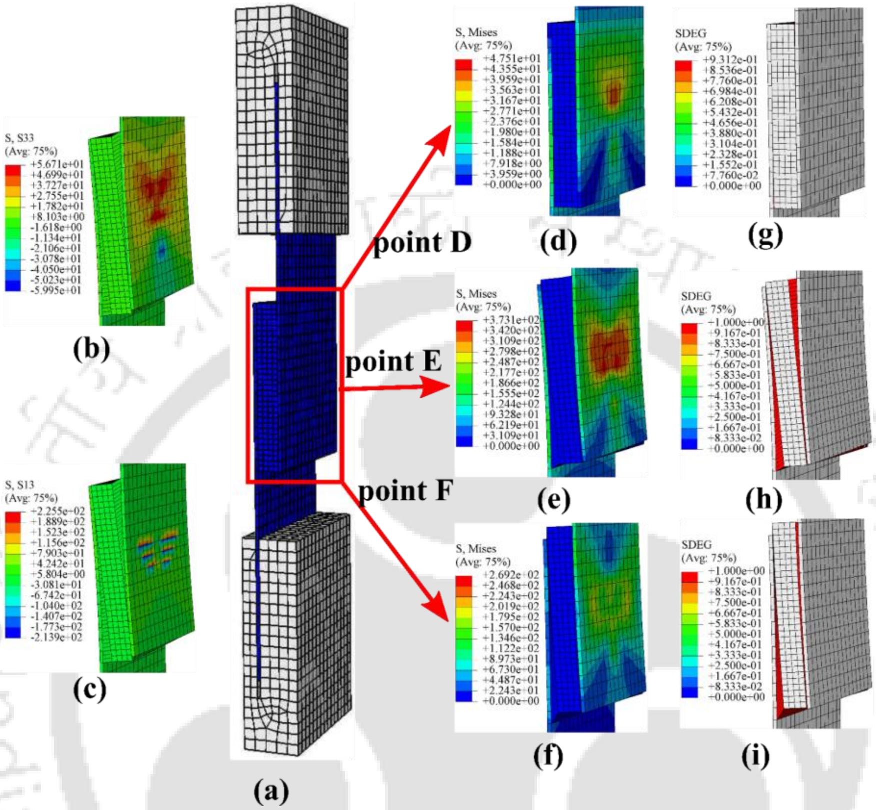

Figure 6.26 Simulation results of the FSSW_D_AB_1200 lap shear test (a) lap shear model, (b) normal stress, and (c) shear stress at peak load. Joint interface stress (d) first curve drop (point D), (e) at the maximum load (point E), (f) final stage (point F) of the lap shear test. Joint interface damage (g) first curve drop (point D), (h) at the maximum load (point E), (i) final stage (point F) of the lap shear test (points D, E, F are referred with respect to Figure 6.18b)

Based on the analysis, it is possible to create a model of large-scale sandwich structures using homogenized cores and corresponding cohesive layers. This approach can help simplifying the computational modelling of complicated structures. Further, stress analysis aids in efficient joint design and appropriate selection of process parameters. Strengthening these joints improves the structural integrity, thereby enabling the sandwich structures to be tailor-made for their intended applications.

6.4 Summary

The study aimed to find potential substitutes for AB sandwich sheets by fabricating them using FSSW. Lap shear performance comparisons were conducted between AB, FSSW_D (disc insert only), and FSSW_D_AB (disc insert and adhesive) through experiments and FE simulations using CZM, with a homogenized core and the equivalent cohesive layer to reduce computational time.

FSSW_D and FSSW_D_AB sandwich sheets showed significant improvements in lap shear peak load (592% to 878%) and peak load-to-weight ratio (542% to 747%) compared to AB sheets, with FSSW_D_AB joints exhibiting a 24% higher lap shear peak load than FSSW_D joints due to adhesive bonding. Stiffness measurements were approximately 0.43 kN/mm for welded joints and 0.63 kN/mm for hybrid joints. Different fracture modes were observed: "nugget pull out" in FSSW_D and "nugget fracture" in FSSW_D_AB sandwiches, indicating more robust joints in the latter. SEM analysis showed dense and large dimples in FSSW_D_1200 and FSSW_D_AB_1200 sheets, indicating improved joint ductility.

Predicted and experimental peak load values for FSSW_D joints were closely aligned, with deviations of 0.1% and 3.6% below experimental data at 750 rpm and 1200 rpm, respectively. Hybrid joint predictions showed slight underestimates (1.05% and 1.75% for FSSW_D_AB_750 and FSSW_D_AB_1200). AB sandwiches had strong agreement between experimental and numerical data, demonstrating that using a homogenized core in simulations efficiently maintained accuracy. FEM stress analysis showed significant adherend rotations, separation at overlap edges, and stress concentrations along the weld nugget perimeter in FSSW_D joints. Shear stresses peaked in specific areas, while normal stresses were highest at the edges of AB joints, while FSSW_D_AB joints had improved shear stress transfer in the inner overlap area due to weld nugget, enhancing performance.

Chapter 7 Peel test performance analysis of honeycomb core sandwich panels fabricated using FSSW strategies

---

7.1 Experimental process

This section describes the methods for conducting FSSW trials, preparing sandwich samples, and performing peel testing. The mechanical properties of skin sheet and honeycomb core are already discussed in Section 3.1.1 in Chapter 3, whereas the mechanical properties of disc insert are discussed in Section 4.1.1 in Chapter 4. All the material properties of sandwich sheets are presented in Table 5.1 of Chapter 5.

7.1.1 Sandwich fabrication methods

The three different joining strategies for fabricating sandwich structures with honeycomb core for the peel test are described here.

7.1.1.1 AB

The joining strategies using AB is already explained in Section 5.1.2.1 of Chapter 5. The fabrication processes of peel specimens are shown in Figure 7.1.

7.1.1.2 FSSW_D

The joining process is the same as discussed in Section 5.1.2.4 of Chapter 5. The welding parameters were as follows: 750 rpm rotating speed, 2 mm/min tool plunge speed, and a dwell duration of 5 s. Plunge depths of 1.8 mm were used on both sides of welding (front side and back side) for the FSSW_D_1.8 specimen. Similarly, plunge depths of 2 mm were used on both sides of welding (front side and back side) for the FSSW_D_2 specimens. A fabricated peel specimen is shown in Figure 7.2.

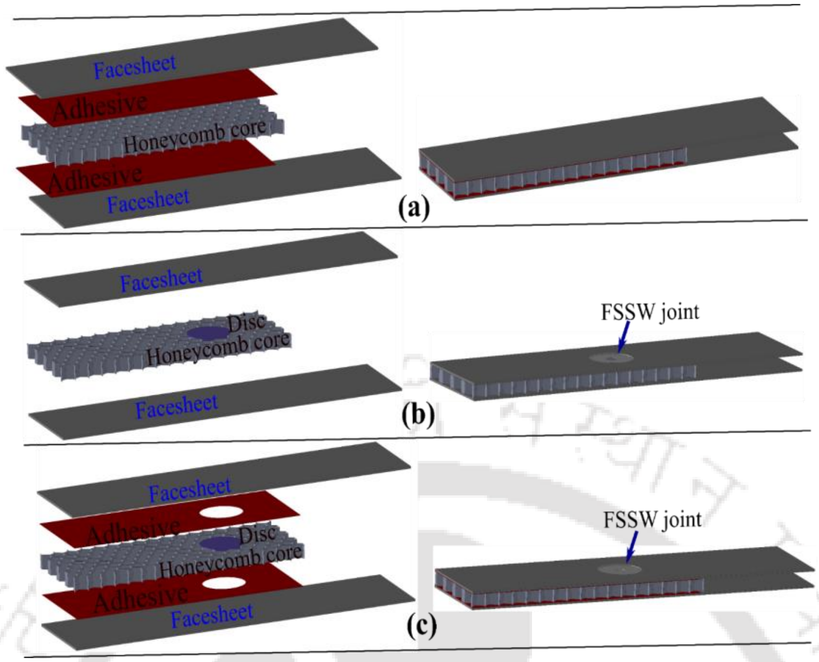

Figure 7.1 Fabrication of sandwich peel specimens by (a) AB (b) FSSW_D (c) FSSW_D_AB

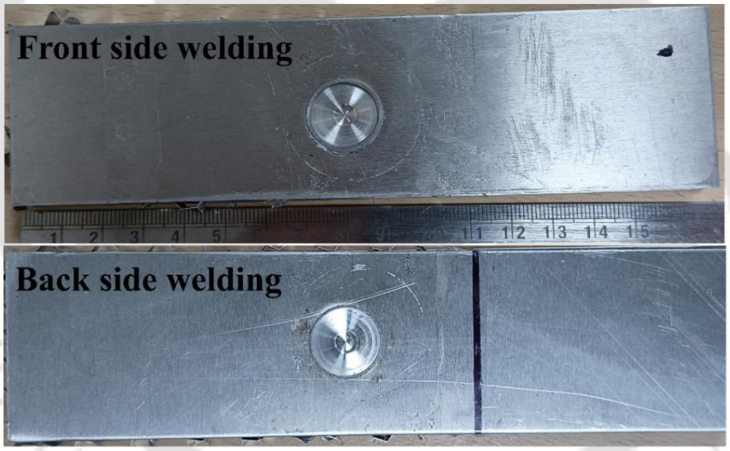

Figure 7.2 Fabricated peel specimen by FSSW_D process

7.1.1.3 FSSW_D_AB

The joining process is the same as discussed in Section 5.1.2.5 of Chapter 5.

7.1.2 Sample preparation

Two types of samples of sandwich sheets, including samples for peel test and macro-crossectional examinations, were prepared. The dimensions of peel specimens are already shown in Figure 3.5(a) of Chapter 3.

7.2 FE modelling

Numerical analysis was carried out in Abaqus® software employing CZM with the honeycomb core featuring a cohesive layer, the homogenized core and equivalent cohesive layer.

7.2.1 CZM

CZM was employed to characterize the bonding at the interfaces between the core and skin, as well as between the skin and disc insert. CZM process is already discussed in Section 6.2.1 of Chapter 6. The crack propagation phenomenon in peel specimen is shown in Figure 7.3.

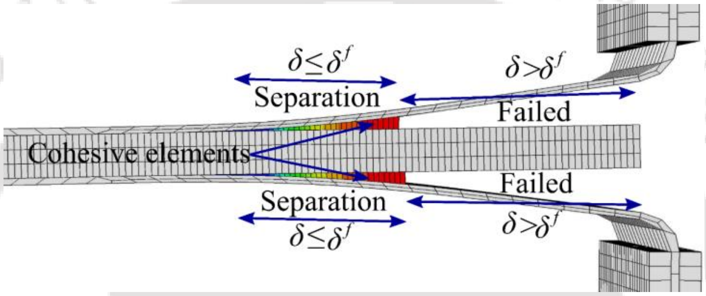

Figure 7.3 Crack propagation in peel sandwich specimen

7.2.2 Homogenized honeycomb core and equivalent cohesive layer

The homogenization process of honeycomb core is already discussed theoretically and numerically in Sections 2.1 and 2.2.1 of Chapter 2. The equivalent cohesive layer is derived and discussed in Section 6.2.2.2 of Chapter 6.

In this work, only a flatwise tensile test was conducted to obtain the interfacial normal strength of the equivalent cohesive layer. The flatwise tensile test primarily focused on evaluating the interfacial strength of a material since it subjected the interface area to a uniform normal load. To achieve the most uniform stress distribution across this interface, the flatwise tensile test specimen was designed to maximize the area of the specimen compared to the area of the interface. Therefore, the value obtained from a flatwise tensile test for interfacial strength can also be expressed as the maximum cohesive strength, as it represents the maximum resistance of the material to separation along the interface when subjected to this specific test configuration [70].

Flatwise tensile (cross tension) test simulations were performed on sandwich structures featuring a 52 mm × 55 mm cross-sectional aluminium plate with a honeycomb core. These sandwich structures were composed of two core configurations: a honeycomb core combined with a cohesive layer and a homogenized core featuring an equivalent cohesive layer. The material properties of the honeycomb core and face sheet are taken from Table 5.1 of Chapter 5, and the orthotropic properties of the homogenized honeycomb core are taken from Table 6.2 of Chapter 6. The CZM parameters for the adhesive used with honeycomb core were taken from Bai *et al.* [115], and presented in Table 7.1. The equivalent cohesive parameters used for the homogenized core are also presented in Table 7.1.

Table 7.1 Cohesive parameters used with honeycomb core and homogenized core

Property	Adhesive (cohesive layer) [115]	Adhesive (equivalent cohesive layer)
Cohesive stiffness (MPa/mm)	22	0.730
Critical stress (MPa)	2.26	0.075
Fracture toughness (N/mm)	0.73	0.026

The boundary conditions, the deformed and undeformed shape of the simulated sandwich specimen with honeycomb core and cohesive layer, and their equivalent forms are shown in Figure 7.4. Mesh convergence analysis for flatwise tensile test of sandwiches having honeycomb core with cohesive layer and homogenized core with equivalent cohesive layer are shown in Figure 7.5(a) and (b), respectively. The sandwich sheet with honeycomb core and cohesive layer converged at 63436 elements, whereas the homogenized core with equivalent cohesive layer at 12666 elements. As shown in Figure 7.5(c), the load-displacement behaviour of both the honeycomb core and the homogenized core was remarkably similar until reaching the maximum load. This observation strongly indicates that the simulation results for these two distinct core configurations displayed comparable mechanical responses during the flatwise tensile test. Additionally, it is worth noting that the CPU time required for simulating the flatwise tensile test with the homogenized core was 107 s, considerably reduced compared to the honeycomb core, which was 1229 s. This suggests that using the homogenized core with the equivalent cohesive layer in simulations offers the advantage of faster computational efficiency while maintaining similar mechanical performance characteristics.

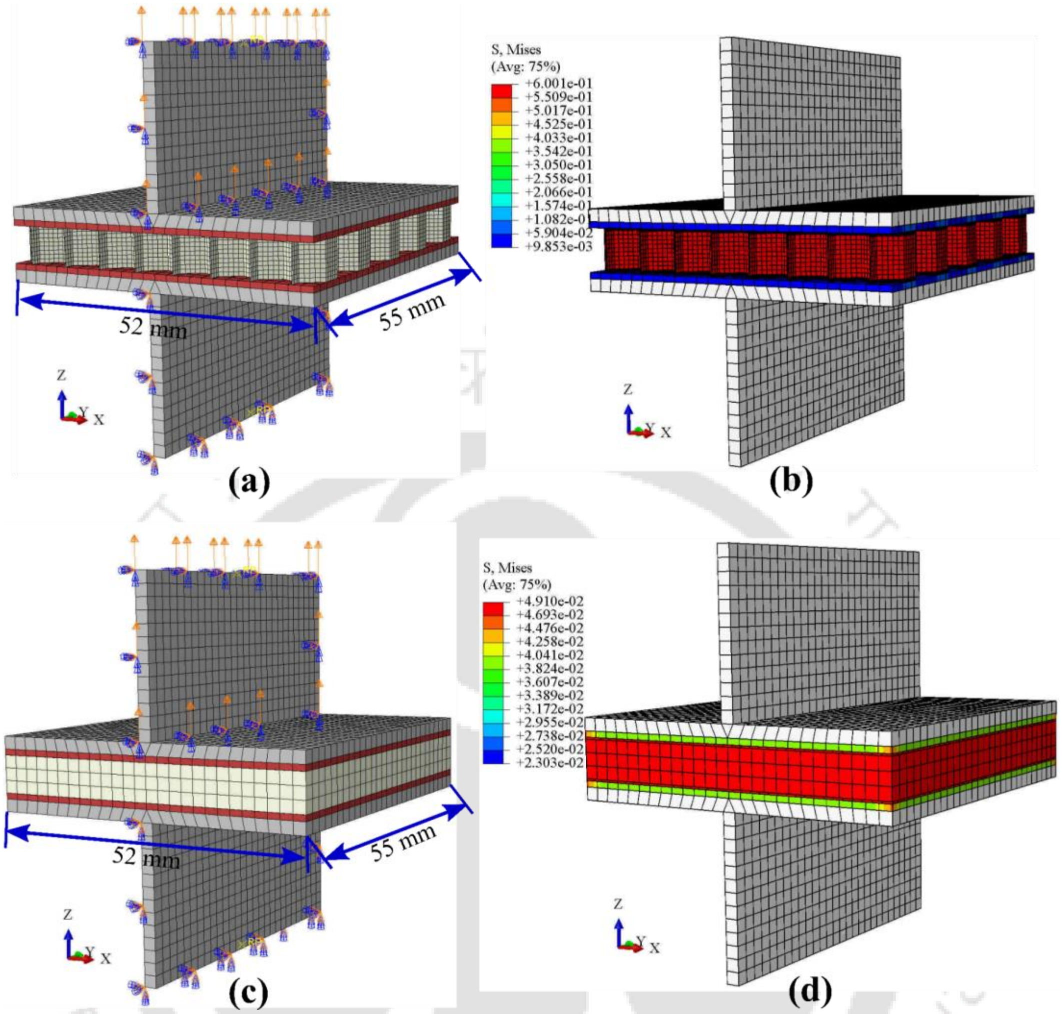

Figure 7.4 Flatwise tensile test simulation of honeycomb core sandwich with cohesive layer (a) undeformed, (b) deformed. Homogenized honeycomb core with equivalent cohesive layer (a) undeformed (b) deformed

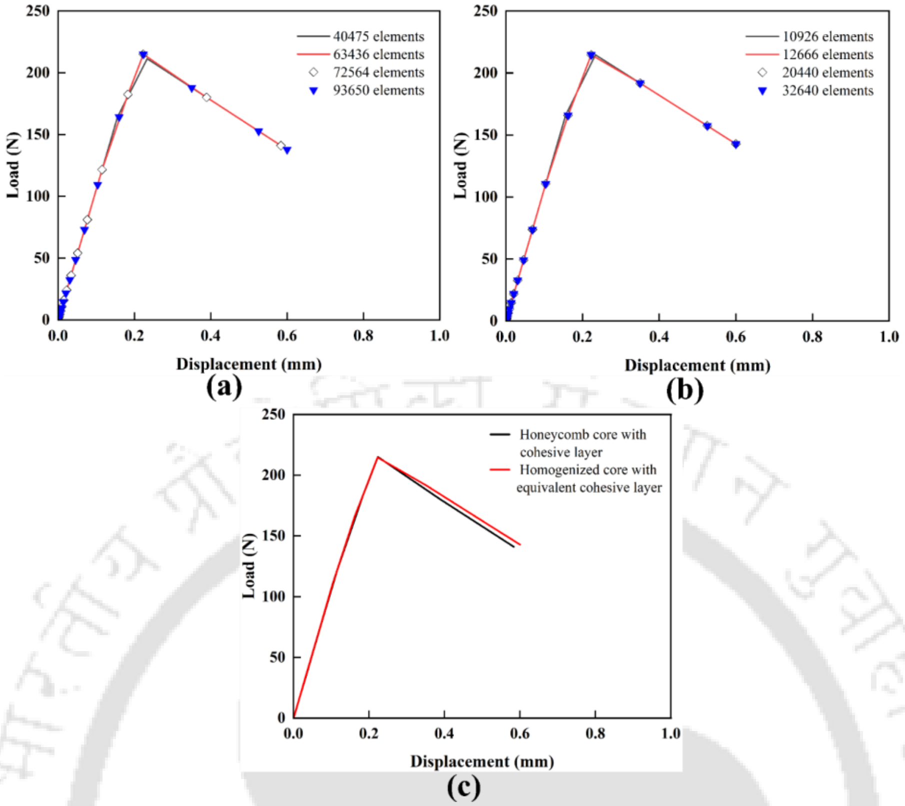

Figure 7.5 Mesh convergence analysis for flatwise tensile test of sandwiches having (a) honeycomb core with cohesive layer, (b) homogenized core with equivalent cohesive layer, (c) comparison of load evolution from both the modelling strategies

7.3 Results and discussion

This section discusses the results from peel test experiments on the joints made by AB, FSSW_D, and FSSW_D_AB. Subsequently, the fracture surfaces of the hybrid bonded specimens were compared. Later, results from numerical simulations are validated and discussed.

7.3.1 Macro cross-section

Figure 7.6(a-e) depicts cross-sectional views of sandwich sheets fabricated using different methods. In Figure 7.6(a), the bond between the skin and the core remains intact during AB. Conversely, in the case of the FSSW_D and FSSW_D_AB specimens (Figure 7.6(b-e)), a metallurgical bond forms between the sheet and the disc. The tool plunge depth affects the circumferential expansion of the top sheet beyond the perimeter of the welding tool. However, the axial load applied by the welding tool restricts the free flow of the top sheet, causing it to bend beyond the contour of the tool. As the tool plunge depth increases, this effect becomes more pronounced, as evident in Figure 7.6(b), (d), and Figure 7.6(c), (e).

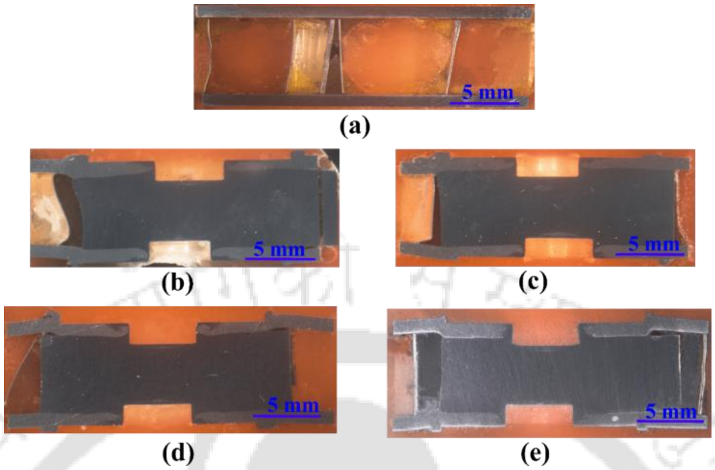

Figure 7.6 Macro cross-sectional views of (a) AB, (b) FSSW_D_1.8, (c) FSSW_D_AB_1.8, (d) FSSW_D_2, and (e) FSSW_D_AB_2 specimens

7.3.2 Peel test experimental results

The load evolution during peel tests of various spot joined samples, including those made at two different plunge depths, such as 1.8 mm and 2 mm, are presented in Figure 7.7(a). When compared to FSSW_D joints, AB samples are weaker, exhibiting the lowest joint strength out of all the cases. Additionally, the hybrid joints, FSSW_D_AB, demonstrate a noticeable increase in the peak load across all plunge depths, and joints show significant improvement in peak load when the plunge depth is increased. This is evident from peak load data in Figure 7.7(b). Specifically, the peak load for FSSW_D_1.8, FSSW_D_AB_1.8, FSSW_D_2, and FSSW_D_AB_2 joints exhibited significant improvement of 254%, 307%, 306%, and 399%, respectively, compared to the AB joints. By increasing the plunge depth from 1.8 mm to 2 mm, there is about 15% and 23% improvement in peak load in the cases of FSSW_D joints and FSSW_D_AB (hybrid) joints. It is also seen in the peel test experiment done on sandwich sheets by Rana *et al.* [116] at different plunge depths that the peak load increases with increase in plunge depth. It can be said that a substantial enhancement in the peak load-carrying capacity of hybrid joints is observed when compared to the original ones.

The significant changes observed in joint strength in FSSW_D_AB specimens are a result of the synergistic combination of FSSW methods with disc insert and adhesive bonding, which together enhance material properties, improve load transfer mechanisms, and optimize joint design parameters, leading to substantial improvements in joint performance compared to traditional adhesive-bonded structures.

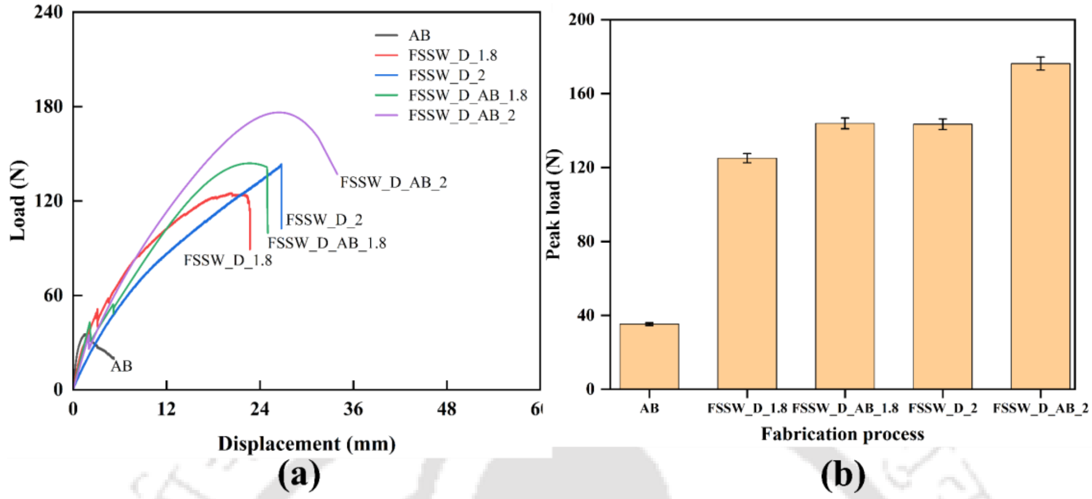

(a) (b)

Figure 7.7 Peel test responses from experiments depicting (a) load-displacement data, (b) peak load variations

The relation between the peak load and the displacement leading to failure was found to be directly proportional. Pathak *et al.* [106] suggested that higher displacements enable joints to absorb more energy before failure, which is generally considered as a better outcome. This implies that FSSW_D_AB required the highest energy to completely separate the weld, indicating its potential for stronger bonding.

In the hybrid joints made by FSSW_D_AB, the load-displacement curves demonstrated a phenomenon of stiffening before reaching the maximum load during joint deformation. Initially, significant bending occurred across the loading locations and the welding nugget. However, at some time, the weld nugget aligned nearly precisely with the load being applied, resulting in an overall stiffer joint than the FSSW_D joint.

The fractured surfaces of sandwich sheets that were subjected to peeling are shown in Figure 7.8. During these tests, all the joints fractured between the upper sheet and the disc in the front side of the spot weld. This indicates a stronger back side which could be due to the additional softening of the front side of the spot joint during back side welding. The predominant mode of fracture observed is "nugget pullout," which remained consistent across different plunge depths employed in the fabrication. However, “nugget fracture” was also found in the FSSW_D_AB specimen made at 2 mm plunge depth, showing robust joint formation in this case.

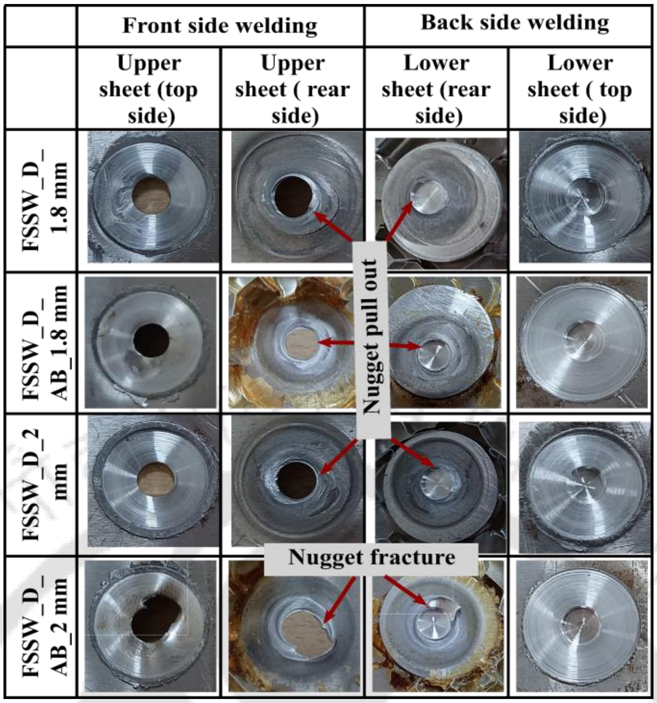

Figure 7.8 Fracture modes in peel test

7.3.3 Peel test numerical results

7.3.3.1 Peel test simulations

FE simulations were conducted using Abaqus® 2017 software, with key objectives such as validating the simulation results using CZM with lab scale experiments, providing designers with a precise modelling tool, and conducting a comprehensive modeling exercise of peel tests of the three spot joints. The need for a 3D analysis resulted from the incorporation of features like the FSSW and disc inserts in the models. C3D8R elements were used to mesh the face sheet, disc insert, and homogenized core in constructing the FE models, and R3D4 elements were used to model rigid loading part. However, triangular CZM elements, COH3D8, were employed to model damage growth in the adhesive layer and spot-weld. A specific mesh control technique called the sweep method played a crucial role in achieving a cohesive layer. To prevent convergence issues during the simulation, a viscosity value of 0.00001 was assigned. Additionally, mesh seeds were used to generate significant number of seeds in the fracture initiation area, with a focus on mesh refinement in regions where precise results were needed. Smaller seeds were concentrated around the spot-welded region to achieve an accurate solution. The cohesive layer was attached to both the upper and lower sheets, and the disc and homogenized core using a "tie" constraint. This constraint ensured that these distinct bodies remained connected, allowing their contact surfaces to undergo identical motion and deformation throughout the simulation. The applied boundary conditions for this analysis can be seen in Figure 7.9.

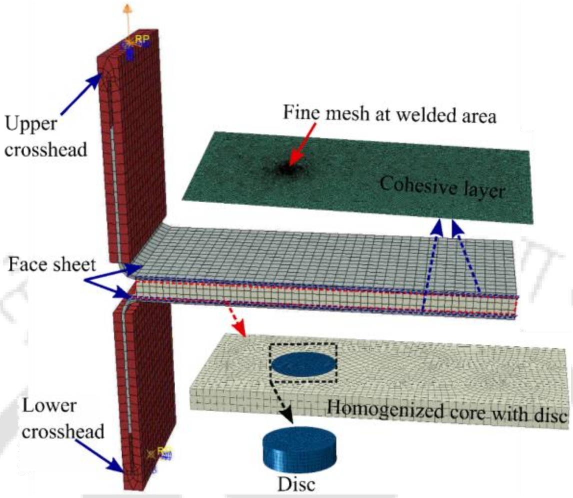

Figure 7.9 FE model of peel test

Several trial simulations were run to determine the appropriate element size for the model.

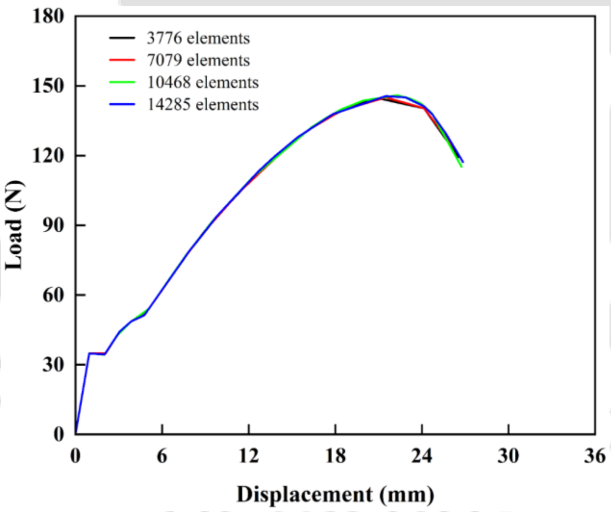

Figure 7.10 Mesh sensitivity analysis during peel test simulations

These simulations specifically focused on changing the element size within the cohesive layer, as deformation in the face sheets and core materials were negligible. The cohesive layer was divided into four sets of elements with varying mesh sizes at both the adhesive and welded regions. During peel test simulations, the load-displacement behavior was monitored and compared for different densities of elements, as illustrated in Figure 7.10. It was observed that modifying the element size had no impact on the outcomes of the peel test.

7.3.3.2 Sandwich sheets with AB

Figure 7.11(a) illustrates the load evolution curves observed during the peel test simulations of AB joints consisting of honeycomb core and skin sheets with adhesive. The data indicate a good agreement between experimental results and numerical simulations, which serve as a representative model for all types of joints. Initially, the behaviour follows a linear pattern and then non-linear until it reaches its maximum load. Subsequently, the load gradually decreases as the crack progresses through the adhesive layer. Furthermore, the load-displacement curve corresponding to the homogenized core, featuring an equivalent cohesive layer, exhibits a good correlation with both experimental and numerical results obtained from the actual honeycomb core with a cohesive layer. The use of the homogenized honeycomb core and equivalent cohesive layer instead of the actual honeycomb core and cohesive layer provides a significant advantage in terms of reducing both the total number of elements and the computational time required to conduct peel tests. This substitution strategy improves computational simulations, modelling, and analyses by simplifying structural representations while retaining the essential properties of the materials involved.

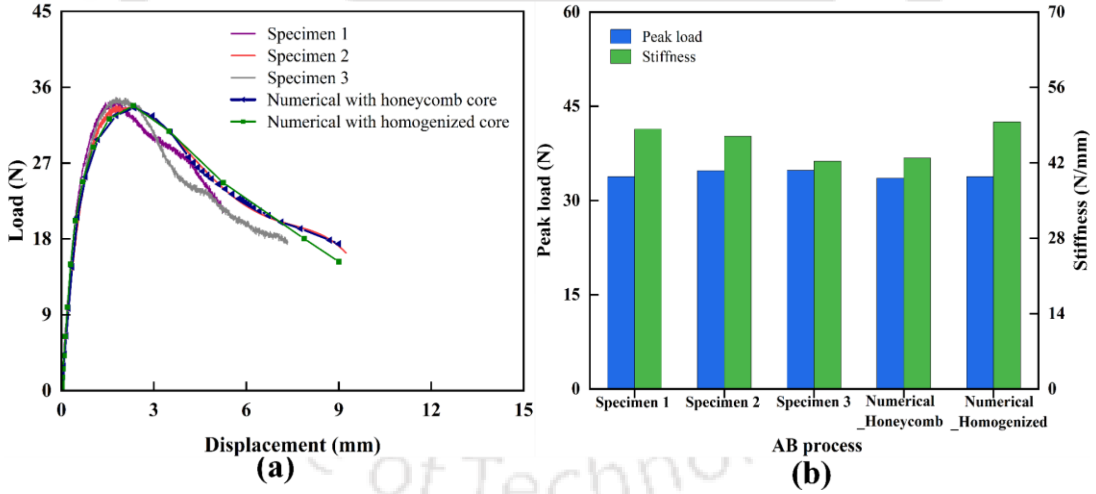

Figure 7.11 Comparison of (a) experimental and numerical load-displacement behaviour of the peel test of the AB sandwich sheets, (b) experimental and numerical peak load and stiffness values

Figure 7.11(b) compares the peak load and stiffness obtained from peel test experiments and numerical simulations for the AB sandwich sheets. There is not much variation in peak load and stiffness values for all the specimens. The properties of the equivalent cohesive layer used with the homogenized core were derived from the cohesive layer properties associated with the honeycomb core which is represented in Table 7.1.

7.3.3.3 Sandwich sheet made by FSSW_D

The experimental results presented in Figure 7.7 illustrate that the average peak load recorded for FSSW spot welded specimens at 1.8 mm plunge depth is 125.04 N. A CZM with a triangular traction-separation law was employed to model the peel test accurately, using a cohesive strength of 11.5 MPa. The cohesive strength of 11.5 MPa was determined through various trial simulations and matched by comparing it with experimental load-displacement curves, as shown in the flow chart in Figure 7.12 [71,117,118].

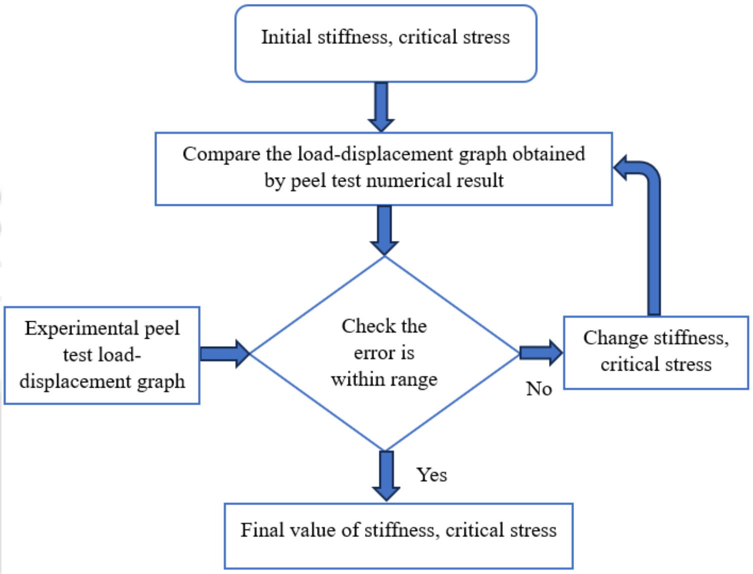

Figure 7.12 Flow chart for optimization of cohesive stiffness and critical stress

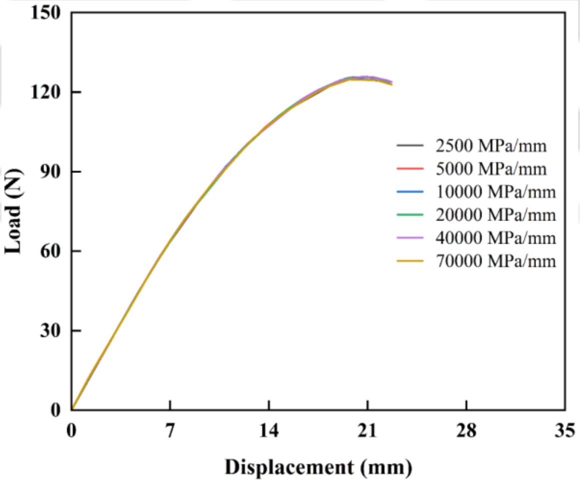

Figure 7.13 Load evolution data obtained from peel test simulations with various cohesive stiffness values

In examining the impact of initial cohesive stiffness, multiple simulations were conducted with consistent fracture toughness values of 80 N/mm but varying stiffness [70]. Interestingly, the load evolution remained relatively unaffected by changes in initial cohesive stiffness (Figure 7.13).

Subsequently, the fracture toughness was plotted within a range of 20 N/mm to 100 N/mm, keeping the initial cohesive stiffness of 2500 MPa/mm. Figure 7.14(a), showcasing the load evolution at various fracture toughness, illustrates significant fluctuations in peak load with changes in fracture toughness. A third-order curve was fit (Figure 7.14b) between peak load and fracture toughness in order to interpolate fracture toughness values for any given peak load.

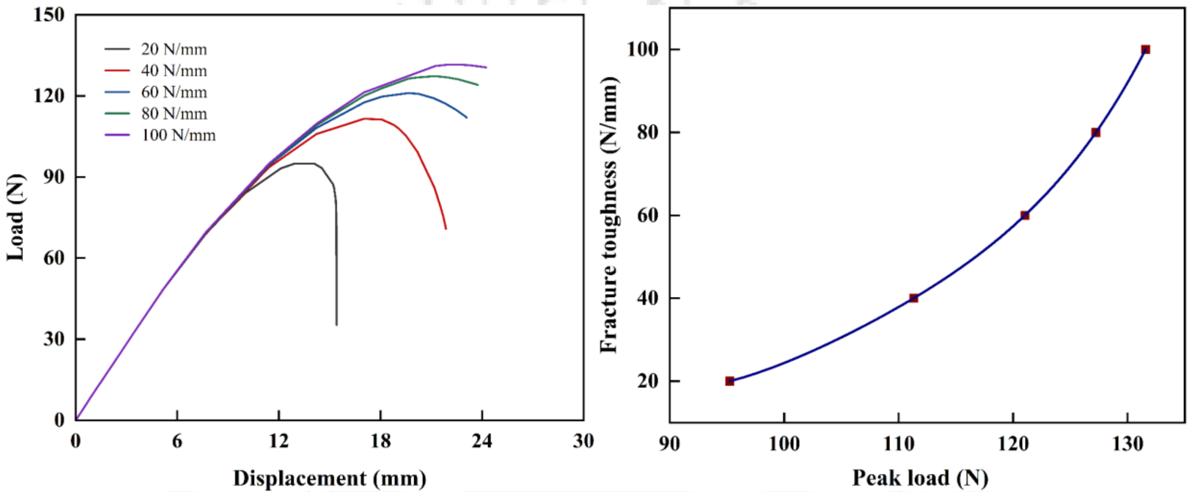

(a) (b)

Figure 7.14 Relating peak load to fracture toughness (a) load-displacement plot for numerically obtained peel test for various fracture toughness values, (b) variation of fracture toughness with peak load

To determine the value of fracture toughness for the FSSW_D_1.8 case, the peak load from peel tests, 125.04 N, was used. Through the calibration shown in Figure 7.14(b), a fracture toughness value of 74.64 N/mm was determined [70]. Using the cohesive zone data, peel test simulations were conducted. Figure 7.15(a) illustrates a good agreement in load evolution between experimental and numerical data for the FSSW_D_1.8 case. A similar procedure for FSSW_D_2 yielded cohesive parameters, and there after, a good agreement in load evolution was obtained for the FSSW_D_2 specimen as well (Figure 7.15b). The cohesive zone parameters for all specimens are summarized in Table 7.2.

It is seen that the fracture toughness of spot welded specimens (FSSW_D_1.8, FSSW_D_2) are significantly higher than that of AB specimens due to the metallurgical bonding, which is believed to enhance their resistance to crack propagation and deformation under applied loads.

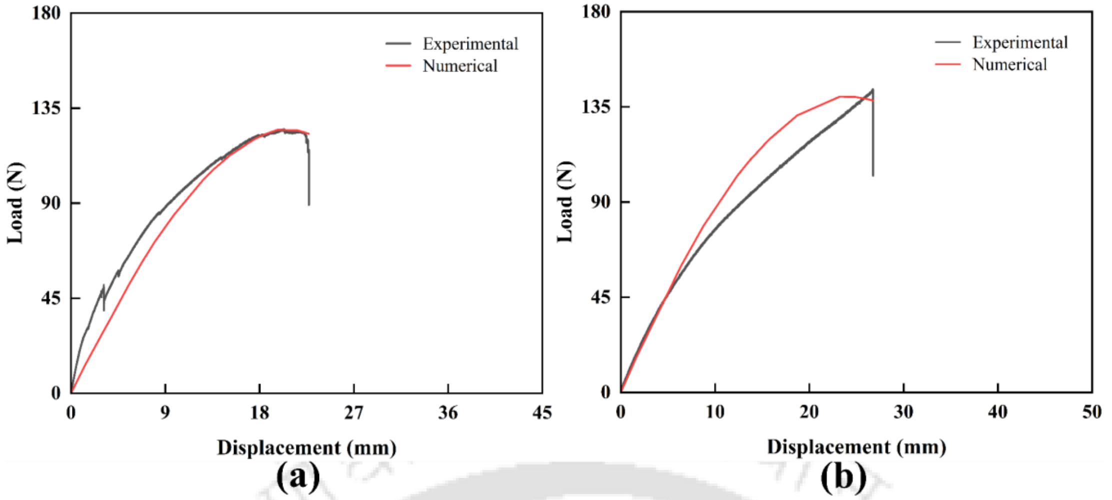

Figure 7.15 Experimental and numerical load-displacement data of the peel test of (a) FSSW_D_1.8 (b) FSSW_D_2 specimens

Table 7.2 Optimized cohesive zone parameters of adhesive and FSSW_D for peel test FE simulations

Property	Adhesive (equivalent) cohesive layer)	FSSW_D at 1.8 mm plunge depth (FSSW_D_1.8)	FSSW_D at 2 mm plunge depth (FSSW_D_2)
Cohesive stiffness (MPa/mm)	0.73	2500	2500
Critical stress (MPa)	0.075	11.5	12
Fracture toughness (N/mm)	0.026	74.64	120

7.3.3.4 Sandwich sheet made by FSSW_D_AB

The cohesive parameters shown in Table 7.2 were incorporated into the numerical model of the peel test of FSSW_D_AB sandwich sheet. A comparison between predicted and tested data revealed good agreement at both the plunge depths (Figure 7.16a, b). Within these curves, specific instances are notable: the initial load drop in FSSW_D_AB_1.8 and the subsequent curve variation in FSSW_D_AB_2, both correspond to the adhesive layer failure around the spot-weld area. The peak load indicates fracture within the weld nugget across all curves, while the subsequent decrease in load just before complete fracture indicates the adhesive failure outside the spot weld. It is clear that the stiffening effect that was initially observed in FSSW_D samples (Figure 7.15) is still present in this case as well. When the numerical and experimental results were compared, it was found that the adherends experienced slight variations in slope before reaching the maximum load, which could be due to the limitations in the numerical damage model followed for the analyses.

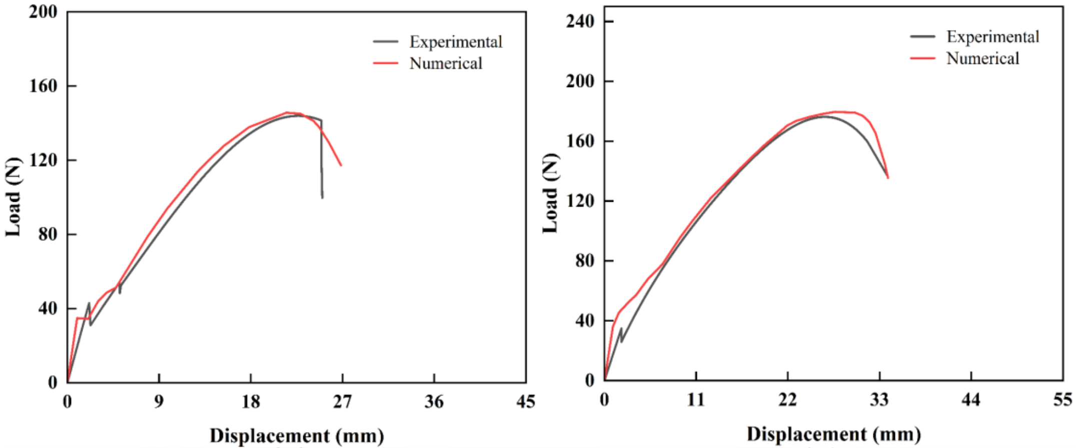

(a) (b)

Figure 7.16 Numerical and experimental load-displacement data of the peel test of (a) FSSW_D_AB_1.8 (b) FSSW_D_AB_2 specimens

Figure 7.17 and Figure 7.18 exhibit the simulation results of the peel test conducted on FSSW_D_AB specimens fabricated at plunge depths of 1.8 mm and 2 mm. Due to the similarities in fracture patterns between the two cases, the explanation focuses solely on the FSSW_AB_D_1.8 specimen. Figure 7.17(a) shows the geometric structure of the peel test sample within the sandwich sheet. Additionally, to ascertain the insignificance of mode II loading concerning mode I loading, distributions of the normal stress and the shear stress through the interface are displayed in Figure 7.17(b) and (c), respectively. Figure 7.17(d) to (f) demonstrate the distribution of Von Mises stress along the joint interfaces at three distinct stages. Moreover, Figure 7.17(g) to (i) illustrate the damage progression within the joint area at intermediate, welded, and final stages, respectively. A value of zero indicates an entirely intact interface, while a value of one signifies complete interface damage. Consequently, an interface displaying total damage exhibits zero Von Mises stress, visualized in blue. The maximum shear stress along the interface is approximately 0.43 MPa, while the highest normal stress on the interface is about 11.27 MPa (Figure 7.17b, c). This observation indicates that the interface primarily experiences mode I loading, while the influence of mode II loading is considered insignificant for this analysis.

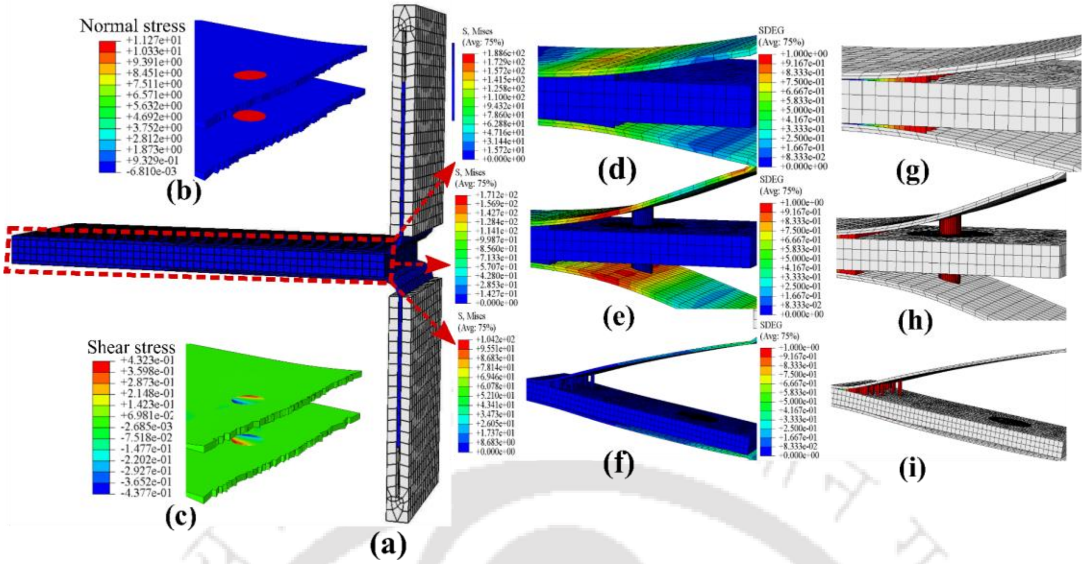

Figure 7.17 Peel test simulation of the hybrid specimen made at 1.8 mm plunge depth (FSSW_D_AB_1.8): (a) model of the peel test. (b) Normal stress, and (c) shear stress along the joint interface cohesive layer during the intermediate stage. Stress along the joint interface (d) intermediate stage, (e) welded stage, (f) final stage of peel test. Damage along the joint interface (g) intermediate stage, (h) welded stage, (i) final stage of peel test.

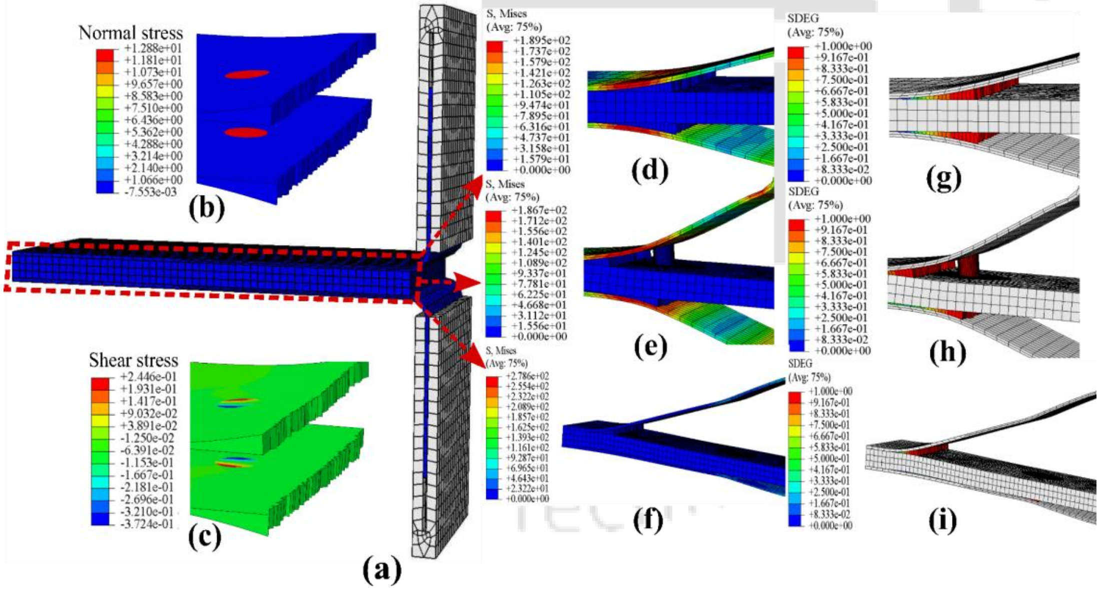

Figure 7.18 Peel test simulation of the hybrid specimen made at 2 mm plunge depth (FSSW_D_AB_2): (a) model of the peel test. (b) Normal stress, and (c) shear stress along the joint interface cohesive layer during the intermediate stage. Stress along the joint interface (d) intermediate stage, (e) welded stage, (f) final stage of peel test. Damage along the joint interface (g) intermediate stage, (h) welded stage, (i) final stage of peel test.

7.3.4 Joint strength

Figure 7.19 illustrates the validation work for numerical peel test predictions and also highlights the significance of the CZM approach in estimating the peel strength of the joints. For FSSW joints, specifically FSSW_D, the numerical model predicts peak load values slightly lower by 0.2% in the case of FSSW_D_1.8 and by 2.5% in the case of FSSW_D_2 when compared to experimental values. In contrast, the numerical predictions for AB joints closely match the experimental peak load. However, the trend of overestimation continues in the numerical predictions for hybrid joints, surpassing the tested data by 1.2% and 2% in case of FSSW_D_AB_1.8 and FSSW_D_AB_2 respectively. On the whole, the numerical predictions using CZM are encouraging. Therefore, the CZM approach is deemed appropriate for modelling and estimating the strength of such joints. Out of these, CZM and FE modeling of AB joints are well documented and attempted by several authors. Application towards the design of FSSW joints, specifically for fabricating sandwich sheets, is the unique contribution from the current work. The results suggest its effective utilization in the design of AB and FSSW joints (including hybrid ones), offering benefits concerning timely completion and project costs.

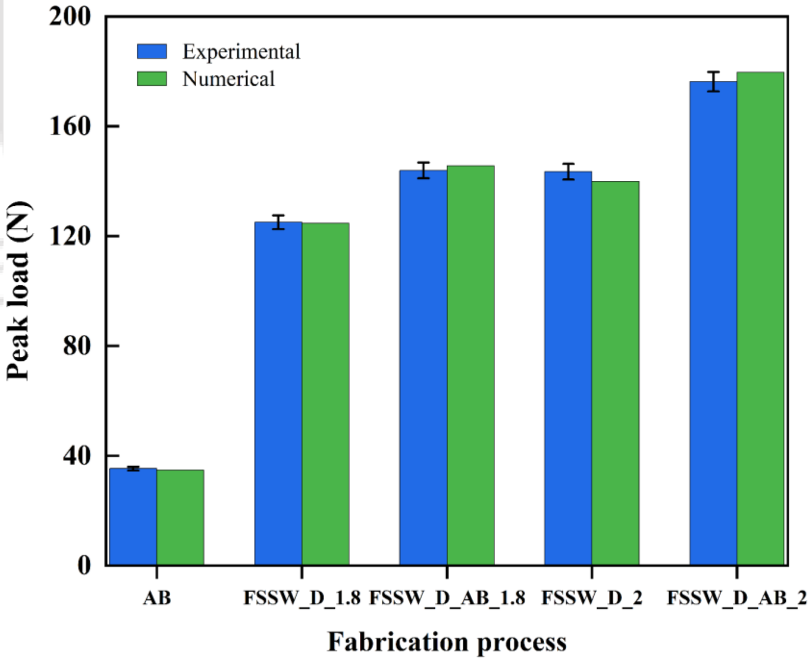

Figure 7.19 Experimental and numerical comparison of joint strength fabricated by different processes

7.4 Summary

The primary objective here was to explore the fabrication of honeycomb core sandwich structures through FSSW strategies as potential alternatives or enhancements to the current AB structures. The research compared two strategies, FSSW_D and FSSW_D_AB, against the peel test performance of traditional AB sandwiches. These strategies differed in terms of disc insert implementation and AB techniques. To demonstrate the strategies, the materials used were AA5052-H32 skins and AA3003 honeycomb core. The peel test FE simulation using CZM was performed, in which a homogenized core with an equivalent cohesive layer was used in place of the actual core and cohesive layer. Using a homogenized honeycomb core and the equivalent cohesive layer instead of the actual ones reduced the elements and computational time for the peel tests, enhanced simulations, and analyses by simplifying structural representations while maintaining material properties.

Specific conclusions drawn from the study are

- There is a significant improvement in peak load for various joints, FSSW_D_1.8, FSSW_D_AB_1.8, FSSW_D_2, and FSSW_D_AB_2, which is about 254%, 307%, 306%, and 399%, respectively, in comparison to AB joints.
- In addition, when comparing hybrid joints to the original ones without AB, there was about 15% and 23% improvement in peak load during peeling at 1.8 mm and 2 mm plunge depths, respectively, which is due to the additional metallurgical bonding in hybrid cases.
- The predominantly observed fracture mode was identified as "nugget pull-out”. Notably, all sandwich sheets with disc inserts fractured between the upper sheet and the disc, signifying robust joints resulting from front-side welding.
- Peak load values predicted by the numerical model of FSSW_D joints were just 0.2% and 2.5% lower than the experimental data at 1.8 and 2 mm plunge depths. The numerical predictions for AB joints, on the other hand, closely matched the experimental values. The trend of overestimation remained in the numerical predictions of hybrid joints (FSSW_D_AB). Based on the results, it can be said that the CZM approach not only predicts the peeling behavior of AB joints accurately, but also the FSSW joints and hybrid joints.

Chapter 8 Mixed mode bending analysis of adhesive bonded and hybrid honeycomb core sandwich structures

8.1 Experimental process

This section describes the methods for conducting FSSW trials, preparing sandwich samples, and performing MMB testing. The mechanical properties of skin sheet and honeycomb core are already discussed in Section 3.1.1 in Chapter 3, whereas the mechanical properties of disc insert are discussed in Section 4.1.1 in Chapter 4. All the material properties of sandwich sheets are presented in Table 5.1 of Chapter 5.

8.1.1 Sandwich fabrication

Two different joining strategies for fabricating sandwich structures with honeycomb core for the MMB test are described here.

8.1.1.1 Adhesive bonding (AB)

The joining strategies using AB is already explained in Section 5.1.2.1 of Chapter 5. The fabrication processes of MMB specimens are shown in Figure 8.1.

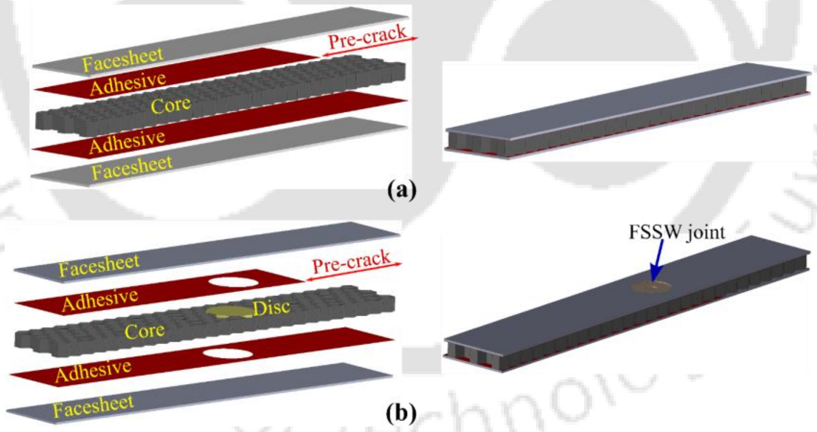

Figure 8.1 Manufacturing of sandwich by (a) AB, (b) hybrid processes

8.1.1.2 FSSW with disc insert and adhesive bonding (FSSW_D_AB)

The joining process is the same as discussed in Section 5.1.2.5 of Chapter 5; additionally, a pre-crack of 20 mm was inserted between the upper sheet and core, as shown in Figure 8.1(b) and Figure 8.2. The welding parameters were configured with a rotating speed of 900 rpm, a tool plunge speed of 2 mm/min, and a dwell period of 5 seconds. The specimen was subjected to a plunge depth of 1.8 mm on both sides of the welding. The manufactured MMB specimen by this hybrid process is shown in Figure 8.2(b).

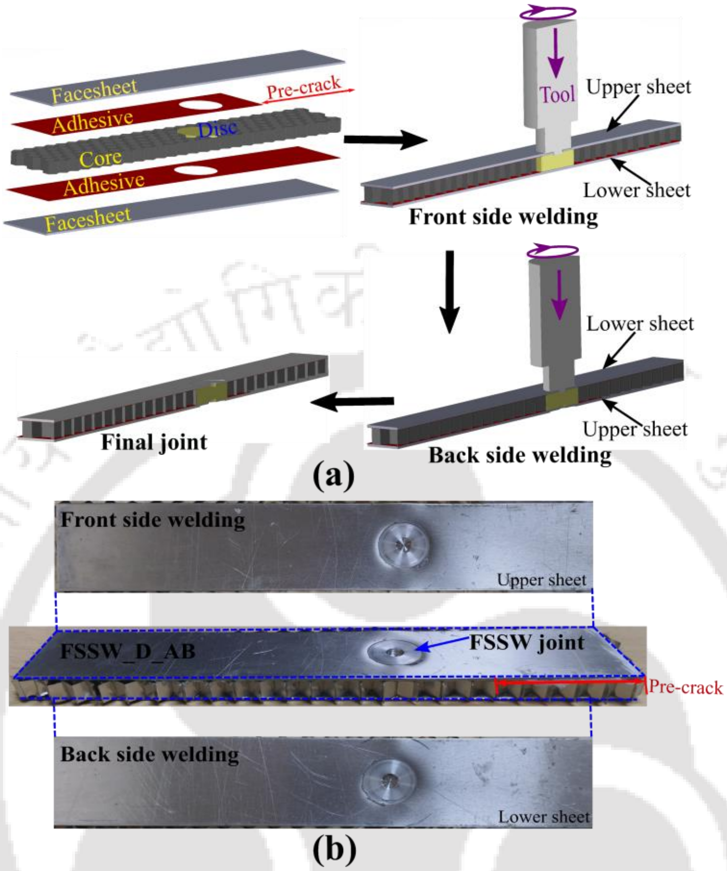

Figure 8.2 Manufacturing of MMB specimen by hybrid process (a) cross-sectional view and (b) actual manufactured specimen

8.1.2 Mixed mode bending test

The schematic of MMB test is shown in Figure 8.3. The specimen dimensions and manufactured specimen with end blocks are shown in Figure 8.4(a) and (b), respectively. The end blocks were attached to specimens with Araldite adhesive and clamped in the bench vice for 24 hours. The experiments were carried out at a 1 mm/min crosshead speed in the Shimadzu UTM with 1 kN load cell, as shown in Figure 8.4(c).

The ability of a material to withstand complex loading conditions and prevent fracture propagation may be evaluated using this test. The span length (2*L*) of the specimen is 100 mm. One can modify the opening-to-shear loading ratio by modifying the fixture's lever length '*c*'. For this investigation, *c* of 80 mm and 65 mm were selected for the initial crack length of 20 mm. Since these lengths correspond to mode mixity phase angle (ψ) of 14.04° (80 mm lever length) and 18.44° (65 mm lever length), respectively, it is possible to study the behaviour of the material under a variety of loading instances.

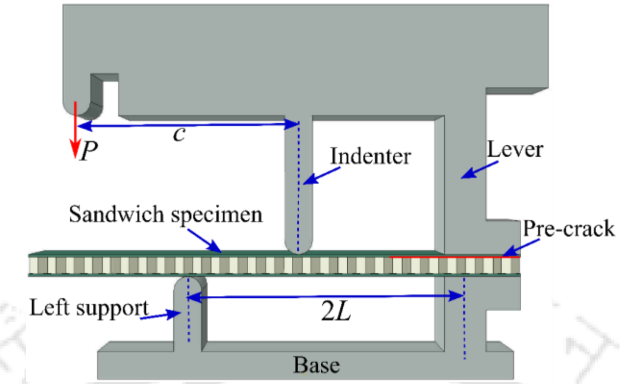

Figure 8.3 Schematic of MMB test

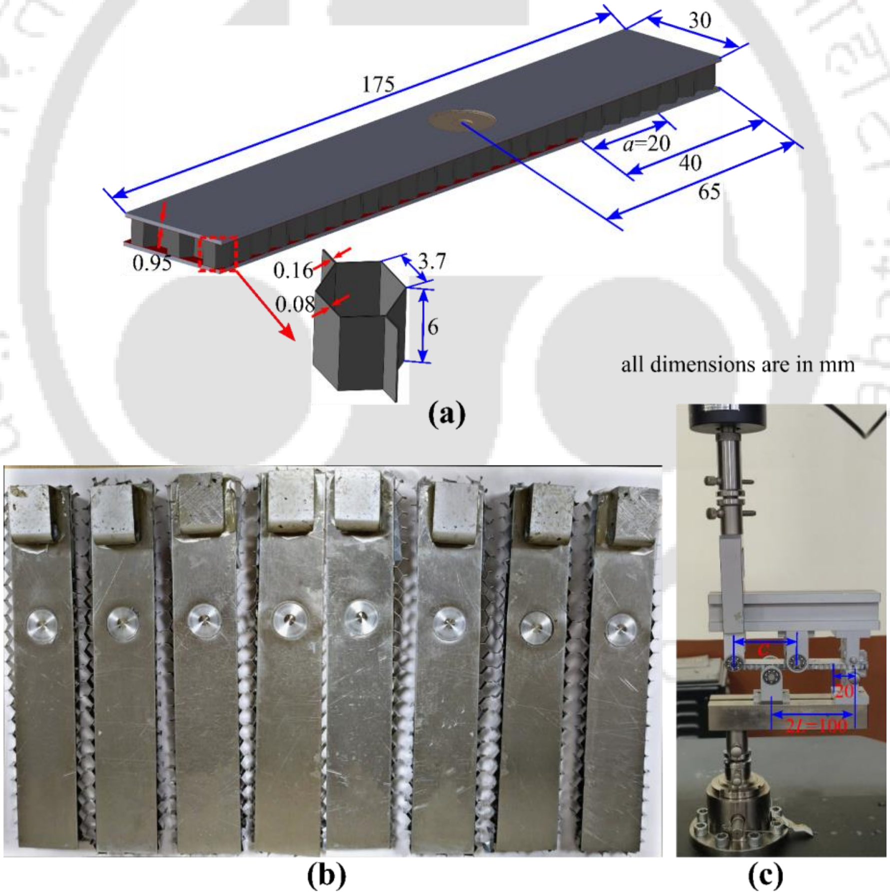

Figure 8.4 MMB test details (a) MMB specimen dimensions, (b) MMB specimens with end-block, and (c) MMB test setup in UTM

The mode mixity phase angle ψ can be defined as

$$\psi = \tan^{-1}\left(\frac{G_{\mathrm{II}}}{G_{\mathrm{I}}}\right) \tag{8.1}$$

To calculate the optimal *c* to obtain the necessary mixed-mode loading ratio, subsequent equations are used [119].

$$c = \frac{3\alpha + 12\beta^2 + 8\beta\sqrt{3\alpha}}{36\beta^2 - 3\alpha} L \tag{8.2}$$

In the equation, *L* represents the half-span length of the specimen, and β α correspond to the non-dimensional crack length correction and the mixed-mode transformation parameter, respectively, given by

$$\alpha = \frac{G_{\mathrm{I}}}{G_{\mathrm{II}}} = \cot\psi \tag{8.3}$$

$$\beta = \frac{\chi d + a}{0.42\chi d + a} \tag{8.4}$$

The delamination length is represented by *a*, *d* is the half thickness of the specimen, and crack length correction parameter is represented by χ, expressed as

$$\chi = \sqrt{\frac{E_{11}}{11G_{13}}\left[3 - 2\left\{\frac{\Gamma}{1+\Gamma}\right\}^2\right]} \tag{8.5}$$

Here, Γ stands for the transverse modulus correction parameter, which has the following definition.

$$\Gamma = 1.18\frac{\sqrt{E_{11}E_{22}}}{G_{13}} \tag{8.6}$$

E_{11} and E_{22} represent the modulus of elasticity in the longitudinal and transverse directions, respectively. The shear modulus in the orthogonal direction is denoted by G_{13}. These parameters of the sandwich structure were computed using the Micromechanics plugin in Abaqus. For this purpose, a RCE of the sandwich was used, as seen in Figure 8.5; the method for obtaining the properties is same as that described in Section 2.2.1 of Chapter 2 for the honeycomb core.

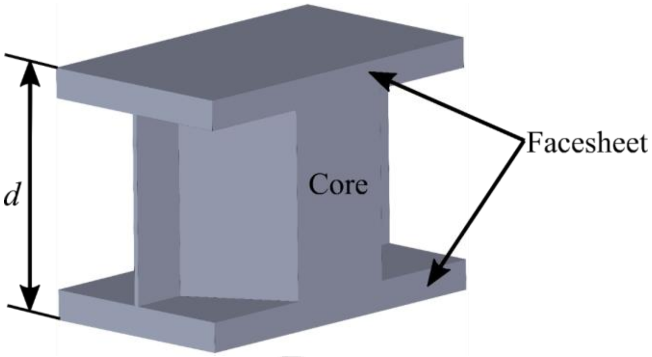

Figure 8.5 RCE of sandwich structure

8.2 Numerical analysis

In the numerical analysis conducted in Abaqus, the CZM-embedded formulation was utilized to assess its efficacy in predicting the strength of adhesive bonded and hybrid joints. The adhesive and weld nugget were represented by CZM laws detailed in Section 6.2.1 of Chapter 6. Simplifications were made in the hybrid models, such as not accounting for variations in aluminium properties near the nugget resulting from heat generated during welding. Furthermore, it was assumed that the adhesive qualities would remain unchanged upon curing at ambient temperature, even if the adhesive might be degraded due to the heat generated during welding. Since no adhesive was used in the disc insert area, adhesive deterioration at the spot perimeter was ignored. 3D models were constructed with specified boundary conditions, as illustrated in Figure 8.6. Meshes for the hybrid bonded joints, with emphasis on smaller elements at the spot welded area, are depicted in Figure 8.6. R3D4 rigid elements, COH3D8 cohesive elements, and C3D8 solid elements were used in the models. The thin adhesive layer and weld nugget were modelled with cohesive elements. The surrounding core (honeycomb and homogenized core), disc, and facesheet portions were modelled using C3D8 elements, while R3D4 was used to model the MMB fixture. A "tie" constraint was used to join the cohesive layer to the disc, the top and bottom sheets, and the core.

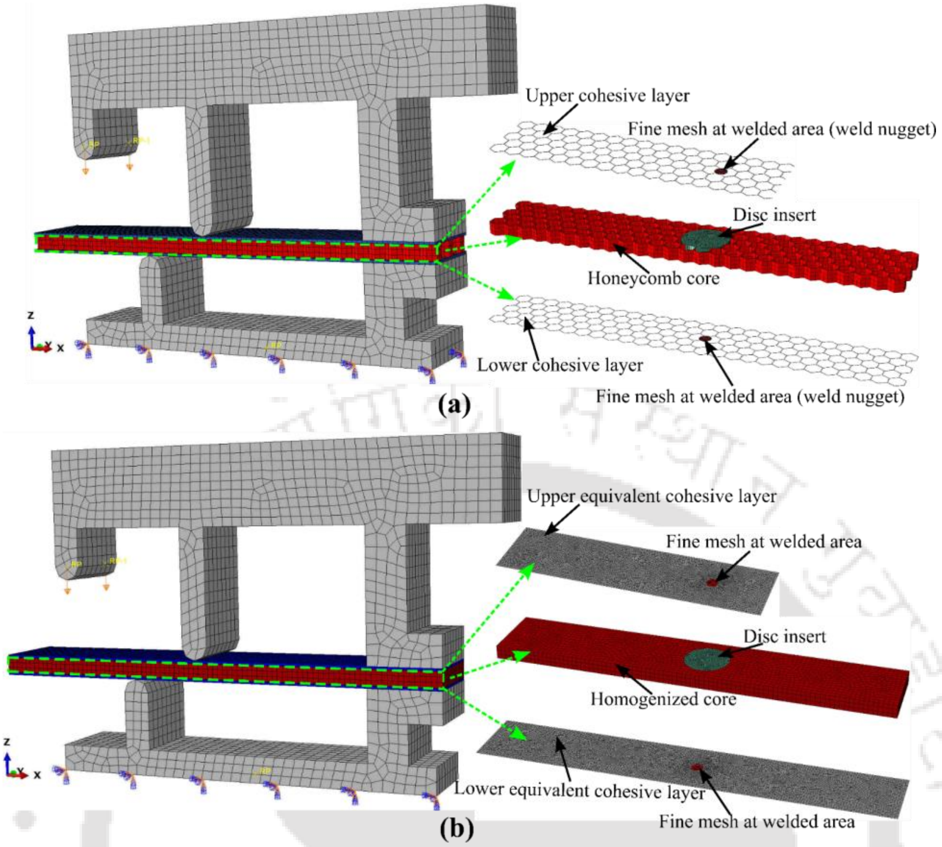

Figure 8.6 FE model of MMB test of sandwich with (a) honeycomb core and (b) homogenized core

8.2.1 Cohesive zone modelling (CZM)

This is already discussed in Section 6.2.1 of Chapter 6. The optimized CZM parameters are shown in Table 8.1.

Table 8.1 CZM parameters obtained from optimization

Layer	K^{n} (MPa/mm)	K^{s} (MPa/mm)	$\sigma^{c}_{\max}$ (MPa)	$\tau^{c}_{\max}$ (MPa)	G^{n}_{c} (N/mm)	G^{s}_{c} (N/mm)
AB (cohesive layer)	22	42	2.26	2	1.41	0.22
welded (FSSW_D)	150	100	31	37	56	50

where K^{n}, $\sigma^{c}_{\max}$, G^{n}_{c}, and, K^{s}, $\tau^{c}_{\max}$ G^{s}_{c} are stiffness, critical stress, and critical fracture toughness in normal and shear directions, respectively.

All cohesive parameters used in the thesis are summarized below in Table 8.2.

Table 8.2 Combined cohesive parameters

Ref. Table	Details	$\sigma^{c}_{\max}$ (MPa)	$\tau^{c}_{\max}$ (MPa)	K^{n} (MPa/mm)	K^{s} (MPa/mm)	G^{n}_{c} (N/mm)	G^{s}_{c} (N/mm)
Table 6.1 & Table 8.1	Adhesive (Cohesive layer)	2.26	2	22	42	1.41	0.22
Table 6.1	FSSW_D_750	38	46	150	100	74	78
Table 8.1	FSSW_D_900	31	37	150	100	56	50
Table 7.2	FSSW_D_1.8	11.5		2500		74.64	
Table 7.2	FSSW_D_2	12		2500		120	
Table 6.1	FSSW_D_1200	47	51	150	115	93	106
Table 6.3	Adhesive (Equivalent cohesive layer)	0.075	0.0665	0.732	1.4	0.046	0.008
Table 7.2	Adhesive (Equivalent cohesive layer)	0.075		0.73		0.026	
Table 7.1	Adhesive (cohesive layer)	2.26		22		0.73	

8.2.2 Homogenization of the honeycomb core and equivalent cohesive layer

The homogenization of the honeycomb core and equivalent cohesive layer is already discussed in Section 6.2.2 of Chapter 6.

8.2.3 Validation of existing MMB test of sandwich structure

The MMB test of foam-cored sandwich structures, as reported by Quispitupa *et al.* [120,121], is validated through FE simulations to capture interfacial crack propagation effectively under mixed-mode condition at 18.9° mode mixity phase angle(ψ). This phase angle was chosen because it closely approximates one of the phase angles used in this study for the MMB test of honeycomb-cored sandwich structures.

Figure 8.7 illustrates the loading process with boundary conditions and dimensions of the sandwich specimen. The material properties of the composite face sheets, the core, and the optimized parameters of the interface are detailed in Table 8.3. The comparison between the numerical predictions at different numbers of elements from the FE model and the experimental data is presented in Figure 8.8. The results demonstrate excellent agreement between the numerical predictions and the experimental observations, confirming the accuracy of model in capturing debonding propagation under mixed-mode loading conditions. This alignment underscores the effectiveness of FE model in simulating the complex behaviour of sandwich structures during MMB tests.

Table 8.3 Material properties [120]

Part	Material properties
Face DBLT-850 (0/45/90/-45)	E= 16.4 GPa, G= 5.8 GPa, v= 0.306
PVC foam core H100	E= 135 MPa, G= 35 MPa, v= 0.32
Interface	K^{n} =8 MP/mm, K^{s} =17 MP/mm, $\sigma^{c}_{\max}$ =1 MPa, $\tau^{c}_{\max}$ =2.2 MPa, G^{n}_{c} =0.5 N/mm, G^{s}_{c} =0.45 N/mm

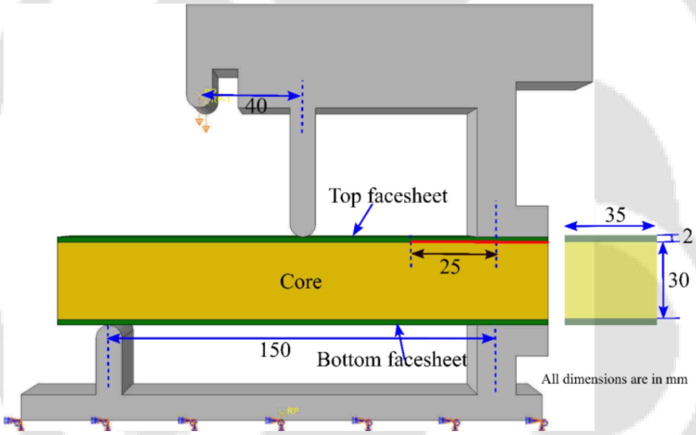

Figure 8.7 Specimen dimensions and boundary conditions of MMB test

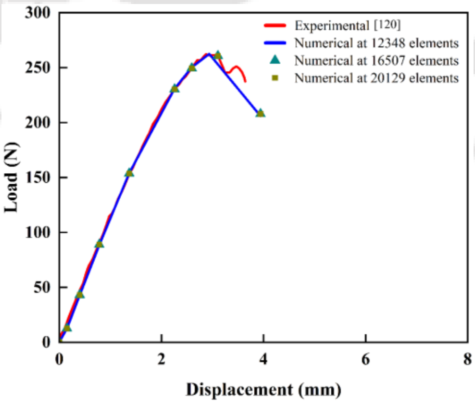

Figure 8.8 Validation of MMB test experimental load-displacement curve of Quispitupa *et al.* [120] by present FE simulations

8.3 Results and discussion

This section presents the experimental results from MMB tests conducted on adhesive, and hybrid joined sandwich structures. Following the experimental results, the section also discusses numerical simulation results, providing a detailed analysis of joint strength, as well as the stress and damage behaviour of the sandwich structures.

8.3.1 MMB test experimental results

Figure 8.9(a) illustrates the load evolution during MMB tests conducted on AB and FSSW_D_AB sandwich structures. The AB specimens exhibit lower joint strength compared to the FSSW_D_AB specimens. For the FSSW_D_AB specimens, there is a noticeable sudden drop in load, which can be attributed to the failure of the adhesive layer. However, unlike the AB specimens, the load does not continue to decrease drastically after adhesive failure. Instead, it is sustained by the spot welds present in the FSSW_D_AB structure. This behaviour highlights the superior performance and enhanced structural integrity provided by the spot joints, which act as an additional reinforcement mechanism after adhesive failure.

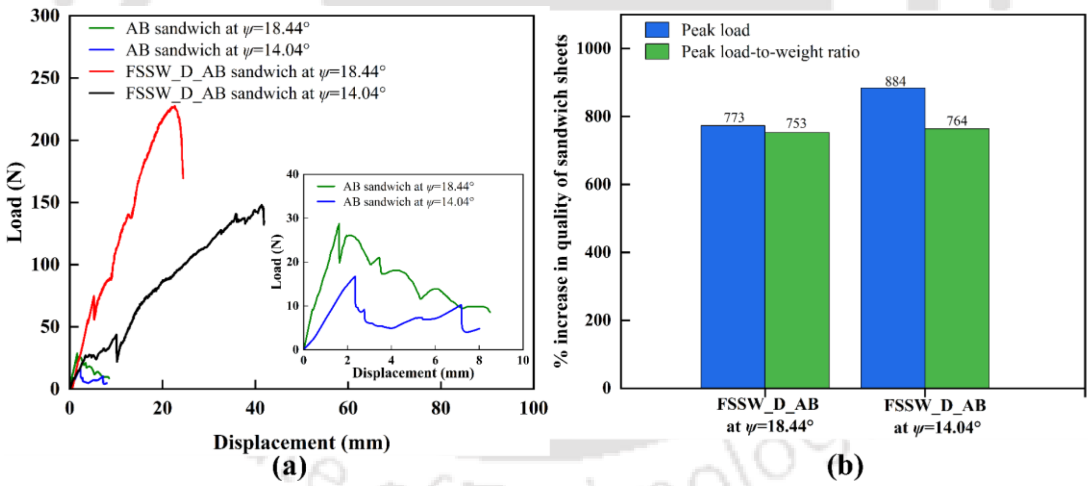

Figure 8.9 MMB test of sandwich structures (a) load evolution, (b) improvement in quality of FSSW_D_AB joints than the AB joints

Furthermore, as the phase angle increases, there is a noticeable improvement in both stiffness and peak load for both the AB and FSSW_D_AB specimens. This indicates that the phase angle has a positive influence on the structural integrity and load-bearing capacity of the joints, further enhancing the performance of the FSSW_D_AB structures compared to purely adhesive-bonded joints.

Figure 8.9(b) shows the improvements in the quality of hybrid joints compared to AB joints: peak loads improved by 773% and 884% for 18.44° and 14.04° phase angles, respectively, along with remarkable improvements (about 753% and 764%) in the peak load-to-weight ratio. The improvements reveal that the FSSW_D_AB approach is effective and suitable for manufacturing honeycomb sandwiches. Figure 8.10 presents the fractured sites of the joints that underwent MMB. All the joints fractured on the front side of the weld, mainly between the disc and upper sheet, and at the nugget for both phase angles, demonstrating good joint formation. The observation correlates well with the peak load data shown in Figure 8.9(b), where FSSW_D_AB samples demonstrated superior joint strength and load-bearing capacity compared to AB samples. The consistency of the fracture location in FSSW_D_AB specimens underscores the reliability and effectiveness of the manufacturing method.

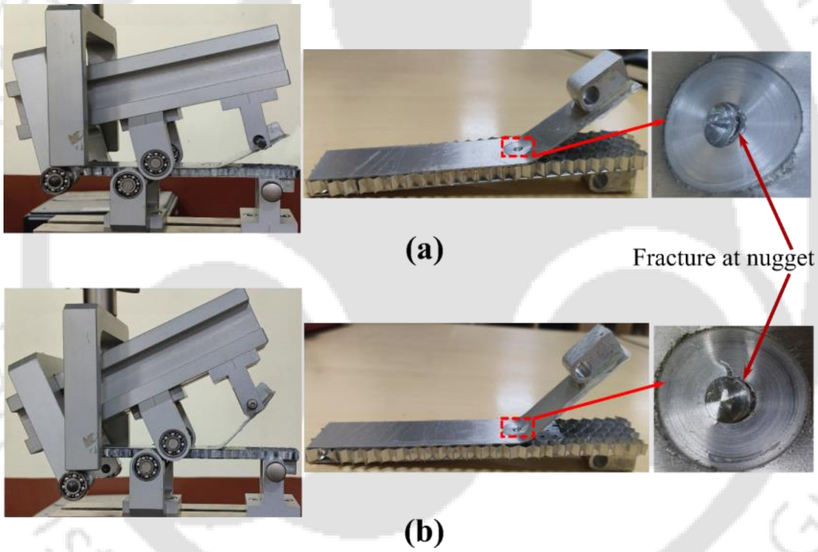

Figure 8.10 Fracture of FSSW_D_AB sandwich specimens at (a) ψ=18.44° (b) ψ=14.04°

8.3.2 MMB test numerical results

This section presents the joint strength, stress, and damage analysis for AB and FSSW_D_AB MMB specimens with honeycomb and homogenized core during MMB.

8.3.2.1 Joint strength analysis

8.3.2.1.1 AB sandwich sheets

Figure 8.11 illustrates the comparison between the load evolution data from the MMB tests and the MMB FE simulations of the sandwich structures of AB. The results highlighted a reasonable agreement between the numerical simulations and the experimental tests. The structural response initially exhibited linear behaviour, indicating elastic deformation with no signs of damage in both cases. However, before reaching the peak load, nonlinear behaviour emerged, indicating the onset of damage in the adhesive layer, predominantly governed by mode-I (opening) fracture. This shift marked before the beginning of crack initiation within the adhesive. After reaching the peak load, the fracture propagation across the adhesive layer became more evident, leading to a nonlinear load-displacement curve. During this phase (at peak load), both mode-I and mode-II (shearing) fracture mechanisms were approximately equally dominant as the crack advanced through the adhesive material, gradually reducing load. When the crack extended to the mid-span position, the propagation stopped. Following this, the applied load began to increase once again, indicating that the structure retained some residual strength. At this stage, the behaviour was once again dominated by mode-I fracture, suggesting that the structure could bear additional load despite significant damage.

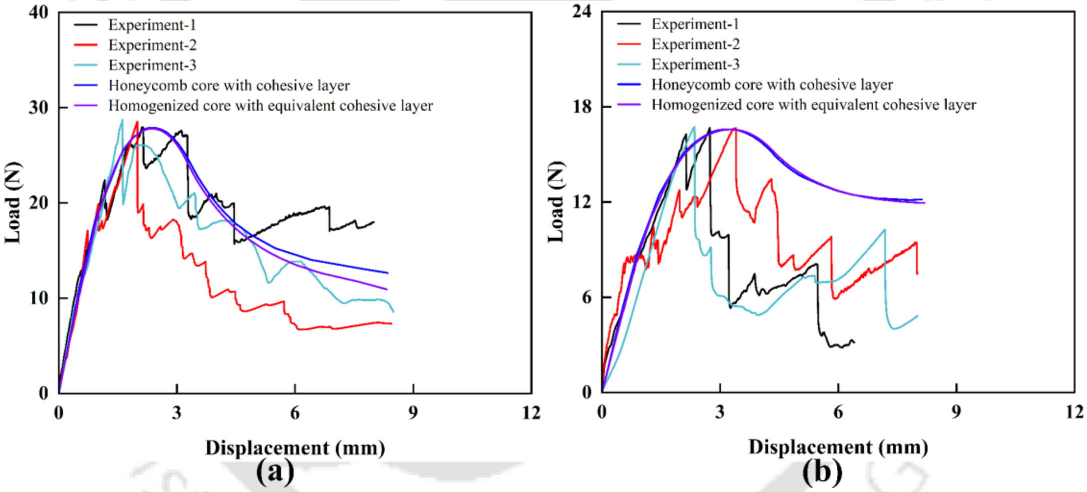

Figure 8.11 MMB responses of AB sandwiches from experiments and FE simulations for (a) ψ=18.44°, (b) ψ=14.04°

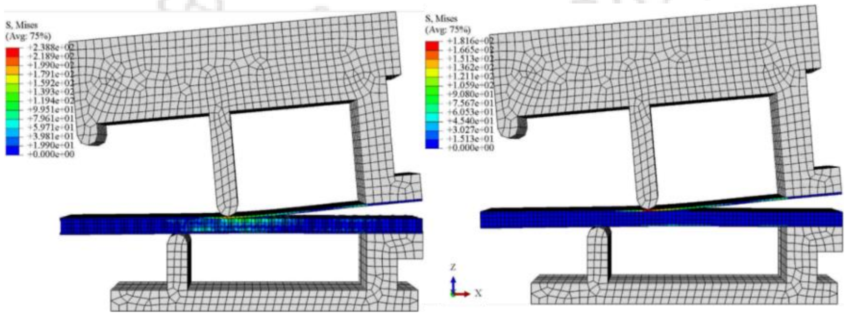

Figure 8.12 MMB FE model showing sandwich deformation at 18.44° phase angle

A notable correlation was observed between the load-displacement curves of the sandwich structure modelled using homogenized core and the data obtained from numerical and experimental tests on real structures. This consistency validates the accuracy and reliability of the homogenized core model. Furthermore, employing this model offers additional benefits, such as a reduction in the number of elements and the computing time. Overall, the homogenized core with an equivalent cohesive layer emerges as a promising approach for accurately modelling large-scale sandwich structures in real-time applications, providing efficiency and precision. Figure 8.12 shows the deformed stages of sandwiches with honeycomb and homogenized cores at 18.44° phase angle.

8.3.2.1.2 FSSW_D_AB sandwich sheets

FE simulations of MMB of FSSW_D_AB sandwich sheets using both a honeycomb core and a homogenized core with their respective cohesive layers were performed to evaluate the load response (Figure 8.13a). Good agreement was demonstrated between the simulation and experimental results at both phase angles.

Numerical models utilizing honeycomb and homogenized cores and their respective cohesive layers provided accurate predictions of the curve behaviour. Initially, the response exhibited slightly nonlinear behaviour at both phase angles, where both mode-I and mode-II were approximately equally dominant. Following this, the curve transitioned to a more linear behaviour until a slight drop in load occurred. At this stage, the opening mode (mode-I) became more dominant than the shearing mode (mode-II), though the difference in dominance was not significantly greater than in subsequent parts of the curve. The observed load drops before reaching the peak were attributed to damage in the lower cohesive layer, likely caused by the bending of the core. As the load approached its peak, damage primarily occurred in the upper adhesive layers, while the lower layer experienced only partial damage. Throughout the entire process, mode-I remained the dominant fracture mechanism, playing a key role in the overall behaviour of the structure. This highlights the effectiveness of the numerical simulations in capturing the complex behaviour of the FSSW_D_AB joints during the MMB, providing valuable insights into their mechanical response and fracture.

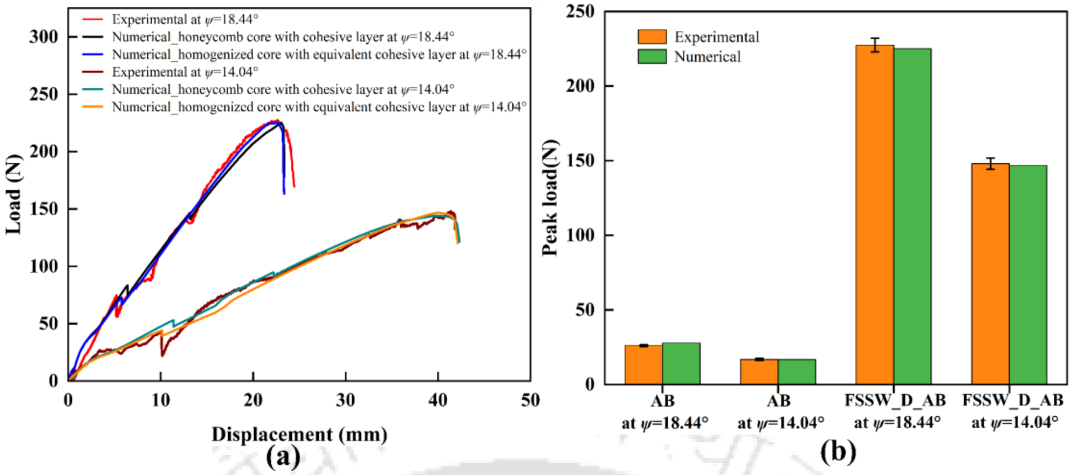

Figure 8.13 MMB responses of hybrid sandwiches from experiments and FE simulations (a) load evolution, (b) strength

Figure 8.13(b) shows that for AB joints, the numerical model predicts a peak load 5.6% higher and 1% lower at phase angles of 18.44° and 14.04°, respectively, compared to the experimental values. On the contrary, the numerical predictions for hybrid joints are slightly less than the experimental data by 1.1% and 0.8% at phase angles of 18.44° and 14.04°, respectively. Despite these minor discrepancies, the numerical predictions for both sandwiches nearly correspond to the observed peak load values, depicting the importance of CZM in predicting joint strength.

8.3.2.2 Stress and damage (SDEG) analysis of AB and hybrid sandwiches

As shown in Figure 8.14, the normal and shear stress distribution in the joint overlap region was estimated at the midpoint of the cohesive layers used with homogenized and honeycomb cores at peak load. The analysis reveals the effectiveness of both modelling approaches in capturing the critical stress concentrations, contributing to a better understanding of joint performance and reliability. In addition, a damage analysis was performed that focused on SDEG of the cohesive elements. The SDEG parameter in the CZM law represents the degradation of the stiffness of the weld nugget or adhesive during MMB, which scales from zero (representing undamaged material) to one (representing the failure of a CZM element). The peak load of the joints indicating adhesive failure in the hybrid joints is used in this section. However, loads are still supported by FSSW.

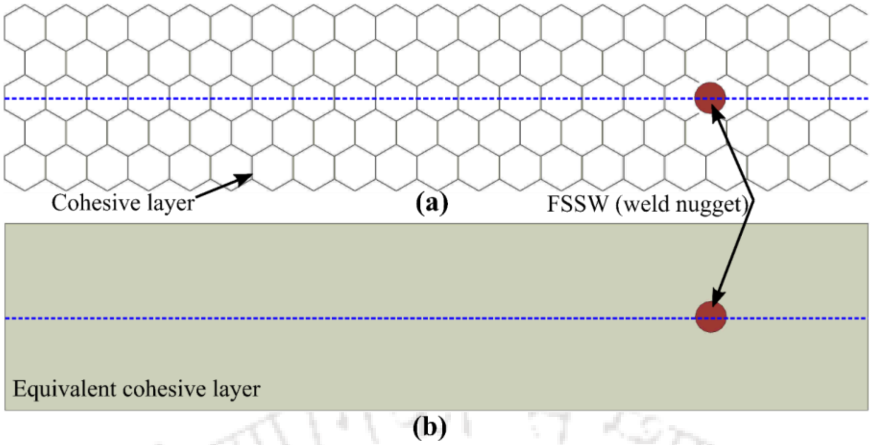

Figure 8.14 Stress and damage analysis at middle of (a) cohesive and (b) equivalent cohesive layer

Figure 8.15 shows the distribution of normal and shear stresses during MMB simulations. The stress patterns observed at the interfaces are notably similar when using both homogenized and honeycomb cores. Specifically, the normal stress distribution exhibits a consistent profile at both phase angles, with the maximum stress occurring at a phase angle of 18.44°. This stress distribution remains nearly constant throughout, while shear stresses initially decrease across the left support and subsequently increase until the maximum shear stress is reached and further decreases. The normal stress behaviour remains relatively stable for both phase angles, except at points where peak stresses are observed. These peak stresses suggest that they dominate the damages at these specific locations. When comparing both phase angles, the maximum stresses are found to occur at nearly identical positions. This consistency in the stress distribution highlights that the structural response of sandwich structures with honeycomb cores is comparable to that with homogenized cores during MMB. This indicates that the core type, whether homogenized or honeycomb, has a similar influence on stress distribution and overall structural behaviour under MMB conditions.

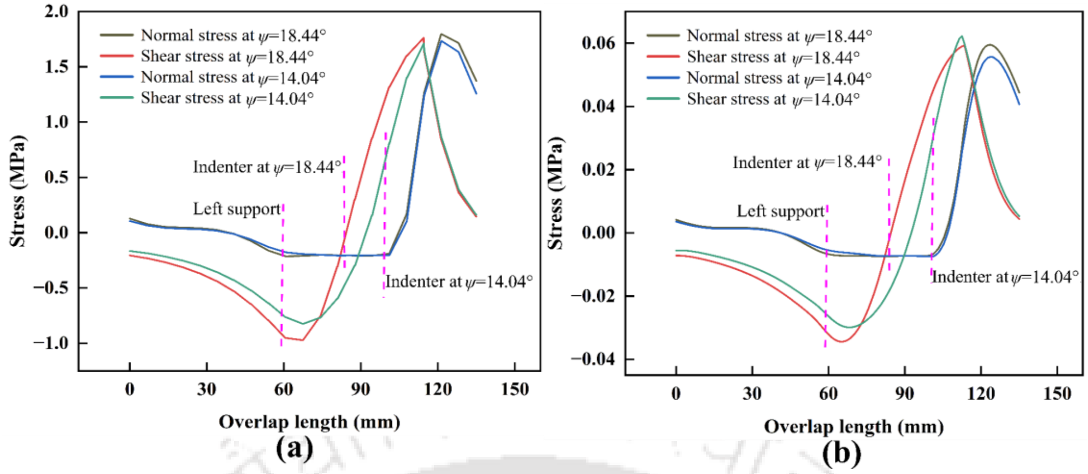

Figure 8.15 AB sandwich: stress distribution when using (a) honeycomb core and (b) homogenized core during modelling of MMB

Figure 8.16 illustrates the damage to the AB sandwich sheets during MMB at peak load. At this stage, the damage value approached unity at both phase angles, indicating the onset of crack propagation. The damage patterns at the interfaces were similar when using homogenized and honeycomb cores, regardless of the phase angles. This consistency indicates that the failure mechanisms are comparable across the different core configurations and phase angles, reinforcing the reliability and effectiveness of using homogenized core models to predict the damage behaviour in large-scale sandwich structures.

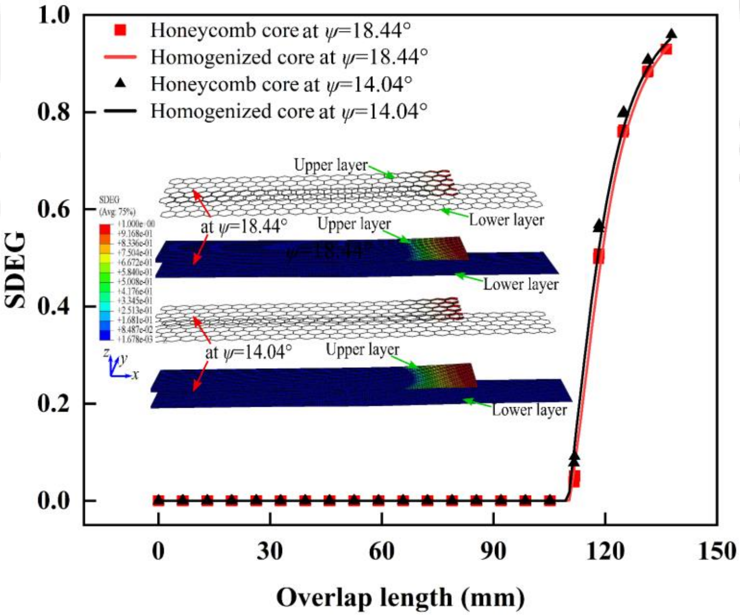

Figure 8.16 Damage response of AB sandwiches at peak load

Figure 8.17 depicts the normal and shear stress distribution for the FSSW_D_AB/hybrid sandwich during MMB. The stress distribution in the FSSW_D_AB joint (Figure 8.17) differ significantly from those in the AB joint (Figure 8.15) and is primarily influenced by the presence of the weld nugget. The weld nugget significantly enhances load transmission within the weaker inner overlap area and is capable of withstanding higher normal stresses than the adhesive. Additionally, the opening mode was observed to be more dominant than the shearing mode at both phase angles, further emphasizing the weld nugget's contribution to the overall performance. At this point, the load-bearing capacity of the structure is primarily maintained by weld nugget, as most of the upper adhesive layers have already been damaged (Figure 8.18).

Although the normal and shear stress distributions are almost the same at the interfaces of both core types, the honeycomb core specimen exhibited negative shear stresses in the adhesive around the weld nugget. The maximum and minimum normal and shear stresses were observed on the left and right sides of the nugget, respectively at both phase angles. These stresses were found to be similar for both types of sandwich structures, highlighting the consistent stress distribution facilitated by the weld nugget across different core configurations.

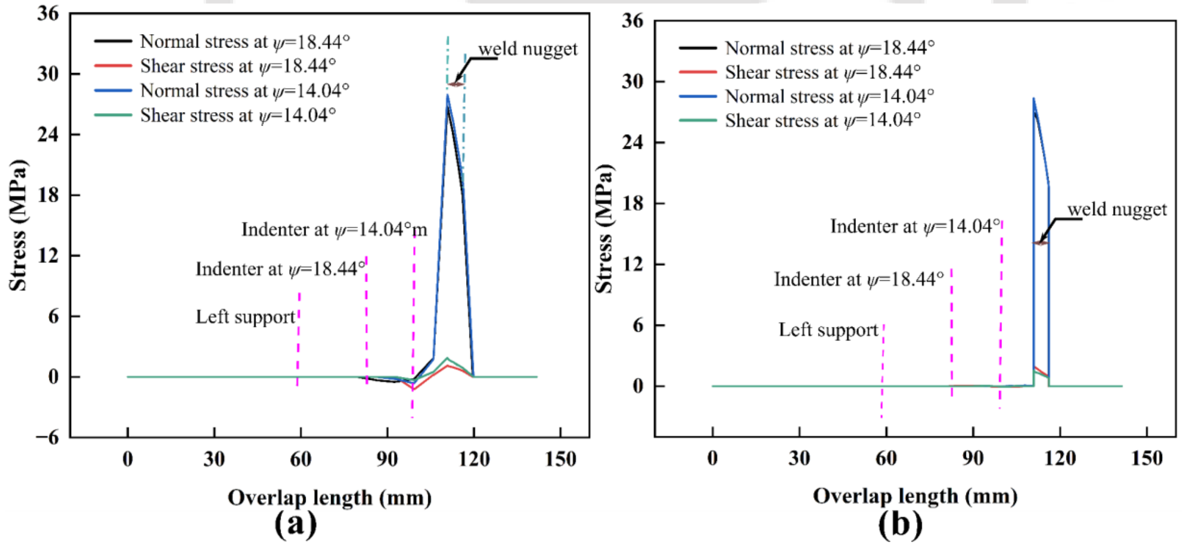

Figure 8.17 Hybrid sandwich: stress distribution when using (a) honeycomb core and (b) homogenized core during modelling of MMB

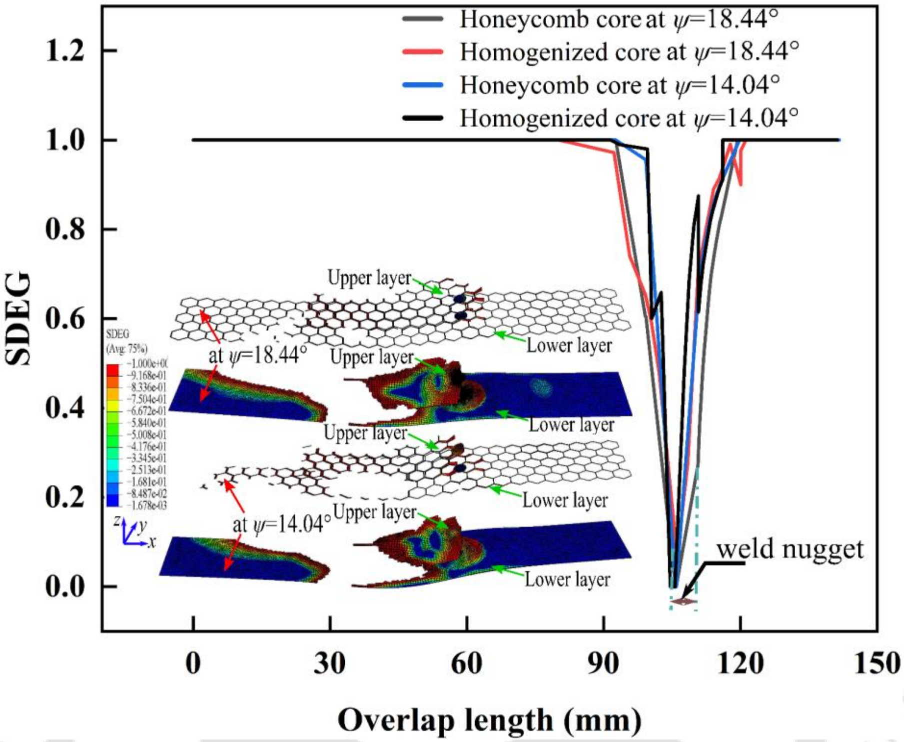

Figure 8.18 Damage response of FSSW_D_AB sandwiches at peak load

Figure 8.18 illustrates the damage distribution of the hybrid sandwich during MMB simulation. The damage patterns are the same at the interfaces of both core types for both phase angles. Failure of the adhesive around the weld nugget causes the damage variable to vary abruptly between damaged and undamaged parts. The weld nugget contributes significantly to achieving a higher peak load than the bonded joint alone due to improved stress transfer. Once the peak load is reached, the failure of the weld nugget occurs swiftly, as indicated in Figure 8.13(a). This rapid failure highlights the critical role of nugget in the spot weld in the overall load-bearing capacity and damage patterns seen in sandwiches.

8.4 Summary

The objective of this study was to identify potential alternatives to AB sandwich sheets by fabricating them using FSSW. A series of experiments and FE simulations, using a CZM, were conducted to compare the MMB test performance at two-phase angles between AB and FSSW_D_AB sheets. Both honeycomb cores with cohesive layers and homogenized cores with equivalent cohesive layers were used in the CZM. The findings revealed that the FSSW_D_AB sandwich sheets significantly increased the peak load (773% and 884%) and the peak load-to-weight ratio (753% and 764%) compared to the AB sheets at both phase angles. The

FSSW_D_AB sandwiches fractured at the weld nugget, indicating the formation of robust joints capable of tolerating larger MMB peak loads. The numerical MMB test load-displacement responses for both honeycomb and homogenized cores with their respective cohesive layers showed strong correlation with the experimental results, suggesting that a homogenized core with an equivalent cohesive layer can provide faster computations while maintaining similar mechanical performance. At peak loads, AB sandwiches exhibited similar stress and damage patterns for both types of core, including consistent compressive normal stresses, negative shear stresses, and comparable failure mechanisms, confirming the reliability of homogenized core models. The presence of the weld nugget in the FSSW_D_AB joint enhanced load transmission and allowed the joints to withstand higher stresses compared to the adhesive alone. Consistent stress patterns and abrupt variations in damage patterns due to adhesive failure around the weld nugget underscored the crucial role of the weld nugget in load bearing and damage distribution.

Chapter 9 Conclusions and future scope

9.1 Conclusions

The primary objective of the thesis was to explore the fabrication of honeycomb core sandwich structures through FSSW strategies as potential alternatives or enhancements to the current AB structures. The research encompassed analytical, numerical, and experimental approaches. The lap shear, peel, and MMB test FE simulations using CZM were performed, in which a homogenized core with an equivalent cohesive layer was used instead of the actual core and cohesive layer, which reduced the elements and computational time, enhanced simulations, and analyses by simplifying structural representations while maintaining material properties.

The key conclusions drawn from the work are outlined below:

- **Elastic Constants and Homogenization:**
  - *Analytical and Numerical Validation:* The study successfully determined all nine elastic constants of the honeycomb core analytically using the strain-energy method. These constants were also estimated through FE analysis with PBCs using a RCE. Both methods yielded results that were in agreement with reference values.
  - *Computational Efficiency:* Homogenized core models led to a 96% reduction in computational time compared to detailed honeycomb core models without compromising accuracy. This efficiency was observed in various tests, including the 3PBT, edge compression, buckling, and modal analysis.
- **FSSW Fabrication Strategies and performances:**
  - *Joining Techniques:* Four FSSW strategies—FSSW, FSSW_AB, FSSW_D and FSSW_D_AB—were compared with traditional AB sandwiches across multiple tests and various process parameters.
  - *Enhanced Performance:* FSSW methods, particularly FSSW_D_AB, demonstrated considerable improvements in load-bearing capacity and robustness compared to traditional adhesive bonding. The weld nugget's role in enhancing load transmission and joint performance was evident.

  - *Peel Test:* FSSW_D_AB joints showed the greatest improvement, with peak load and peak load-to-weight ratio increase ranges from 254%-705% and 639%, respectively compared to AB joints. Other FSSW processes also exhibited significant increases in peel test performance.
  - *Lap Shear Test:* FSSW_D_AB joints outperformed AB joints with peak load and peak load-to-weight ratio increase ranges from 592%-878% and 542%-726%, respectively. Other FSSW methods also demonstrated substantial improvements over AB joints.
  - *3PBT:* The FSSW_D_AB joints showed a 6.12% improvement in peak load and a 46% increase in specific stiffness compared to AB panels. The 3-PBT results aligned well with numerical simulations up to the peak load, but discrepancies beyond this point suggest further refinement is needed.
  - *MMB Test:* FSSW_D_AB sandwiches achieved peak load increases of 773% and 884% compared to AB sandwiches at two mode-mixity phase angles. The presence of the weld nugget significantly enhanced load-bearing capacity.

- **Numerical Simulations and Experimental Validation:**
  - *Simulation Accuracy:* CZM were employed to predict lap shear, peel, and MMB test performances. Numerical predictions matched experimental results closely, especially for FSSW_D and FSSW_D_AB joints.
  - *Homogenized Core Models:* Using homogenized honeycomb cores with the developed equivalent cohesive layers in simulations simplified structural representations and reduced computational time while maintaining mechanical performance.
  - *Stress Analysis:* FEM stress analysis revealed significant stress concentrations around the weld nugget and adherend rotations at overlap edges. These insights are crucial for improving joint design and FSSW process parameters.
  - *Stress Concentration:* Key stress concentration areas, such as weld-nugget perimeters and bonding overlap edges, were identified. Targeting these areas for strengthening could further enhance joint designs and FSSW process efficiency.

9.2 Future scope

- Alternative facesheet, core, and disc insert materials with different dimensions, including different alloys and composites, can potentially enhance the performance of hybrid joined-fabricated sandwich structures. Different adhesive materials and optimizing FSSW process parameters, such as rotational speed, plunge depth, and tool design, can be explored to fabricate sandwich structures. These processes can also be used to join one sandwich sheet to another, creating larger or more complex structures.
- The scalability of hybrid processes for large-scale industrial applications can be explored to assess feasibility. Long-term durability and performance of hybrid joints under various environmental conditions, such as temperature, humidity, and corrosive environments, can provide valuable insights.
- Hybrid joining methods that combine other welding methods with adhesive bonding methods can be developed and tested to improve joint strength and durability.
- Machine learning and artificial intelligence can be utilized to predict and optimize the fabrication process parameters and joint performance, leading to significant advancements in the efficiency and effectiveness of joining processes.
- Fatigue testing and non-destructive testing techniques can be done to inspect hybrid joints in sandwich structures.

References

[1] Bitzer T. Honeycomb Technology. 1997. https://doi.org/10.1007/978-94-011-5856-5.

[2] Gibson LJ, Ashby MF. Cellular Solids: Structure and Properties. Cambridge Solid State Science Series; 1997.

[3] Hedayati R, Sadighi M, Aghdam MM, Zadpoor AA. Mechanical properties of additively manufactured thick honeycombs. Materials (Basel) 2016;9:613. https://doi.org/10.3390/ma9080613.

[4] Malek S, Gibson L. Effective elastic properties of periodic hexagonal honeycombs. Mech Mater 2015;91:226–40. https://doi.org/10.1016/j.mechmat.2015.07.008.

[5] Sorohan S, Sandu M, Constantinescu DM, Sandu AG. On the evaluation of mechanical properties of honeycombs by using finite element analyses. INCAS Bull 2015;7:135.

[6] Qiu C, Guan Z, Jiang S, Li Z. A method of determining effective elastic properties of honeycomb cores based on equal strain energy. Chinese J Aeronaut 2017;30:766–79. https://doi.org/10.1016/j.cja.2017.02.016.

[7] Zhao Y, Ge M, Ma W. The effective in-plane elastic properties of hexagonal honeycombs with consideration for geometric nonlinearity. Compos Struct 2020;234:111749. https://doi.org/10.1016/j.compstruct.2019.111749.

[8] Penado FE. Effective Elastic Properties of Honeycomb Core with Fiber-Reinforced Composite Cells. Open J Compos Mater 2013;03:89–96. https://doi.org/10.4236/ojcm.2013.34009.

[9] Catapano A, Montemurro M. A multi-scale approach for the optimum design of sandwich plates with honeycomb core. Part II: The optimisation strategy. Compos Struct 2014;118:677–90. https://doi.org/10.1016/j.compstruct.2014.07.058.

[10] Kelsey S, Gellatly RA, Clark BW. The shear modulus of foil honeycomb cores: A theoretical and experimental investigation on cores used in sandwich construction. Aircr Eng 1958;30:294–302.

[11] Pan SD, Wu LZ, Sun YG, Zhou ZG, Qu JL. Longitudinal shear strength and failure process of honeycomb cores. Compos Struct 2006;72:42–6. https://doi.org/10.1016/j.compstruct.2004.10.011.

[12] Goswami S. On the prediction of effective material properties of cellular hexagonal honeycomb core. J Reinf Plast Compos 2006;25:393–405. https://doi.org/10.1177/0731684405060567.

[13] Masters IG, Evans KE. Models for the elastic deformation of honeycombs. Compos Struct 1996;35:403–22.

[14] Elsevier C, Burton WS, Noor AK. Computer mathods in applied mechmics and enginaarlng Assessment of continuum models for sandwich panel honeycomb cores. Methods Appl Mech Engrg 1997;145:341–60.

[15] Balawi S, Abot JL. The effect of honeycomb relative density on its effective in-plane elastic moduli: An experimental study. Compos Struct 2008;84:293–9. https://doi.org/10.1016/j.compstruct.2007.08.009.

[16] Mukhopadhyay T, Adhikari S. Equivalent in-plane elastic properties of irregular honeycombs: An analytical approach. Int J Solids Struct 2016;91:169–84.

https://doi.org/10.1016/j.ijsolstr.2015.12.006.

[17] Aydincak I, Kayran A. An approach for the evaluation of effective elastic properties of honeycomb cores by finite element analysis of sandwich panels. J Sandw Struct Mater 2009;11:385–408. https://doi.org/10.1177/1099636209102891.

[18] Grediac M. A finite element study of the transverse shear in honeycomb cores. Int J Solids Struct 1993;30:1777–88.

[19] Meraghni F, Desrumaux F, Benzeggagh ML. Mechanical behaviour of cellular core for structural sandwich panels. Compos Part A Appl Sci Manuf 1999;30:767–79. https://doi.org/10.1016/S1359-835X(98)00182-1.

[20] Johnson AF, Sims GD. Mechanical properties and design of sandwich materials. Composites 1986;17:321–8. https://doi.org/10.1016/0010-4361(86)90749-4.

[21] Kopp R, Abratis C, Nutzmann M. Lightweight sandwich sheets for automobile applications. Prod Eng Res Dev 2004;11:55–60.

[22] Kee Paik J, Thayamballi AK, Sung Kim G. Strength characteristics of aluminum honeycomb sandwich panels. Thin-Walled Struct 1999;35:205–31. https://doi.org/10.1016/S0263-8231(99)00026-9.

[23] Zhang Y, Yan L, Zhang W, Su P, Han B, Guo S. Metallic tube-reinforced aluminum honeycombs: Compressive and bending performances. Compos Part B Eng 2019;171:192–203. https://doi.org/10.1016/j.compositesb.2019.04.044.

[24] Yan L, Zhu K, Chen N, Zheng X, Quaresimin M. Energy-absorption characteristics of tube-reinforced absorbent honeycomb sandwich structure. Compos Struct 2021;255:112946. https://doi.org/10.1016/j.compstruct.2020.112946.

[25] Wang Z, Qin Q, Chen S, Yu X, Li H, Wang TJ. Compressive crushing of novel aluminum hexagonal honeycombs with perforations: Experimental and numerical investigations. Int J Solids Struct 2017;126–127:187–95. https://doi.org/10.1016/j.ijsolstr.2017.08.005.

[26] Liu Q, Fu J, Wang J, Ma J, Chen H, Li Q, et al. Axial and lateral crushing responses of aluminum honeycombs filled with EPP foam. Compos Part B Eng 2017;130:236–47. https://doi.org/10.1016/j.compositesb.2017.07.041.

[27] Al Antali A, Umer R, Zhou J, Cantwell WJ. The energy-absorbing properties of composite tube-reinforced aluminum honeycomb. Compos Struct 2017;176:630–9. https://doi.org/10.1016/j.compstruct.2017.05.063.

[28] Ozbek Y, Yildirim C, Yakin F, Topal S, Yildiz M, Sas H. Enhancing adhesive bonding and mechanical properties of composite sandwich panels through atmospheric plasma activation. Polym Compos 2024. https://doi.org/10.1002/pc.29290.

[29] Zebrine D, Anders M, Centea T, Nutt S. Path-dependent bond-line evolution in equilibrated core honeycomb sandwich structures. Adv Manuf Polym Compos Sci 2020;6:127–41. https://doi.org/10.1080/20550340.2020.1800194.

[30] Thomas WM. Improvements relating to friction welding 1991.

[31] Threadgill PL. Terminology in friction stir welding. Sci Technol Weld Join 2007;12:357–60. https://doi.org/10.1179/174329307X197629.

[32] Gerlich A, Su P, North TH. Tool penetration during friction stir spot welding of Al and Mg

alloys. J Mater Sci 2005;40:6473–81. https://doi.org/10.1007/s10853-005-1568-9.

[33] Rana PK, Narayanan RG, Kailas S V. Effect of rotational speed on friction stir spot welding of AA5052-H32/HDPE/AA5052-H32 sandwich sheets. J Mater Process Technol 2018;252:511–23. https://doi.org/10.1016/j.jmatprotec.2017.10.016.

[34] Smith CB, Hinrichs JF, Ruehl PC. Friction Stir and Friction Stir Spot Welding-Lean , Mean and Green, 2004.

[35] Zhang Z, Yang X, Zhang J, Zhou G, Xu X, Zou B. Effect of welding parameters on microstructure and mechanical properties of friction stir spot welded 5052 aluminum alloy. Mater Des 2011;32:4461–70. https://doi.org/10.1016/j.matdes.2011.03.058.

[36] Uğurlu M, Çakan A. The Effect of Tool Rotation Speed on Mechanical Properties of Friction Stir Spot Welded (FSSW) AA7075-T6 Aluminium Alloy Sheets. Eur Mech Sci 2019;3:97–101. https://doi.org/10.26701/ems.520139.

[37] Prasomthong S, Sangsiri P, Kimapong K. Friction Stir Spot Welding of AA5052 Aluminum Alloy and C11000 Copper Lap Joint. Int J Adv Cult Technol 2015;3:145–52. https://doi.org/10.17703/ijact.2015.3.1.145.

[38] Rana PK, Narayanan RG, Kailas S V. Friction stir spot welding of AA5052-H32/HDPE/AA5052-H32 sandwich sheets at varying plunge speeds. Thin-Walled Struct 2019;138:415–29. https://doi.org/10.1016/j.tws.2019.02.016.

[39] Rao HM, Yuan W, Badarinarayan H. Effect of process parameters on mechanical properties of friction stir spot welded magnesium to aluminum alloys. Mater Des 2015;66:235–45. https://doi.org/https://doi.org/10.1016/j.matdes.2014.10.065.

[40] Bozzi S, Helbert-Etter AL, Baudin T, Klosek V, Kerbiguet JG, Criqui B. Influence of FSSW parameters on fracture mechanisms of 5182 aluminium welds. J Mater Process Technol 2010;210:1429–35. https://doi.org/10.1016/j.jmatprotec.2010.03.022.

[41] Mitlin D, Radmilovic V, Pan T, Chen J, Feng Z, Santella ML. Structure-properties relations in spot friction welded (also known as friction stir spot welded) 6111 aluminum. Mater Sci Eng A 2006;441:79–96. https://doi.org/10.1016/j.msea.2006.06.126.

[42] Arul SG, Miller SF, Kruger GH, Pan TY, Mallick PK, Shih AJ. Experimental study of joint performance in spot friction welding of 6111-T4 aluminium alloy. Sci Technol Weld Join 2008;13:629–37. https://doi.org/10.1179/136217108X363900.

[43] Bilici MK, Yukler AI. Effects of welding parameters on friction stir spot welding of high density polyethylene sheets. Mater Des 2012;33:545–50. https://doi.org/10.1016/j.matdes.2011.04.062.

[44] Shen Z, Yang X, Zhang Z, Cui L, Yin Y. Mechanical properties and failure mechanisms of friction stir spot welds of AA 6061-T4 sheets. Mater Des 2013;49:181–91. https://doi.org/10.1016/j.matdes.2013.01.066.

[45] Choi DH, Ahn BW, Lee CY, Yeon YM, Song K, Jung SB. Formation of intermetallic compounds in Al and Mg alloy interface during friction stir spot welding. Intermetallics 2011;19:125–30. https://doi.org/10.1016/j.intermet.2010.08.030.

[46] Lin YC, Liu JJ, Lin BY, Lin CM, Tsai HL. Effects of process parameters on strength of Mg alloy AZ61 friction stir spot welds. Mater Des 2012;35:350–7. https://doi.org/10.1016/j.matdes.2011.08.050.

[47] Yin YH, Sun N, North TH, Hu SS. Influence of tool design on mechanical properties of AZ31 friction stir spot welds. Sci Technol Weld Join 2010;15:81–6. https://doi.org/10.1179/136217109X12489665059384.

[48] Lin PC, Pan J, Pan T. Failure modes and fatigue life estimations of spot friction welds in lap-shear specimens of aluminum 6111-T4 sheets. Part 2: Welds made by a flat tool. Int J Fatigue 2008;30:90–105. https://doi.org/10.1016/j.ijfatigue.2007.02.017.

[49] Badarinarayan H, Shi Y, Li X, Okamoto K. Effect of tool geometry on hook formation and static strength of friction stir spot welded aluminum 5754-O sheets. Int J Mach Tools Manuf 2009;49:814–23. https://doi.org/10.1016/j.ijmachtools.2009.06.001.

[50] Garg A, Bhattacharya A. On lap shear strength of friction stir spot welded AA6061 alloy. J Manuf Process 2017;26:203–15. https://doi.org/10.1016/j.jmapro.2017.02.019.

[51] Feng M, Li Y, Zhao C, Luo Z. Mechanical properties and interface morphology of Mg/Al ultrasonic spot weld bonding welds. Sci Technol Weld Join 2016;21:688–99. https://doi.org/10.1080/13621718.2016.1144262.

[52] Afkhami S, Amraei M, Gardner L, Piili H, Wadee MA, Salminen A, et al. Mechanical performance and design optimisation of metal honeycombs fabricated by laser powder bed fusion. Thin-Walled Struct 2022;180:109864. https://doi.org/10.1016/j.tws.2022.109864.

[53] Pierre J, Iervolino F, Farahani RD, Piccirelli N, Lévesque M, Therriault D. Material extrusion additive manufacturing of multifunctional sandwich panels with load-bearing and acoustic capabilities for aerospace applications. Addit Manuf 2023;61. https://doi.org/10.1016/j.addma.2022.103344.

[54] Wang Z, Wang Y, He J, Dong K, Zhang G, Li W, et al. Additive Manufacturing of Continuous Fiber-Reinforced Polymer Composite Sandwich Structures with Multiscale Cellular Cores. Chinese J Mech Eng Addit Manuf Front 2023;2:100088. https://doi.org/10.1016/j.cjmeam.2023.100088.

[55] Antolak-Dudka A, Płatek P, Durejko T, Baranowski P, Małachowski J, Sarzyński M, et al. Static and dynamic loading behavior of Ti6Al4V honeycomb structures manufactured by Laser Engineered Net Shaping (LENSTM) technology. Materials (Basel) 2019;12. https://doi.org/10.3390/ma12081225.

[56] Oliveira PR, Bonaccorsi AMS, Panzera TH, Christoforo AL, Scarpa F. Sustainable sandwich composite structures made from aluminium sheets and disposed bottle caps. Thin-Walled Struct 2017;120:38–45. https://doi.org/10.1016/j.tws.2017.08.013.

[57] De Matteis G, Landolfo R. Mechanical fasteners for cladding sandwich panels: interpretative models for shear behaviour. Thin-Walled Struct 1999;35:61–79. https://doi.org/10.1016/S0263-8231(99)00017-8.

[58] Pickin CG, Young K, Tuersley I. Joining of lightweight sandwich sheets to aluminium using self-pierce riveting. Mater Des 2007;28:2361–5. https://doi.org/10.1016/j.matdes.2006.08.003.

[59] Xie Y, Meng X, Wang F, Jiang Y, Ma X, Wan L, et al. Insight on corrosion behavior of friction stir welded AA2219/AA2195 joints in astronautical engineering. Corros Sci 2021;192:109800. https://doi.org/10.1016/j.corsci.2021.109800.

[60] Singh VP, Patel SK, Ranjan A, Kuriachen B. Recent research progress in solid state friction-stir welding of aluminium–magnesium alloys: A critical review. J Mater Res Technol 2020;9:6217–56. https://doi.org/10.1016/j.jmrt.2020.01.008.

[61] Rana PK, Narayanan RG, Kailas S V. Friction stir spot welding of AA5052-H32/HDPE/AA5052-H32 sandwich sheets at varying plunge speeds. Thin-Walled Struct 2019;138:415–29. https://doi.org/10.1016/j.tws.2019.02.016.

[62] Ravi KK, Narayanan RG, Rana PK. Friction Stir Spot Welding of Al6082-T6/HDPE/Al6082-T6/HDPE/Al6082-T6 sandwich sheets: Hook formation and lap shear test performance. J Mater Res Technol 2019;8:615–22. https://doi.org/10.1016/j.jmrt.2018.05.011.

[63] Naik RK, Panda SK, Racherla V. A new method for joining metal and polymer sheets in sandwich panels for highly improved interface strength. Compos Struct 2020;251. https://doi.org/10.1016/j.compstruct.2020.112661.

[64] Pouranvari M, Safikhani E. Mechanical properties of martensitic stainless steel weld/adhesive hybrid bonds. Sci Technol Weld Join 2018;23:227–33. https://doi.org/10.1080/13621718.2017.1363453.

[65] Wang H, Liu L, Liu F. The characterization investigation of laser-arc-adhesive hybrid welding of Mg to Al joint using Ni interlayer. Mater Des 2013;50:463–6. https://doi.org/10.1016/j.matdes.2013.02.085.

[66] Campilho RDSG, Pinto AMG, Banea MD, Da Silva LFM. Optimization study of hybrid spot-welded/bonded single-lap joints. Int J Adhes Adhes 2012;37:86–95. https://doi.org/10.1016/j.ijadhadh.2012.01.018.

[67] de Almeida FJS, Campilho RDSG, Silva FJG. Strength prediction of T-peel joints by a hybrid spot-welding/adhesive bonding technique. J Adhes 2018;94:181–98. https://doi.org/10.1080/00218464.2016.1244013.

[68] Marques GP, Campilho RDSG, Da Silva FJG, Moreira RDF. Adhesive selection for hybrid spot-welded/bonded single-lap joints: Experimentation and numerical analysis. Compos Part B Eng 2016;84:248–57. https://doi.org/10.1016/j.compositesb.2015.09.002.

[69] Zhang X, Cai Z yi, Gao J xin, Wang M wei. Numerical analysis of face sheet/core debonding failure in the plastic forming of aluminum foam sandwich panel. Int J Adv Manuf Technol 2023;128:2285–300. https://doi.org/10.1007/s00170-023-12087-5.

[70] Kulkarni SS, Gupta V, Ortiz A, Das H, Upadhyay P, Barker E, et al. Determining cohesive parameters for modeling interfacial fracture in dissimilar-metal friction stir welded joints. Int J Solids Struct 2021;216:200–10. https://doi.org/10.1016/j.ijsolstr.2021.01.023.

[71] Rana PK, Narayanan RG. Numerical and experimental response of FSSW of AA5052-H32/epoxy/AA5052-H32 sandwich sheets with varying core properties. Int J Mater Form 2021;14:1297–317. https://doi.org/10.1007/s12289-020-01596-3.

[72] Kanani AY, Liu Y, Hughes DJ, Ye J, Hou X. Fracture mechanisms of hybrid adhesive bonded joints: Effects of the stiffness of constituents. Int J Adhes Adhes 2020;102:102649. https://doi.org/10.1016/j.ijadhadh.2020.102649.

[73] Naik RK, Das AK, Mahale PR, Panda SK, Racherla V. Design optimization of high interface strength metal–polymer–metal sandwich panels. Compos Part A Appl Sci Manuf 2023;171:107544. https://doi.org/10.1016/j.compositesa.2023.107544.

[74] Geng J, Liu C. A methodology for parameter identification and calibration of the cohesive element based meso-scale concrete model. Constr Build Mater 2023;393. https://doi.org/10.1016/j.conbuildmat.2023.132075.

[75] Feng D, Wu J. Phase- fi eld regularized cohesive zone model (CZM) and size e ff ect of concrete 2018;197:66–79.

[76] Saikia PJ, Kumar M, Kumar A, Muthu N. Experimental estimation and numerical validation of cohesive zone parameters in hydroxyl functionalized MWCNTs-reinforced CFRP under pure mode II loading. Polym Compos 2024.

[77] Kumar M, Kumar P, Bhadauria SS. Numerical simulation of delamination growth in fiber reinforced polymer laminates using cohesive zone modeling. Mech Adv Mater Struct 2022;29:213–29. https://doi.org/10.1080/15376494.2020.1758257.

[78] Jang J, Sung M, Han S, Yu WR. Prediction of delamination of steel-polymer composites using cohesive zone model and peeling tests. Compos Struct 2017;160:118–27. https://doi.org/10.1016/j.compstruct.2016.10.025.

[79] Liu JG, Liu W, Wang JX. Influence of interfacial adhesion strength on formability of AA5052/polyethylene/AA5052 sandwich sheet. Trans Nonferrous Met Soc China (English Ed 2012;22:s395–401. https://doi.org/10.1016/S1003-6326(12)61737-3.

[80] Stigh U, Alfredsson KS, Andersson T, Biel A, Carlberger T, Salomonsson K. Some aspects of cohesive models and modelling with special application to strength of adhesive layers. Int J Fract 2010;165:149–62. https://doi.org/10.1007/s10704-010-9458-9.

[81] Gilchrist MD, Smith RA. Development of cohesive fatigue cracks in T-peel joints. Int J Adhes Adhes 1993;13:53–7. https://doi.org/10.1016/0143-7496(93)90009-X.

[82] Campilho RDSG, Pinto AMG, Banea MD, Da Silva LFM. Optimization study of hybrid spot-welded/bonded single-lap joints. Int J Adhes Adhes 2012;37:86–95. https://doi.org/10.1016/j.ijadhadh.2012.01.018.

[83] Park H, Kim SJ, Lee J, Kim JH, Kim D. Delamination behavior analysis of steel/polymer/steel high-strength laminated sheets in a V-die bending test. Int J Mech Sci 2020;173. https://doi.org/10.1016/j.ijmecsci.2020.105430.

[84] Akour SN, Maaitah HZ. Effect of core material stiffness on sandwich panel behavior beyond the yield limit. WCE 2010 - World Congr Eng 2010 2010;2:1321–30.

[85] Liu Y, Liu W, Gao W. Out-of-plane shear property analysis of Nomex honeycomb sandwich structure. J Reinf Plast Compos 2021;40:165–75. https://doi.org/10.1177/0731684420943285.

[86] Kanit T, N'Guyen F, Forest S, Jeulin D, Reed M, Singleton S. Apparent and effective physical properties of heterogeneous materials: Representativity of samples of two materials from food industry. Comput Methods Appl Mech Eng 2006;195:3960–82. https://doi.org/10.1016/j.cma.2005.07.022.

[87] Moulinec H, Suquet P. A numerical method for computing the overall response of nonlinear composites with complex microstructure. Comput Methods Appl Mech Eng 1998;157:69–94.

[88] Xia ZH, Zhang YF, Ellyin F. On Application of Periodic Boundary Conditions in Micro/Meso Multi-Scale Analyses of Composites. Key Eng Mater 2007;345–346:983–6. https://doi.org/10.4028/www.scientific.net/KEM.345-346.983.

[89] Shedbale AS, Singh I V., Mishra BK. Heterogeneous and homogenized models for predicting the indentation response of particle reinforced metal matrix composites. Int J Mech Mater Des 2017;13:531–52. https://doi.org/10.1007/s10999-016-9352-3.

[90] Li X, Liu Q, Zhang J. A micro-macro homogenization approach for discrete particle assembly - Cosserat continuum modeling of granular materials. Int J Solids Struct 2010;47:291–303. https://doi.org/10.1016/j.ijsolstr.2009.09.033.

[91] Gornet L, Marguet S, Marckmann G. Finite element modeling of Nomex® honeycomb cores: Failure and effective elastic properties. Comput Mater Contin 2006;4:63–74.

[92] Ijaz H, Saleem W, Zain-Ul-Abdein M, Mabrouki T, Rubaiee S, Salmeen Bin Mahfouz A. Finite Element Analysis of Bend Test of Sandwich Structures Using Strain Energy Based Homogenization Method. Adv Mater Sci Eng 2017;2017. https://doi.org/10.1155/2017/8670207.

[93] Dirrenberger J, Forest S, Jeulin D. Effective elastic properties of auxetic microstructures: Anisotropy and structural applications. Int J Mech Mater Des 2013;9:21–33. https://doi.org/10.1007/s10999-012-9192-8.

[94] Rakesh P, More A, Kumar M, Muthu N. Probabilistic failure prediction in a double composite cantilever beam with single and double source uncertainty. Compos Struct 2022;279:114870. https://doi.org/10.1016/j.compstruct.2021.114870.

[95] Xia Z, Zhang Y, Ellyin F. A unified periodical boundary conditions for representative volume elements of composites and applications. Int J Solids Struct 2003;40:1907–21. https://doi.org/10.1016/S0020-7683(03)00024-6.

[96] Somireddy M, Czekanski A, Singh CV. Development of constitutive material model of 3D printed structure via FDM. Mater Today Commun 2018;15:143–52. https://doi.org/10.1016/j.mtcomm.2018.03.004.

[97] Sun CT, Vaidya RS. Prediction of composite properties from a representative volume element. Compos Sci Technol 1996;56:171–9.

[98] Zhang J, Ashby MF. The out-of-plane properties of honeycombs. Int J Mech Sci 1992;34:475–89.

[99] Terada K, Hori M, Kyoya T, Kikuchi N. Simulation of the multi-scale convergence in computational homogenization approaches. Int J Solids Struct 2000;37:2285–311. https://doi.org/10.1016/S0020-7683(98)00341-2.

[100] ASTM E8. ASTM E8/E8M standard test methods for tension testing of metallic materials 1. Annu B ASTM Stand 4 2010;i:1–27. https://doi.org/10.1520/E0008.

[101] ASTM A. C365/C365M-11a Standard Test Method for Flatwise Compressive Properties of Sandwich Cores. Washingt ASTM 2011.

[102] ASTM Standard E9-09. Standard Test Methods of Compression Testing of Metallic Materials at Room Temperature. Annu B ASTM Stand 2012;3.01:92–100. https://doi.org/10.1520/E0009-09.2.

[103] Saju TP, Narayanan RG, Roy BS. Effect of pinless tool shoulder diameter on dieless friction stir extrusion joining of AA 5052-H32 and AA 6061-T6 aluminum alloy sheets. J Mech Sci Technol 2019;33:3981–97. https://doi.org/10.1007/s12206-019-0136-1.

[104] ASTM Standard C273. ASTM C393-06 Standard Test Method for Core Shear Properties of Sandwich Constructions by Beam Flexure. ASTM Int 2010;i:1–7. https://doi.org/10.1520/C0273.

[105] Xu J, Wu Y, Wang L, Li J, Yang Y, Tian Y, et al. Compressive properties of hollow lattice truss reinforced honeycombs (Honeytubes) by additive manufacturing: Patterning and tube alignment effects. Mater Des 2018;156:446–57. https://doi.org/10.1016/j.matdes.2018.07.019.

[106] Pathak N, Bandyopadhyay K, Sarangi M, Panda SK. Microstructure and mechanical performance of friction stir spot-welded aluminum-5754 sheets. J Mater Eng Perform 2013;22:131–44. https://doi.org/10.1007/s11665-012-0244-x.

[107] Uematsu Y, Tokaji K. Comparison of fatigue behaviour between resistance spot and friction stir spot welded aluminium alloy sheets. Sci Technol Weld Join 2009;14:62–71. https://doi.org/10.1179/136217108X338908.

[108] Camanho PP, Davila CG, de Moura MF. Numerical Simulation of Mixed-Mode Progressive Delamination in Composite Materials. J Compos Mater 2003;37:1415–38. https://doi.org/10.1177/0021998303034505.

[109] Alfano G, Crisfield MA. Finite element interface models for the delamination analysis of laminated composites: Mechanical and computational issues. Int J Numer Methods Eng 2001;50:1701–36. https://doi.org/10.1002/nme.93.

[110] Qu Y, Sun Z, Spettmann C, Xing B, Xia Y, Zhou Q. Model development of laser welding in lithium-ion prismatic cell for enhancing failure prediction. Int J Mech Sci 2023;259. https://doi.org/10.1016/j.ijmecsci.2023.108637.

[111] Naik RK, Panda SK, Racherla V. Failure analysis of metal-polymer-metal sandwich panels with wire mesh interlayers: Finite element modeling and experimental validation. Compos Struct 2022;280. https://doi.org/10.1016/j.compstruct.2021.114813.

[112] Bagheri B, Abbasi M, Givi M. Effects of Vibration on Microstructure and Thermal Properties of Friction Stir Spot Welded (FSSW) Aluminum Alloy (Al5083). Int J Precis Eng Manuf 2019;20:1219–27. https://doi.org/10.1007/s12541-019-00134-9.

[113] Darwish SM, Al-Samhan AM. Peel and shear strength of spot-welded and weld-bonded dissimilar thickness joints. J Mater Process Technol 2004;147:51–9. https://doi.org/10.1016/j.jmatprotec.2003.11.029.

[114] Pires VDC, Ribeiro FCC, Carbas RJC, Marques EAS, da Silva LFM. The reduction of stress concentrations in adhesive joints with the use of curved aluminum adherends. Mech Adv Mater Struct 2023. https://doi.org/10.1080/15376494.2023.2299936.

[115] Bai R, Ou H, Peng K, Wu W, Lei Z, Liu T, et al. Failure study of honeycomb sandwich structure with embedded part under axial pullout loading. Thin-Walled Struct 2020;146:106489. https://doi.org/10.1016/j.tws.2019.106489.

[116] Rana PK, Ganesh Narayanan R, Kailas S V. Influence of Tool Plunge Depth During Friction Stir Spot Welding of AA5052-H32/HDPE/AA5052-H32 Sandwich Sheets. In: Dixit US, Narayanan RG, editors. Strength. Join. by Plast. Deform., Singapore: Springer Singapore; 2019, p. 95–121.

[117] Naik RK, Panda SK, Racherla V. Failure analysis of metal-polymer-metal sandwich panels with wire mesh interlayers: Finite element modeling and experimental validation. Compos Struct 2022;280:114813. https://doi.org/10.1016/j.compstruct.2021.114813.

[118] Kulkarni SS, Das H, Tamayo DR, Ma X, Wang T, Zhang D, et al. A Combined Experimental and Modeling Approach to Investigate the Performance of Joint Between AZ31 Magnesium and Uncoated DP590 Steel Using Friction Stir-Assisted Scribe Technique. J Mater Eng Perform 2021;30:8296–308. https://doi.org/10.1007/s11665-021-06060-0.

[119] D6671M A. Standard Test Method for Mixed Mode I-Mode II Interlaminar Fracture Toughness of Unidirectional Fiber Reinforced Polymer Matrix Composites. ASTM Int 2006:15. https://doi.org/10.1520/D6671.

[120] Quispitupa A, Berggreen C, Carlsson LA. Design analysis of the mixed mode bending sandwich specimen. J Sandw Struct Mater 2010;12:253–72. https://doi.org/10.1177/1099636209104533.

[121] Quispitupa A, Berggreen C, Carlsson LA. On the analysis of a mixed mode bending sandwich specimen for debond fracture characterization. Eng Fract Mech 2009;76:594–613. https://doi.org/10.1016/j.engfracmech.2008.12.008.

List of publications

Journals

[1] A. Kumar, N. Muthu, and R. G. Narayanan, “Equivalent orthotropic properties of periodic honeycomb structure: strain-energy approach and homogenization,” *International Journal of Mechanics and Materials in Design*, no. 0123456789, 2022, https://doi.org/10.1007/s10999-022-09620-x.

[2] A. Kumar, R. G. Narayanan, and N. Muthu, “Manufacture of honeycomb core sandwich structures by hybrid approaches: Analysis using lab scale experiments and numerical simulation,” *Thin-Walled Structures*, vol. 198, no. November 2023, 2024, https://doi.org/10.1016/j.tws.2024.111739.

[3] A. Kumar, N. Muthu, and R. Ganesh Narayanan, “Prediction of peel strength of sandwich sheets made of aluminium alloys fabricated by friction stir spot welding based hybrid process using cohesive zone modeling and finite element simulations,” *Engineering Failure Analysis*, vol. 162, no. February, pp. 1–24, 2024, https://doi.org/10.1016/j.engfailanal.2024.108381.

[4] A. Kumar, R. G. Narayanan, and N. Muthu, “Enhancing the Performance of Honeycomb Core Sandwich Panels through Friction Stir Spot Welding Strategies and Fracture of Lap Shear Specimen,” *Mechanics of Advanced Materials and Structures*, 2024, https://doi.org/10.1080/15376494.2024.2388883.

[5] A. Kumar, P. J. Saikia, R. G. Narayanan, and N. Muthu, “Experimental and numerical analysis of mixed mode bending of adhesive-bonded and hybrid honeycomb core sandwich structures,” *International Journal of Solids and Structures.*, p. 113177, 2024, https://doi.org/10.1016/j.ijsolstr.2024.113177.

Book chapter

[1] A. Kumar, R. G. Narayanan, and N. Muthu, “A preliminary investigation on friction stir spot welding of honeycomb core sandwich sheet with disc insert,” in *Reference Module in Materials Science and Materials Engineering*, Elsevier, 2023, https://doi.org/10.1016/B978-0-323-96020-5.00175-8.

Conferences

[1] A. Kumar, N. Muthu, and R. G. Narayanan, “Equivalent In-plane Elastic Properties of Periodic Re-entrant Honeycombs – Strain-energy approach and FE modelling,” in *International Conference on Experimental and Computational Methods in Manufacturing (ICECMM 2021)*, 2021, p. paper_48, [Online]. Available: https://drive.google.com/file/d/15AavwXIoNfR7C27ISsOypNnaQMauuzc9/view?usp=sharing.

[2] A. Kumar, R. Ganesh Narayanan, and N. Muthu, “Friction Stir Spot Welding of Honeycomb Core Sandwich Structure,” in *Low Cost Manufacturing Technologies*, 2023, pp. 73–79, https://doi.org/10.1007/978-981-19-8452-5_6.